TECHNISCHE UNIVERSITÄT MÜNCHEN
Lehrstuhl für Physik funktionaler Schichtsysteme, E10

Spin Waves in Antidot Lattices: From Quantization to Magnonic Crystals

Sebastian Neusser

Short Abstract

Spin-wave (SW) propagation was studied in periodic arrays of 120 nm large holes, so called antidot lattices (ADLs). They were created by focused ion beam lithography into 25 nm thin permalloy $Ni_{80}Fe_{20}$ films. GHz SW spectroscopy was performed all electrically by micro- and nanoscale coplanar waveguides. The ADL periodicity ranged from 300 to 4000 nm. For 300 nm periodicity, coherent backscattering was found to cause magnonic miniband formation in the SW dispersion and large group velocities of 6 km/s. For 800 nm periodicity and long SW wave lengths, the ADL showed signatures of an unstructured plain film with effective properties, i.e. metamaterial behavior. These effectively continuous properties were also found to describe well SW transmission into the ADL.

Es wurde Spinwellen (SW)-Propagation in periodischen Anordnungen von 120nm großen Löchern, so genannten Antidot-Gittern (ADL), untersucht. Diese wurden mittels fokussierter Ionenstrahllithographie in 25nm dünnen Permalloy $Ni_{80}Fe_{20}$ Filmen erzeugt. GHz-SW- Spektroskopie wurde rein elektrisch mittels mikro- und nanoskaligen koplanaren Wellenleitern durchgeführt. Die ADL Periodizität reichte von 300 bis 800nm. Bei 300nm-Periodizität wurde kohärente Rückstreuung als Ursache für magnonische Miniband-Bildung in der Spinwellen-Dispersion und hohe Gruppengeschwindigkeiten von 6km/s gefunden. Bei 800nm-Periodizität und langen SW-Wellenlängen zeigte das ADL Kennzeichen eines unstrukturierten Films mit effektiven Eigenschaften, d.h. Metamaterial-Eigenschaften. Auf Basis dieser effektiv kontinuierlichen Eigenschaften wurde auch die Transmission von SW in das ADL hinein gut beschrieben.

Abstract

Nanomagnetism is a field of research where one aims for modification and control of magnetic properties through tailored geometry on the nanoscale. Nanostructured ferromagnets offer broad functionality due to manifold magnetization states they exist in [Sta10]. Dynamic phenomena in such systems in the GHz range have generated increasing scientific interest in recent years. Here spin waves (SWs) or magnons are of particular attraction. Magnons are the particle-like quantized spin excitations, whereas their wave-like counterpart is referred to as spin waves. Advancements in patterning techniques have recently allowed to precisely tailor these excitations [Neu09].

In this thesis, 22 to 30 nm thin films of permalloy, i.e. $Ni_{80}Fe_{20}$, with saturation magnetization M_{Sat} ranging from 760 to 830 kA/m are nanostructured by focussed ion beam lithography to create a periodic square array of circular holes, i.e. an antidot lattice (ADL). From sample to sample, the edge-to-edge separation is varied between 40 and 4000 nm. The hole diameter is $86 - 120$ nm In this parameter regime, the following phenomena have been observed:

- **Quantization and localization of spin waves.** For, both, large edge-to-edge separations and periodicities p of the ADL, SW quantization is observed. Different eigenmodes are resolved experimentally, which reside in different parts of the ADL. A propagating mode is found to extend through the lattice in spin-wave nanochannels formed in between neighboring holes perpendicular to the external field. The measured propagation characteristics of this mode show a strong characteristic anisotropy. Group velocities v_g between 2.5 and 3.5 km/s are measured. Furthermore, a localized mode is found to exist in between neighboring holes parallel to the field ($v_g = 0$).

- **Effectively continuous material properties.** For SW excitations of wavelength λ_{SW}, which are much larger than the periodicity p,

it is found that a $p = 800$ nm ADL behaves as being an effectively continuous plain film with a reduced saturation magnetization $M_{\mathrm{Sat}}^{\star} = 600$ kA/m. The holes have a diameter of $d = 120$ nm. This is verified in an experiment where long-wavelength SWs are injected into such an ADL. Reflectivity and transmittivity are well described by the wave vector mismatch of two (effectively) continuous materials of different magnetic properties. The ADL is thus found to act as a metamaterial for spin waves.

- **Magnonic properties.** Movement in a periodic potential is known to alter the propagation properties of wave-like excitations. This is investigated in this thesis for spin waves. Allowed minibands and forbidden frequency gaps are provoked by, e.g., coherent backscattering. Results on SWs suggest that, starting from large edge-to-edge separation (large p), localized modes residing close to holes' edges become coupled for sufficiently small p. Being similar to a tight-binding approach, this is in contrast to the mechanism based on coherent backscattering from periodic holes and pitches as reported for photonic, plasmonic, and phononic crystals. Advantageously large group velocities $v_{\mathrm{g}} = 5$ to 6 km/s are found for the magnonic mode which is in excess of the plain film value at the same magnetic field value.

Experimental methods used to obtain these results included all electrical spin-wave spectroscopy (AESWS). Highly sensitive and electromagnetically isolated SW emitters and detectors with micro/nanoscale extensions were designed and fabricated using electron-beam nanolithography. For the first time SWs propagating through ferromagnetic nanostructures were observed all electrically using a broadband magnetic probe station. Experiments were modeled using micromagnetic simulations. In the course of this thesis, scientific collaborations were initiated. Providing tailored ferromagnetic nanostructures to experimental groups in Regensburg, Germany[1], and Perugia, Italy,[2] spin-wave propagation was studied using the spatially and time resolved magneto-optical Kerr effect and Brillouin light

---

[1]Institut für Experimentelle und Angewandte Physik, Universität Regensburg, D-93040 Regensburg, Germany

[2]CNISM, Dipartimento di Fisica, Universita di Perugia, Via A. Pascoli, I-06123 Perugia, Italy

scattering, respectively. In the theory group of M. Krawczyk in Poznan, Poland,[1] the so-called plane wave method was developed further and applied to the antidot lattices investigated here. The techniques and the theoretical approach were applied to gain further microscopic insight into the spin-wave physics at the nanoscale.

Contents

Scientific Collaboration

Parts of this thesis have been conducted as a scientific collaboration. The author would like to state the content of this collaboration:

- The plane wave method (PWM) has been adapted by Dr. Maciej Krawczyk and Dr. M.L. Sokolovskyy in Poznan, Poland[1] stimulated by experimental data obtained in this thesis. In close collaboration, experimental and theoretical data was analyzed and processed. The main relevant parts of this thesis are Secs. 2.3.2 and 8.1.2.

- Measurements on samples prepared as part of this thesis employing the time resolved magneto optical Kerr effect (MOKE) have been conducted by the collaborators at the Institut für Experimentelle und Angewandte Physik, Universität Regensburg[2] by Hans Bauer, Prof. Dr. Christian Back, and Dr. Georg Woltersdorf. The data was analyzed and processed in close collaboration. The main relevant parts of this thesis are Secs. 3.2.3, 7.3, and 8.4.

- Measurements on samples prepared as part of this thesis employing the magneto optical Kerr effect (MOKE) and Brillouin light scattering have been conducted by the collaborators at the CNISM, Dipartimento di Fisica, Universita di Perugia[3] by Dr. Gianluca Gubbiotti, Dr. Marco Madami, Dr. Silvia Tacchi. Experiments and analysis were carried out by the respective group in close collaboration with the author. The main relevant parts of this thesis are Secs. 3.2.3, 3.2.4, 7.1, 7.4, 8.2, 8.3, and 8.4.

The author would like to express his sincere gratitude for the fruitful collaboration.

---

[1] Surface Physics Division, Faculty of Physics, Adam Mickiewicz University, Umultowska 85, Poznań 61-614, Poland.

[2] Institut für Experimentelle und Angewandte Physik, Universität Regensburg, D-93040 Regensburg, Germany

[3] Via A. Pascoli, I-06123 Perugia, Italy

1 Motivation and State of Research

Technological promises

Transistor based logic gates are widely employed. Novel device circuitry seeks to overcome problems in scalability of the complementary metal-oxide-semiconductor (CMOS) [Raz01] logic circuits. Shrinkage of CMOS logic gates is challenging: firstly, power dissipation will grow for smaller transistor dimensions. Second, interconnection between logic gates becomes difficult to establish for higher integration densities [Khi08a].

One geometry with the potential to provide release from these constrictions is the spin-wave (SW) bus. Firstly, SWs of different frequency can be used for parallel logic operations by superposition of waves[Cho06, Lee08, Khi08b]. Parallel computation promises higher integration and faster processing speed. Second, a further advantage lies in the opportunity to reduce the devices to smaller and smaller scales: the wavelength of magnons is orders of magnitude shorter than that of electromagnetic waves (photons) of the same frequency. Magnonics thus inherently fosters the development of nanoscale devices.

Despite this tempting concept for nanoscale devices, first pioneering experiments have demonstrated logic operations only for prototypes of macroscopic dimensions [Kos05, Sch08a]. For nanoscale integrated circuits, these are the crucial points: First, to overcome the relatively small group velocities v_{g} and short relaxation times τ of SWs. They cause short spatial decay lengths. Second, to obtain reliable and sensitive electrical excitation and detection of SWs with nanoscale emitters and detectors.

Beyond this, further functionality can be obtained from nanostructured devices. Ultimate control and functionality of SW based logic is expected from a so-called magnonic crystal (MC) where an artificially tailored band structure is formed with allowed minibands and forbidden frequency gaps for SWs. This perspective has triggered significant research efforts [AW99, Gul03, Pus03, Kru06, Gub06, Gub07, Gio07, Chu08, Lee09, Chu09a, Top10, Tac10c, Kru10, Ser10].

However, severe obstacles and drawbacks have existed which have hin-

dered potential applications of MCs in microwave electronics. Relevant issues were the following: First, SW propagation velocities v_g were much smaller if compared to unstructured films [Gub06, Gub07, Gio07, Per08, Lee09, Top10, Tac10c] suggesting slow signal processing in nanostructures. For large v_g, MC unit cells were of micrometer [Chu08] and even millimeter dimensions [Chu09a] making miniaturization impossible.

Second, inelastic light scattering, i.e., Brillouin Light Scattering (BLS), was used to probe the SW propagation across the periodic arrays [Gub06, Gub07, Tac10c, Wan10]. Here it is an experimental challenge to provide such a large wave vector resolution that v_g can be measured close to $k = 0$ [Kos10] which is found to be important in this work. Still BLS remains a powerful tool for physical investigation of MC properties. For device application, however an all electrical solution is preferred.

Third, for an individual magnetic element of lateral dimension p, the smallest excitable wave vector is on the order π/p. This is due to spin-wave quantization [Jor99]. For $1 \ \mu m > p > 10$ nm, theory predicts that SWs reside in an intermediate regime between dipolar dominated and exchange dominated SW excitations [Kal86] where group velocities are particularly small.

Relevance to the physics community

Several aspects make the understanding of physical phenomena related to spin waves relevant for the broader physics community:

First, the search for magnonic crystals follows the successful implementation of photonic, plasmonic, and phononic crystals in dielectric, metallic, and semiconducting materials, respectively. Here periodic arrays of nanoholes or nanopitches have led to the functionalization of the corresponding materials [Joa08, Gao10, Yu10]. Allowed minibands and forbidden frequency gaps have been provoked by coherent backscattering of waves from the holes or pitches. Due the complex anisotropic and long-range dipolar interaction, magnonic crystals differ from their optical and acoustic counterparts e.g. by the mechanism of formation of minibands [Kos10].

Second, based on giant magnetoresistance multilayers [Bai88], where a spin-polarized current traverses a stack of nanometer thick metallic layers with alternating magnetic and non-magnetic properties, the spin-transfer torque effect was recently discovered [Tso00, Kis03]. Here a DC current

excites magnetization precession in a GMR nanopillar at microwave frequencies. This is the so-called spin-transfer torque microwave nanoscale oscillator (STNO). Phase locking of several STNOs [Kak05] could enable fabrication of nanoscale microwave sources. Phase locking could become possible via spin waves [Ber96, Dem10b]. As long as efficient SW sources in the form of STNO are not available, inductive excitation of SWs is needed to study the related physical phenomena and to set the field for future application in integrated STNO-SW devices.

Propagating spin-waves were investigated in a number of nanostructure geometries including width modulated wave guides [Lee09, Chu09b], arrays of closely packed circular dots [Gub06, Gio07, Kos08a], and wires [Kos04, Kos08b, Wan09, Wan10].

A study of SWs propagating through antidot lattices is so far missing. However, intriguing physical phenomena are expected. In the antidot lattice, only a part of the material is removed from the plain film. Differently to the case of isolated nanostructures, it is expected that a fundamental mode originating from quantization of the uniform precession of a plain film inherently exists [Pec05]. However, similar to the case of isolated nanostructures, one also expects strongly localized modes in potential wells formed by the demagnetization field close to holes edges [Tse09]. From a physical perspective, it is intriguing to test the influence of lattice periodicity on these two types of modes: For the fundamental mode, the situation resembles the introduction of periodicity into an initially undisturbed dispersion. This is described by a Bloch wave approach [Blo29] and discussed in this thesis in Secs. 8.1, 8.2, and 8.3.3. For the modes localized at the individual holes, a tight binding discussion [Sla54] is appropriate to describe the coupling of the modes initially uncoupled for large hole separations. This is discussed in Secs. 8.1, 8.3, and 8.3.3.

2 Theory

In this chapter a brief theoretical background of ferromagnetism is provided. This chapter is organized as follows.

In Sec. 2.1.1 a phenomenological classification of magnetic materials is given. This is followed by a thermodynamical motivation of magnetic ordering in Sec. 2.1.2; based on this, in Sec. 2.1.3, the microscopic origin of magnetic moments is discussed. Different energy contributions relevant for a system of magnetic moments are discussed in Sec. 2.1.5.

In Sec. 2.2, dynamic excitations of the ferromagnetic ground state are discussed. In Sec. 2.2.1 the equation of motion of magnetic moments is introduced. Based on this, in Sec. 2.2.2 and Sec. 2.2.3, a solution is derived and discussed (Sec. 2.2.4) for uniform precession. Finite wave length spin waves are subject of Sec. 2.3. Finally, in Secs. 2.3.2 and 2.3.3, two numerical methods (plane wave method and micromagnetic simulations) solving the equation of motion in a complex system are presented.

In Sec. 2.4 aspects of microwave transmission are discussed. This is done to finally enable derivation of the measured signal quantities, merging transmission line theory and spin-wave dynamics.

2.1 Ferromagnetism

Ferromagnetic materials are materials that show spontaneous magnetization $\mathbf{M}$ even with no applied external field $\mathbf{H}$.

2.1.1 Phenomenology

Classification of magnetic materials can be achieved by testing the influence of a magnetic field $\mathbf{H}$ on the magnetization $\mathbf{M}$ of the material. The magnetization $\mathbf{M}$ is defined as the magnetic moment $\boldsymbol{\mu}$ of a sample (see Sec. 2.1.3) per volume Ω. The magnetic moments are conserved; therefore $|\mathbf{M}(\mathbf{r})| =: M_{\mathrm{Sat}}(\mathbf{r})$, the saturation magnetization, stays constant.

Denotation	χ	Remarks	Typical values
Ferromag.	$>> 0$	Spontaneous magnetization	see Sec. 2.1.5
Antiferromag.	≈ 0	Two ferromagnetic sublattices; no macroscopic magnetization.	see Sec. 2.1.5
Ferrimag.	$>> 0$	Two ferromagnetic sublattices; macroscopic magnetization.	see Sec. 2.1.5
Paramag.	> 0	No spontaneous magnetization	$10^{-3}...10^{-6}$
Diamag.	< 0	No spontaneous magnetization	$-10^{-3}... - 10^{-6}$

Table 2.1: Phenomenological classification of magnetic materials using susceptibility χ.

The tensor relating $\mathbf{M}$ with $\mathbf{H}$ is the magnetic susceptibility $\hat{\chi}$

$$\mathbf{M} = \hat{\chi} \cdot \mathbf{H}. \tag{2.1}$$

Generally both $\mathbf{H}$ and $\mathbf{M}$ are position and time dependent. However, in a simple, static picture, where $\mathbf{H}$ and $\mathbf{M}$ are neither time dependent nor spatially varying, classification of magnetic materials is possible using the absolute value and sign of χ, see Tab. 2.1.

The focus of this thesis is on ferromagnetic materials. Examples of ferromagnetic materials are elements iron Fe, cobalt Co, nickel Ni, and combinations thereof, such as the alloy Permalloy $Ni_{80}Fe_{20}$ (Py). For Py, nominally $M_{Sat} = 860 \times 10^3$ A/m.

The magnetic field strength $\mathbf{B}$ is given by

$$\mathbf{B} = \mu_0(\mathbf{M} + \mathbf{H}) = \mu_0(\chi + 1)\mathbf{H}, \tag{2.2}$$

where μ_0 is the permittivity of vacuum, $\mu_0 = 4\pi \cdot 10^{-7} \frac{\text{Vs}}{\text{Am}}$. The value

$$\mu_p := \chi + 1, \tag{2.3}$$

is defined as the permittivity of a material. The unit of $\mathbf{B}$ is Tesla $\text{T} = \text{Vs}/\text{m}^2$.

2.1.2 Magnetization and total energy

In this section, a thermodynamical approach towards ferromagnetism is given. The energy E of a magnetic moment μ in a magnetic field described by the magnetic flux density $\mathbf{B}$ is given by

$$E = -\boldsymbol{\mu}\mathbf{B}. \tag{2.4}$$

This motivates the thermodynamical internal energy differential dU:

$$dU = TdS - pdV - \mathbf{M}d\mathbf{B}, \tag{2.5}$$

where T is the temperature, S the entropy, p the pressure, and V the volume associated with the system. Here the first term on the right hand side of Eq. 2.5 refers to the heat as known from thermodynamics, whereas the last two terms on the right hand side refer to the work that is performed on the system. Due to the fact that in a solid state system temperature and volume are usually conserved as in the present case, one transforms to the free energy F, defined as

$$F = U - T \cdot S, \tag{2.6}$$

yielding

$$dF = -SdT - pdV - \mathbf{M}d\mathbf{B}. \tag{2.7}$$

This formula allows to directly extract the magnetization from the free energy:

$$\mathbf{M} = \frac{\partial F}{\partial \mathbf{B}} \mid_{V,T} . \tag{2.8}$$

In a one-dimensional (1D) case, using Eq. 2.1,

$$\chi = \frac{1}{V}\frac{\partial^2 F}{\partial B^2}. \tag{2.9}$$

Usually the magnetization **M** remains constant and the field B is swept. Then the above formulas apply. If the field is kept constant and the magnetization is changed

$$\mathbf{H} = -\frac{1}{\mu_0} \frac{\partial F}{\partial \mathbf{M}}. \tag{2.10}$$

2.1.3 Magnetic moment

First, the orbital magnetic momentum $\boldsymbol{\mu}_L$ is considered. Classically, the orbital momentum can be understood by considering a negatively charged electron performing a circular motion around the positively charged nucleus. In a quantum mechanical picture, the energy eigenstates of the electrons called orbitals are classified by the quantum number of the orbital momentum μ_L

$$\boldsymbol{\mu_L} = -\mu_B \frac{\hat{L}}{\hbar}, \tag{2.11}$$

where $\mu_B = (e\hbar)/(2m_e) = 10^{-4}$ eV/T and $\hat{L}$ is the quantum mechanical operator for the orbital momentum. e denotes the electron charge and m_e the electron mass. $\hbar = h/2\pi$, where h is Planck's number. Second, the electron itself has a magnetic moment μ_s which cannot be understood classically taking the electron to be a particle without extension. Naive pictures attribute spin magnetic momentum originating from a rotating, charged sphere.

$$\boldsymbol{\mu_s} = -g_s \cdot \mu_B \frac{\hat{S}}{\hbar}, \tag{2.12}$$

where g_s is the Landee factor and $\hat{S}$ is the quantum mechanical operator for the spin momentum. g_s can be interpreted as the difference to the classically expected case, where $g_s = 1$. For a free electron $g_s \approx 2$. The total magnetic moment is a combination of both the spin and orbital momentum. Coupling of spin and orbital moment can be motivated classically, when transforming into the rest frame of the electron, where, due to orbital movement, the nucleus will create a magnetic field. The strength of the spin-orbital coupling scales as the square of the nucleus charge, see Ref. [Fli00] for details.

Magnetic moments in an insulator

The coupling of orbital momentum and spin is discussed for isolated and located magnetic moments. If spin orbital coupling is comparably weak, the total magnetic moment is yielded by, firstly, summing over individual electron spins and individual electron angular momenta separately. Secondly, the total spin and the total angular momentum is added [Nol05]

$$\hat{j} = \sum_i \hat{S}_i + \sum_i \hat{L}_i. \tag{2.13}$$

In an external field defining the z axis, the z components of $\hat{L}$, $\hat{S}$, and $\hat{j}$, i.e. m_L, m_S, and m_j are quantized. Summing of quantum mechanical operators gives

$$m_j = m_L + m_S = m_L \pm 1/2. \tag{2.14}$$

The possibilities for j are limited to $|L - S| \leq j \leq L + S$. The magnetic moment is then

$$\boldsymbol{\mu_j} = \frac{g_j \mu_B}{\hbar} \hat{j}, \tag{2.15}$$

with

$$g_j = 1 + \frac{j(j+1) + S(S+1) - L(L+1)}{2j(j+1)}. \tag{2.16}$$

This set of formulas describes macroscopic phenomena: together with Hund's rules, allowing prediction of the orbital occupation, one can estimate the atomic momentum for magnetic insulator.

For simplicity, the gyromagnetic ratio γ is defined:

$$\gamma = -g_j \frac{\mu_B}{\hbar}, \tag{2.17}$$

in units of Hz / T. For a free electron, this gyromagnetic ratio can be calculated very precisely, as g_s is known at great accuracy, $\gamma = 2\pi \cdot 28.5$ GHz/T.

Magnetic moments in a conductor

In this thesis, the material under investigation is permalloy (Py) $Ni_{80}Fe_{20}$, an alloy of the magnetic elements nickel Ni and iron Fe. Both elements show strong magnetization while being a conductor. E.g. for iron, $\mu =$

$2.2\mu_B$ and $\mu = 0.6\mu_B$ for nickel [Sko08]. This non-integer number cannot be understood in the picture of Sec. 2.1.3, i.e. isolated magnetic moments filling up the atomic orbitals. The band structure of the material and delocalized electrons need to be considered. The interaction of each electron with the surrounding itinerant electrons via exchange interaction causes an energy difference between the two spin states (see Sec. 2.1.4). This energy difference in the band structure causes non-integer total magnetic moments per atom. This is referred to as itinerant ferromagnetism.

2.1.4 Exchange interaction

Phenomenologically it is found that in a ferromagnet at room temperature regions (domains) exist, where all magnetic moments $\boldsymbol{\mu}$ are aligned. The dipolar interaction of two magnetic dipoles in a lattice amounts to a few hundred microelectron volts. However, thermal energy at room temperature is in the order of millielectron volts. Therefore, dipolar energy cannot be the microscopic origin of occupation of the ferromagnetic state where all magnetic moments are aligned.

Exchange interaction is introduced to explain ferromagnetic ordering at room temperature. It can be understood as a direct consequence of Pauli's law. Two electrons of the same quantum numbers cannot occupy the same quantum mechanical state. Therefore, if neighboring atoms have the same alignment of the magnetic moments, the mean distance of the electrons is larger. Coulomb energy is reduced. For localized, individual magnetic moments, see Sec. 2.1.3, this is parameterized in the exchange interaction Hamiltonian [VV50]

$$\sum_{i>j} J_{ij}\,\mathbf{S}_i \cdot \mathbf{S}_j, \tag{2.18}$$

where J_{ij} is a measure for the strength of the exchange interaction between spins. Summation extends over all pairs of spins.

Exchange interaction for itinerant ferromagnetism

For a treatment of ferromagnetism in conductors where electrons are delocalized, the exchange interaction is denoted as interaction between a magnetic moment and a surrounding mean field. This is typically done in the Stoner formalism [Blu01]. Assuming an energy difference δE between spin up and spin down electrons in a magnetic field one can show that

ferromagnetic ordering is favored if

$$\mu_0\mu_B^2\lambda_{St}g(\epsilon_F) \geq 0, \tag{2.19}$$

where $g(\epsilon_F)$ is the density of states at the Fermi level and λ_{St} is an empirical parameter describing the average exchange field. This is the so-called Stoner criterion giving an understanding of the influencing factors for the formation of itinerant ferromagnetism. Still, λ_{St}, a measure for the exchange strength, remains unknown within this theory. However, the density of states at the Fermi level for the ferromagnetic transition elements iron, cobalt, and nickel is large, therefore providing the prerequisite of fulfilling 2.19.

2.1.5 Energy contributions

Quantum mechanical Hamiltonian of ferromagnetism

For a rigorous treatment of ferromagnetism, a quantum mechanical approach becomes necessary. The Hamiltonian $\hat{H}$ that will yield the energy eigenstates reflects the idea of this microscopic model [VV50]

$$\begin{aligned}
\hat{H} &= -2 \cdot \sum_{i>j} J_{ij}\mathbf{S}_i \cdot \mathbf{S}_j + g\mu_B \sum_i \mathbf{S}_i \cdot \mathbf{B} + \tag{2.20}\\
&\quad + \sum_{i>j} D_{ij}\left[\mathbf{S}_j\mathbf{S}_i - 3r_{ij}^{-2}(\mathbf{r}_{ij} \cdot \mathbf{S}_j)(\mathbf{r}_{ij} \cdot \mathbf{S}_i)\right],
\end{aligned}$$

where $\mathbf{r}_{ij}$ is the vector between spin i and spin j and D_{ij} is the parameterized dipole-dipole interaction strength. The first sum denotes the exchange interaction. The second sum on the right hand side corresponds to the Zeeman energy, i.e. interaction of the spins with the external field. The third sum on the right hand side is the dipole-dipole interaction.

Magnetic moments in a ferromagnet of volume Ω are oriented to minimize the total energy of the system. Via Eq. 2.10, each energy contribution is related to an effective magnetic field.

Effective field

The microscopic Hamiltonian of Eq. 2.20 can be generalized for a continuum approach [Hub00]. Then, major energy contributions are written

as

- Zeeman energy E_Z. Energy of the magnetic moments with respect to the external field H

$$E_Z = -\mu_0 \int_\Omega \mathbf{MH}. \qquad (2.21)$$

This energy is minimized for parallel orientation of all magnetic moments with respect to the external field.

- Demagnetization field energy E_D. The field H_D is the stray field of all magnetic moments within the sample.

$$E_D = -\frac{M_{\text{Sat}}^2}{2} \int_\Omega \mathbf{M}(\mathbf{r})\mathbf{H}_D(\mathbf{r}), \qquad (2.22)$$

where $\mathbf{H}_D(\mathbf{r})$ is the position dependent demagnetization field. This energy is therefore connected with the magnetic field generated by the magnetic body itself. $\mathbf{H}_D$ itself depends on the orientation of the magnetic moments

$$\mathbf{H}_D(\mathbf{r}) = \int_\Omega \frac{3\mathbf{e}\left(\mathbf{M}(\mathbf{r}') \cdot \mathbf{e}\right) - \mathbf{M}(\mathbf{r}')}{\Delta r^3}, \qquad (2.23)$$

where $\Delta \mathbf{r} = \mathbf{r} - \mathbf{r}'$, $\mathbf{e} = \Delta \mathbf{r}/\Delta r$. This relation is described by the demagnetization field tensor $\hat{N}$ via

$$\mathbf{H}_D = \hat{N}\mathbf{M}. \qquad (2.24)$$

$\hat{N}$ depends on the geometrical shape of the sample. For magnetic nanostructures, this energy contribution results in a spatially inhomogeneous magnetization orientation. Stray field minimization results in magnetic domain formation, see below.

In general, it is possible to calculate $\hat{N}$ via

$$\hat{N} = \int_\Omega d\mathbf{r}' \hat{G}(\mathbf{r}', \mathbf{r}), \qquad (2.25)$$

where $\hat{G}$ is the corresponding Green's function [Jac62]. In three

dimensions, for this particular case, the Green's function is given by

$$\hat{G}(\mathbf{r}', \mathbf{r}) = \nabla_r \nabla_{r'} \frac{1}{\Delta \mathbf{r}}. \tag{2.26}$$

The Green's function has also been calculated for a thin magnetic film [Kal86] and ferromagnetic wires [Gus02]. For more complex structures, i.e. periodic arrangement of holes, this has not been done so far.

To motivate Eq. 2.25, it is necessary to consider the magnetostatic Maxwell's equations

$$\mu_0 \nabla(\mathbf{M} + \mathbf{H}_{\mathrm{D}}) = 0, \tag{2.27}$$
$$\nabla \times \mathbf{H}_{\mathrm{D}} = 0, \tag{2.28}$$

which are valid in this form for zero current density. Because of Eq. 2.27, it is possible to write $\mathbf{H}_{\mathrm{D}}$ as the gradient of a scalar potential

$$\mathbf{H}_{\mathrm{D}} = -\nabla \phi_{\mathrm{m}}. \tag{2.29}$$

ϕ_{m} fulfills Poisson's equation

$$\triangle \phi_{\mathrm{m}} = -\rho_{\mathrm{m}}, \tag{2.30}$$

where $\rho_{\mathrm{m}} = -\nabla \mathbf{M}$. The solution of Eq. 2.30 is a standard problem of classical electrodynamics. The solution is Green's function. Introducing boundary conditions [Jac62] finally yields Eq. 2.25.

- Exchange energy E_{Ex}

$$E_{\mathrm{Ex}} = \frac{A}{M_{\mathrm{Sat}}} \int_\Omega \left[(\nabla m_x^2) + (\nabla m_y^2) + (\nabla m_z^2) \right], \tag{2.31}$$

where A is the exchange constant and uniform exchange interaction is assumed [Ber91]. Eq. 2.31 can be derived from Eq. 2.18 via a Taylor approximation [Gie05a]. In a more general case, where both A and $\mathbf{M}$ are position dependent, the exchange field H_{Ex} is given by [Kra08]

$$\hat{\mathbf{H}}_{\mathrm{Ex}} = \left(\nabla \lambda_{\mathrm{Ex}}^2 \nabla \right) \mathbf{M}, \tag{2.32}$$

where λ_{Ex} is the exchange length

$$\lambda_{\mathrm{Ex}} = \sqrt{\frac{2A}{\mu_0 M_{\mathrm{Sat}}^2}}. \tag{2.33}$$

- Crystal anisotropy. Due to lattice symmetry, certain orientations of the magnetization are energetically favored. The microscopic origin of this is the spin-orbit coupling, see Sec. 2.1.3. The lattice symmetry can lift the energetic degeneracy of orbitals with differing m_l. Then the occupation of orbitals with $\hat{L}$ pointing in a defined spatial direction is energetically favored. The material of this study, permalloy, shows negligible crystal anisotropy.

The total energy E of the system is then, using Eq. 2.21 - 2.31,

$$E = E_{\mathrm{Z}} + E_{\mathrm{D}} + E_{\mathrm{Ex}}. \tag{2.34}$$

An equilibrium magnetization configuration is reached if E is minimal. Different energy contributions have a different effect on the orientation of the magnetization.

Domains and hysteresis

For geometrically confined ferromagnets, the demagnetization field energy influences the orientation of magnetic moments considerably. In particular, domains are formed. Domains are regions where neighboring magnetic moments are orientated parallel to each other. Parallel orientation minimizes the exchange energy of Eq. 2.31. However, to minimize the demagnetization energy of Eq. 2.22, neighboring domains exhibit different magnetization orientation. In between two domains, a domain wall is formed. As a function of the external field, the domain configuration varies. For nanomagnets in the deep-submicron regime, the magnetization configuration is typically varying on the length scale of the specimen geometry itself. In particular, to minimize the stray field and, therefore, the demagnetization energy, spins along a geometrical edge tend to align parallel with the edge. This is illustrated in Fig. 2.1. The orientation of magnetic moments is obtained from micromagnetic simulations, see Sec. 2.3.3, and presented in color-code for a magnetic square and disk.
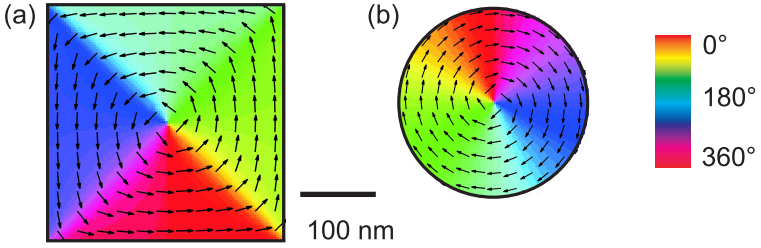
Figure 2.1: Color coded magnetic ground state $\mathbf{M}(\mathbf{r})$ of (a) a magnetic square of 500 nm side length and (b) a magnetic disc of 400 nm diameter obtained from micromagnetic simulations, see Sec. 2.3.3. The black arrows highlight the local orientation of the magnetic moments. Parameters are: $\mu_0 H = 0$ mT, saturation magnetization $M_{\mathrm{Sat}} = 860$ kA/m, film thickness $t_{\mathrm{s}} = 30$ nm. Both square and disk are in the so-called closed flux state, i.e. the averaged magnetization parallel to the direction of the previously applied field amounts to $\langle M \rangle = 0$. The demagnetization field of Eq. 2.24 is minimized.

Macroscopically, domains cause a complex response of $\mathbf{M}(\mathbf{r})$ on the external field $\mathbf{H}$. $\mathbf{M}(\mathbf{r})$ depends on the history of the external magnetic field $\mathbf{H}$, i.e. no simple function $\mathbf{M}(\mathbf{r}, \mathbf{H})$ can be stated. One way to formally treat this, is the concept of a hysteresis loop. Starting point is a defined magnetic state, where all magnetic moments are saturated to point parallel to the external field, i.e. no domain walls exist. Let $\langle M_\parallel \rangle$ denote the averaged magnetization component parallel to the external field. Then, $\langle M_\parallel \rangle / M_{\mathrm{Sat}} = 1$, where M_{Sat} is the saturation magnetization. Next, the external field H is decreased. At $H = 0$, the remanent magnetization $M_R \equiv \langle M_\parallel \rangle (H = 0)$ is reached. At a certain field H, irreversible reorientation of magnetic moments and domains occurs. The field for which $\langle M_\parallel \rangle / M_{\mathrm{Sat}} = 0$ is called coercive field H_{C}. A typical hysteresis curve obtained for a plain film of Py using the magneto optical Kerr Effect, see Sec. 3.2.3, is depicted in Fig. 3.6. Depending on the direction of field change, i.e. the sign of ΔH, different values of $\langle M_\parallel \rangle$ are resolved. This behavior is called hysteretic, because the history of the applied field influences the measured response.

Beyond this dependence on the field strength, a magnetic material, e.g. a mesoscopic structured magnet, may show an angular dependence of H_{C}

and M_R. This is called magnetic anisotropy. Anisotropy can have its origin in the lattice structure of the solid (crystal anisotropy) or in the geometrical shape of the ferromagnet (shape anisotropy). Crystal anisotropy in the case of permalloy is negligible as stated above.

2.2 Ferromagnetic Dynamics

2.2.1 Landau-Lifshitz equation of motion

Consider a magnetic moment $\boldsymbol{\mu}$ in an effective field $\mathbf{H}_{\text{eff}}$. The equation of motion reads as [Kit48]

$$-\frac{1}{\gamma}\frac{\partial \boldsymbol{\mu}}{\partial t} = [\boldsymbol{\mu} \times \mathbf{H}_{\text{eff}}]. \tag{2.35}$$

The right hand side of Eq. 2.35 is the torque acting on $\boldsymbol{\mu}$ exerted by the magnetic field. $\mathbf{H}_{\text{eff}}$ is given by

$$\mathbf{H}_{\text{eff}} = \mathbf{H} + \mathbf{H}_{\text{Ex}} + \mathbf{H}_{\text{D}}, \tag{2.36}$$

where $\mathbf{H}$ is the external field, $\mathbf{H}_{\text{Ex}}$ is the exchange field of Eq. 2.32, and $\mathbf{H}_{\text{D}}$ is the demagnetization field of Eq. 2.24.

For simplicity, only within this section, denotation is $\mathbf{H} \equiv \mathbf{H}_{\text{eff}}$. For a continuum approach, the magnetic moment $\boldsymbol{\mu}$ is replaced by a magnetization $\boldsymbol{M}(\boldsymbol{r})$.

The same equation of motion can be deduced from a quantum mechanical Hamiltonian such as 2.20. The relevant time evolution of the spin operator $\hat{S}_i$ is calculated according to

$$\frac{\partial \hat{S}_i}{\partial t} = \frac{2\pi i}{\hbar}\left[\hat{S}_i\mathbf{H} - \mathbf{H}\hat{S}_i\right]. \tag{2.37}$$

Using the approximation that the wavelength is much larger than the sample, i.e. uniform excitation, this was shown by VanVleck [VV50] and detailed derivation is out of the scope of the thesis.

Eq. 2.35 represents an idealized case where no damping term is included. In literature, two damping terms are known. First, the Gilbert

damping term [Gil55]. The equation of motion 2.35 becomes

$$\frac{\partial \mathbf{M}}{\partial t} = -\gamma[\mathbf{M} \times \mathbf{H}] + \frac{\alpha_{\mathrm{LLG}}}{M_{\mathrm{Sat}}}\mathbf{M} \times \frac{\partial \mathbf{M}}{\partial t}, \qquad (2.38)$$

where α_{LLG} is the Gilbert damping parameter. α_{LLG} is a dimensionless phenomenological parameter. Without discussing in detail the Lagrangian deduction of the damping term, it can be motivated twofold: First, damping terms in classical mechanics are proportional to the first temporal derivative of the generalized coordinate. This is analogous in the Gilbert damping term. Second, the length of the magnetization M is conserved, i.e. $\mathbf{M} \cdot \partial \mathbf{M}/\partial t = 0$; this is consistent with the physics of ferromagnetism. $\mathbf{M} \cdot \partial \mathbf{M}/\partial t = 0$ is proved by scalar multiplication of Eq. 2.38 with $\mathbf{M}$:

$$\mathbf{M}\frac{\partial \mathbf{M}}{\partial t} = -\gamma\mathbf{M}[\mathbf{M} \times \mathbf{H}] - \mathbf{M}\left[\frac{\alpha_{\mathrm{LLG}}}{M_{\mathrm{Sat}}}\mathbf{M} \times \frac{\partial \mathbf{M}}{\partial t}\right] = 0. \qquad (2.39)$$

Also used in literature is another form of Eq. 2.38. It is possible to deduce the Landau-Lifshitz form from the Gilbert damping form to show equality. The equation of motion with the Gilbert damping Eq. 2.38 is vector multiplied with $\mathbf{M}$. This yields

$$\mathbf{M} \times \frac{\partial \mathbf{M}}{\partial t} = -\gamma\mathbf{M} \times (\mathbf{M} \times \mathbf{H}) + \frac{\alpha_{\mathrm{LLG}}}{M_{\mathrm{Sat}}}\mathbf{M} \times \left[\mathbf{M} \times \frac{\partial \mathbf{M}}{\partial t}\right]. \qquad (2.40)$$

Using the identity $[\mathbf{a} \times \mathbf{b}] \times \mathbf{c} = (\mathbf{a}\mathbf{c})\mathbf{b} - (\mathbf{b}\mathbf{c})\mathbf{a}$ to expand the double cross product of the last term in Eq. 2.38 yields:

$$\begin{aligned}
\mathbf{M} \times \frac{\partial \mathbf{M}}{\partial t} =\ & -\gamma\mathbf{M} \times [\mathbf{M} \times \mathbf{H}] + \qquad\qquad (2.41)\\
& + \frac{\alpha_{\mathrm{LLG}}}{M_{\mathrm{Sat}}}\mathbf{M}\left[\mathbf{M} \times \frac{\partial \mathbf{M}}{\partial t}\right] - \alpha_{\mathrm{LLG}}M_{\mathrm{Sat}}\frac{\partial \mathbf{M}}{\partial t},
\end{aligned}$$

where the second term on the right hand side is again zero. Next, the left

hand side is replaced by the respective term of Eq. 2.38. This yields:

$$\frac{\partial \mathbf{M}}{\partial t} = -\frac{\gamma}{1 + \alpha_{\mathrm{LLG}}^2} [\mathbf{M} \times \mathbf{H}] - \qquad (2.42)$$
$$-\frac{\gamma \alpha_{\mathrm{LLG}}}{M_{\mathrm{Sat}}(1 + \alpha_{\mathrm{LLG}}^2)} [\mathbf{M} \times (\mathbf{M} \times \mathbf{H})].$$

This is the Landau-Lifshitz form of the equation of motion. For the materials discussed here $\alpha_{\mathrm{LLG}}^2 \ll 1$. α_{LLG} amounts to $\alpha_{\mathrm{LLG}} =\approx 10^{-2}$ for Py $\mathrm{Ni_{80}Fe_{20}}$. This is the case of low damping. Then one finds

$$\frac{\partial \mathbf{M}}{\partial t} = -\gamma [\mathbf{M} \times \mathbf{H}] - \frac{\lambda_{\mathrm{LL}}}{M_{\mathrm{Sat}}^2} [\mathbf{M} \times (\mathbf{M} \times \mathbf{H})], \qquad (2.43)$$

where

$$\lambda_{\mathrm{LL}} = \alpha_{\mathrm{LLG}} \gamma \mu_0 M_{\mathrm{Sat}} \qquad (2.44)$$

Eq. 2.43 is called the Landau and Lifshitz equation. The damping parameter λ_{LL} is in units of $1/\mathrm{s}$.

2.2.2 Linearized Landau-Lifshitz equation

For small oscillation amplitudes it is possible to linearize the undamped equation of motion for the magnetization Eq. 2.35. Ingredients to this calculation are

- A thin film, infinitely extended in the xy plane. The demagnetization factors are $N_x = N_y = 0$ and $N_z = 1$, see Eq. 2.24.

- All anisotropy fields are zero or neglected.

- The static magnetization is aligned with the external field $\mathbf{H} = H\mathbf{e}_x$. A small harmonic excitation field $\mathbf{h}$ of angular frequency ω is orientated along the y axis. The effective field is then

$$\mathbf{H}_{\mathrm{eff}} = \begin{pmatrix} H \\ h_y \exp i\omega t \\ 0 \end{pmatrix} + \mathbf{H}_{\mathrm{Ex}} + \mathbf{H}_{\mathrm{D}}. \qquad (2.45)$$

- $\mathbf{m}$ is the dynamic component of the magnetization and $\mathbf{h}_{\mathrm{D}}$ is the dynamic component of the demagnetization field. Because $\mathbf{M} \parallel \mathbf{e}_x$,

the static demagnetization field components are zero. A dynamic demagnetization field $\mathbf{h}_D$ prevails.

- The dynamic component $\mathbf{m}$ is assumed to be small compared to the saturation magnetization.

$$|\mathbf{m}| \ll M_z \approx M_{\text{Sat}}. \tag{2.46}$$

- The dynamic component $\mathbf{m}$ depends harmonically on the time t and precession occurs around the x axis. The total magnetization reads

$$\mathbf{M} = \begin{pmatrix} M_{\text{Sat}} \\ m_y \exp i\omega t \\ m_z \exp i\omega t \end{pmatrix} \tag{2.47}$$

- The dynamic demagnetization field $\mathbf{h}_D$ has to fulfill the magneto-static Maxwell's equations Eqs. 2.27 and 2.28, i.e., it can be described by a Green's function, see Eq. 2.26.

Inserting all this into Eq. 2.35 and neglecting all terms with squared $\mathbf{M}$ or $\mathbf{H}$ yields a set of coupled linear differential equations (see e.g. [Vas96] Eq. 8, [Kra08] Eqs. 6-8, [Top09] Eqs. 2.38, 2.39).

Uniform precession is a particularly simple case, because $\mathbf{h}_D = -m_z \mathbf{e}_z$ as $N_z = 1$ and no care has to be taken about fulfilling Maxwell's equations. Furthermore, because no spatial variation of magnetization is allowed, $\mathbf{H}_{\text{Ex}} = 0$ as follows from Eq. 2.32. The resulting oscillation occurs uniformly in space, i.e. the wavelength λ_{SW} is infinite, and the wave vector amounts to

$$k = \lambda_{\text{SW}}^{-1} = 0. \tag{2.48}$$

The uniform precession is known in literature as ferromagnetic resonance (FMR) [Kit48]. The coupled set of linearized equations of motion reads

$$
\begin{aligned}
(\omega_H - i\alpha_{\text{LLG}}\omega)m_y - i\omega m_z &= \omega_M h_y \\
(\omega_H - i\alpha_{\text{LLG}}\omega)m_z + i\omega m_y &= \omega_M h_z,
\end{aligned}
\tag{2.49}
$$

where $\omega_M = \gamma\mu_0(1 + \alpha_{\text{LLG}}^2)M_{\text{Sat}}$, $\omega_H = \gamma\mu_0(1 + \alpha_{\text{LLG}}^2)H$ and i is the imaginary constant.

2.2.3 Ferromagnetic resonance

Solving Eq. 2.49 following Refs. [Cou04, Gie05a, Bil07a], gives the susceptibility

$$\chi_{yy}(\omega) = \frac{\omega_M(\omega_H + \omega_M - i\alpha_{\mathrm{LLG}}\omega)}{\omega_r^2 - \omega^2 - i\alpha_{\mathrm{LLG}}\omega(2\omega_H + \omega_M)}, \tag{2.50}$$

where

$$\omega_r^2 = (\omega_H^2 + \omega_M\omega_H). \tag{2.51}$$

For $\omega = \omega_r$, χ_{yy} takes an extremal value. This is interpreted as resonant excitation of uniform precession of all spins, i.e., ferromagnetic resonance (FMR). The expressions for ω_M and ω_H can be interpreted as Larmor frequencies [Blu01]. Eq. 2.51 is the so called Kittel formula.

For a magnetic thin film, one obtains the resonance frequency

$$f_{\mathrm{r}}(k = 0) = \frac{\omega_{\mathrm{r}}}{2\pi} = \frac{\gamma\mu_0}{2\pi}\sqrt{H^2 + M_{\mathrm{Sat}}H}. \tag{2.52}$$

Typically $M_{\mathrm{Sat}} >> H$.[1] Then, Eq. 2.52 yields

$$\frac{\partial\left(f_{\mathrm{r}}(k = 0)^2\right)}{\partial H} = \left(\frac{\gamma\mu_0}{2\pi}\right)^2 M_{\mathrm{Sat}}. \tag{2.53}$$

Eq. 2.53 can be used to experimentally determine M_{Sat} using FMR measurements. Solving Eq. 2.52 for H yields

$$H(f_{\mathrm{r}}(k = 0)) = -\frac{M_{\mathrm{Sat}}}{2} + \sqrt{\left(\frac{2\pi f_{\mathrm{r}}(k = 0)}{\gamma\mu_0}\right)^2 + \left(\frac{M_{\mathrm{Sat}}}{2}\right)^2}. \tag{2.54}$$

Calculation of real and imaginary part of Eq. 2.50 yields

$$\Re(\chi_{yy}(\omega)) = \frac{\omega_M(\omega_H + \omega_M)(\omega_{\mathrm{r}}^2 - \omega^2)}{(\omega_{\mathrm{r}}^2 - \omega^2)^2 + \alpha_{\mathrm{LLG}}^2\omega^2(2\omega_H + \omega_M)^2} \tag{2.55}$$

---

[1]For permalloy, $\mu_0 M_{\mathrm{Sat}} \approx 1000$ mT. This is much larger than available field strengths in the experimental setup of Sec. 3.1, where $\mu_0 H \leq 100$ mT.

and

$$\Im(\chi_{yy}(\omega)) = \frac{\alpha_{\mathrm{LLG}}\omega\omega_M[\omega^2 + (\omega_H + \omega_M)^2]}{(\omega_{\mathrm{r}}^2 - \omega^2)^2 + \alpha_{\mathrm{LLG}}^2\omega^2(2\omega_H + \omega_M)^2}. \qquad (2.56)$$

It is possible to approximate the imaginary susceptibility $\Im(\chi_{yy}(\omega))$ by a Lorentzian distribution function. The full width at half maximum, i.e. the linewidth, is given by the frequency distance of the two extrema (minimum and maximum) of the real part, i.e. by

$$\Delta\omega = \omega_{\mathrm{r}}\left(\sqrt{1-\mathcal{C}} - \sqrt{1+\mathcal{C}}\right), \qquad (2.57)$$

where

$$\mathcal{C} = \frac{\alpha_{\mathrm{LLG}}(2\omega_H + \omega_M)}{\omega_{\mathrm{r}}}.$$

For $\omega_{\mathrm{r}} >> \Delta\omega$, one can use the Taylor approximation $(1+x)^n \approx 1 + nx$ to obtain

$$\Delta\omega = \alpha_{\mathrm{LLG}}\gamma\mu_0(2H + M_{\mathrm{Sat}}) \approx \alpha_{\mathrm{LLG}}\gamma\mu_0 M_{\mathrm{Sat}}. \qquad (2.58)$$

Note that $\Delta\omega$ stated in Eq. 2.58 relates to an effective damping (or relaxation) giving directly the frequency linewidth of the resonance. Many different contributions can enter this term, such as two or three magnon scattering [Ari99] and inhomogeneous linewidth broadening [Cou04]. Different contributions depend differently on the frequency. For so-called Gilbert like damping one defines the corresponding field full width at half maximum by

$$\Delta H = \frac{2\alpha_{\mathrm{LLG}}}{\mu_0\gamma}\omega_{\mathrm{r}}. \qquad (2.59)$$

The linear dependence of the field linewidth ΔH on the resonance frequency ω_{r} is referred to as Gilbert-like damping. Contributions not obeying this scaling law are referred to as extrinsic. In this thesis, the linewidth is stated in connection to intrinsic and extrinsic contributions and the parameter α only containing intrinsic contributions.

2.2.4 Relaxation and damping

Frequency linewidth

The field linewidth ΔH for separated extrinsic and intrinsic contributions, see Eq. 2.59, is given by [Hei85, Kal06]

$$\Delta H = \Delta H_0 + \frac{4\pi\alpha f_r(k=0)}{\gamma}. \tag{2.60}$$

In this thesis, the frequency linewidth Δf is determined rather than ΔH, see Sec. 3.1.1. It is possible to convert Δf into ΔH in order to obtain α from Eq. 2.60 [Kam75, Kua05, Kal06]. For small linewidths, i.e. $\Delta f \ll f_r(k=0)$, a linear approach

$$\Delta f = \Delta H \frac{\partial f_r(k=0,H)}{\partial H}, \tag{2.61}$$

can be used. In Eq. 2.61, $f_r(k=0,H)$ denotes the Kittel formula Eq. 2.52 describing the relation between external field H and resonance frequency $f_r(k=0)$. Differentiation yields

$$\frac{\partial f_r(k=0,H)}{\partial H} = \frac{\gamma\mu_0}{4\pi}\frac{2H+M}{\sqrt{H(H+M)}}. \tag{2.62}$$

To eliminate H, the dependence $H(f)$ of Eq. 2.54 is inserted in Eq. 2.63, which yields

$$\begin{aligned}
\frac{\partial f_r(k=0,H)}{\partial H} &= \frac{\gamma\mu_0}{2\pi}\sqrt{1+\left(\frac{\gamma\mu_0 M_{\mathrm{Sat}}}{4\pi f_r(k=0)}\right)^2} \\
&=: \frac{\gamma\mu_0}{2\pi}P_A(f_r(k=0)).
\end{aligned} \tag{2.63}$$

Finally, one obtains

$$\Delta f = \left(\frac{\gamma\Delta H_0}{2\pi} + 2\alpha f_r(k=0)\right)P_A(f_r(k=0)). \tag{2.64}$$

Eq. 2.64 can be used to obtain α from the resonance linewidth.

Temporal relaxation

The solution of Eq. 2.43 for a step-like field excitation

$$\mathbf{h} = \mathbf{h}_0 \Theta(t - t_0), \tag{2.65}$$

where Θ is the Heaviside step functions, is possible in spherical coordinates [Sil99]. One obtains an exponentially damped dynamic magnetization component

$$m_y \propto m_{y,0} \exp -\frac{t}{\tau}. \tag{2.66}$$

The parameter τ is the relaxation time and can be directly measured in e.g. time resolved experiments. It is connected to the Landau-Lifshitz damping λ_{LL} [Sil99], see Eq. 2.43, via

$$\lambda_{\mathrm{LL}} = 2/\tau. \tag{2.67}$$

Using Eq. 2.44 one can relate λ_{LL} to the Gilbert damping α_{LLG} and via Eq. 2.58 one finds

$$\Delta f = \frac{\lambda_{\mathrm{LL}}}{2\pi}, \tag{2.68}$$

i.e., λ_{LL} (or τ) is a direct measure for the frequency full width at half maximum of the susceptibility.

Sometimes the reciprocal spatial decay length ζ is used rather than the relaxation time. They relate by

$$\zeta = (v_{\mathrm{g}} \tau)^{-1}, \tag{2.69}$$

where v_{g} is the SW group velocity, see Sec. 2.3.1. ζ corresponds to the imaginary part of the SW wave vector k.

2.3 Dipolar Spin Waves

2.3.1 Dispersion relation

It is possible to solve a linearized equation of motion given by Eq. 2.43, see Sec. 2.2.2. This yields a solution including magnetostatic interactions of spin waves with finite wave vector k . For an extended thin film this has been done by Kalinikos and Slavin [Kal86] by setting up the appropriate
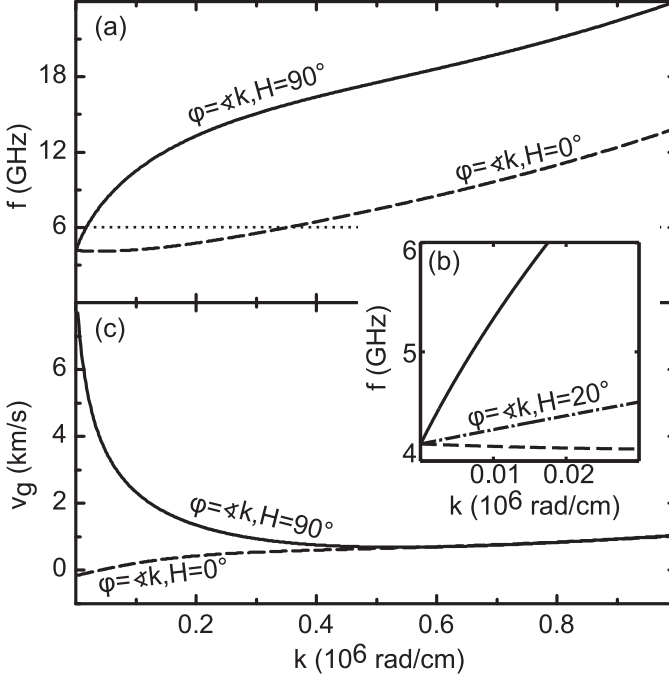
Figure 2.2: (a) Spin-wave dispersion $f_r(k, \mu_0 H = 20$ mT) calculated using Eq. 2.73 for two different orientations of the wave vector **k** with respect to the external field **H**. Parameters are: $\mu_0 H = 20$ mT, $M_{\text{Sat}} = 830$ kA/m, $t_s = 25$ nm, vertical quantization parameter $p = 0$. $\varphi = 90°$ (solid line): magnetostatic surface wave or Damon-Eshbach mode (MSSW). $\varphi = 0°$ (dashed line): magnetostatic backward volume mode (MSBVW). (b) Calculated $f_r(k)$ for $0 \leq k \leq 0.03 \times 10^6$ rad/cm for $\varphi = 90°$ (full line), $\varphi = 20°$ (dash-dotted line), and $\varphi = 0°$ (dashed line). This range of k corresponds to the regime addressed in the experiment. (c) Calculated group velocity $v_g = 2\pi \, \mathrm{d}f_r(k)/\mathrm{d}k$ for $\varphi = 90°$ (full line) and $\varphi = 0°$ (dashed line). For small k the MSBVM mode ($\varphi = 0°$) exhibits $v_g < 0$, i.e. phase and group velocity have opposite sign.

Green's function and boundary conditions. It is possible to calculate a spin-wave dispersion $f_r(k, H)$ and susceptibility $\chi(k)$.

Let the thin film be in the xy plane. The film thickness is t_s. Film extensions in x and y direction are sufficiently large to be considered as infinite. The effective internal field $\mathbf{H}$ and the magnetization $\mathbf{M}$ are oriented in the xy plane along the axis $\mathbf{e}_H$. The total wave vector $\mathbf{k}$ consists of an in-plane component $\mathbf{k}_\zeta$ (in the xy plane) and an out-of-plane component $\mathbf{k}_p$ (perpendicular to the xy plane). $\mathbf{k}_\zeta$ is orientated along the axis $\mathbf{e}_\zeta$. k is given by

$$k^2 = k_\zeta^2 + k_p^2. \tag{2.70}$$

The out-of-plane component of the wave vector is quantized due to the geometrical constrain in the perpendicular direction, i.e.,

$$k_p = \frac{p\pi}{t_s}, p = 0, 1, 2, ... \tag{2.71}$$

The in-plane component k_ζ is decomposed in a component parallel to the magnetic field H, $k_\parallel$, and a component perpendicular to the magnetic field, $k_\perp$, i.e.,

$$k_\zeta^2 = k_\perp^2 + k_\parallel^2. \tag{2.72}$$

The dispersion of spin waves with frequencies ω_p ($p = 0, 1, ...$) is given by [Kal86]

$$\omega_r^2(k, H) \mid_p = (\omega_H + \alpha\omega_M k^2)[\omega_H + \omega_M \cdot (\alpha k^2 + F_{pp}(k_p))], \tag{2.73}$$

where $F_{pp}(k_p)$ is the dipolar interaction matrix element. The dipolar interaction of spin waves causes, at small k vectors up to 10^5 rad/cm, a deviation from a quadratic dispersion relation. $F_{pp}(k_p)$ is given by

$$F_{pp}(k_p) = 1 - P_{pp}\cos^2\varphi + \omega_M \frac{P_{pp}(1 - P_{pp})\sin^2\varphi}{\omega_H + \alpha\omega_M k^2}, \tag{2.74}$$

where φ is the angle between $\mathbf{e}_\zeta$ and $\mathbf{e}_H$.[1] In the case of totally unpinned

---

[1] In the experimental setup employed in this thesis, see Fig. 3.3, if the transferred SW wave vector, i.e. the coplanar waveguide, is aligned with the field correctly, one obtains $\eta = 90° - \varphi$ where η is the angle of the field with the CPW, see Fig. 3.3.

surface spins,

$$P_{pp} = \frac{k_\zeta^2}{k_p^2} + \frac{2k_\zeta^3}{t_s k_p^4} \frac{1}{1 + \delta_{0p}} \left[1 - (-1)^p \exp\left(-k_\zeta t_s\right)\right]. \qquad (2.75)$$

In Fig. 2.2, the spin-wave dispersion of a plain film according to Eq. 2.73 is plotted for $\mu_0 H = 20$ mT, $M_{\text{Sat}} = 830$ kA/m, and $t_s = 25$ nm (reflecting standard Py parameters). In Fig. 2.3, an isofrequency plot for the same magnetic parameters at $f = 6$ GHz is depicted. The strong anisotropy of the spin-wave dispersion becomes visible.

Eq. 2.73 is denoted for a quantization of k_p only. However, in a further approach, this equation can be expanded to cover lateral quantization phenomena. Then $k_\perp, k_\parallel \rightarrow k_{\perp,n}, k_{\parallel,m}$ are assumed to be quantized, too. Rigorous treatment of lateral quantization, however, involves an adapted Green's function and appropriate boundary conditions. This has been done for, e.g., ferromagnetic wires [Gus02].

The group velocity v_{g} is defined by

$$v_{\text{g}} = \frac{\partial \omega}{\partial k}. \qquad (2.76)$$

For small k (in the dipolar regime), using Eq. 2.73, one yields [Mel01]

$$v_{\text{g}} = t_s \frac{(\gamma \mu_0 M_{\text{Sat}})^2}{8\pi f}, \qquad (2.77)$$

i.e. the group velocity v_{g} is inversely dependent on the frequency.

Generally, it is possible to distinguish between propagating and standing spin waves.

1. Propagating spin waves. Propagating SWs have a finite group velocity, $|v_{\text{g}}| > 0$. Energy and information is transferred in space. The amplitude $m(\mathbf{r}) \propto \exp(i\mathbf{kr})$ [Bai01].

2. Standing spin waves. Standing SWs have zero group velocity $v_{\text{g}} = 0$. Neither energy nor information is transferred in space. Formally, the standing SW can be described by interference of two counter-propagating SWs, i.e. $m(\mathbf{r}) \propto \exp(i\mathbf{kr}) + \exp(-i\mathbf{kr})$. Standing SWs are also referred to as localized SWs, as they can occur spatially
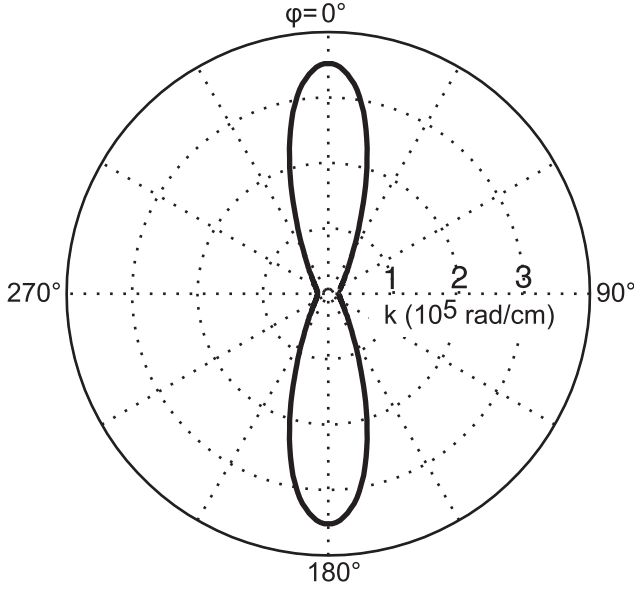
Figure 2.3: Calculated isofrequency plot for $f = 6$ GHz using the spin-wave dispersion Eq. 2.73 with $\mu_0 H = 20$ mT, $M_{\text{Sat}} = 830$ kA/m, $t_{\text{s}} = 25$ nm, vertical quantization parameter $p = 0$. Data corresponds to the dashed horizontal line of Fig. 2.2. A strong anisotropy is observed with a maximum k for the magnetostatic backward volume mode (MSBVW), i.e. $\varphi = 0°$ or $180°$.

confined within local potential wells [Jor99]. Such potential wells can be formed, e.g., by the internal field entering Eq. 2.73.

For $\varphi = 90°$, one finds the so-called magnetostatic surface wave or Damon-Eshbach mode (MSSW). Based on Eq. 2.73, the susceptibility $\chi(k)$ can be calculated [Har68, Per08] according to

$$\chi_{zx}^{\text{DE}} = \left(\frac{-i\omega M_{\text{Sat}}}{\mu_0 \gamma} \right) \times \mathcal{A}^{-1}, \tag{2.78}$$

39

where

$$\mathcal{A} = \left(\mathcal{B} + M_{\text{Sat}}\frac{1 - \exp(-kd)}{kd}\right) \times$$
$$\times \left(\mathcal{B} + M_{\text{Sat}}\frac{kd - 1 + \exp(-kd)}{kd}\right) - \left(\frac{\omega}{\mu_0\gamma}\right)^2,$$

and

$$\mathcal{B} = \frac{2Ak^2}{\mu_0 M_{\text{Sat}}} + H - \frac{i\alpha\omega}{\mu_0\gamma}.$$

The susceptibility χ_{zx}^{DE} of Eq. 2.78 becomes relevant in the analysis of measured signal obtained by the all-electrical spin-wave spectroscopy (AESWS) technique in Sec. 6. The measured signal is calculated using Eq. 2.78 in Fig. 6.4.

2.3.2 Plane wave method

The plane wave method (PWM) is a standard technique to calculate dispersion relations for periodic composite systems, e.g. photonic [Leu93], phononic, or, in the case of spin waves, magnonic systems [Vas96, Kra08]. The PWM has been adapted by Dr. Maciej Krawczyk and Dr. M.L. Sokolovskyy in Poznan, Poland[1] stimulated by the experimental data obtained in this thesis. See Sec. 8.1.2.

The PWM relies on the possibility to solve an eigenvalue problem numerically. For systems with spatial periodicity, this results in the transformation of the problem into reciprocal space via Fourier transformation. Using the ansatz of plane waves to solve the problem is based on Bloch's theorem that the solution of a differential equation with periodic coefficients can be represented as a product of plane-wave envelope functions and a periodic Bloch function [Kra08].

In particular, for magnonic systems, this results in the following ingredients:

1. Linearized equation of motion, see Sec. 2.2.2, formulated in the reciprocal space, including the demagnetization field (magnetostatic potential), and other periodic material properties.

---

[1]Surface Physics Division, Faculty of Physics, Adam Mickiewicz University, Umultowska 85, Poznań 61-614, Poland.

2. Ansatz of plane waves solving the equation

$$
\begin{aligned}
\mathbf{m}(\mathbf{r}) \ &= \ \mathbf{m_k}(\mathbf{r})\exp(i\mathbf{kr}) = \\
&= \ \sum_{\mathbf{G}} \mathbf{m_k}(\mathbf{G})\exp(i(\mathbf{k}+\mathbf{G})\mathbf{r}),
\end{aligned}
\tag{2.79}
$$

where $\mathbf{k}$ denotes a reciprocal lattice vector and $\mathbf{k}$ is defined within the first Brillouin zone.

3. Usage of a a sufficiently large, but finite number of reciprocal lattice vectors $\mathbf{G}$ that ensures convergence of the problem

The problem can then be formulated in the form

$$
\hat{\mathcal{M}}(\mathbf{G})\mathbf{m_k} = i\Omega\mathbf{m_k},
\tag{2.80}
$$

where $\hat{\mathcal{M}}$ is a 2x2 matrix, see Eqs. 22-44 of [Kra08], and $\mathbf{m}$ the dynamic magnetization. The system of equations given by Eq. 2.80 can be solved numerically.

In the case of the antidot lattice geometry, which consists of air holes in a ferromagnetic surrounding and has been investigated as part of this thesis, a particularity of the PWM has to be considered. Modeling of non-magnetic material in PWM-based calculations of magnonic spectra has not been possible so far. This is due to the formulation of the equation of motion Eq. 2.35 for inhomogeneous media. In nonmagnetic media the magnetization is zero and Eq. 2.35 becomes an identity. However, in the PWM the system dynamic is described by a superposition of a number of plane waves given by Eq. 2.79, which are continuous functions and propagate throughout the medium. Thus, each plane wave must be defined also in the nonmagnetic medium. To do so, one can model the holes by a region of strongly reduced M_{Sat}. Then the set of solutions can be subdivided into physical and non physical results: physical solutions have close to zero precession amplitude within the holes represented by reduced M_{Sat} and vice versa for the non-physical solutions. The relevance of this approach goes beyond the system of magnonic crystals: similar challenges are encountered in the application of the PWM to the calculation of the band structure of phononic crystals consisting of a solid and a liquid or gas [Gof01, Pen10].[1]

---

[1]Similarly to the SWs confined to magnetic material in the MC, in phononic crystals trans-

First, the static demagnetizing field in the model system must reproduce well the demagnetizing and the stray fields in the real ADL. This is particularly important for edge modes (see Sec. 8.3), which are formed in the local minima of the demagnetizing field. A value of M_{Sat} at least ten times lower than in Py allows to reproduce the shape and value of the static demagnetizing field with good accuracy (less than 10% error). The assumption of a specific M_{Sat} involves a compromise between high accuracy of the results obtained (which requires a small M_{Sat}) and short time necessary for the calculations (which benefits from a large M_{Sat}). As the number of plane waves to be taken into account in the expansions to obtain the same accuracy grows with the magnetization difference between holes and matrix, a large difference implies long calculation time. In the presented calculations, see Sec. 8.1.2, 1681 plane waves were used in the Fourier series.

Secondly, the physical and nonphysical solutions must be separated. To do so, one must ensure that nonphysical solutions reside in a different frequency regime than physical solutions. In the present system of the antidot lattice, the effective field H_{eff} forms minima within the ferromagnetic material (here the edge mode resides) and maxima within the holes (modeled by low M_{Sat}). This causes the nonphysical solutions localized within the holes to shift to higher frequencies, see Eq. 2.73.

2.3.3 Micromagnetic simulations

Micromagnetic simulations allow for the numerical calculation of the ferromagnetic ground state, i.e. the equilibrium magnetization configuration $\mathbf{M(r)}$ by minimizing the total energy of the system, see Eqs. 2.7, see Sec. 2.3.3. Furthermore, for a given initial ground state, response of the system to a dynamic field $\mathbf{h}$ is calculated numerically solving the equation of motion including damping Eq. 2.43 or Eq. 2.38, see Sec. 2.3.3.

---

verse vibrations do not occur in constituting liquids and gases. The abrupt vanishing of these vibrations at the border between the solid and the gas leads to non-physical extra solutions in the PWM. Material parameters are chosen to properly model the gas medium and eliminate the nonphysical solutions from the relevant frequency range without affecting the frequencies of the proper (physical) modes.

Quasistatic simulations

To find an equilibrium magnetization state, minimizing the total energy of Eq. 2.34 is a task which in general is not possible to be treated analytically. Micromagnetic simulations allow a numerical treatment. For this, a ferromagnetic body is discretized into N simulation cells, indexed by $j = 1...N$, of defined volume Ω_j each with magnetization $\mathbf{M}_j$.[1] The vectors $\mathbf{r}_{ij}$ connect the i-th simulation cell with the j-th simulation cell. The energy terms of Sec. 2.1.5 are formulated in a discretized manner; this is readily done for the Zeeman energy 2.21. The exchange interaction is of local nature allowing for the gradient representation of Eq. 2.31. Only contributions over a few neighbors need to be taken into consideration in a standard code [Ber93, Her01]. The need for computational power for Zeeman and exchange energy contributions is low. This is different for the long range demagnetization field interaction. The dipolar interaction between two magnetization vectors of the i-th and j-th cell is given by the discretized equivalent of Eq. 2.23. The summation extends for every simulation cell over all $N - 1$ remaining simulation cells, i.e. the need for computational power scales as $\propto O(N^2)$.[2]

For minimization of the total energy E, different computational iteration processes are employed; one of these is explained for the software Micro-Magus which is employed in the course of this thesis [Ber08]. Using Eq. 2.5 and Eq. 2.10, the effective internal field at simulation cell j, $\mathbf{H}_{\text{eff},j}$, is given by the vector derivative

$$\mathbf{H}_{\text{eff},j} = -\frac{\delta E}{\delta \mathbf{M}_j}. \tag{2.81}$$

A minimum of energy is reached if $\mathbf{H}_{\text{eff},j}$ and $\mathbf{M}_j$ are collinear [Sch88],

---

[1]The simulation cells can be either of cubic shape of fixed size [Ber93]. Cubic shaped simulation cells translate into square shaped cells for 2d simulations.or, using a finite element approximation, of tetrahedral shape [Her01].

[2]For simulation cells of fixed size and therefore periodic discretization, the demagnetization field calculation can be accelerated considerably using a fast Fourier transformation (FFT) approach [Yua92]. This approach exploits that the interaction between two cells only depends on their relative distance, i.e., on $i - j$. Eq. 2.24 can be formulated accordingly [Ber98]. For discretization using uniform simulation cells, this results in computational power scaling $\propto O(N)$.

i.e.

$$\mathbf{H}_{\text{eff},j} \times \mathbf{M}_j = 0.$$

The constraint is that the length of $\mathbf{M}_j$ is conserved, i.e. $M_{\text{Sat}} = \text{const.}$. In detail, the iteration process [Ber93] calculates firstly $\mathbf{H}_{\text{eff},j}$ using Eq. 2.81 for a given magnetization configuration $\mathbf{M}_j^{\text{old}}$. Second, the abort condition

$$|\mathbf{M}_j^{\text{old}} \times \mathbf{H}_{\text{eff},j}| < \varsigma,$$

is tested where ς is the defined threshold for convergence. If not fulfilled, a new magnetization configuration $\mathbf{M}_j^{\text{new}}$ is calculated using a Landau-Lifshitz and Gilbert equation 2.43 without a precession term, i.e.

$$\mathbf{M}_j^{\text{new}} = \mathbf{M}_j^{\text{old}} - \alpha^{\star} \left[\mathbf{M}_j^{\text{old}} \times (\mathbf{M}_j^{\text{old}} \times \mathbf{H}_{\text{eff},j}) \right], \qquad (2.82)$$

where the damping parameter $\alpha^{\star}$ is chosen for sufficiently fast, yet accurate convergence. $\alpha^{\star}$ does not necessarily reflect the specific damping α of the given material, but a value set to fit the needs of an efficient convergence of the iteration. Eq. 2.82 changes the length of $\mathbf{M}_j^{\text{new}}$ in the second order of $|\mathbf{M}_j^{\text{old}} - \mathbf{M}_j^{\text{new}}|$. Subsequent renormalization of $\mathbf{M}_j^{new}$ modifies the results little for small α.

Time dependent simulation

For the simulation of magnetization dynamics, the Landau-Lifshitz and Gilbert equation (Eq. 2.43) is considered. An initial magnetization configuration is defined using static micromagnetic simulations, see Sec. 2.3.3. For small temporal intervals τ_i, $\partial \mathbf{M}_{i,j}/\partial t$ is replaced by $\Delta \mathbf{M}_{i,j}/\tau_i$ and is numerically calculated for each simulation cell $j = 1...N$ and $\tau_i \in [0, T]$. Then, the effective internal field $\mathbf{H}_{\text{eff}}$ is calculated as described in Sec. 2.3.3 anew for inputting into the next iteration of solving Eq. 2.38.

Application

In the course of this thesis the software *MicroMagus*[1] has been used to model static and dynamic properties of nanostructured ferromagnetic systems. Subject of this thesis is the periodic arrangement of air holes in a thin

---

[1]Innovent Technology Development e.V., Jena, Germany
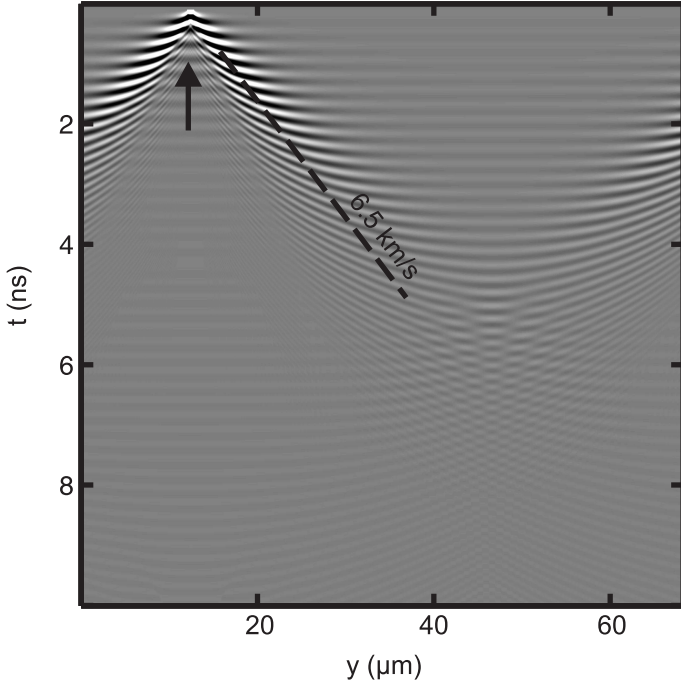
Figure 2.4: Spatio-temporal spin-wave propagation along the y axis in a plain thin film obtained from micromagnetic simulations for $\mu_0 H = 20$ mT (applied in x direction), $M_{\text{Sat}} = 830$ kA/m, $t_s = 25$ nm. Plotted is the out-of-plane component of the dynamic magnetization m_z, where dark (bright) colors denote a large positive (negative) amplitude. Simulated is a slab of material with extensions in y direction of 68 μm and x direction of 0.8 μm with a simulation discretization unit cell of 16.7 nm, i.e. the number of simulation unit cells amounts to $N = 48 \times 4096 \times 2 \approx 4 \times 10^6$. Simulation unit cell volume is $\Omega = 16.7 \times 16.7 \times 12.5$ nm^3. Two-dimensional periodic boundary conditions were used. Simulation parameter set A, see A.3. Magnetization dynamics are excited by a field pulse orientated out of the plane: rise and fall time of 25 ps at $t = 0.05$ ns and $y = 12 - 12.8$ μm, field strength $\mu_0 h_{\text{rf}} = 0.1$ mT. Propagation of the spin wave packet is indicated by the dashed line which exhibits a group velocity $v_{\text{g}} = \text{d}\omega/\text{d}k = 6.5$ km/s. The SW propagates in $+$ and $-y$ direction. The periodic boundary conditions cause the spin wave packet propagating in $-y$ direction to reappear at $y = 68$ μm. Saved time step interval: $\Delta\tau = 6$ ps. Simulated time period $T = 10$ ns.

permalloy plain film, i.e. an antidot lattice (ADL) as introduced in greater detail in Sec. 3.1.2. The holes in the ADL are arranged with a periodicity of p and the ADL extends in the xy plane. For the simulated geometries $120 \leq p \leq 800$ nm. Detailed parameter sets of micromagnetic simulations employed throughout this thesis are stated in the appendix, see Sec. A.3.

First, the simulated geometry is chosen. Let M_y define the number of antidot unit cells of periodicity p simulated in y direction and M_x respectively in x direction. Either a single ADL unit cell is simulated, i.e. $M_x = M_y = 1$ or a number of unit cells $M_y > 1$ is simulated in y direction (still, $M_x = 1$). Latter case is depicted schematically in Fig. 2.5. The simulated geometry comprises N_x (N_y, N_z) simulation unit cells in x (y, z) direction. Each of the simulation unit cells comprises a spatial volume Ω. The x and y coordinate of each simulation unit cell is denoted by x_i and y_j, respectively. Then it follows that $i \leq N_x$ and $j \leq N_y$. Typically, $N_z = 2$. Periodic boundary conditions are used in the xy plane, i.e. two-dimensional (2d) periodic boundary conditions.

The ferromagnetic ground state is calculated as described in Sec. 2.3.3. In particular, results of such calculations are the spatial magnetization profile $\mathbf{M}(x_i, y_j)$, see Fig. 2.1, and for an antidot lattice with periodicity $p = 800$ nm Figs. 7.3, 7.4; also obtained is the spatial demagnetization field profile $\mathbf{H}_{\mathrm{D}}(x_i, y_j)$ which is depicted for antidot lattices with $p = 800$ nm and 300 nm in Figs. 7.5 and 7.6.

If the simulated geometry is chosen such that $M_x = M_y = 1$, the field pulse $\mathbf{h}_{\mathrm{rf}}$ exciting magnetization dynamics in the radio frequency (rf) regime, i.e. up to 50 GHz, is applied uniformly across the simulated single ADL unit cell. Because there is no spatial variation of h_{rf}, the wave vector transferred by the exciting field pulse is 0 (infinite wavelength of h_{rf}). Furthermore, the 2d periodic boundary conditions do not allow for a wave vector with $k < 2\pi/p$.[1] The spatially resolved spectral response $P(f, x_i, y_j)$ is obtained via Fourier transformation (FFT) of the temporal evolution of the out-of-plane magnetization m_z of every simulation unit cell (i, j), i.e. by

$$P(f, x_i, y_j) = \mathrm{FFT}_t \left(m_z(x_i, y_j, t) \right), \qquad (2.83)$$

---

[1] Typical parameters of such simulations are $\Omega = 5 \times 5 \times 10$ nm^3, i.e. simulation cell side lengths are of the order of the exchange length λ_{Ex}, see Eq. 2.33. Simulation cells $N = 10^3...10^5$. The field pulse is typically directed $45°$ out of the xy plane and has an amplitude amounting to $\mu_0 h_{\mathrm{rf}} = 0.5 - 3$ mT.
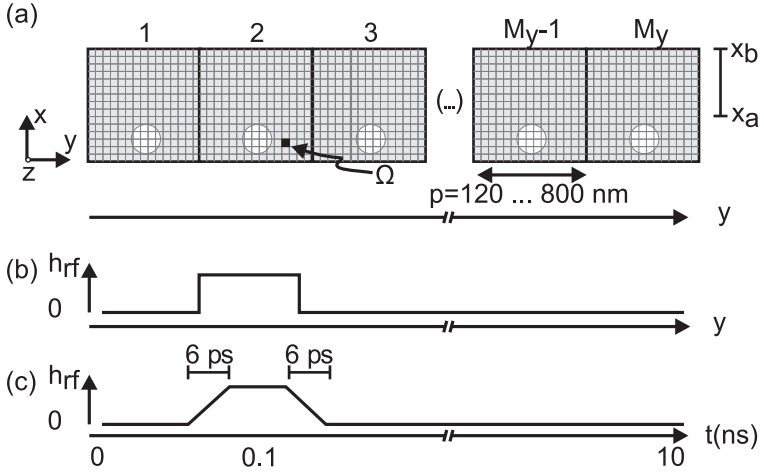
Figure 2.5: (a) Schematic illustration of the micromagnetic simulation of an anti-dot lattice (ADL), i.e. a periodic arrangement of circular shaped air holes (white areas) in the xy plane contained in a thin permalloy film (gray area). p denotes the antidot lattice periodicity and for the geometries simulated in this thesis $120 \leq p \leq 800$ nm. For a detailed description of the ADL geometry, see Sec. 3.1.2. 2d Periodic boundary conditions are used in the xy plane. M_x and M_y denote the numbers of ADL unit cells simulated in x and y direction, respectively. The ADL periodicity is p. In x direction, a single ADL unit cell is simulated, i.e. $M_x = 1$. In y direction, $M_y > 1$, typically $40 \leq M_y \leq 80$. The ADL geometry is discretized into simulation unit cells indicated by light gray lines. There is a total of N_x, N_y, and N_z simulation unit cells in x, y, and z direction. Each simulation unit cell size corresponds to a spatial volume Ω as indicated. (b) and (c) To trigger magnetization dynamics, a short field pulse $\mathbf{h}_{\mathrm{rf}}$ is applied directed $45°$ out of the xy plane. It has, e.g., an extension of p in y direction as indicated in (b). There is no dependence on the x and z direction. The short field pulse has a rise and fall time of 6 ps in the time domain as indicated in (c). This is sufficient to excite magnetization dynamics in the radio-frequency regime up to 50 GHz. The simulated time T amounts to $T = 10$ ns, typically.

where FFT_t denotes the Fourier transformation from time into frequency space. Such spatial spin-wave precession maps are shown for ADLs of periodicity $p = 800$, 300 and 120 nm in Figs. 7.18, 7.21, and 7.23.

The integrated spectral response $P(f)$ is obtained via Fourier transformation (FFT) of the temporal evolution of the out-of-plane magnetization m_z of every simulation unit cell and subsequent summation over all simulation unit cells, i.e. by

$$P(f) = \sum_{i \leq N_x, j \leq N_y} \mathrm{FFT}_t \left(m_z(x_i, y_j, t) \right). \tag{2.84}$$

The integrated spectral response is shown for antidot lattices of periodicity $p = 800$, 300 and 120 nm in Figs. 7.17, 7.20, and 7.22.

If spin-wave propagation is simulated, i.e. if the simulated geometry is chosen such that $M_x = 1$ and $M_y > 1$, the excitation field $\mathbf{h}_{\mathrm{rf}}$ is spatially localized in y direction to an extent of, e.g., p. There is no dependence of $\mathbf{h}_{\mathrm{rf}}$ on the x coordinate, c.f. Fig. 2.5.[1] The wave vector transferred by the excitation field is obtained by the Fourier transform of the field profile in y direction, i.e. by $\mathrm{FFT}h_{\mathrm{rf}}(y_i)$.[2] To obtain the integrated spectral response with wave vector resolution, i.e. $P(f, k)$, a two dimensional Fourier transformation is performed. Only certain x_i are considered for this, defined by $a \leq i \leq b$ [c.f. Fig. 2.5].[3] Only for these given values of x_i, the out-of-plane magnetization component m_z is summed up

$$m_z(y_j, t)|_{\bar{x}_i} = \sum_{x_a \leq x_i \leq x_b} m_z(x_i, y_j, t),$$

---

[1]Typical parameters of such simulation are $\Omega = 17 \times 17 \times 12$ nm^3, i.e. simulation cell side lengths are larger than the exchange length λ_{Ex}, see Eq. 2.33. Simulation cells $N \approx 32 \times 2056 \times 2 \approx 1 \times 10^5$. $M_y = 40...80$. The field pulse is typically directed $45°$ out of the xy plane, has no dependence on x coordinate, a spatial extent in y coordinate of $300 - 1000$ nm, and amplitude of $\mu_0 h_{\mathrm{rf}} = 0.1 - 1$ mT. Typically, the stored time increment of simulation is $\Delta\tau = \tau_i - \tau_{i-1} = 6$ ps, so that the maximum resolved frequency corresponds to roughly 80 GHz according to Nyquist theorem. Furthermore, typically the simulated time is $T = 10$ ns, so that the frequency resolution corresponds to roughly 0.1 GHz.

[2]This is analogous to Sec. 5 where the excitation spectrum of a CPW is obtained from a Fourier transformation of the simulated field profile.

[3]x_a and x_b are chosen so that each x_i with $a \leq i \leq b$ has a sufficiently large distance to the holes. This is done in order to avoid artifacts from the geometrical periodicity induced by the holes.

In Fig. 2.4, $m_z(y_j, t)|_{\bar{x}_i}$ is depicted for a plain film for $a = 1$ and $b = N_x$. The simulation parameters are stated in the Figure caption. A two-step Fourier transformation yields $P(f, k)$ so that one yields

$$P(f, k) = \text{FFT}_y \, \text{FFT}_t \left(m_z(y_j, t)|_{\bar{x}_i} \right), \qquad (2.85)$$

where FFT_y denotes the Fourier transformation from time into wave vector space. $P(f, k)$ obtained on a plain film is depicted in Fig. 2.6 as a gray scale plot. Data is compared with the calculated spin-wave dispersion $f_r(k)$ according to Eq. 2.73. Good agreement is found for small wave vectors k. The disagreement between simulation and calculation at large values of k originates from the large simulation discretization cell size of $\Omega = 16.67 \times 16.67 \times 12.5 \, \text{nm}^3$.

2.4 Microwave Excitation

2.4.1 Transmission line model

In order to describe the microwave response of a linear element, it is convenient to use the transmission line theory. A transmission element dx is considered which is small if compared to the wavelength λ_{em} of the electromagnetic (em) wave, i.e. $dx << \lambda_{\text{em}}$ is considered. The transmission element comprises two conductors which are separated in space by a dielectric. One conductor is denoted as signal line, the other conductor as ground line.[1] Relevant values are voltage V and current I along the transmission element, as well as resistance R and inductance L of the conductors, conductance G of the dielectric, and capacitance C between the conductors. They are related by the formulas

$$\begin{aligned}
\frac{\partial V}{\partial x} &= -\left(RI + L\frac{\partial I}{\partial t} \right). \qquad (2.86) \\
\frac{\partial I}{\partial x} &= -\left(GV + C\frac{\partial V}{\partial t} \right).
\end{aligned}$$

---

[1]A particular form of a transmission element is the coplanar waveguide (CPW) which is formed with two ground lines symmetrically arranged with respect to the signal line. The CPW is used throughout this thesis, see Sec. 3.1.2. Via appropriate conformal mapping techniques [Sim01], this geometry can be transferred into the more general case of a single ground line discussed here.
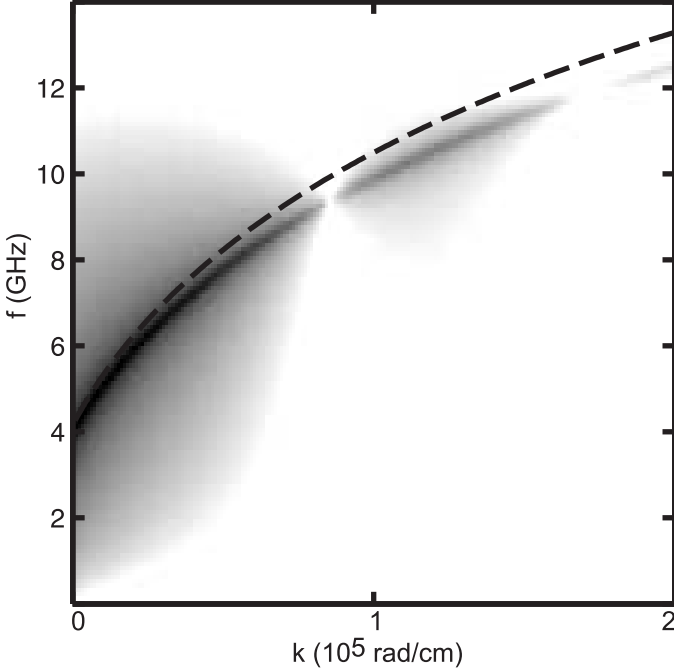
Figure 2.6: Spin-wave dispersion obtained from micromagnetic simulations considering $\mu_0 H = 20$ mT, $M_{\text{Sat}} = 830$ kA/m, $t_{\text{s}} = 25$ nm, where dark (bright) denotes large (small) SW amplitude. Data is obtained from a two-dimensional Fourier transform of Fig. 2.4. The dashed line indicates the calculated spin-wave dispersion obtained from Eq. 2.73 and depicted in Fig. 2.2. The disagreement between simulation and calculation at large values of k originates from the large simulation discretization cell size of $\Omega = 16.67 \times 16.67 \times 12.5$ nm^3. The slope of the dispersion for small k yields a value of the group velocity $v_{\text{g}} = 2\pi \, \mathrm{d}f/\mathrm{d}k = 6.5$ km/s.

Assuming a sinusoidal time dependence of angular frequency ω, i.e.

$$
\begin{aligned}
V(x,t) &= \Re(\tilde{V}(x)\exp(j\omega t)) \\
I(x,t) &= \Re(\tilde{I}(x)\exp(j\omega t)),
\end{aligned}
\tag{2.87}
$$

allows to eliminate the time dependence from Eq. 2.86 to yield

$$
\begin{aligned}
\frac{\partial \tilde{V}}{\partial x} &= -(R+i\omega L)\,\tilde{I}, \\
\frac{\partial \tilde{I}}{\partial x} &= -(G+i\omega C)\,\tilde{V}.
\end{aligned}
\tag{2.88}
$$

Further differentiation yields two independent second order differential equations which can be solved in the form of wave equations

$$
\begin{aligned}
\tilde{V}(x) &= \tilde{V}^{+}\exp(-\gamma x)+\tilde{V}^{-}\exp(\gamma x), \\
\tilde{I}(x) &= \tilde{I}^{+}\exp(-\gamma x)+\tilde{I}^{-}\exp(\gamma x),
\end{aligned}
\tag{2.89}
$$

where

$$
\gamma = \sqrt{(R+j\omega L)(G+j\omega C)},
\tag{2.90}
$$

and $\tilde{V}^{+}, \tilde{V}^{-}, \tilde{I}^{+}, \tilde{I}^{-}$ are integration constants resulting from solving the two coupled differential equations of second order. Interpreting Eq. 2.89 as two counter propagating waves for voltage $V(x,t)$ and current $I(x,t)$, each, yields that $\Re\gamma$ corresponds to the spatial decay of the voltage (current) amplitude along the transmission element. Voltage and current are related via the impedance

$$
Z_c = \frac{\tilde{V}^{+}}{\tilde{I}^{+}} = \frac{\tilde{V}^{\cdot}}{\tilde{I}^{-}}.
\tag{2.91}
$$

For low loss lines, where

$$
\begin{aligned}
R &<< \omega L \\
G &<< \omega C,
\end{aligned}
\tag{2.92}
$$

ohmic losses in the conductor (dielectric) are small if compared to inductive (capacitive) losses. For nanoscale coplanar waveguides (CPWs), see Sec. 3.1.2, Eq. 2.92 is not always fulfilled. For low loss transmission ele-

ments the impedance is given by

$$Z_c = \sqrt{\frac{L}{C}}. \tag{2.93}$$

In this case, the ohmic resistance R is not relevant for the high frequency (rf) impedance.

2.4.2 Scattering Parameters

Consider a transmission element of Sec. 2.4.1 and define the two sides of the element as ports $i = 1$ and port 2. One defines the complex and normalized waves

$$
\begin{align}
a_i &= \frac{V_i + Z_{ci}I_i}{2\sqrt{Z_{ci}}} \tag{2.94}\\
b_i &= \frac{V_i - Z_{ci}I_i}{2\sqrt{Z_{ci}}},
\end{align}
$$

where $i = 1, 2$. Inserting the solutions of voltage and current waves Eqs. 2.89 into Eq. 2.94, one obtains

$$
\begin{align}
a_i &= \frac{V_i^+}{Z_{ci}} \exp{-\gamma x} \tag{2.95}\\
b_i &= \frac{V_i^-}{Z_{ci}} \exp{\gamma x}.
\end{align}
$$

Eq. 2.95 can be used to interpret a_i and b_i as incoming and outgoing voltage waves at port i. Based on this, the scattering parameters S_{ij} (S-Parameters) are defined for two ports according to

$$
\begin{pmatrix} b_1 \\ b_2 \end{pmatrix} = \begin{pmatrix} S_{11} & S_{12} \\ S_{21} & S_{22} \end{pmatrix} \begin{pmatrix} a_1 \\ a_2 \end{pmatrix} \tag{2.96}
$$

In the following two particular examples for scattering parameters are stated [Bil07a]. First, for the simple case of a transmission element of length l,

$$S_{11} = S_{22} = 0,$$

i.e. no back reflection, and

$$S_{12} = S_{21} = \exp{-\gamma l}.$$

Second, for a lumped impedance Z_x on a transmission line of impedance Z_0,

$$S_{11} = S_{22} = \frac{Z_x}{Z_x + Z_0},$$

and

$$S_{12} = S_{21} = 2S_{11}.$$

2.4.3 Voltage induction and measured quantities

This section deals with the theoretic foundations of the excitation and detection mechanism of SWs employed in the all electrical spin-wave spectroscopy (AESWS) technique, see Sec. 3.2.2.

A precessing magnetization $\mathbf{M}$ induces a voltage in the signal line of a coplanar waveguide (CPW). The CPW extends along the x axis. In general, the magnetization precession can be excited by a current through a first CPW 1 and a voltage can be induced in a second CPW 2. The magnetic flux within CPW 2, Φ_2, can be directly derived from reciprocity arguments [Gie05a] and is given by the magnetization $\mathbf{M}$ and the dynamic magnetic field $\mathbf{h}_2^{\mathrm{rf}}$ by

$$\Phi_2 = \mu_0 \int_{V_s} \frac{\mathbf{h}_2^{\mathrm{rf}}}{I_2} \cdot \mathbf{M} dV, \tag{2.97}$$

where V_s is the sample volume and

$$\begin{aligned}
\mathbf{h}_2^{\mathrm{rf}} &= h_{y_0,2}(y) H_2 \mathbf{e}_y. \\
&= h_{y_0,2}(y) \frac{I_2}{w_2} K \mathbf{e}_y.
\end{aligned} \tag{2.98}$$

The magnetic field $\mathbf{h}_2^{\mathrm{rf}}$ is orientated along the y axis only. This is a simplification of the real case, where $\mathbf{h}_2^{\mathrm{rf}}$ also has a finite z component, see Sec. 5. K is a proportionality constant, I the current, and w the CPW inner conductor width, see Sec. 3.1.2. H_2 multiplied by the proportionality constant K, respectively, give the absolute field value. The spatial depen-

dence is included in $h_{y_0,2}$ which is defined so that $\int dy h_{y_0,2} = 1$. For simplicity, it is instructive to first consider a case where the lateral extents of the magnetic material are identical to the lateral extents of the inner conductor. Here the y dependence of $H_{y_0,2}(y)$ is small and Eq. 2.97 simplifies to

$$\Phi_2 = \mu_0 M_y(t) t_s l, \tag{2.99}$$

where l is the length of the inner conductor and t_s the thickness of the magnetic material. For a more general case,

$$\Phi_2 = \frac{\mu_0 t_s l \sin \delta K}{w_2} \int dy \left(h_{y_0,2}(y) M_y(y,t) \right), \tag{2.100}$$

where δ is the angle between the magnetization $\mathbf{M}$ and the y axis. This angle corresponds to the angle η used for the all electrical measurements and defined in Fig. 3.3 via $\eta = 90° - \delta$. The induced voltage is given by

$$
\begin{aligned}
V_2 &= -\frac{d\Phi}{dt} = \\
&= -\frac{\mu_0 t_s l \cos \eta}{w_2} \int dy h_{y_0,2}(y) \frac{dM_y(y,t)}{dt} = \\
&= -\frac{\chi_{\text{tot}}(\omega') \mu_0 t_s l \cos \eta}{w_2} \int dy h_{y_0,2}(y) \frac{dh_{y,1}^{\text{rf}}(y,t)}{dt}.
\end{aligned}
\tag{2.101}
$$

Here $\chi_{\text{tot}}(\omega')$ is the total susceptibility of the material given by all contributing wave vectors k that are excited [Cou04, Sch04, Per08].

$$\chi_{\text{tot}}(\omega') = \int dk \chi(\omega', k) \rho(k) \exp(-iks), \tag{2.102}$$

where $\chi(\omega', k)$ is the spin wave susceptibility (see e.g. Eq. 2.78), $\rho(k)$ is the excitation efficiency for a given wave vector k, see Sec. 5, and s is the distance between the two CPWs [Per08, Vla10]. The magnetization is driven by the time dependent field of CPW 1, i.e.

$$\mathbf{h}_1^{\text{rf}} = h_{y_0,1}(y) \frac{I_1}{w_1} K \exp(i\omega t) \mathbf{e}_y. \tag{2.103}$$

Following an approach by Giesen [Gie05a], the Fourier transformation of

Eq. 2.101 eliminates the time dependence and yields

$$V_2 = iI_1\omega \cdot \frac{2\pi\mu_0 t_s l \chi_{\text{tot}}(\omega')\delta(\omega - \omega')\cos\eta}{w_1 w_2} \times \tag{2.104}$$
$$\times \int \mathrm{d}y \left(h_{y_0,2}(y)h_{y_0,1}(y) \right).$$

From Eqs. 2.104 and 2.102 it is clear that the maximum maximum signal is not necessarily obtained for the resonance frequency of uniform precession denoted $f_{\text{r}}(k = 0)$ in Eq. 2.56. The frequency shift can be calculated straightforwardly, see Eq. 18 in Ref. [Cou04].

The spatial convolution between detector and emitter field shall be denoted as sensitivity

$$\Sigma(y) = h_{y_0,2}(y)h_{y_0,1}(y). \tag{2.105}$$

In the case of a single CPW, $\int \mathrm{d}y\Sigma(y) = 1$. For two different coplanar waveguides, $0 \leq \int \mathrm{d}y\Sigma(y) \leq 1$. This results in a suppressed signal contribution from non-local excitation and detection. This signal is to be regarded as parasitic in the case of all electrical spin wave spectroscopy, where one aims at measuring propagating spin waves having traveled between emitter and detector. Comparing Eq. 2.104 with Eq. 2.88 shows that the ferromagnet response can be treated as a change in the system's induction L because both the system's inductance, as well as the induced signal are proportional to $i\omega I_1$. The change in induction is then given by

$$\Delta L \propto \chi_{yy}\omega\chi_{\text{tot}}(\omega). \tag{2.106}$$

This change in the system's inductance changes the impedance Z_c via Eq. 2.93 and of the scattering parameters, see Sec. 2.4.1. The measured signal corresponding to χ_{tot} is denoted as spin-wave spectrum.

Eq. 2.104 highlights the important dependencies of the measured signal.

- The signal strength depends linearly on ω.

- The signal depends on the angle between the rf-field $\mathbf{h}_{\text{rf}}$ and the magnetization $\mathbf{M}$ via $\cos\eta$.

- The signal depends on the spatial convolution of excitation and detection field Σ.

- The signal is directly proportional to the susceptibility $\chi_{\text{tot}}(\omega)$.

For further details on derivation of the susceptibility from the measured signal see [Kua05, Kal06, Bil07b, Vla10].[1] It is out of the scope of this thesis to provide full quantitative description of χ. In the following, χ is stated in arbitrary units. From Ref. [Kal06] it follows that this does not affect the determination of e.g. the damping significantly.

2.4.4 Electromagnetic field simulation

The measured signal given by Eq. 2.104 is strongly influenced by the magnetic field strength and spatial profile of the microwave antennae, i.e., in the present case of the coplanar waveguides (CPWs). Different ways exist in literature to obtain the spatial field profile of a CPW, including full scale analytical calculation using Maxwell's equations [Vla10] or via the field produced by a current strip [Sil99, Sch04, Gie05b]. While the first analysis is very involved, the second approach neglects effects of the insulator or the complex geometry of CPWs used for experiments described in Sec. 3.2.2.

A further method involves electromagnetic field simulation. A three dimensional object is discretized into simulation cells. For each simulation cell the electric and magnetic fields given by Maxwell's equation are calculated obeying the continuity conditions at the simulation cell boundaries. Within this thesis the software *Microwave Studio*[2] is used to simulate the magnetic field $\mathbf{h}(\mathbf{r})$ produced by a CPW. For further details see [Wei08].

---

[1]Different techniques have been proposed to obtain the a fully quantitative description susceptibility. They range from measuring the scattering parameters only [Kua05], via a numeric compensation of the intermixing between real and imaginary part of the S-parameters [Kal06], to a full deembedding of the coplanar waveguide contributions to the signal [Bil07b]. While the last method requires a dataset obtained for the raw coplanar waveguide, which is not possible for integrated samples, the intermixing between real and imaginary parts of the susceptibility can be taken care of. This is done by an appropriate rotation of the signal phase.

To obtain a reliable measure for the *absolute* value of the susceptibility proves to be very difficult. Numerous signal contributions from different field orientations, non-local spin-wave excitation, and, most importantly, the absolute value of the exciting magnetic field h_{rf} have to be considered. In literature, even a full scale calculation of the electromagnetic fields obtained from Maxwell's equations, combined with the magnetization dynamics described by Landau-Lifshitz and Gilbert equation 2.43 requires an empirical scaling factor to obtain results in agreement with experiment [Vla10].

[2]CST Corp., Darmstadt, Germany

3 Experimental Setup and Techniques

In this Chapter the experimental methods and techniques are introduced. The chapter is organized as follows:

In Sec. 3.1.1 the broadband microwave probe station is introduced which is used to measure samples described in Sec. 3.1.2.

The measurement techniques are described in Sec. 3.2, in particular all electrical spin-wave spectroscopy (AESWS) in Sec. 3.2.2.

3.1 Measurement Apparatus and Sample Design

3.1.1 Broadband microwave probe station

Spin wave excitations in ferromagnetic material typically cover the GHz frequency (10^9 Hz) regime. To study spin-wave resonances all electrically, a broadband microwave measurement setup, i.e. a probe station, is required. Two identical probe stations were employed TUM, see Fig. 3.1. The probe station comprises the following elements:

1. A sample as described in Sec. 3.1.2 with integrated coplanar waveguides (CPWs).

2. Microwave source and detector in the form of a vector network analyzer (VNA). The VNA has two microwave ports, see Sec. 2.4.2. The VNA creates and outputs a sinusoidal microwave defined by the voltage wave **a** of frequency f, see Eq. 2.95. It detects the returning waves **b** at both ports. Both phase and amplitude are measured. For measurements presented hereafter, a *PNA-X* [1] VNA is employed. The rf microwave output power is typically 1 mW.

3. Microwave cables, tips, and a positioning / retaining system. Microwave contact is established between both ports of the VNA with

---

[1] Agilent Corp., Santa Clara, CA, USA
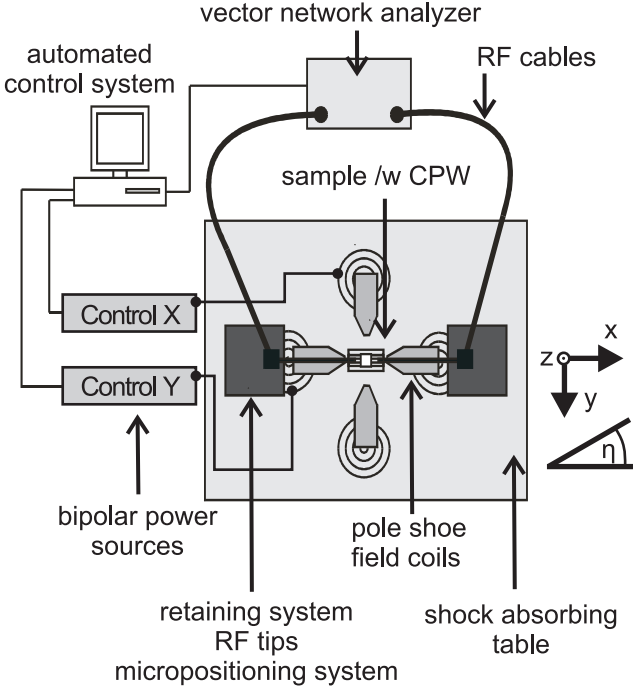
Figure 3.1: Schematic illustration of the broadband probe station setup used in this thesis. A vector network analyzer (VNA) outputs a sinusoidal voltage of frequency $f \leq 26$ GHz. Using microwave cables orientated by a retaining system, the microwave is fed into RF tips. These tips establish microwave connection between the microwave cables and a coplanar waveguide (CPW). The sample is positioned within a magnetic field $\mathbf{H}$ of variable magnitude and orientation in the xy plane. The magnetic field is controlled by an automated control system, bipolar power sources, Hall sensors, and lock-in amplifiers (see text). The automated control system also controls the VNA.

the CPW. This is done in a fashion to minimize impedance mismatch between the VNA and the CPW, see Sec. 2.4.2. Microwave cables and tips are impedance matched. They are positioned and subsequently retained in a fixed position to contact the CPW and suppress movement in a magnetic field gradient during measurements. Microwave tips provide impedance matched RF contact to gold contact pads of a coplanar waveguide. For measurements presented hereafter, *FPC-GSG*[1] RF tips and *UFA-210A* semi-rigid cables[2] were employed.

4. Two pairs of current coils and two ferromagnetic pole shoes for the generation of a magnetic field **H**. A static magnetic field **H**, with $\mu_0 H \leqq 100$ mT is generated. The pairs of magnetic field coils are connected via a single pole shoe each and orientated perpendicular with respect to each other. By this a magnetic field of arbitrary horizontal angle η with respect to the xy coordinates is generated via the superposition of fields generated by a single pair of field coils.

5. System for automated control and data acquisition. A computer software programm designed to control the VNA and the magnetic field. Data acquisition is fully automated and synchronized with magnetic field control.

6. A magnetic field control system comprising the two pairs of magnetic field coils, two bipolar power sources, three Hall sensors, and two lock in amplifiers. The bipolar power sources *BOP*[3] provide a control interface which is connected to the system for automated control and data acquisition. A set voltage is input into the bipolar power sources. The voltage output of the bipolar power sources is altered and by this the current flow through the magnetic field coils. Three Hall sensors, orientated to be sensitive in the three orthogonal spatial directions, output a voltage proportional to the magnetic field. Lock-in amplifiers amplify the modulated Hall sensor signal and the generated voltage is used as a reference input to the bipolar power sources. Reference and set input are leveled. This system allows for continuous field sweeps through zero field, an actively stabilized

---

[1] Cascade Corp., Beaverton, OR, USA
[2] Rosenberger Corp., Tittmoning, Germany
[3] Kepco Corp., Flushing, NY, USA

magnetic field generation, and a compensation for hysteretic effects of the magnetic pole shoes used.

7. Setup for shielding off environmental noise; comprising a shock absorbing table to suppress any vibrations and a laminar flow box with soft-PVC curtains to suppress dust and air draft.

3.1.2 Sample design

A sample consists of a substrate, a coplanar waveguide (CPW) [Sim01], a permalloy (Py) mesa which can be structured to comprise magnetic nanostructures, in particular antidot lattices (ADLs), and an insulator electrically insulating the Py mesa from the CPW. Typical materials and their thicknesses are: substrate $350\ \mu\mathrm{m}$ GaAs (semi insulating), coplanar waveguide consisting of thin layers of chromium (4.5 nm), silver (80 nm), gold (25 nm), insulator SiO_2 $(10-30\ \mathrm{nm})$ or *FOX-12*[1] spin-on glass $(1-2\mu\mathrm{m})$. For fabrication techniques see Sec. 4. The vertical order in z direction [c.f. Fig. 3.3] is typically (from bottom to top): substrate, permalloy mesa, insulator SiO_2, CPW. In another embodiment the arrangement in z direction is (from bottom to top): substrate, CPW, insulator *FOX-12*, permalloy mesa. In this embodiment, all parts of the permalloy mesa is optically accessible from the top. This is relevant for Brillouin light scattering technique, see Sec. 3.2.4.

Coplanar waveguide design

A CPW comprises three electrical connection lines extending in parallel to each other along x direction, see Fig. 3.3 [Sim01]. In particular, a CPW with finite width ground lines is used in this thesis [Pon97, Pon98]. The electrical connection lines are denoted outer conductor 1 (OC_1, ground line), inner conductor (IC, signal line), and outer conductor 2 (OC_2, ground line). The CPW is symmetric with respect to the inner conductor line. The lines are typically made of silver and capped with gold. The width of OC_1 and OC_2 and IC in y direction is w_{oc} and w_{ic}, respectively. The thickness of the lines in z direction is t_{cpw}. s_{icoc} denotes the distance between the center conductor edge and the outer conductor edge. A CPW consists of two pad regions, i.e. pad 1 and pad 2 region, two taper regions, i.e.

---

[1]Dow Corning, Midland, USA
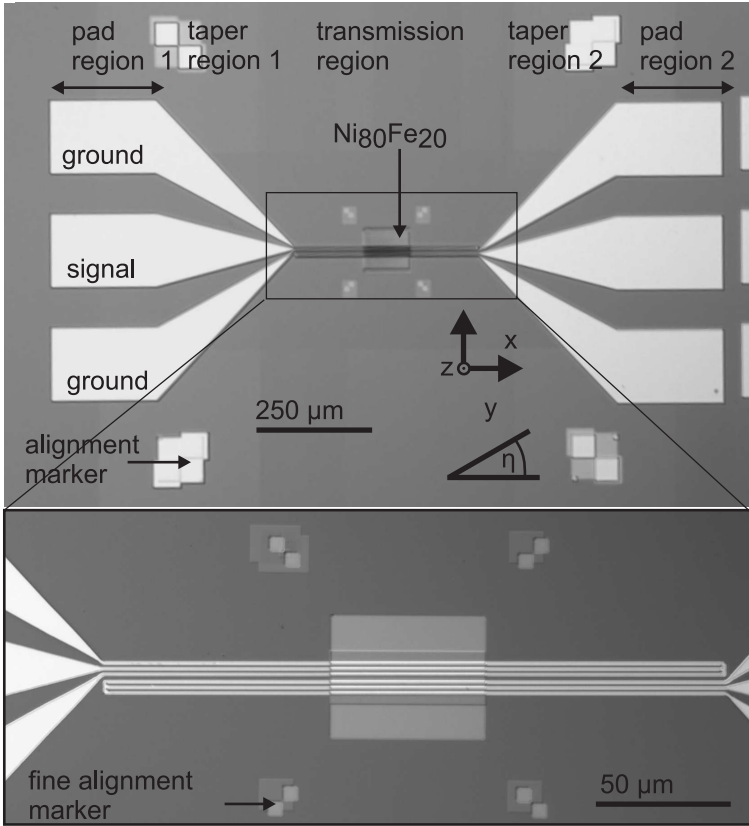
Figure 3.2: Optical micrograph of a CPW. (a) The thin-film coplanar waveguide (CPW) comprises a metallic signal line with two ground lines on either side. The CPW consists of two pad regions, two taper regions, and a transmission region. The pad regions are designed to connect to rf microwave tips and the taper regions are designed to connect the transmission region with the pad region. Underneath the transmission region, a Py mesa is visible. (b) In the depicted embodiment, the transmission region is formed to electrically isolate two CPWs connected to one transmission region, respectively. The two CPWs are referred to as SW emitter and detector. SW emitter and detector are both shorted at one end of the transmission region. Using the SW-transmission CPW, it is possible to measure propagating spin waves using the AESWS technique, see Sec. 3.2.2.
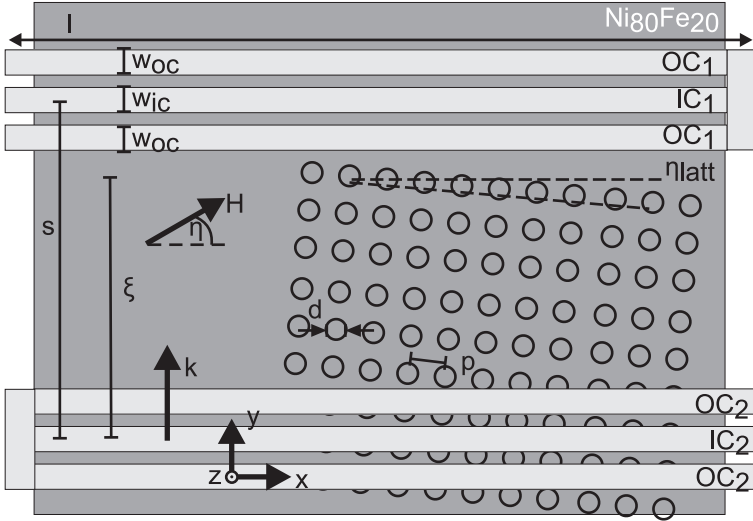
Figure 3.3: Schematic of the transmission region of a SW-transmission CPW. Two coplanar waveguides consist each of two outer conductors (OC) and one inner conductor (IC) in parallel (inner conductor width w_{ic}, outer conductor width w_{oc}) and extend along y direction. They are placed in a distance s with respect to each other and are shorted at one end of the transmission region. An antidot lattice (ADL) with square unit cell is structured in parts of the permalloy mesa (dark gray) of thickness t_s in z direction underneath (on top of) the CPWs. The ADL extends from one end of the permalloy mesa. Only a part ξ of the transmission distance s is structured into an ADL. The ADL hole diameter is d and periodicity p. An external magnetic field $\mathbf{H}$ is applied in the xy plane under angle η with respect to the CPW and x axis. If the CPW is aligned correctly with the external field direction, the transferred wave vector k is orientated along the y axis. Then the angle η corresponds to the angle φ defined for the SW dispersion Eq. 2.73 via $\eta = 90° - \varphi$. The magnetic field is limited to $\mu_0 H < 100$ mT.

taper 1 and taper 2 region, and a transmission region, see Fig. 3.2. In the transmission region, the inner conductor width w_{ic} is much smaller than in the pad region. Typically, in the transmission region, $w_{ic} = 4\ \mu m\ ...\ w_{ic} = 0.34\ \mu m$ and in the pad region $w_{ic} = 80\ \mu m$. Further details of the lateral CPW geometry are discussed in Sec. 5. The taper region connects the pad regions with the transmission region and has a w_{ic} dependent on x position. The pad regions are formed to connect to RF tips of the microwave setup, see Sec. 3.1.1. In the following, the inner conductor widths w_{ic} are stated only for the transmission region.

Different embodiments of CPWs are employed in this thesis.

- In one embodiment, the transmission region is designed to electrically connect the taper region 1 and 2 in the form of a standard CPW. This embodiment is referred to as standard CPW.

- In a second embodiment, the transmission region is designed to electrically isolate taper regions 1 and 2 in the form of two CPWs placed in parallel to each other in a distance s, see Fig. 3.3. The two CPWs are denoted as SW emitter and detector because they are used for all-electrical spin-wave spectroscopy measurements of propagating SWs as discussed in detail in Sec. 3.2.2. This embodiment of the CPW is referred to as SW-transmission CPW. A standard SW-transmission CPW used in this thesis has the following parameters in the transmission region: $w_{ic} = w_{oc} = 2\ \mu m$. Center to center distance of the two inner conductors $s = 12\ \mu m$. Distance between outer and inner conductors $s_{icoc} = 1.6\ \mu m$. The ends of SW emitter and detector are electrically shorted.

Underneath the transmission region, a permalloy $Ni_{80}Fe_{20}$ (Py) mesa is located which is designed to extend fully underneath and beyond the electrical connections. The thickness of the permalloy is denoted t_s. Typically, $t_s = 22...30$ nm. The CPW further comprises alignment markers and fine alignment markers positioned with respect to the CPW to allow alignment with the permalloy mesa or a subsequent lithography step such as focussed ion beam lithography, see below.

Antidot lattice design

In one sample embodiment, a part of the permalloy mesa is structured e.g. by focussed ion beam lithography, see Sec. 4.3 to form a squared periodic

array of holes, i.e. an antidot lattice (ADL). The area structured into an ADL extends for a distance ξ from one lower edge of the Py mesa [c.f. Fig. 3.3]. The hole diameter is given by d and the periodicity is p. There is a slight misalignment between the orientation of the primitive unit cell vectors of the ADL and the x axis defined by the CPW, i.e. η_{latt} which typically amounts to $\eta_{\text{latt}} = 1 - 2°$. This misalignment originates from, e.g., an unintentional rotation of the ion beam coordinates due to inaccurate alignment and drifts after alignment.

3.2 Measurement Techniques

3.2.1 VNA ferromagnetic resonance technique

The vector network analyzer ferromagnetic resonance (VNA-FMR) technique was established for the excitation of spin waves with (or close to) $k = 0$ [Gie05b, Neu06b, Bil07b, Bil07a]. This techniques employs a standard CPW with a comparably large inner conductor width w_{ic}. By this, the spin-wave excitation spectrum $\rho(k)$ has only small contributions for $k > 0$ [Cou04]. Similar techniques were also employed in the time domain [Sil99, Nib03]. To obtain FMR data, either the reflected signal (S_{22} or S_{11}) or the transmitted signal (S_{12} or S_{21}) is measured.

In order to extract the SW signal a_{11} and a_{12} from background signal, a reference technique is employed. S_{11} and S_{12} are recorded at the measurement field $\mu_0 H$ and angle η. From this dataset, S_{11} and S_{12} obtained for $\mu_0 H = 100$ mT and $\eta = 90°$ are subtracted, respectively. The signal due to the in-plane component of the exciting field $\mathbf{h}^{\text{rf}} = h_{y,0}\mathbf{e}_y$ is zero for $\eta = 90°$, see Eq. 2.104.[1] Only a small signal contribution is present for a non-vanishing out-of-plane z component of $\mathbf{h}^{\text{rf}}$. The resulting effective signal is denoted as a_{11} and a_{12}. The signal phase is denoted as $\phi(a_{11})$ and the magnitude or amplitude as $|a_{22}|$. For VNA-FMR, the data obtained from a_{11} and a_{12} is complementary [Bil07a] and a measure of the susceptibility χ_{tot} of the material, see Sec. 2.4.3 and Eq. 2.102. The samples are symmetric with respect to the two pad regions of the CPW, therefore data obtained from a_{11} and a_{22} (a_{12} and a_{21}) is complementary.

---

[1] For a non-ellipsoidal magnet there might be edge regions which are still excited. These are not addressed here.

3.2.2 All electrical spin-wave spectroscopy

The all electrical spin-wave spectroscopy (AESWS) technique relies on the excitation of spin waves of different wave vectors k. For this one makes use of a micro- or nanostructured CPW providing a finite spin-wave distribution Δk. This technique is also known in literature as propagating spin-wave spectroscopy [Mel01, Bai01, Bai03, Bao08]. Similar techniques were also employed in the time domain [Cov02, Liu07, Sek10]. This measurement technique comprises two microwave antennae spatially separated by the known distance s which are in close proximity of a ferromagnetic material, in the case of this thesis permalloy Py. The CPW embodiment used for AESWS measurements is the SW-transmission CPW, see Sec. 3.1.2. The magnetic stray field of the CPW [c.f. Fig. 6.2] shows a y dependence and thus excites SWs of different wave vector k in the Py. The excitation spectrum is given by $\rho(k)$ and the signal is proportional to the susceptibility via Eq. 2.102. Using a SW-transmission CPW of Sec. 3.1.2, two measurements are possible: the signal reflected by one CPW (S_{11}) and the signal transmitted between CPW 1 and 2 (S_{12}). The reference technique as described in Sec. 3.2.1 is applied. a_{11} here as well is a measure of the susceptibility χ_{tot} of the material, see Sec. 2.4.3 and Eq. 2.102. The transmission signal a_{12} contains additional contributions of the phase accumulated by the propagating SW. This is because the SW phase ϕ at the detector site (i.e. the phase of the signal at the second CPW site of a SW-transmission CPW) depends on the wave vector of the SW k via

$$\phi = ks, \tag{3.1}$$

where s is the propagation distance, see Sec. 3.1.2. Using the VNA, the change of phase $\Delta\phi$ is recorded for a change in the frequency Δf. Via variation the frequency f and thus of k within $\rho(k)$, it is possible to extract the group velocity v_{g} of the SWs. For this the change of the signal phase $\Delta\phi$ is measured for changing frequency Δf using a vector network analyzer (VNA). v_{g} is given by

$$v_{\text{g}} = \frac{\partial \omega}{\partial k} = 2\pi s \left(\frac{\Delta\phi}{\Delta f} \right)^{-1}. \tag{3.2}$$

The signal amplitudes $|a_{22}|$ and $|a_{12}|$ relate to each other via

$$
\begin{aligned}
|a_{12}(f)| &= \beta(\mathbf{H})|a_{22}(f)|\exp\left(-\frac{t(f)}{\tau}\right) \quad\quad (3.3)\\
&= \beta|a_{22}(f)|\exp\left(-\frac{s}{v_{\mathrm{g}}(f)\tau}\right),
\end{aligned}
$$

where τ is the SW relaxation time of Eq. 2.67 and $\beta(\mathbf{H})$ is a phenomeno-logical factor describing the excitation efficiency. The parameter β reflects the non-reciprocity. To justify the exponential decay of Eq. 3.3, compare with Eq. 2.66. a_{11} (or a_{22}) represents the excitation (or detection) strength. They contain complimentary information for homogeneous samples, i.e. samples which are uniformly structured into an ADL or not structured at all.

The non-reciprocity parameter $\beta(\mathbf{H})$ depends on the orientation of the dynamic magnetic field created by the CPW with respect to the magnetization orientation and is known to result in an non-reciprocal signal, i.e. $a_{12} \neq a_{21}$ [Dem09, Sek10]. In this thesis, positive values of H, i.e. signals a_{12} or a_{21}, are defined such that $\beta(H > 0) = 1$ and $0 < \beta(H < 0) < 1$. In particular, $\beta = 1$ is not explicitly stated and the value β given in Sec. 6.2 refers to $\beta(H < 0)$. Furthermore, when compensating for the non-reciprocity of excitation β, the signals a_{12} and a_{21} are found to be symmetric with respect to H. Keeping this in mind, a_{12} is discussed in the following.

Via a variation of f, it is possible to obtain different values of v_{g} from Eq. 2.77. By measuring a_{12}, a_{22}, and v_{g}, one can obtain τ from Eq. 3.3. Via Eq. 2.67, the damping parameters λ_{LL} and α_{LLG} are evaluated.

3.2.3 Magneto optical Kerr effect technique

Magneto optical Kerr effect

Measurements on samples prepared as part of this thesis employing the magneto optical Kerr effect (MOKE) have been conducted by the collaborators at the Institut für Experimentelle und Angewandte Physik, Universität Regensburg[1] by Hans Bauer, Prof. Dr. Christian Back, and Dr. Georg

---

[1] Institut für Experimentelle und Angewandte Physik, Universität Regensburg, D-93040 Regensburg, Germany
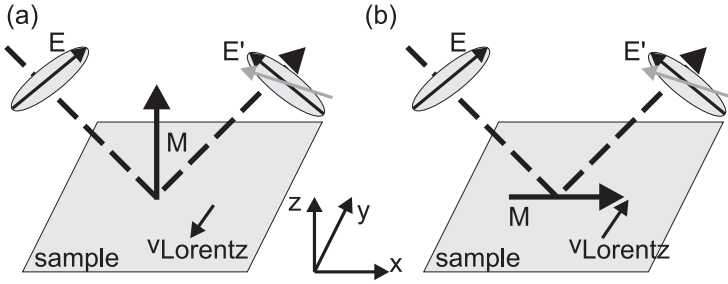
Figure 3.4: Schematic illustration of (a) the polar and (b) longitudinal magneto optical Kerr effect (MOKE). Incident light is linearly polarized as indicated by the electrical field **E**. Due to Lorentzian motion v_{Lorentz} of the charge carriers in the sample, the orientation of the polarization is slightly shifted. The polar MOKE is stronger than the longitudinal, which relies on a tilt of the incident light with respect to the plane of incidence.

Woltersdorf and at the CNISM, Dipartimento di Fisica, Universita di Perugia[1] by Dr. Gianluca Gubbiotti, Dr. Marco Madami, Dr. Silvia Tacchi. Experiments were carried out by the respective group in close collaboration with the author.

The MOKE effect is well established in literature and a more detailed discussion can be found in textbooks, e.g. Ref. [Hub00]. Linearly polarized light from a laser is focussed on the sample surface. The polarization angle is changed due to the interaction with electrons.

The change of the angle of polarization in the reflected light is measured. The dielectric permittivity ϵ is weakly dependent on the magnetization orientation. A change in the magnetization results in a change of the optical constants altering the reflection.[2]

Depending on the relative orientation of **M** with respect to **E** and the sample plane, different effects are distinguished. The strongest effect is the polar MOKE, where **M** is orientated out-of-plane and perpendicular to

---

[1] Via A. Pascoli, I-06123 Perugia, Italy

[2] In a classical microscopic picture, the electrical field of the incident electromagnetic wave will cause electrons in the material to move. This movement is subject to the Lorentz force, which induces a secondary movement proportional to $v_{\text{Lorentz}} = -\mathbf{M} \times \mathbf{E}$, where **E** is the electrical field. This leads to an alteration of the polarization angle.

the polarization direction of $\mathbf{E}$, see Fig. 3.4 (a). Also employed as part of this thesis is the longitudinal MOKE, where $\mathbf{M}$ is orientated in the plane and along polarization direction of $\mathbf{E}$. $\mathbf{E}$ needs to be tilted with respect to the sample surface, see Fig. 3.4 (b).

Application

Two embodiments of measurement setups employing the MOKE effect have been used in the course of this theses. In the first embodiment at Universita di Perugia, the longitudinal MOKE setup is employed. Light from a laser is shone through a polarizer and thus linearly polarized, focussed onto the sample surface under a given angle with respect to the surface normal, i.e. z direction, see Fig. 3.4. The laser spot diameter on the sample surface, i.e. xy plane, is on the order of $100\ \mu$m. An external field $\mu_0 H$ is applied in the xy plane. Using a polarization analyzer of known orientation with respect to the polarizer, the amplitude of the light becomes a measure for the change of polarization, i.e. the MOKE signal. The MOKE signal is measured as a function of the magnitude of the external field $\mu_0 H$. It is possible to map out the hysteresis curves of the remagnetization process of films or for individual nanoelements including antidot lattices. Because of the large size of the laser spot if compared to the typical length scale p of a magnetic nanostructure, the average magnetization parallel to the external field $\langle M_{\parallel} \rangle$, see Sec. 2.1.5, is measured. In Fig. 3.6 a hysteresis loop for a plain film of Permalloy prepared as part of this thesis is depicted, see Sec. 4. Here $\mu_0 H_{\mathrm{C}} \approx 2$ mT. This experimental method is well established and has been applied to a wide range of magnetic nanostructures including antidot lattices [Gue00, Yu00, Wan06, Hey06, Tri10].

In a second embodiment, spatial resolution in the xy plane and temporal resolution is provided. Such measurements were conducted at the Universität Regensburg [Neu06a, Bau11].[1] A Ti:sapphire laser system provides optical pulses of 150 fs temporal duration at a wavelength of 800 nm and 80 MHz repetition rate. This wavelength is doubled via second harmonic generation to increase the spatial resolution which is directly related to the wavelength of the probing light. The laser system triggers an electrical pulse generator. Temporal resolution is provided by stroboscopic measurements of the magnetization dynamics. The frequency doubled laser

---

[1] Institut für Experimentelle und Angewandte Physik, Universität Regensburg, D-93040 Regensburg, Germany
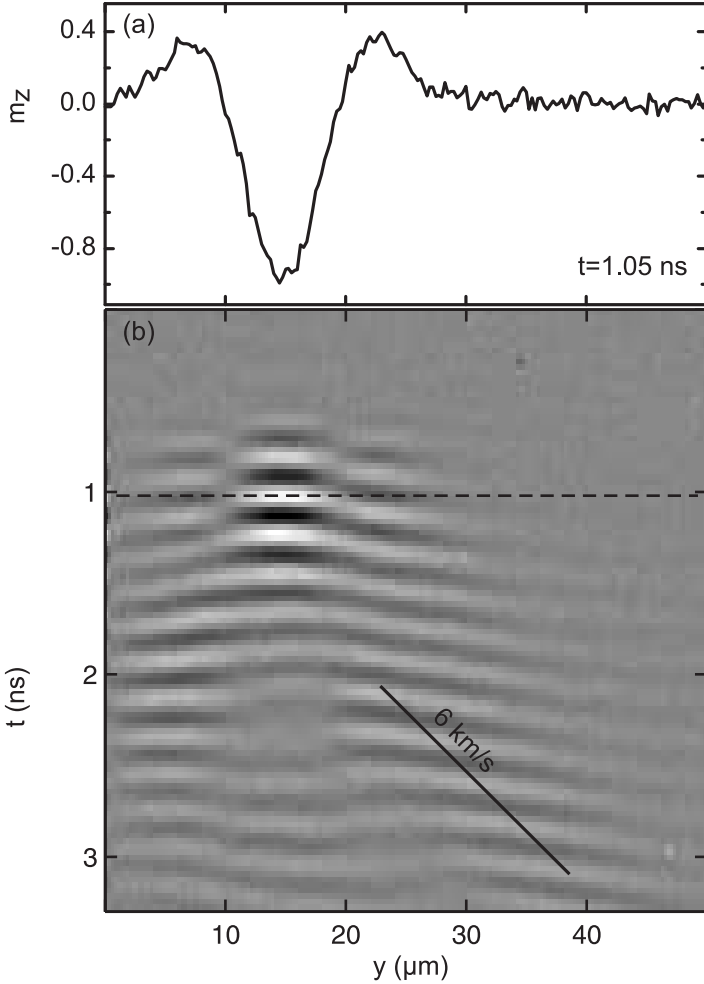
Figure 3.5: (a) MOKE signal m_z obtained from pulsed excitation at $t = 1.05$ ns measured in a $t_\mathrm{s} = 28$ nm thin Py film on top of a CPW [Bau11]. Parameters are: $\mu_0 H = 20$ mT. $\eta = 0°$. The CPW is prepared underneath the Py mesa. (b) Respective gray-scale coded spatio-temporal map of m_z. Dark and bright corresponds to large $|m_z|$. The horizontal line indicates $t = 1.05$ ns of (a). SWs propagate away from the CPW (solid line resembling $v_\mathrm{g} = 6$ km/s. The film ends at $y = 0$ μm and backreflection of SWs takes place there.
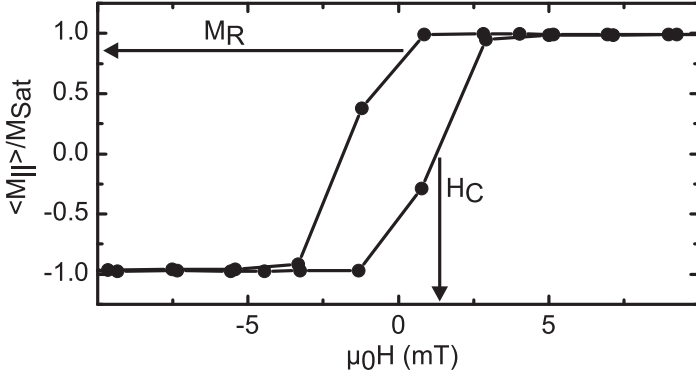
Figure 3.6: Hysteresis curve quantifying magnetization reversal for a plain film of permalloy (SN089-1). The film is prepared as part of this thesis as described in Sec. 4 and has been measured by the Perugia group. The coercive field amounts to $\mu_0 H_C \approx 2$ mT and the remanent magnetization to $M_R/M_{Sat} \approx 0.8$.

beam passes an optical delay path and a polarizer. The length of the delay path translates into a delay of the arrival of the laser at the sample. Magnetization dynamics is launched electrically by the pulse generator at a known time prior to the arrival of the probe laser beam. The laser beam is focussed onto the sample surface with a spot diameter of $200 - 300$ nm. Using the polar MOKE, see Fig. 3.4, the out-of-plane component of the precessing magnetization is measured by a fast photodiode. By moving the sample underneath the probing laser spot, lateral spatial resolution is achieved. Subsequent measurements with different delays imposed to the probe laser pulse yield temporal resolution. Spatio-temporal maps of the magnetization precession are achieved; such a measurement is depicted in Fig. 3.5 (b) for a 25 nm thick plain film prepared on top of a coplanar waveguide (CPW). In Fig. 3.5 (a), the spatial excitation profile of the CPW is plotted for a fixed time $t = 1.02$ ns. The experimentally obtained result depicted in Fig. 3.5 (b) can be compared directly to results obtained from micromagnetic simulations, see Fig. 2.4. From a Fourier transform of the obtained temporal evolution for a given position, the different spectral components of the oscillation can be extracted. It is possible to reconstruct a frequency resolved spatial spin-wave amplitude profile from such data

analysis [Bue04, Per08]. Such information can also be obtained from a continuous wave (cw) excitation of given frequency f [Neu06b]. By synchronizing the probing laser pulse to two given phases of the cw excitation, amplitude and phase information is obtained from such measurements.

3.2.4 Brillouin light scattering spectroscopy

Brillouin light scattering (BLS) describes an experimental technique which allows direct measurement of the spin-wave spectrum with wave vector k resolution. The principle of BLS is interaction of photons with given momentum and energy with magnons of given momentum and energy, i.e. the elementary quanta of spin waves. For room temperature, thermally exited magnons annihilate when scattering with incident photons. In the inverse process, a magnon is created. By conservation of energy and momentum, measurement of the change of the photon energy and of the solid angle which the photon is observed in, allows direct conclusions on the energy and momentum of the annihilated or created magnon. Details of the physical processes are explained in great detail in literature [Dem01]. It is possible to calculate the scattering cross section with magnons in periodic potentials [Kos10].

The experimental apparatus used in this thesis is located at CNISM, Dipartimento di Fisica, Universita di Perugia[1] and operated by this group. The measurements were performed as a joint project. Experiments were carried out by the respective group in close collaboration with the author.

Light of a laser with a given frequency f_0 and wavelength $\lambda_{\mathrm{L}} 532$ nm at 220 mW power is focussed on the sample using a camera objective having f-number 2 and 50 mm focal distance. The laser spot diameter is about 30 μm. The light scattered from the sample is collected and sent through a $(3 + 3)$ tandem Fabry-Prot interferometer. Only light of a certain frequency f_1 is allowed to pass through the interferometer. This frequency selected light is subsequently detected by a photomultiplier. The frequency difference $f_1 - f_0$ relates to the energy of the scattered magnon. A magnetic field $\mathbf{H}$ is applied in the film plane and perpendicular to the plane of the incident and reflected light beam. A goniometer implemented in the sample stage allows to vary the incident angle of the light. The in-plane component of the spin wave wave vector k is

---

[1]Via A. Pascoli, I-06123 Perugia, Italy

linked to the incidence angle of light θ via $k = 4\pi/\lambda_\text{L} \sin\theta$. By sweeping the incident angle of light one can measure the SW dispersion (frequency vs wave vector). Spectroscopy on magnons using BLS has been performed extensively since the late 1990s [Erc97, Jor99] and since then in a great number of systems [Gub02, Jor02, Wan02, Dem04a, Bay05] including antidot lattices [Tse09, Tac10b, Tac10a]. Recently, microfocusing of the BLS laser spot has allowed for spatial sensitivity at the cost of k resolution. Embodiments of this technique are micro-focussed BLS [Dem04a, Per05, Sch08c, Dem08, Mad10], phase resolved micro-focussed BLS [Vog09] and nano-BLS [Jer10]. To enhance the signal, density of magnons is increased by electrical excitation with a RF source frequency synchronized to the optical interferometer.

4 Preparation

Optical and electron beam fabrication techniques of coplanar wave guides are presented. Focussed ion beam preparation technique of antidot lattices is discussed.

In Fig. 4.1, a scanning electron micrograph (SEM) image of a typical, fully prepared sample is depicted. The substrate is Gallium Arsenide 001 (GaAs). Thickness is $350\ \mu$m. A SW-transmission CPW with $w_{ic} = 2\ \mu$m is visible on top of a permalloy mesa. The CPW is electrically insulated from the permalloy by SiO_2. The CPW and the permalloy mesa are prepared by optical lithography, see below. In another embodiment, the CPW is prepared by electron beam lithography, see Sec. 4.2. The permalloy mesa is structured by focussed ion beam (FIB) lithography, see Sec. 4.3, to form an antidot lattice, i.e. a periodic arrangement of holes.

4.1 Optical Lithography Preparation

Optical lithography is employed to prepare parts of the samples described in Sec. 3.1.2, including the permalloy mesa and the CPW.

Steps of preparation:

1. Masks for optical lithography are prepared using a laser mask writer at the Walter Schottky Institut, Garching, Germany. For the mask layout, the commercial software *Layout Editor*[1] and *Elphy Quantum*[2] are used.

2. Cleaning of GaAs substrate with acetone and isopropanol under ultrasonic agitation.

3. Application of resist system. A commercially available bilayer resist system is used. Bilayer resist systems create undercut resist struc-

---

[1] Juspector Corp., Unterhaching, Germany
[2] Raith Corp., Dortmund, Germany
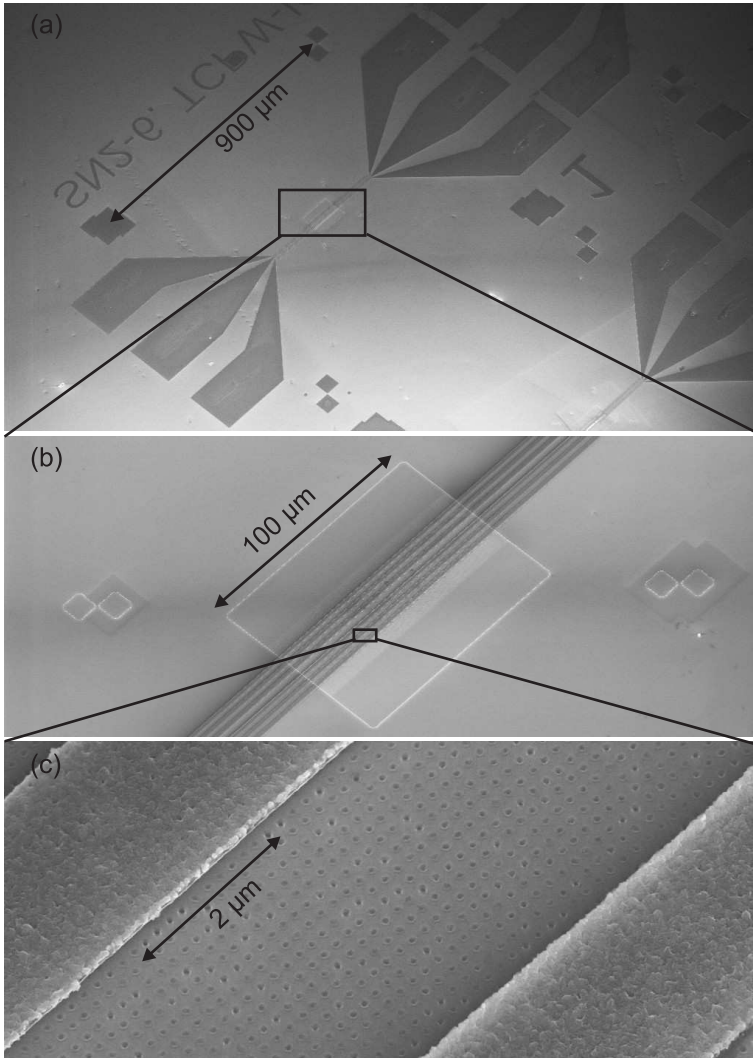
Figure 4.1: SEM image of a fully prepared sample. Visible is (a) the CPW with inner conductor width $w_{ic} = 2$ μm, (b) the permalloy Py mesa, and (c) the structured antidot lattice with periodicity $p = 300$ nm and hole diameter $d = 120$ nm. The depicted sample is SN89-1-LO.

tures enabling easy lift off. First, *LOR-3A* resist[1] is deposited by spin coating on the cleaned and dried GaAs substrate and subsequently baked. Prebake: 5 min, at temperature $200°C$, spin speed: 4.5 krpm, postbake: 60 s at temperature $160 - 180°C$ depending on the undercut value of the LOR resist to be achieved. Second, *S1813* resist[2] is deposited on the LOR-3A layer. Spin speed: 6.5 krpm, postbake at temperature 60 s at temperature $115°C$.

4. Ultraviolet light exposure. For exposure, an optical mask aligner *MJB-3* [3] is used. Exposure times varied between $3 - 6$ s, depending on the minimum feature size.

5. Development. Development of the structures is done using *MF CD-26* developer[4]. Development durations vary between $45 - 60$ s, depending on the undercut of the LOR to be achieved.

6. Electron gun deposition. For material deposition, both a thermal coating plant, as well as a high vacuum electron beam coating plant are used. Typical thicknesses of material deposition for the CPWs are: chromium Cr 45 nm, silver Ag 800 nm, and gold Au 22 nm. Cr establishes adhesion between the conduction material Ag and the substrate GaAs. Au is used to prevent oxidization. Pressures during deposition vary in the range $1 \cdot 10^{-7}$ mbar to $1 \cdot 10^{-6}$ mbar.

7. Material lift off. Lift off is achieved by using a comercially available remover product, *Microposit Remover 1165* [5]. Two bath system with lift-off times in the range of 40 min $- 90$ min at temperature $45°C$. No ultrasonic agitation for lift-off assistance.

4.2 Electron Beam Lithography Preparation

For coplanar waveguide preparation, electron beam lithography is employed if $w_{ic} < 1 \ \mu$m.

---

[1]MicroChem Corp., Newton, MA, USA.
[2]Shipley Corp., Marlborough, MA, USA.
[3]Karl Suss Corp., Waterbury Center, VA, USA.
[4]Shipley Corp., Marlborough, MA, USA.
[5]Shipley Corp., Marlborough, MA, USA.
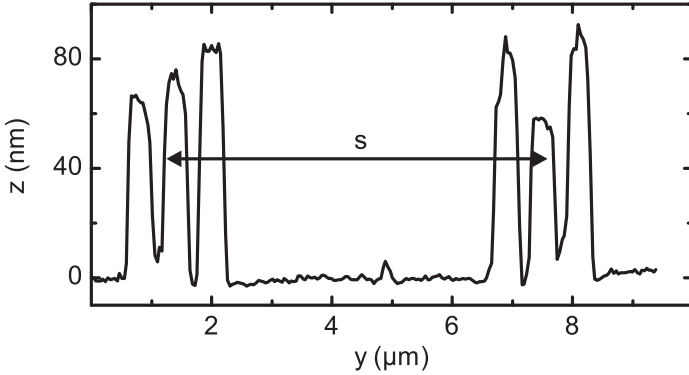
Figure 4.2: Atomic force microscopy height data of a coplanar waveguide (CPW) with propagation distance $s = 6.5$ μm, $w_{ic} = w_{oc} = 340$ nm, c.f. Fig. 3.3.

1. Cleaning of GaAs substrate with acetone and isopropanol under ultrasonic agitation.

2. Application of resist system. A commercially available trilayer resist system is used. Two layers of *AR-P 649.04*[1] are spin coated subsequently. Spin speed 4.5 krpm, duration 60 s, post bake 5 min at $160°$ C. Following to this, a single layer of *AR-P 671.02*[2] is spin coated. Spin speed 4.5 krpm, duration 60 s, post bake 5 min at $160°$ C.

3. Electron beam exposure. The sample is exposed to electrons in an *E-Line* Scanning-Electron Microscope (SEM)[3] in a two step exposure. First, the transmission region of the CPW, see Sec. 3.1.2 is exposed. Area exposure mode. Acceleration voltage 20 kV, aperture 20 μm, dose 160 μC/cm^2. Second, the pad and the taper regions are exposed. Acceleration voltage 20 kV, aperture 120 μm, dose 200 μC/cm^2. Write field size is 1 mm in both steps.

[1]Allresist Corp, Strausberg, Germany
[2]Allresist Corp, Strausberg, Germany
[3]Raith Corp., Dortmund, Germany

4. Development. Development of structures is done using *AR-600-56*[1]. Duration 60 s. Followed by a isopropanol bath. Duration 30 s. Followed by a water bath, duration 30 s.

5. Electron gun deposition. See Sec. 4.1.

6. Material lift off. See Sec. 4.1.

4.3 Focussed Ion Beam Lithography Preparation

Antidot lattices (ADL) are prepared into permalloy mesas. For focussed ion beam (FIB) lithography, a dual beam system comprising a scanning electron microscope (SEM) and a FIB microscope *NVision-40*[2] are used.

1. Alignment: For alignment with the permalloy mesa, optical alignment markers are used, see Fig. 3.2.

2. Exposure. Dot exposure mode of the FIB is used. Write field size is 330 μm. For holes of $\approx$ 120 nm diameter, the current amounts to 15 nA. Exposure time is 15 ms. The current and exposure time are set to ensure complete material etching through the Py mesa of thickness t_s. For smaller holes, the current is 1 nA.

In Fig. 4.3, an atomic force microscopy (AFM) image [Bin86] of an antidot lattice prepared by FIB lithography is shown. The surface roughness of the permalloy is resolved. It can be seen that the holes' depth is roughly 40-50 nm, which is larger than the film thickness of $t_s \approx 25$ nm. In Fig. 4.4, a scanning electron micrograph (SEM) image of an antidot lattice of periodicity $p = 120$ nm is shown. The hole diameter is evaluated to be 86 nm from this image.

---

[1]Allresist Corp, Strausberg, Germany
[2]Carl Zeiss NTS Corp., Oberkochen, Germany
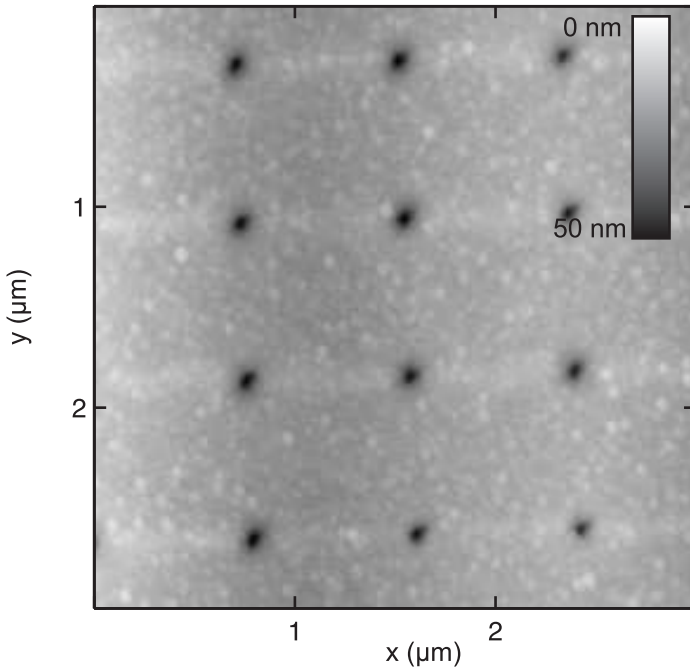
Figure 4.3: Gray-scale coded atomic force microscopy data of an $p = 800$ nm antidot lattice prepared by focussed ion beam etching into permalloy Py of thicknes $t_s = 25$ nm. Dark (bright) colors correspond to low (high) elevation level. Hole diameter is $d = 120$ nm. Visible is the polycrystalline structure of the permalloy.
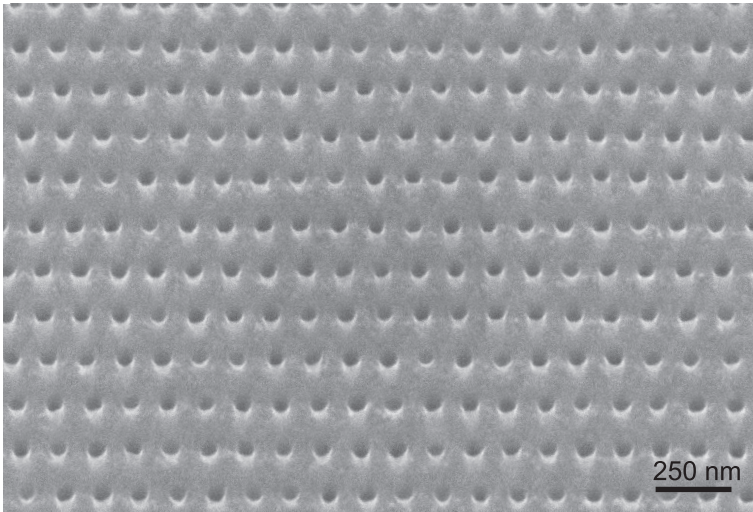
Figure 4.4: SEM micrograph of a $p = 120$ nm ADL. Sample is SN61-3-3. The hole diameter is evaluated to be 86 nm.

5 Electromagnetic Properties of a CPW

Experimental data characterizing the electromagnetic properties of SW-transmission CPWs is presented. The spatial field profiles are analyzed to obtain the wave vector excitation spectrum. Electromagnetic crosstalk is evaluated and found to describe well the magnitude of magnetic signal contributions originating from non-local excitation and detection.

The CPW design, see Sec. 3.1.2, is an essential part of the all electrical spin-wave spectroscopy technique (AESWS). Electromagnetic simulations are used to model the AESWS data. Before discussing AESWS data, it is important to investigate in detail the electromagnetic properties of the CPWs. The following issues need to be considered:

- The detected signal depends on the excitation spectrum $\rho(k)$ via Eq. 2.102. Depending on the inner conductor width w_{ic}, either a broad or small wave vector distribution Δk is excited [Cou04].

- Electromagnetic crosstalk between the two CPWs is influenced by the CPW geometry and the isolating material (dielectric) used. Direct crosstalk is minimized in order to avoid parasitic signals besides the propagating SW signal.

- The lateral CPW design determines the rf susceptibility [Ghi87]. Standard parameters are: $w_{ic} = w_{oc} = 2$ μm. Center to center distance of the two CPWs in the transmission region is $s = 12$ μm. Distance between outer and inner conductors is $s_{icoc} = 1.6$ μm. This design corresponds to an impedance of roughly 60 Ω according to Fig. 8 (a) of Ref. [Ghi87].

- Low ohmic losses ensure operation in the low loss region as described in Eq. 2.93. The CPW materials gold and silver are chosen accordingly.

In particular, for a SW-transmission CPW, see Sec. 3.1.2, the signal a_{12} has two contributions: Firstly, the signal originating from propagating SWs. Secondly, the signal originating from non-local excitation and detection. This signal is of parasitic nature, because it does not contain information about the SW propagation properties. In the following, this parasitic signal is denoted magnetic crosstalk. To minimize and separate the magnetic crosstalk signal from the AESWS signal is one of the main challenges of the AESWS experimental technique (Sec. 5.4).

5.1 Measured Scattering Parameters

The CPW is electrically characterized by the S-parameters. Consider the CPW as a transmission element as defined in Sec. 2.4.2. Excitation occurs at port 1, i.e. port 1 is the emitter. Then $a_2 = 0$ and $b_2 = S_{21}a_1$ as follows from Eq. 2.96. The magnitude of S_{12} in dB is a measure of signal fraction detected at the detector site (port 2) via [Hie07]

$$S_{21}(\text{dB}) = 20 \log(S_{21}) = 20 \log\left(\frac{b_2}{a_1}\right). \tag{5.1}$$

Analogous for S_{12}. S_{12} and S_{21} are found to be symmetric in the case of the CPWs used in this thesis. In the following, S_{12} is denoted only. In Fig. 5.1, the S_{12} parameters of three different SW-transmission CPWs consisting of two parallel waveguides. The qualitative behavior of the S-parameters remains the same over a large number of samples as listed in A.1. In particular, for smaller s the value of S_{12} is increasing. This can be seen from curves i-iii where s is decreasing from $s = 19.5$ μm to $s = 6.5$ μm.

5.2 Modeled Scattering Parameters

To model the S-parameters, a full scale electromagnetic field simulation is employed, see Sec. 2.4.4. For this the mask layout used for CPW preparation by optical lithography, see Sec. 4, is used for the simulation geometry. Simulation parameters are listed in A.4. The S-parameters can be assumed to be a fingerprint of the simulated geometry: good agreement between measured and simulated signal is an indication for successful modeling of the device.
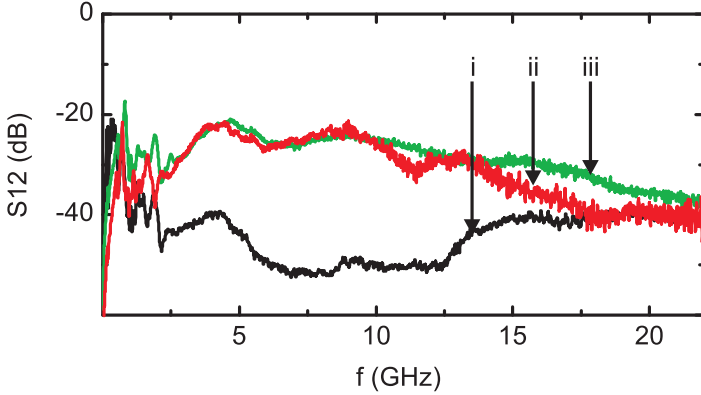
Figure 5.1: Raw data of the magnitude of S_{12} measured with a vector network analyzer (VNA) on three different coplanar waveguides in the transmission embodiment, see Sec. 3.1.2. (i) CPW with $s = 19.5\ \mu$m and $w_{\text{ic}} = 4\ \mu$m (sample SN75-4-4). (ii) CPW with $s = 12\ \mu$m and $w_{\text{ic}} = 2\ \mu$m and a different thickness of the isolator compared to SN75-4-4 in the range $10-30$ nm (sample SN089-4). (iii) CPW with $w_{\text{ic}} = 340$ nm and $s = 6.5\ \mu$m (sample SN88-1-A-M, c.f. Fig. 4.2).

Electromagnetic field simulations are performed for a SW-transmission CPW with $w_{\text{ic}} = 2\ \mu$m and propagation path (distance between the centers of the two center conductors) $s = 12\ \mu$m. For such a geometry, the accuracy of electromagnetic simulations is fundamentally limited by the large differences in the relevant length scales. The CPW metallization of $0.2\ \mu$m is much thinner than the substrate size of $350\ \mu$m. The isolator thickness of $0.01 - 0.03\ \mu$m and Py film thickness are much thinner than the CPW metallization of $0.2\ \mu$m. This requires long simulation times.

Characteristic minima and maxima in frequency, as well as the absolute values of S_{12} are well reproduced by the simulation. This good qualitative agreement allows to proceed to simulations of the magnetic and electric field profile. Remaining discrepancies are attributed to the large differences in relevant length scales making it difficult to generate an optimum mesh for the simulations.
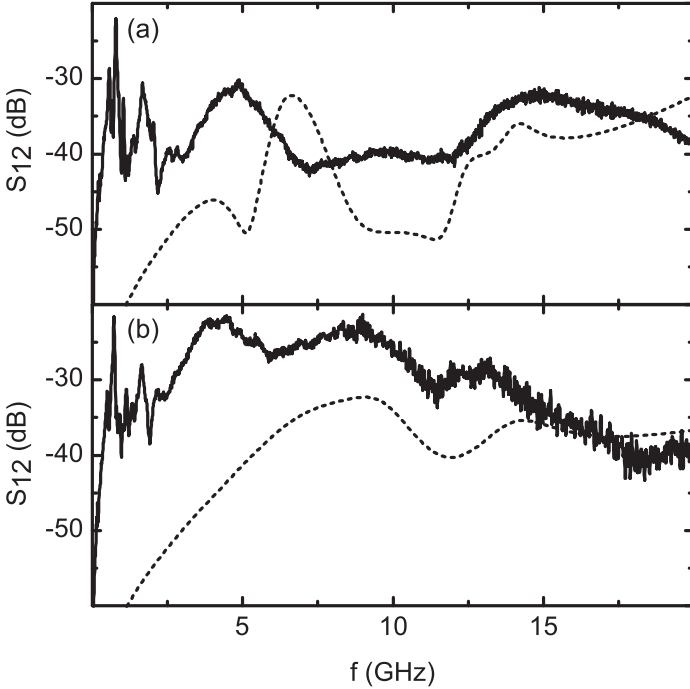
Figure 5.2: Raw data of the magnitude of S_{12} obtained from electrical characterization using a VNA (full lines) and electromagnetic field simulations (dotted lines) of SW-transmission CPWs with $w_{ic} = 2$ μm and $s = 12$ μm. No magnetic field applied. (a) Sample SN082-2-LU. Simulated isolator thickness $t_{\mathrm{iso}} = 15$ nm. (b) Sample SN89-4-D. Simulated isolator thickness $t_{\mathrm{iso}} = 35$ nm. For thicker isolator layers, a general shift towards larger S_{12}, i.e. larger electric crosstalk, is evidenced. The isolator thickness varied in the experiment and is not measured for every sample.
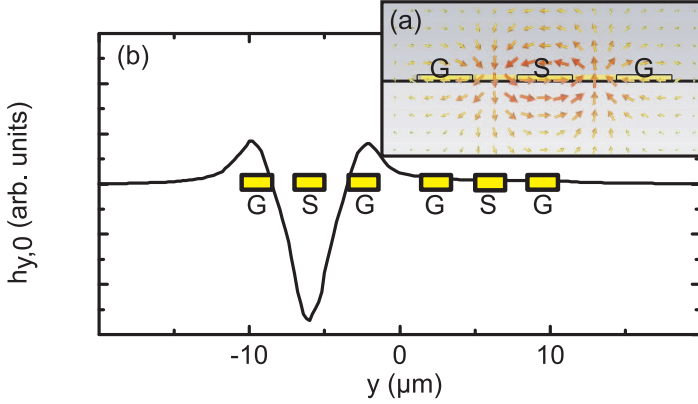
Figure 5.3: Dynamic magnetic field $\mathbf{h}_{\rm rf}$ obtained from micromagnetic simulations. (a) Vector field plot of the field orientation and magnitude in logarithmic scale for the emitter CPW. (b) Field plot of the spatial dependence of the in-plane rf magnetic field $h_{y,0}(y)$ as defined in Eq. 2.103 and obtained from electromagnetic field simulations (see text for simulation details). Due to technical reasons, the amplitude obtained from simulation did not reflect the experimental value. Only the spatial distribution is considered to be significant. Data is relevant for the transmission region, c.f. Fig. 3.3 within the permalloy layer. Indicated are the CPW metallic signal and ground lines. $w_{\rm ic} = 2\ \mu$m is assumed.

5.3 Modeling of the spatial Field Profile

In Fig. 5.3 (a) the dynamic magnetic field $h_y(y)$ is depicted in the yz plane [c.f. Fig. 3.3]. The characteristic asymmetric CPW mode [Pon97, Sim01] is observed. In Fig. 5.3 (b), the y component of the dynamic magnetic field $h_y(y)$ is depicted as evaluated in the Py layer ($t_{\rm s} = 25$ nm). h_y has the largest value if compared to h_z and h_x and therefore predominantly determines the interaction with the magnetization dynamics.

A discrete fast Fourier transformation of $h_y(y)$ is depicted in Fig. 5.4 (b). This corresponds to the excitation spectrum $\rho(k)$. A maximum of $\rho(k)$ is observed for $k = k_{\rm CPW} = 0.6 \times 10^4$ rad/cm $= 0.6$ rad/μm. $k_{\rm CPW}$ is the wave vector for which SWs are most prominently excited by the CPW. The first minimum is located at $k = k_{\rm Max} = 1.7 \times 10^4$ rad/cm. This is associated with a wave vector distribution Δk. In a first approximation the
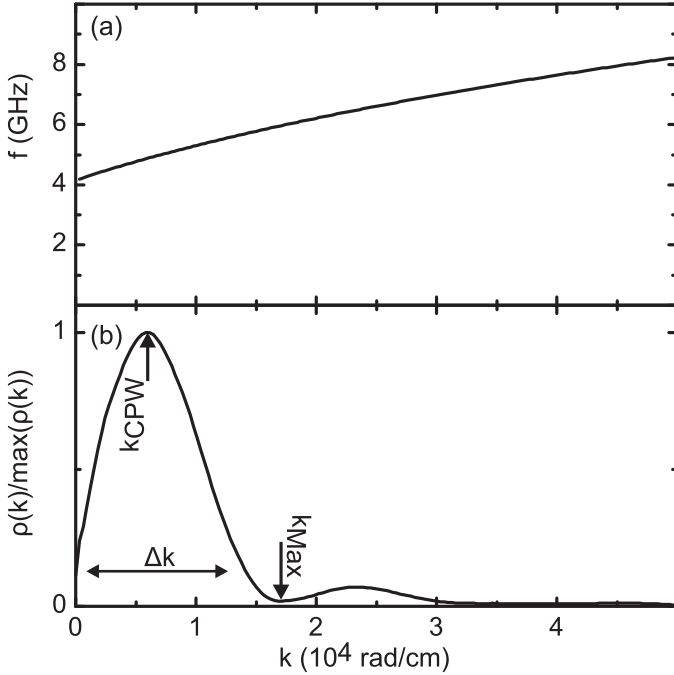
Figure 5.4: (a) SW dispersion for $\mu_0 H = 20$ mT, $\eta = 0°$, $t_s = 25$ nm, and $M_{Sat} = 830$ kA/m, c.f. Fig. 2.2. This dispersion is obtained from Eq. 2.73 and used for the transformation $\rho(k) \rightarrow \rho(f(k))$. (b) Normalized excitation spectrum $\rho(k)$ of a CPW $w_{ic} = 2$ μm obtained from a Fourier transformation of $h_y(y)$ as obtained from em field simulations (for details, see text). See Fig. 5.3. The prominently excited wave vector distribution Δk is indicated. The wave vector for which $\rho(k)$ is maximum is labeled $k_{CPW} = 0.6 \times 10^4$ rad/cm and the first minimum of $\rho(k)$ is labeled $k_{Max} = 1.7 \times 10^4$ rad/cm. Visible is a second maximum for $k = 2.4 \times 10^4$ rad/cm.

SW excitation spectrum $\rho(k)$ translates into frequency space by the SW dispersion $f(k)$ of Eq. 2.73. This is depicted in Fig. 5.4 (a) for $\mu_0 H = 20$ mT, $\eta = 0°$, $t_s = 25$ nm, and $M_{\mathrm{Sat}} = 830$ kA/m. A small nonlinear behavior is observed for the relevant wave vector regime described by Δk.

It is possible to compare the simulated values for k_{Max} with values obtained from literature. In Ref. [Cou04] it is stated that

$$k_{\mathrm{Max}} = \pi/w,$$

which yields a value of $k_{\mathrm{Max}} = 1.5 \times 10^4$ rad/cm in good agreement with the simulation result of $k_{\mathrm{Max}} = 1.7 \times 10^4$ rad/cm.

In Ref. [Ken07] it is stated that

$$k_{\mathrm{Max}} = \frac{2\pi}{w + 2s_{\mathrm{icoc}}}$$

which yields $k_{\mathrm{Max}} = 1.2 \times 10^4$ rad/cm.

The data obtained for $h_y(y)$ allows to calculate the spatial sensitivity Σ entering the measured voltage signal in Eq. 2.104. This is depicted for the same SW-transmission CPW in Fig. 5.5 (a) for a reflection measurement (corresponding to a_{22}), i.e. $h_{y_0,2} = h_{y_0,1}$ in Eq. 2.105. Note that the scale is divided by a factor 100 in order to compare with Σ for the transmission measurement (corresponding to a_{12}) in (b). From Fig. 5.5 (a) it follows that for the reflection measurements $\approx 80\%$ of the signal is obtained right underneath the inner conductor and respectively 10% underneath the outer conductors (see right scale). This is different in the transmission measurement. Only $\approx 30\%$ of the signal amplitude is acquired underneath each of the two inner conductors. The remaining 40% of the signal amplitude originate from spatial regions underneath the four outer conductors. This finding motivates labeling of the magnetic crosstalk signal as non-local signal contributions as this signal originates from many different areas of the sample.

5.4 Electromagnetic Crosstalk

The non-local signal strength (magnetic crosstalk) is quantified as a function of the S_{12} value for various samples. The samples used for this analysis are SN88-1-A-M, SN75-4-4, SN83-1-LO, SN89-4-4, see A.1. Because
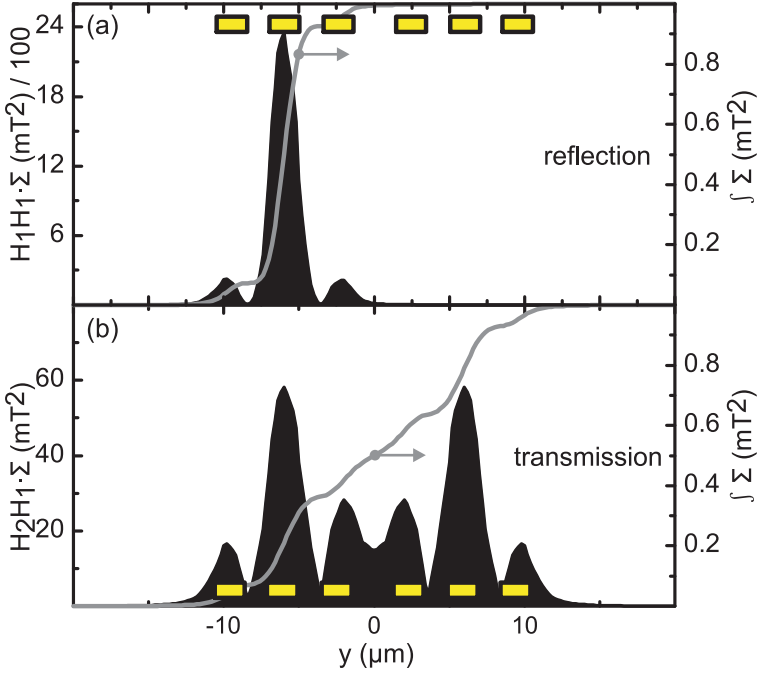
Figure 5.5: (a) Spatial sensitivity Σ of a SW-transmission CPW used for reflection measurements, i.e. a_{11} measurement, see Eq. 2.105 (dark spectrum, left axis). Indicated are the CPW metallic signal and ground lines with $w_{ic} = 2\ \mu m$. Evaluated is the $h_y(y)$ of Fig. 5.3. The light gray line (right axis) indicates $\int \Sigma$. The sensitivity mainly ($\approx 80\%$) arises from underneath the inner conductor. (b) Spatial sensitivity Σ of the same CPW but used for transmission measurement, i.e. a_{12} is considered (dark spectrum, left axis). Sensitivity is strongly reduced if compared to the reflection measurement. The light gray line (right axis) indicates $\int \Sigma$. 50% of the sensitivity is spatially located underneath the excitation (detection) CPW. Note that the absolute values of the sensitivity do not reflect experimental values due to technical reasons.
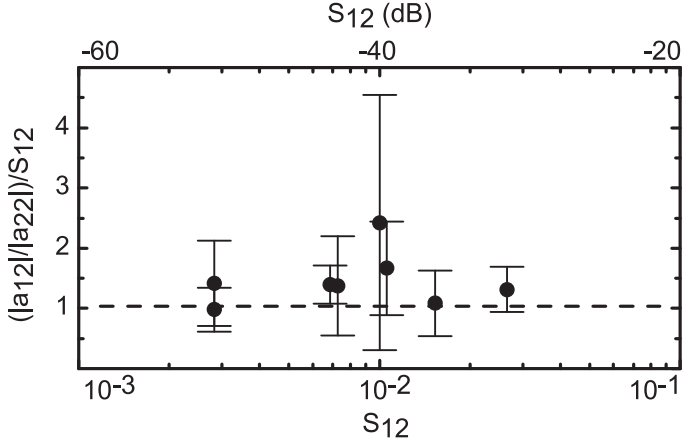
Figure 5.6: Non-local signal contributions $|a_{12}|/|a_{22}|$ related to electromagnetic coupling S_{12} for different values of S_{12}. Data is obtained for various samples for modes which *are known not to propagate*, i.e. $v_\mathrm{g} = 0$. Therefore, signal from propagating SWs is excluded. The measured signal corresponds only to magnetic crosstalk. Different CPWs are used and s varied between 6 and 20 μm. Data is evaluated for different f, where the various CPWs showed different S_{12}, see Fig. 5.1. Within error margins, non-local signal contributions and electromagnetic crosstalk are of the same value.

of the different CPWs used (6.5 μm $\leq s \leq$ 19.5 μm), these samples show a variation of S_{12} between -50 dB and -30 dB, i.e. the electromagnetic crosstalk varies over roughly one order of magnitude. The signal $|a_{12}|$ is measured for modes that *are known not to propagate*. The normalized measured signal $|a_{12}|/|a_{22}|$ is related to the measured S_{12} (in linear scale, see Eq. 5.1). This fraction is, with errors, close to unity, see Fig. 5.6. Therefore, the design goal for optimized AESWS SW antennae must be to minimize electromagnetic crosstalk and, by this, minimize non-local SW excitation and detection, i.e. the magnetic crosstalk.

The average value of $(|a_{12}|/|a_{22}|)/S_{12}$ is slightly above 1. This can be motivated as follows: The electrical crosstalk is given by the field strength at the detector site. Care has to be taken, because, both, the asymmetric and symmetric mode are excited. The symmetric mode (slot-line mode) does

not match the potential levels of the connected circuitry, therefore is not detected, and is regarded parasitic [Pon97]. For the non-local excitation, the convolution between $h_{y_0,2}$ and $h_{y_0,1}$ needs to be considered: magnetization dynamics, which is non-locally excited by the first CPW, is picked up by the second CPW. In other words, the non-local crosstalk is mediated over the whole length of s by the magnetic material and is therefore larger than the electromagnetic crosstalk which relies on direct inductive pickup.

6 Plain Film Measurements

All electrical spin wave spectroscopy (AESWS) is employed on a $t_{\mathrm{s}} = 25$ nm thick Py film which is deposited on top of the Gallium Arsenide semi-insulating substrate using optical lithography, see Sec. 4.1. On top of the permalloy silicon dioxide is sputtered[1]. The CPW parameters are $w_{\mathrm{ic}} = 2$ μm, outer conductor widths $w_{\mathrm{oc}} = w_{\mathrm{ic}}$ and center to center distance $s = 12$ μm. The CPW is prepared using optical lithography. The considered sample is SN89-4-D.

6.1 Phenomenology

The signals a_{22} and a_{12}, see Sec. 3.2.2, are depicted in Fig. 6.1 for $\eta = 0°$ [c.f. Fig. 3.3] and $\mu_0 H = 20$ mT. $\eta = 0°$ corresponds to $\triangleleft(\mathbf{k}, \mathbf{H}) = 90°$. In Fig. 6.1 (a), a_{22} is depicted. The solid line marks the amplitude $|a_{22}|$, while dotted (dashed) lines mark imaginary $\Im a_{22}$ (real part $\Re a_{22}$) of the signal. Two resonances are observed for $f_{\mathrm{r}} = 4.9$ GHz and $f_{\mathrm{r}} = 6.7$ GHz and are marked by vertical arrows. In Sec. 6.2.1 it is shown that these resonances originate from the excitation spectrum $\rho(k)$ excited by the CPW, see Eq. 2.102. Fig. 6.1 (b) depicts $\Im a_{22}$ for $\eta = 70°$. Different to the case of $\eta = 0°$, only a single resonance is resolved which is of Lorentzian shape. Fig. 6.1 (c) depicts $|a_{22}|$ (thick black line) and $\Re a_{12}$ ($\Im a_{12}$) as thin black (grey) lines. As expected from Eqs. 2.102 and 3.1, real and imaginary part oscillate due to the accumulated phase of propagating spin waves. Plotting the phase $\phi(a_{12})$ in Fig. 6.1 (d) reveals the phase change $\Delta\phi/\Delta f$ of Eq. 3.1 for frequencies well within the resonance linewidth of a_{22}, i.e. for $4 < f < 7$ GHz.

Next, the dependence of a_{22} and a_{12} on the magnetic field strength $\mu_0 H$ and the orientation of the external field with respect to the CPW is measured. Fig. 6.2 (a) depicts the magnitude $|a_{22}|$ ($|a_{12}|$) taken over all frequencies f as a thick (light) line. $|a_{22}|$ shows a response almost perfectly symmetric with respect to H, i.e. $|a_{22}(+\mu_0 H)| = |a_{22}(-\mu_0 H)|$. Fur-

---

[1]50 W sputter power, 10% O_2 and 90% Ar_2 atmosphere
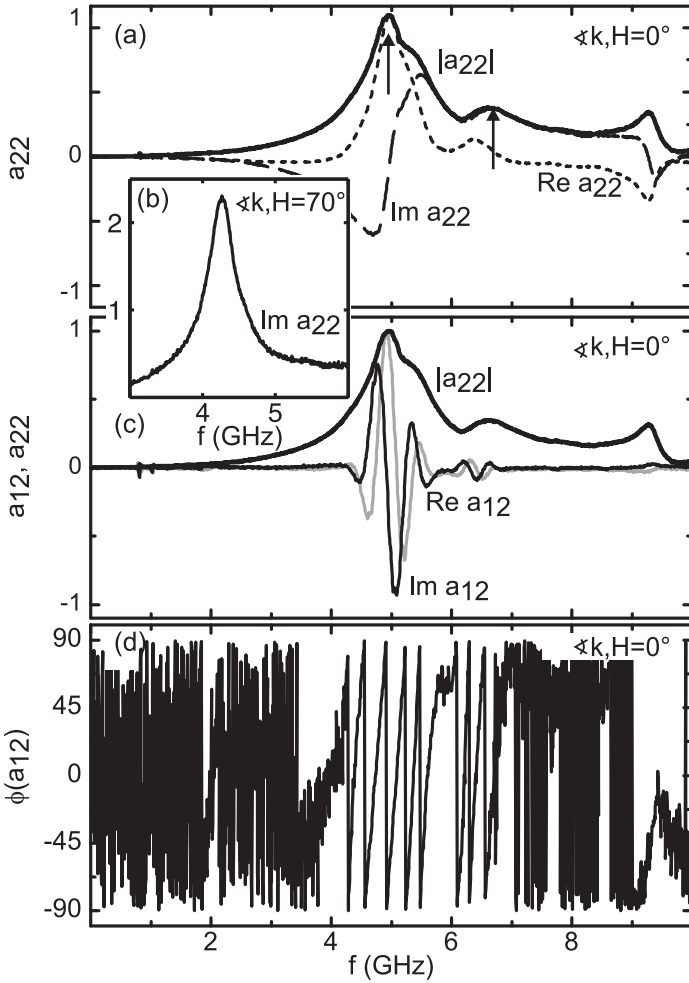
Figure 6.1: (a) Normalized signal a_{22} measured in reflection for $\eta = 0°$ and $\mu_0 H = 20$ mT. Data is obtained for a plain film (sample SN89-4-D). $|a_{22}|$ (full thick line). $\Im a_{22}$ (dashed line). $\Re a_{22}$ (dotted line). Vertical arrows mark resonance positions. (b) $\Im a_{22}$ for $\eta = 70°$ and $\mu_0 H = 20$ mT. (c) $|a_{22}|$ (full thick line). $\Im a_{12}$ (full thin line). $\Re a_{12}$ (full thin light gray line). All at $\eta = 0°$, $\mu_0 H = 20$ mT. (d) Phase $\phi(a_{12})$. $\eta = 0°$, $\mu_0 H = 20$ mT.
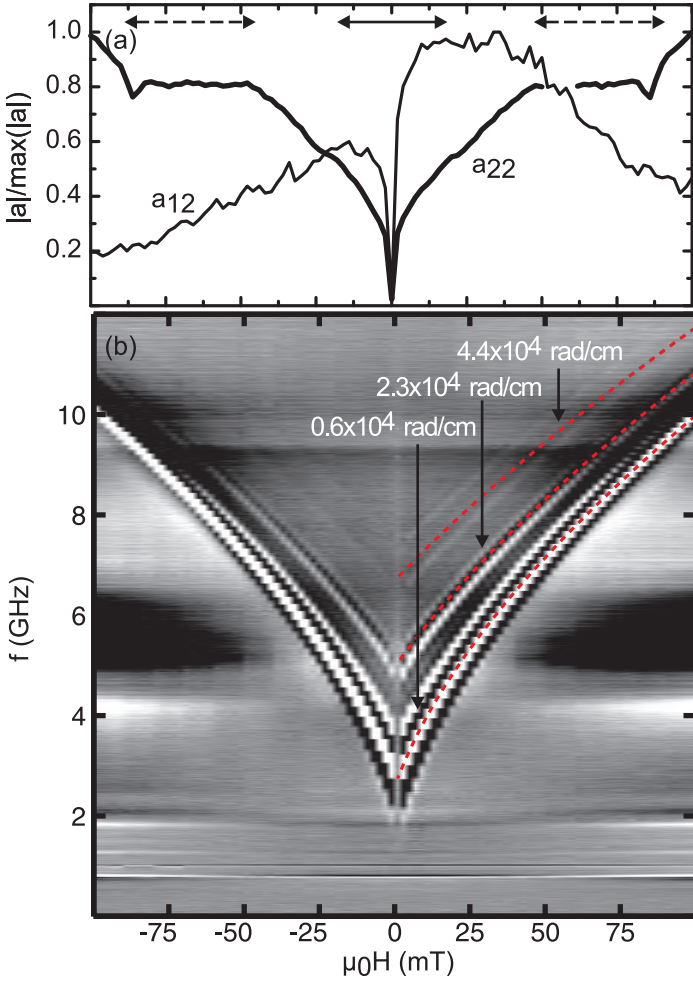
Figure 6.2: Data is obtained for a plain film at $\eta = 0°$ (sample SN89-4-D). (a) Normalized amplitudes $|a_{22}|/\max|a_{22}|$ (thick line) and $|a_{12}|/\max|a_{12}|$ (thin line). Horizontal arrows mark regimes where a_{22} or a_{12} deviate from the standard behavior, see text. (b) Gray-scale plot for $\Re a_{12}$. Contrast is enhanced to show high frequency excitations. Thin red dashed lines mark calculated resonance frequencies $f_r(\mu_0 H)$ for $k = 0.6 \times 10^4$, $k = 2.3 \times 10^4$, and $k = 4.4 \times 10^4$ rad/cm using Eq. 2.73.
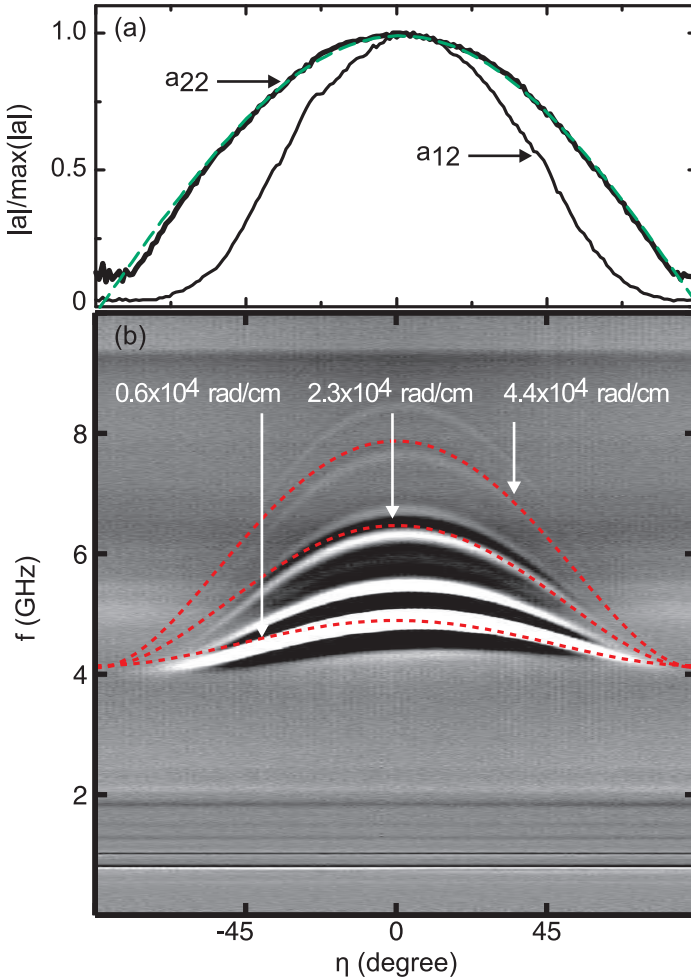
Figure 6.3: Data is obtained for a plain film at $\mu_0 H = 20$ mT (sample SN89-4-D). (a) Normalized amplitudes $|a_{12}|/\max|a_{12}|$ (thin line) and $|a_{12}|/\max|a_{12}|$ (thick line). The dashed line is a $\cos \eta$ fit, see Eq. 2.104. (b) Gray-scale plot for $\Re a_{12}$. Contrast is enhanced to show high frequency excitations. Thin red dashed lines mark calculated $f_r(\mu_0 H)$ for $k = 0.6 \times 10^4$, $k = 2.3 \times 10^4$, and $k = 4.4 \times 10^4$ rad/cm using Eq. 2.73.

thermore, $|a_{22}|$ increases monotonically with the H, i.e. $|a_{22}(+\mu_0 H)| \leqslant |a_{22}(+\mu_0(H+\delta H))|$ with $\delta H > 0$. In contrast, for $\mu_0|H| > 10\,\text{mT}$, $|a_{12}|$ shows a very different response, being asymmetric with respect to the external field, i.e. $|a_{12}(+\mu_0 H)| > |a_{12}(-\mu_0 H)|$. Furthermore, the signal is monotonically decreasing, i.e. $|a_{12}(+\mu_0 H)| \geqslant |a_{12}(+\mu_0(H+\delta H))|$. In Fig. 6.2 (b), $\Im(a_{12})$ is depicted for various field strengths $\mu_0 H$ (gray-scale plot). The contrast is enhanced in order to show weak features for larger frequencies f. Four resonances are resolved. They are marked by horizontal yellow arrows for $\mu_0 H = 20\,\text{mT}$. The resonances at $f_\text{r} = 4.9\,\text{GHz}$ and $f_\text{r} = 6.7\,\text{GHz}$ are identical to those observed in Fig. 6.1 (a). Due to the increased contrast, two further resonances are resolved at $f_\text{r} = 7.9\,\text{GHz}$ and $f_\text{r} = 8.6\,\text{GHz}$. For all resonances, a monotonic increase in the resonance frequency with increasing field is observed. A quantitative analysis is presented in Sec. 6.2.

Last, the dependence of a_{22} and a_{12} on η is discussed. In Fig. 6.3 (a) the thick (thin) solid line denotes the maximum $|a_{22}|$ ($|a_{12}|$) taken over all frequencies f. Both values decrease for larger values of $|\eta|$. They are symmetric with respect to η, i.e. $a_{22}(+\eta) = a_{22}(-\eta)$ and $a_{12}(+\eta) = a_{12}(-\eta)$. For $|a_{12}|$ a stronger decrease as a function of η is observed if compared to $|a_{22}|$. In Fig. 6.3 (b), $\Re a_{12}$ is depicted for various η. The contrast is enhanced in order to show weak features for larger frequencies f. A monotonic decrease in the resonance frequency for increasing $|\eta|$ is observed. Four resonances are observed with $f_\text{r} = 4.9, 6.7, 7.9$, and $8.6\,\text{GHz}$ for $\eta = 0°$. They correspond to the resonances observed in the field dependent data depicted in Fig. 6.2. A quantitative analysis of the angular dependent magnitude is presented in the following section 6.2.

6.2 Interpretation and Analysis

6.2.1 Susceptibility and inhomogeneous broadening

In order to interpret the data obtained for a_{22} and a_{12} as presented in the previous section Sec. 6.1, it is instructive to first calculate the expected signal response. This response is proportional to the total susceptibility χ_tot via Eq. 2.102. The contributions to the measured susceptibility χ of different wave vectors excited by the non-homogeneous field distribution, i.e. the excitation spectrum $\rho(k)$, need to be summed up. Here $\rho(k)$ is obtained via full scale simulations of the electromagnetic fields
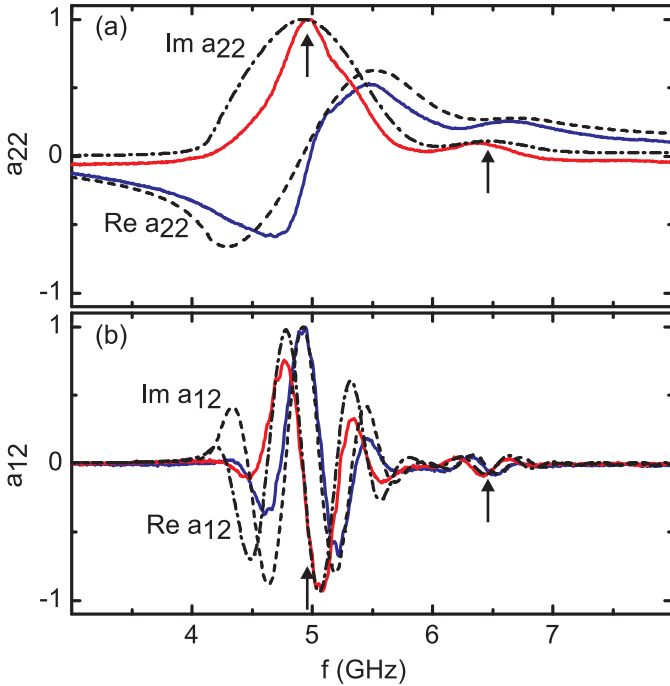
Figure 6.4: (a) Full lines are measured quantities $\Re a_{22}$ and $\Im a_{22}$ replotted from Fig. 6.1. Data is obtained on a plain film (sample SN89-4-D). Dashed-dotted and dashed lines are calculated $\Im a_{22}$ and $\Re a_{22}$ signals, respectively, using a simulated field distribution $h_y(y)$, see Sec. 5 and χ_{tot} given by Eq. 2.102 for $M_{\text{Sat}} = 830$ kA/m, $t_s = 25$ nm, $\alpha = 0.005$, and $s = 0$ μm. All data is normalized to its maximum value. (b) Full lines are measured quantities $\Re a_{12}$ and $\Im a_{12}$, c.f. Fig. 6.1. Dashed-dotted and dashed lines are calculated $\Re a_{12}$ and $\Im a_{12}$ signals using a simulated field distribution $h_y(y)$, see Sec. 5 and χ_{tot} given by Eq. 2.102. All data is normalized to its maximum value.

in the investigated systems, see Fig. 5.4 (b) and Sec. 5. For $\eta = 0°$, the relevant susceptibility χ is stated in Eq. 2.78. The obtained values for a_{22} and a_{12} are plotted in Fig. 6.4 as dashed and dashed-dotted lines. Each curve is normalized to its maximum value. The calculated response models all features of the measured data. Best agreement is obtained for $M_{\mathrm{Sat}} = 830$ kA/m, $t_{\mathrm{s}} = 25$ nm. Some differences remain in the signal amplitudes for 4 GHz $\leqslant f \leqslant 4.6$ GHz and for 5.4 GHz $\leqslant f \leqslant 6$ GHz due to uncertainties in $\rho(k)$ obtained from electromagnetic field simulations. In particular, two major resonances observed experimentally in Figs. 6.1 (a) and 6.4 (a) are remodeled and marked by vertical arrows. To clarify the origin of the multipeak structure of the spectrum, it is instructive to study the agreement between a_{12} and $\rho(f(k))$, where wave vectors k are related to frequencies f via the spin-wave dispersion Eq. 2.73 for $M_{\mathrm{Sat}} = 830$ kA/m, $t_{\mathrm{s}} = 25$ nm, and standard permalloy parameters. From Fig. 6.5 one can see good agreement in the position and magnitude of the excitation spectrum with a_{12}. Three of the four peaks observed in Fig. 6.2 are remodeled and marked by the vertical arrows.

It is possible to conclude that the complex excitation spectrum consisting of multiple peaks originates from the excitation spectrum $\rho(k)$ [c.f. Fig. 5.4] of the spatially non-uniform magnetic field $h_y(y)$ [c.f. Fig. 5.3] of the CPW. Frequency positions of the resonances are given via the dispersion relation $f(k)$, see Eq. 2.73. The measured response a_{12} and a_{22} is a direct measure for the susceptibility χ_{tot} as given by Eq. 2.102. The contributions to the resonance linewidth Δf due to $\rho(k)$ are known in literature as inhomogeneous broadening [Sch04, Cou04]. Δf is not a direct measure for the SW relaxation time τ via Eq. 2.64.

The dependence of $|a_{22}|$ on the field H and the angle η as depicted in Figs. 6.2 (a) and 6.3 (a), respectively, is analyzed next. Equation 2.104 predicts a linear dependence of the signal amplitude $|a_{22}|$ on the resonance frequency f_{r}, as well as a $\cos(\eta)$ dependence of $|a_{22}|$ on the alignment of the external field with respect to the CPW (wave vector). To test this, one extracts the resonance frequency f_{r} where $\Im a_{22}$ exhibits a maximum value, f_{r} for various values of $\mu_0 H$ from Fig. 6.2 (b). This is done in Fig. 6.6. For $f_{\mathrm{r}} < 7$ GHz a linear dependence of $|a_{22}|$ is observed in agreement with Eq. 2.104. This is illustrated by the dashed gray line. For 7 GHz $< f_{\mathrm{r}} < 9$ GHz, $|a_{22}|$ remains almost constant. These values of f_{r} relate to $50 \leq \mu_0 H \leq 100$ mT. In this field regime, a superposition of the reference dataset with the measured data is observed: the resonance
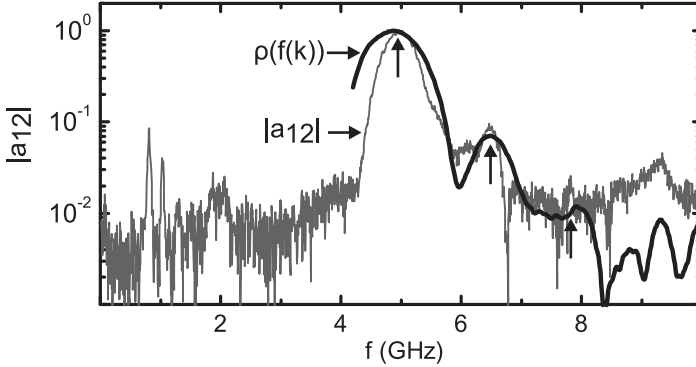
Figure 6.5: Normalized excitation spectrum $\rho(f(k))$ (thick line) obtained from electromagnetic field simulations, see Sec. 2.4.4, compared to measured data $|a_{12}|$. The in-plane magnetic field $h_y(y)$ is evaluated within the permalloy layer. A subsequent Fourier transformation yields $\rho(k) \multimap h_y(y)$ which is then mapped into frequency space using the spin-wave dispersion $f(k)$ of Eq. 2.73 for $M_{\mathrm{Sat}} = 830$ kA/m, $t_{\mathrm{s}} = 25$ nm and $\mu_0 H = 20$ mT. The thin gray line corresponds to $|a_{12}|/\max|a_{12}|$ obtained from the plain film sample SN89-4-D for $\mu_0 H = 20$ mT. In $\rho(k)$ three maxima are resolved and marked by the vertical arrows indicating that the multiple resonances observed for a_{12} originate from $\rho(k)$ via Eq. 2.102.

frequency of the reference data sets is degenerate with the resonance frequency at the measurement field. By substraction of the reference data, the measured signal comprises a superposition of both resonances and the value of $|a_{22}|$ is thereby reduced.

Equation 2.104 predicts a $\cos(\eta)$ dependence of $|a_{22}|$ evaluated at f_{r}. Such a dependence is plotted as a dashed green line in Fig. 6.3 (a). Good agreement between measured data and the sinusoidal dependence is verified. For $\eta \approx 90°$, a small $|a_{22}| > 0$ is observed. This is due to a finite out-of-plane component of $\mathbf{h}_{\mathrm{rf}}$. $|a_{12}|$ shows a stronger dependence on η than $|a_{22}|$. The discussion of this is postponed to later in this Section.
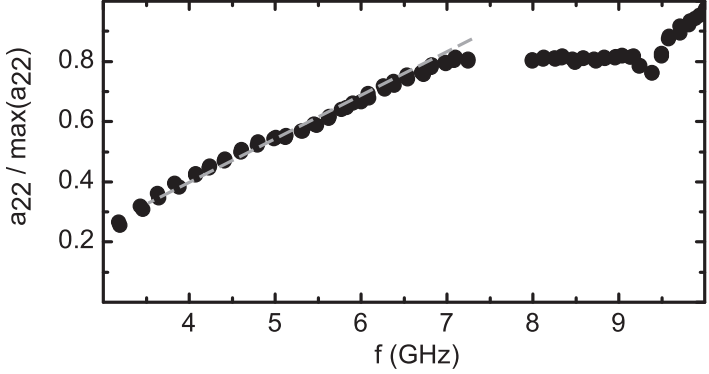
Figure 6.6: Normalized $|a_{22}|/\mathrm{max}|a_{22}|$. Data is evaluated at f_{r}, i.e. at the frequency of maximum amplitude for various values of $\mu_0 H$ at $\eta = 0°$. For $f < 8$ GHz, a linear dependence (indicated by the dashed line) is observed as expected from Eq. 2.104. For $f > 8$ GHz, a superposition of the reference data with the measured data causes deviation from the expected dependence (see text).

6.2.2 Wavevector selective analysis

In Sec. 6.1 it is found that the absorption $\Im a_{22}$ resembles a Lorentzian for $\eta = 70°$ [c.f. Fig. 6.1]. In the following it is shown that this originates from negligible inhomogeneous broadening for this angle if compared to $\eta = 0°$. For this the slope of the spin-wave dispersion $f(k)$ is considered for the excited wave vector distribution Δk. The slope of the SW dispersion $v_{\mathrm{g}} = 2\pi \mathrm{d}f(k)/\mathrm{d}k$, see Eqs. 2.73, 3.2 flattens for small wave vectors $0 \leqslant k \leqslant 10^4$ rad/cm for increasing η. $v_{\mathrm{g}}(\eta = 70°) \approx 0.1 v_{\mathrm{g}}(\eta = 0°)$. This is illustrated in Fig. 2.2 (b) for $\varphi = 20°$, i.e. $\eta = 90° - \varphi = 70°$ for parallel alignment of the CPW with the x axis. $\eta = 70°$ marks a trade off between low v_{g} (small inhomogeneous broadening) and signal strength, c.f. Fig. 6.3 (a). It is possible to estimate the contributions from inhomogeneous broadening as done in the following. For a wave vector distribution $\Delta k \approx 1.2 \times 10^4$ rad/cm, these inhomogeneously broadened linewidths compare as follows: $\Delta f(\Delta k = 1.2 \times 10^4 \text{ rad/cm}, v_{\mathrm{g}} = 7.5 \text{ km/s}) = 1.4$ GHz at $\eta = 0°$ and $\Delta f(\Delta k = 1.2 \times 10^4 \text{ rad/cm}, v_{\mathrm{g}} = 0.75 \text{ km/s}) = 0.14$ GHz at $\eta = 70°$. Fitting a Lorentzian curve according

to Eq. 2.56 to the data $\Im\chi_\text{tot}$ depicted in Fig. 6.1 (b) yields a linewidth of $\Delta f = 310\,\text{MHz}$. The measured linewidth by relaxation is a factor 2 larger than the contribution expected from the excitation process, i.e. the inhomogeneous broadening. The measured linewidth Δf is therefore dominated by SW relaxation for $\eta = 70°$. Following this evaluation, a_{22} measured at $\eta = 70°$ is considered to reflect the characteristics of a spectrum taken at $k = 0$, i.e., the FMR data.

Equation 2.51 describes $f_\text{r}(H)$ for $k = 0$, i.e. uniform precession. For $\eta = 70°$, indeed the measured eigenfrequencies come close to the $k = 0$ case. It is therefore possible to use Kittel's equation Eq. 2.51 for fitting to field dependent data obtained for $\eta = 70°$. Doing so yields $M_\text{Sat} = 830\,\text{kA/m}$. Such an approach is consistent with the VNA-FMR technique which inherently relies on SWs excited close to $k = 0$ [Cou04, Gie05b, Bil07b]. The value obtained for the saturation magnetization obtained from this method is in agreement to the M_Sat obtained from fitting $\rho(k)$ and χ_tot, see Figs. 6.4 and 6.5.

To obtain $f_\text{r}(k > 0, \eta)$ one has to consider the spin-wave dispersion Eq. 2.73. For $k = 0.6 \times 10^4\,\text{rad/cm}$, $k = 2.3 \times 10^4\,\text{rad/cm}$, and $k = 4.4 \times 10^4\,\text{rad/cm}$, $\rho(k)$ takes a local maximum. The corresponding frequencies $f(k)$ are plotted for various H at $\eta = 0°$ in Fig. 6.2 and for various η at $\mu_0 H = 20\,\text{mT}$ in Fig. 6.3 as thin red dashed lines. The calculated dependencies follow the measured data very well.

6.2.3 Propagation velocity

It is possible to obtain the group velocity v_g from AESWS measurements of a_{12}. This can be done by considering the oscillation period of the $\Re a_{12}$ or $\Im a_{12}$ signal which is given via the $\exp(-iks)$ term in Eq. 2.102. The oscillation period corresponds to a 2π shift of the SW phase, which transfers into a wave vector change given by Eq. 3.1. In practice it proved feasible to obtain v_g by considering the frequency difference Δf of two maxima of either $\Re a_{12}$ or $\Im a_{12}$ corresponding to f_1 and f_2. This implies approximation of a linear dispersion (constant v_g for $f_1 \leq f \leq f_2$). Moreover, data for v_g is not necessarily obtained for k_CPW, i.e. not necessarily for the wave vector for which $\rho(k)$ exhibits a maximum.

Values for v_g for different fields $\mu_0 H$ are plotted in Fig. 6.7. Data is evaluated for the largest maximum of $\Re a_{12}$ ($\Im a_{12}$) located at f_1 and the neighboring maximum at higher frequency f_2. The frequency difference

Δf corresponds to a 2π phase shift. With increasing H, the group velocity v_{g} decreases as expected from Eq. 2.77. For small $k < 5 \times 10^4 \,\mathrm{rad/cm}$, the dependence of v_{g} on k is very strong, i.e. $\mathrm{d}v_{\mathrm{g}}/\mathrm{d}k$ is large. This is illustrated in Fig. 2.2 (c) for $\eta = 0°$ as the solid line. In order to compare the predicted dependence of v_{g} on H by Eq. 2.73, it is therefore necessary to consider the finite k at which v_{g} is obtained. In Fig. 6.7 the solid lines mark v_{g} calculated from Eq. 2.73 for $k = 0.6 \times 10^4 \,\mathrm{rad/cm}$ and $k = 1.0 \times 10^4 \,\mathrm{rad/cm}$. The obtained results describe the measured data very well. From this it is found that the wave vector k which is effectively used to obtain values for v_{g} corresponds to approximately $1 \times 10^4 \,\mathrm{rad/cm}$. This value of k is well within the excited wave vector distribution Δk given by the excitation spectrum ρ [c.f. Fig. 5.4 (b)].

Similarly to the decrease in v_{g} for increasing $\mu_0 H$, a decrease in v_{g} is expected for increasing angle η. This relates to the transition from Damon-Eshbach (MSSW) modes to backward volume modes (MSBVW) as illustrated in Fig. 2.2 (b). MSSW modes have the largest v_{g} if compared to modes with a reduced angle between $\mathbf{k}$ and $\mathbf{H}$ [Kal86]. Quantitative evaluation (data not shown) again yields good agreement between theory and experiment. Exemplarily, $v_{\mathrm{g}}(\eta)$ obtained on a plain film (KT-003-5) is depicted as open triangles in Fig. 8.5 (a).

Using the values obtained for v_{g}, it is possible to motivate the behavior of $|a_{12}|$ which is very different from $|a_{22}|$, see Figs. 6.2 and 6.3. The relation between the amplitude measured in transmission $|a_{12}|$ and the amplitude measured in reflection $|a_{22}|$ is given by Eq. 3.3. Using values of v_{g} as obtained from the analysis described above and as depicted in Fig. 6.7, it is possible to test Eq. 3.3. This is depicted in Fig. 6.9 (a) for $\eta = 0°$ and $\eta = 45°$. Only data points are considered where $|a_{22}|$ is not corrupted by the reference field as discussed above. Furthermore, from Fig. 6.2 (a) it is visible that for small absolute values of $|\mu_0 H| < 20 \,\mathrm{mT}$, a_{12} is very small. This regime is attributed to the switching of the magnetization and is not considered for the analysis. The solid curves are fits to the data with the exponential dependence of Eq. 3.3. As can be seen the data is well described by the exponential decay. The relaxation τ of Eq. 3.3 is used as a fitting parameter. The values obtained for τ by this method are discussed in detail in the following Sec. 6.2.4.

Next, analysis relates the $|a_{12}|$ data and $|a_{22}|$ data. In particular, the asymmetry $|a_{12}|(+H) > |a_{12}|(-H)$ is addressed. In Fig. 6.8, the non-reciprocity $\beta = |a_{12}|(-H)/|a_{12}|(+H)$ is plotted as a function of H (com-
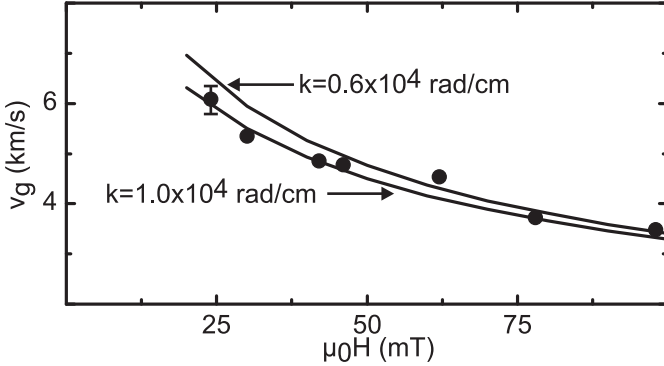
Figure 6.7: Group velocity v_g obtained for 25 mT $\leq \mu_0 H \leq$ 100 mT from AESWS measurements (full circles) at $\eta = 0°$. Data is obtained by Eq. 3.2 considering a 2π phase shift which is evaluated from Δf between to local maxima or minima of either $\Re a_{12}$ or $\Im a_{12}$, see text. Errors in v_g are about 0.2 km/s which is about the diameter of the data points. Full lines are calculated $v_g(H)$ obtained from Eq. 2.73 for $k = 0.6 \times 10^4$ rad/cm and $k = 1.0 \times 10^4$ rad/cm, as well as $M_{\mathrm{Sat}} = 830$ kA/m and $t_s = 25$ nm. Measured and calculated data agree well and reflect the inverse dependence of v_g on f as predicted from Eq. 2.76 for $k = 0$.

pare with Eq. 3.3). For $\mu_0 H > 30$ mT, β remains constant at $\beta \approx 0.45$. In particular, β is not dependent on $v_g(H)$ [c.f. Fig. 6.7], i.e. the propagation duration s/v_g. It is therefore not an effect of propagation, but is due to excitation. This finding and the absolute value of non-reciprocity agree well with literature [Dem09, Sek10]. Non-reciprocity of excitation is caused by an asymmetric excitation process underneath the CPW [Sch08b]. The orientation of the z component of the dynamic external field h_{rf} is asymmetric with respect to the CPW. Therefore, the internal field determining m_z is different resulting in different excitation strengths on the two sides of the CPW.

6.2.4 Relaxation and damping

To extract the frequency linewidth Δf without contributions from inhomogeneous broadening due to the finite excitation spectrum $\rho(k)$ of the
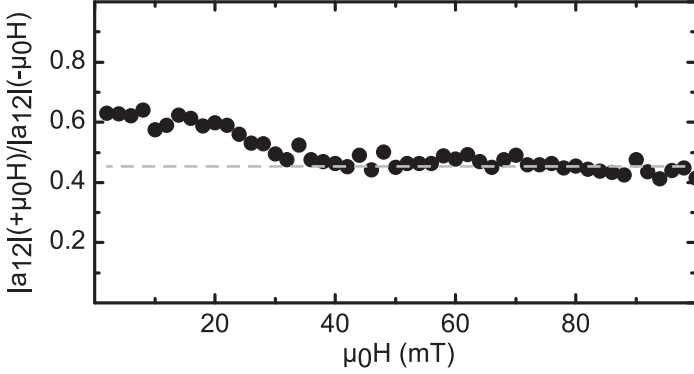
Figure 6.8: Non-reciprocity $\beta = |a_{12}|(-\mu_0 H)/|a_{12}|(+\mu_0 H)$ for different values of $\mu_0 H$ at $\eta = 0°$. β is constant for $\mu_0 H > 30$ mT as indicated by the dashed horizontal line.

CPW, it is possible to use $\Im a_{22}$ data obtained for $\eta = 70°$. As described above, fitting a Lorentzian yields Δf. This is done for various field $\mu_0 H$. Data of Δf as a function of $f(H)$ is depicted in Fig. 6.9 (b) as full circles. Using this method, it is not useful to extract Δf for $\eta < 70°$, because inhomogeneous broadening due to $\rho(k)$ distorts the line shape and dominates Δf.

However, it is possible to extract Δf from a_{12}. In Fig. 6.9 (a), the exponential dependence of $|a_{12}|/|a_{22}|$ as described by Eq. 3.3 is depicted. Fitting an exponential decay, where τ is used as a fitting parameter, yields $\tau = 0.94 \pm 0.16$ ns and $\tau = 0.60 \pm 0.22$ ns (45°). Via Eqs. 2.67 and 2.68, this corresponds to frequency linewidths of $\Delta f = 338 \pm 60$ MHz and $\Delta f = 530 \pm 191$ MHz. These values, together with data obtained directly from $\Im \chi$ for $\eta = 70°$ are depicted in Fig. 6.10. Within errors, no siginifcant dependence of Δf on η is resolved as expected for the plain film. Moreover, this value agrees well with data measured in literature, see Tab. 6.1. $\Delta f \approx 310$ MHz translates into an apparent damping $\alpha_{\mathrm{app}} = 0.01$ via Eq. 2.58.

Contributions from extrinsic factors as discussed in Sec. 2.2.4 are included in α_{app}. The α relevant for, e.g., solving the Landau-Lifshitz and Gilbert equation numerically using micromagnetic simulations, i.e. α_{LLG},
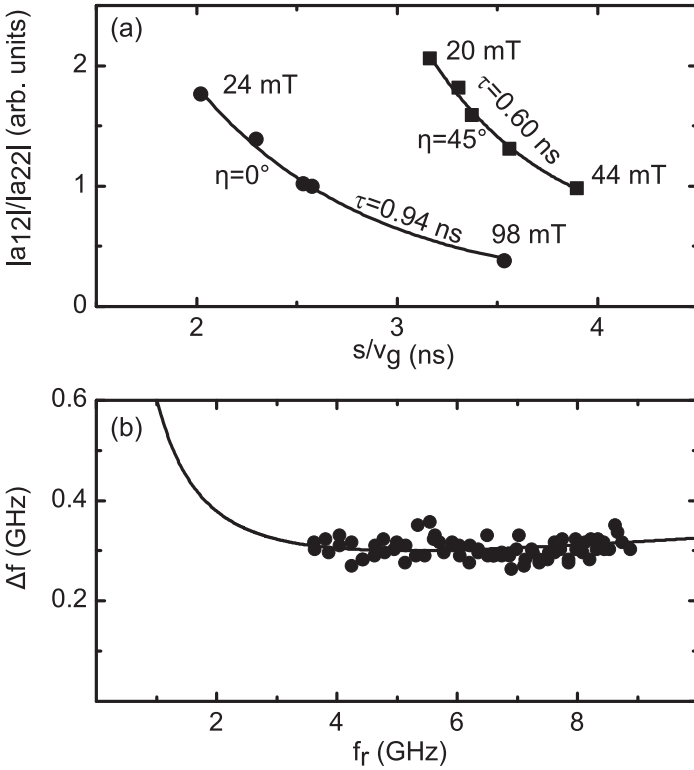
Figure 6.9: (a) Measured transmission amplitude normalized on reflection amplitude $|a_{12}|/|a_{22}|$ for $\eta = 0°$ (full circles) and $\eta = 45°$ (full squares) for different values of $s/v_{\mathrm{g}}(H) = 12~\mu\mathrm{m}/v_{\mathrm{g}}(H)$. Data is obtained by variation of the external field $\mu_0 H$ as indicated. Full lines are fits to the data using Eq. 3.2 where the relaxation time τ is used as a fit parameter. $\tau(\eta = 0°) = 0.94 \pm 0.16$ ns and $\tau(\eta = 45°) = 0.60 \pm 0.22$ ns. (b) Resonance linewidth Δf for $\eta = 70°$ for different resonance frequencies $f_{\mathrm{r}}(H)$. Data is obtained from Lorentzian fits to $\Im a_{22}$ data. Such data is depicted in Fig. 6.1. f_{r} is varied by variation of the external field $\mu_0 H$. The full line is a fit to the data using Eq. 2.64. Fit parameters were $\mu_0 \Delta H_0 = 8$ mT and Gilbert damping $\alpha = 0.0045$.
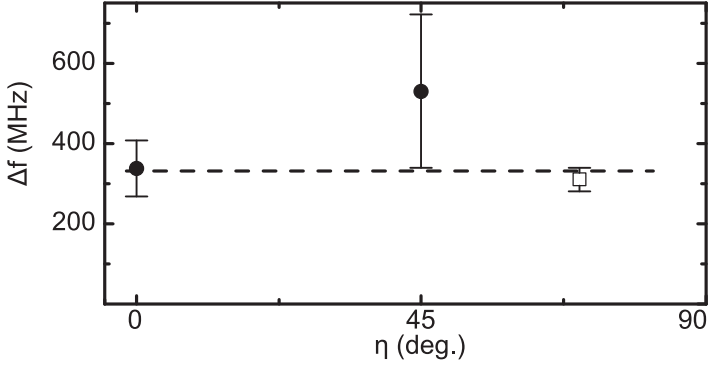
Figure 6.10: Δf for different angles η of the external field $\mathbf{H}$ with respect to the wave vector $\mathbf{k}$. Data is obtained via Eq. 3.2 from transmission measurements (full circles, $\eta = 0°, 45°$) and reflection measurements (open squares, $\eta = 70°$). The dashed horizontal line indicates $\Delta f \approx 330$ MHz.

Reference	t_s (nm)	Δf (MHz) or α_{app}
[Vla10]	20	$\alpha_{\mathrm{app}} = 0.011$
[Kal06]	50	$\Delta f = 240$
[Sil99]	50	$\Delta f = 300$
[Cou04]	50	$\Delta f = 150 - 250$
[Cov02]	27	$\Delta f = 400$
[Liu07]	10	$\Delta f = 227$
[San99]	50	$\alpha_{\mathrm{app}} = 0.013$

Table 6.1: Measured linewidths Δf or apparent damping α_{app} in literature. They are related via Eq. 2.58. Data compares well with own data of $\Delta f = 310$ MHz ($\alpha_{\mathrm{app}} = 0.01$).

see Sec. 2.3.3, can differ considerably from α_{app} and cannot be deduced straightforwardly.[1]

One way to obtain an approximate value of α excluding extrinsic contributions is via Eq. 2.64. This relies on values of Δf obtained for different resonance frequencies f_{r}.[2] Typically a respective method is employed for out-of-plane measurements where a large range of resonance frequencies f_{r} is addressed. Moreover, in FMR measurements, one can directly measure the field-swept linewidth ΔH. Here the slope of Δf or ΔH versus the resonance frequency f_{r} is analyzed. This allows for very precise determination of α [Pat75]. For in-plane data obtained from $|a_{22}|$ at $\eta = 70°$, it is possible to fit Eq. 2.64. The solid curve in Fig. 6.9 (a) is the fit for $M_{\mathrm{Sat}} = 830\,\mathrm{kA/m}$, $\mu_0 \Delta H_0 = 8\,\mathrm{mT}$, and $\alpha = 0.0045 \pm 0.003$. This value for α is in good agreement with literature where values $\alpha = 0.005 - 0.006$ are reported for thin films for in-plane orientation of the external magnetic field **H** [Pat75, Wol09]. The comparably large uncertainty in this measurement arises from the small range of resonance frequencies $4 \leq f_{\mathrm{r}} \leq 8.5$ GHz that are addressed for the in-plane measurements. To obtain more precise values of α, it is advisable to use out-of-plane measurements. This is out of the scope of this thesis.

---

[1]This is illustrated by the fact that in literature, both, Ref. [Cov02] and [Liu07] use α in simulations as a fitting parameter to obtain good agreement between micromagnetic simulation data and experimental data obtained in the temporal domain.

[2]Note that the technique introduced above, based on the evaluation of $|a_{12}|$, neglects the small dependence of Δf on f_{r} and is therefore not suitable to yield the net α only containing intrinsic contributions, see Sec. 2.2.4.

7 Antidot Lattices: Static and Dynamic Characterization

This chapter is organized as follows: First, in Sec. 7.1, the magnetic ground state for ADLs is studied by experiment and micromagnetic simulation. Second, in Sec. 7.2, the phenomenological experimental findings by AESWS and MOKE are presented. Based on this, in Sec. 7.3, data is analyzed in various forms. Because of the spectrum of different physical phenomena discussed, abstracts are given for every section in this chapter.

In this thesis, nanostructured square arrays of holes, so called antidot lattices (ADLs) are studied. From sample to sample the ADL periodicity p is changed from 0.12 to 4.0 μm while the hole diameter is $d = 120$ nm for all samples with $p \geq 200$ nm ($d = 86$ nm for $p = 120$ nm). A characteristic describing each sample is the permalloy filling fraction

$$\mathcal{F} = 1 - \frac{\pi(d/2)^2}{p^2}. \tag{7.1}$$

In Fig. 7.1, all ADL geometries used for measurements throughout this thesis are depicted. The filling fraction $\mathcal{F}$ varies between 0.6 and 1. A number of different samples is used for measurements of the different ADL geometries. In A.1, a listing of all samples which are used for measurements discussed in this thesis is provided. In A.3 the corresponding micromagnetic simulation parameter sets are listed.

7.1 Static Magnetization

The hysteresis curves and magnetization profiles of ADL are discussed. A dependence of the coercive field on the ADL periodicity p is found. A field of $\mu_0 H = 40$ mT is found to be sufficient to saturate ADLs with $p \geq 200$ nm.
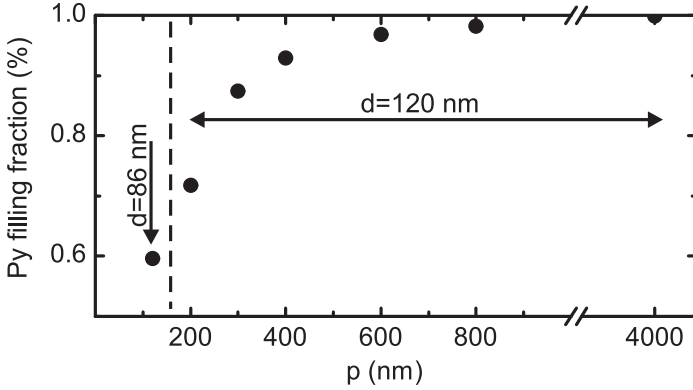
Figure 7.1: Overview on the studied ADL samples in this thesis. The permalloy filling fraction is calculated according to Eq. 7.1. For $p \geq 200$ nm the hole diameter is 120 nm.

The magnetic ground state $\mathbf{M}(\mathbf{r})$ is known to significantly influence the spin-wave eigenmodes. The magnetic ground state can be altered, both, by the magnetic field [Pod06] or via variations in the geometry [Gie07]. Therefore, it is necessary to discuss the dependence of $\mathbf{M}(\mathbf{r})$ on field $\mu_0 H$ and periodicity p.

7.1.1 Magnetization Reversal

First, the magnetization reversal is measured using MOKE, see Sec. 3.2.3. The hysteresis curve, see Sec. 2.1.5, for a $p = 800$ nm antidot lattice (ADL) (data not shown) does not deviate significantly from the plain film hysteresis curve depicted in Fig. 3.6. The hole diameter d amounts to roughly 120 nm, so that only $\mathcal{F} = 1.7\%$ of the magnetic material is removed, see Eq. 7.1. The very small coercive field of $\mu_0 H_C < 1$ mT, close to the plain film value, results from this.

For larger values of $\mathcal{F}$ realized via smaller p, this changes as indicated in Fig. 7.2. Larger values of H_C obtained amounting to $\mu_0 H_C \approx 5$ mT ($p = 400$ nm) and $\mu_0 H_C \approx 15$ mT ($p = 200$ nm) for $\eta = 0°$. The respective values for $\eta = 45°$ are all larger. The value of $\langle M_{||} \rangle$ is reduced for larger values of $|\mu_0 H|$ as indicated by the vertical arrows. In particular,

for $\mu_0 H \geq 40$ mT, $< M_{||} > /M_{\mathrm{Sat}} \approx 1$ for all discussed p.

7.1.2 Micromagnetic Ground State

In order to explain the microscopic origin of the hysteresis curves depicted in Fig. 7.2, it is instructive to perform micromagnetic simulations of the ferromagnetic ground state $\mathbf{M}(\mathbf{r})$, see Sec. 2.3.3. The obtained hysteresis curve is exemplarily shown for $p = 300$ nm in Fig. 7.2 (b) as open circles for $\eta = 0°$ and open squares for $\eta = 45°$. The simulation resembles measured data very well.

Based on the good agreement between simulated and measured hysteresis curves, it is instructive to analyze the micromagnetic ground state, i.e. the spatial dependence on the orientation of the magnetization $\mathbf{M}(\mathbf{r})$ obtained from micromagnetic simulations. This is depicted in Fig. 7.3 for $\eta = 0°$ and in Fig. 7.4 for $\eta = 45°$.

The results can be summarized for three field regimes, A, B, and C, as indicated in Fig. 7.2 (c). References are made to regimes σ as indicated in Fig. 7.3 (b).

- Regime A, saturated magnetization. For fields $\mu_0 H \geq 40$ mT, the magnetic ground state does not change significantly. This is illustrated in Figs. 7.3, 7.4 (a) $\mu_0 H = 100$ mT and (b) $\mu_0 H = 40$ mT, where the orientation of $\mathbf{M}(\mathbf{r})$ is not changed significantly for the two values of $\mu_0 H$. In particular, $\mathbf{M} \parallel \mathbf{H}$ for all regions away from the immediate edges of the holes. This corresponds to $\langle M_{||} \rangle / M_{\mathrm{Sat}} \approx 1$ in Fig. 7.2.

- Regime B, unsaturated magnetization. For $\eta = 0°$ and 0 mT $< \mu_0 H < 40$ mT, the magnetization $\mathbf{M}(\mathbf{r})$ begins to rotate away from the external field direction [c.f. Fig. 7.3 (c)]. This corresponds to $\langle M_{||} \rangle / M_{\mathrm{Sat}} < 1$ in Fig. 7.2. This is marked by the vertical arrows.

- For the remanent state $\mu_0 H = 0$ mT, the magnetization encloses a $45°$ angle with the direction of the swept field (x direction) for region σ_4, c.f. Fig. 7.3 (b). Only for region σ_3 the magnetization is aligned with the y direction. In particular $\mathbf{M}(\mathbf{r}, \eta = 0°) = \mathbf{M}(\mathbf{r}, \eta = 45°)$. The remanent magnetic ground state of the antidot lattice system is not found to be dependent on the magnetic field history.
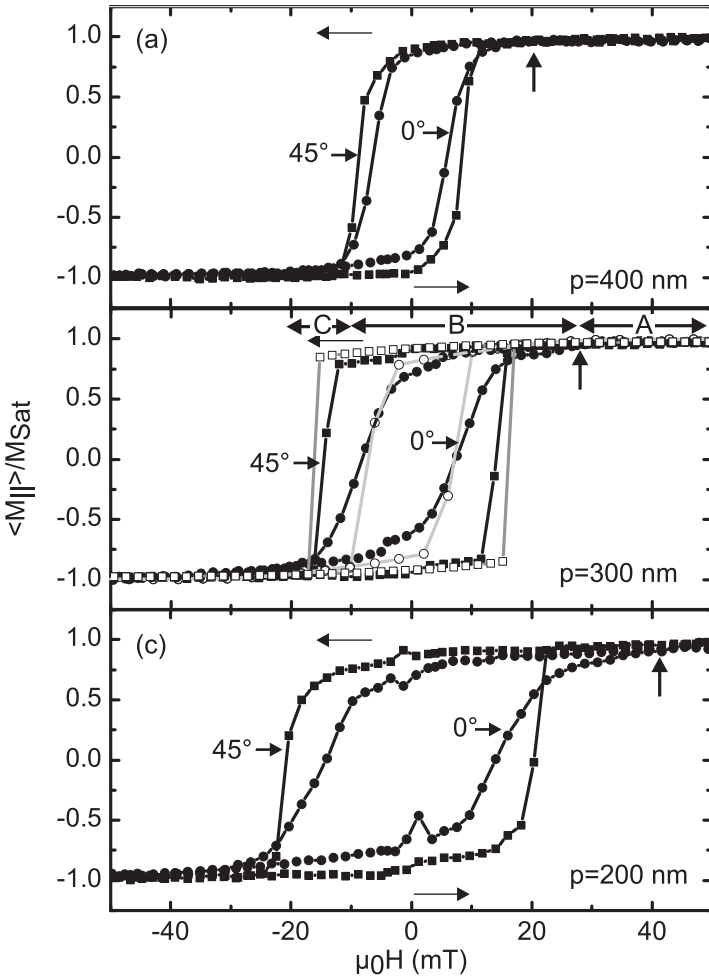
Figure 7.2: Hysteresis curves obtained for antidot lattices of various periodicity p. All from sample SN089-1. (a) $p = 400$ nm. (b) $p = 300$ nm. (c) $p = 200$ nm. Full symbols indicate MOKE data obtained from measurements at Perugia University. Open symbols in (b) indicate micromagnetic simulation data according to set B, see A.3. Circles correspond to $\eta = 0°$ and squares to $\eta = 45°$. Generally, $H_C(\eta = 45°) > H_C(\eta = 0°)$ and $M_R(\eta = 45°) > M_R(\eta = 0°)$. $\eta = 0°$ corresponds to an easy axis. For $p = 400$ nm, $\mu_0 H_C \approx 5$ mT, while for $p = 200$ nm, $\mu_0 H_C \approx 15$ mT for $\eta = 0°$.
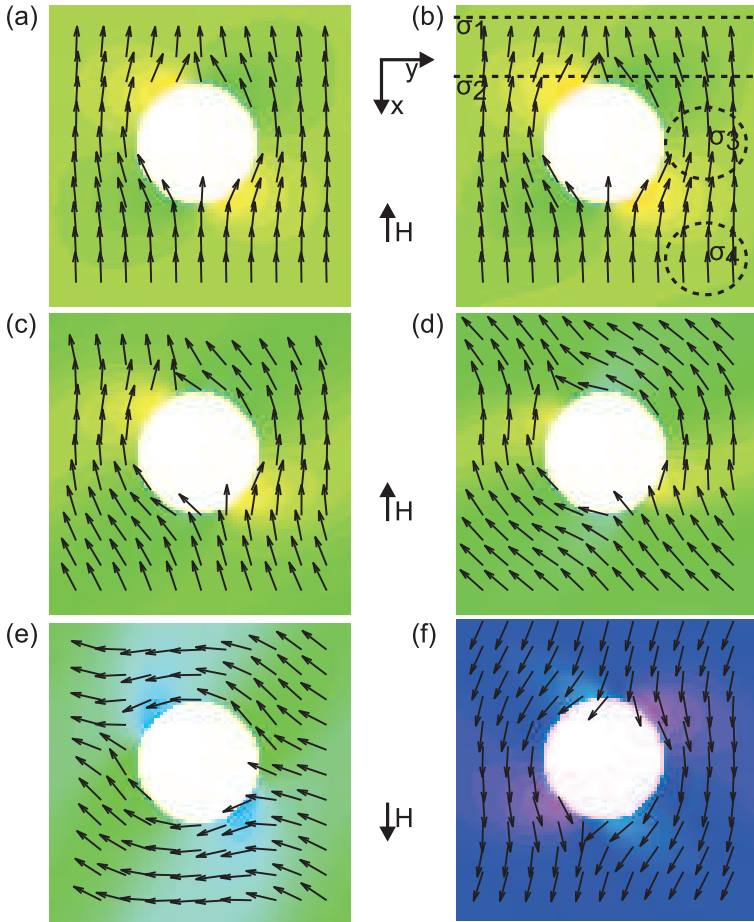
Figure 7.3: Magnetization configuration $\mathbf{M}(\mathbf{r})$ (magnetic ground state) obtained from micromagnetic simulations for a $p = 300$ nm antidot lattice for $\eta = 1°$ and $\mu_0 H = $ (a) 100 mT, (b) 40 mT, (c) 20 mT, (d) 0 mT, (e) -6 mT, (f) -20 mT. The color code illustrates the magnetization orientation indicated by the black arrows. The regions and lines labeled σ in (b) correspond to regions discussed in the text. Holes are depicted as white area in the center. $d = 120$ nm. Simulations according to set B, see A.3.

- Regime C, remagnetization. For $\mu_0 H < 0$ mT, the rotation of $\mathbf{M}(\mathbf{r})$ continues until eventually the magnetization aligns again with the external field. This remagnetization process is complex [Hey06] and not discussed within this thesis.

As part of this thesis, only the saturated magnetization of regime A is addressed. The remagnetization [Hey06] or hysteretic, reprogrammable groundstates [Top10] are, in particular, not addressed.

It is possible to extract the values of the demagnetization field H_D from micromagnetic simulations. For the $p = 300$ nm ADL with $d = 120$ nm, this is done in Fig. 7.5. Regions of positive H_D are localized in between holes neighboring in the direction perpendicular to the external field. Regions of negative H_D extend through the lattice perpendicular to the external field in between holes which are neighboring parallel to the field.

For data analysis further below, it is instructive to extract $\mu_0 H_\mathrm{D}$ along the y axis for a path perpendicular to the external field direction and centered in between two neighboring holes edges (path σ_1 of Fig. 7.3 (b)) for $p = 800$ nm and orientated at the hole's edge (path σ_2 of Fig. 7.3 (b) and dashed line in Fig. 7.5 (a)) for $p = 300$ nm as done for $\mu_0 H = 40$ mT. Results are depicted in Fig. 7.6. Analyzing H_D along σ_2 for $p = 300$ nm yields a strong peak-to-peak variation $\mu_0 \Delta H_\mathrm{D} \approx 100$ mT [c.f. light line in Fig. 7.6]. The amplitude of this variation is found to depend almost only on the hole shape and not on the ADL period p. In contrast, the peak-to-peak variation for a $p = 800$ nm ADL along line σ_1 is much weaker and amounts only to $\mu_0 \Delta H_\mathrm{D} \approx 0.1$ mT. This is because line σ_1 is much further away from the hole's edges where uncompensated magnetic charges generate a large H_D.
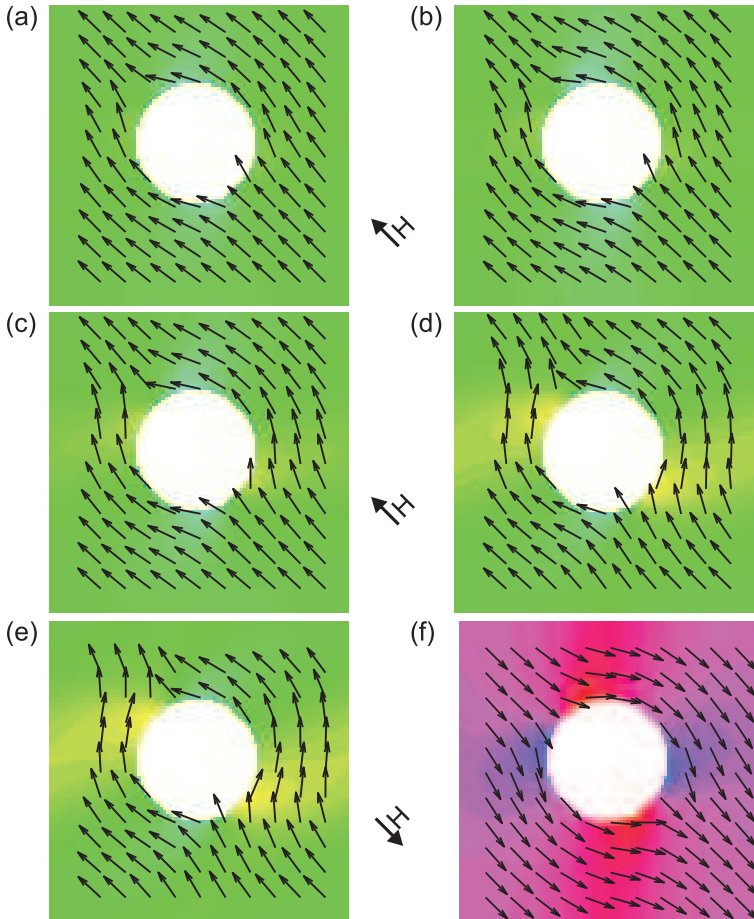
Figure 7.4: Magnetization configuration $\mathbf{M}(\mathbf{r})$ (magnetic ground state) obtained from static micromagnetic simulations for a $p = 300$ nm andtidot lattice for $\eta = 45°$ and $\mu_0 H =$(a) 100 mT, (b) 40 mT, (c) 20 mT, (d) 0 mT, (e) -6 mT, (f) -20 mT. The color code illustrates the magnetization orientation indicated by the black arrows. Holes are depicted as white area in the center. Simulations according to set B, see A.3.
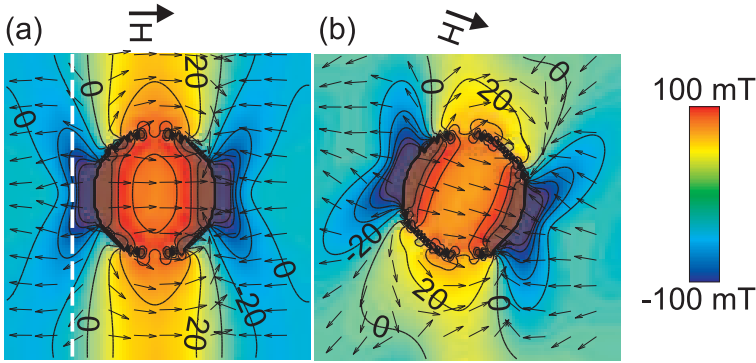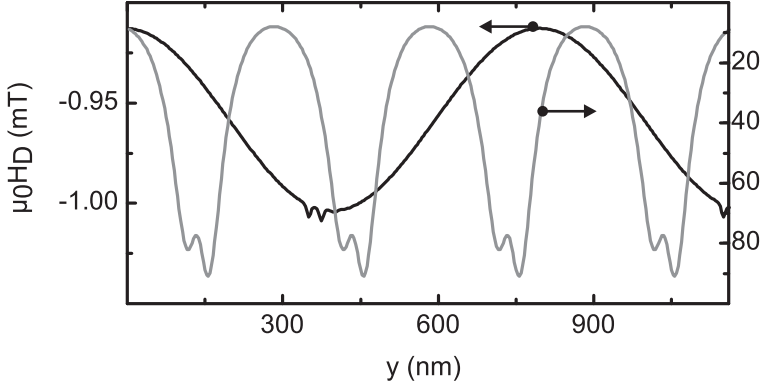
Figure 7.5: Simulated demagnetization field $\mathbf{H}_D$ parallel to the external field H (color code) for (a) $\eta = 0°$ and (b) $\eta = 20°$. $\mu_0 H = 40$ mT. Colors indicate the magnitude $\mu_0 H_D$ for $-100...100$ mT, arrows indicate the direction of $\mathbf{H}_D$. Plotted are contour lines in 20 mT spacing to visualize the data further. Simulations according to set B, see A.3.

7.2 Phenomenology of Magnetization Dynamics

VNA-FMR and AESWS measurements reveal that the spin-wave spectrum changes significantly for $p = 400$ nm. For $p > 400$ nm, only two modes with opposed dependence of the resonance frequency f_r on alignment with the external field η are observed. For $p < 400$ nm, an additional low frequency mode is resolved.

In this Section, measurements of spin-wave modes for antidot lattices of various periodicity are presented. ADLs have been prepared as presented in chapter 4. In particular, the resolved SW eigenmodes are classified based on the phenomenological findings such as

- Absolute value of the eigenfrequency f_r.

- Dependence of the mode amplitude $a_{22}(f_r)$ and $a_{12}(f_r)$ on $\mu_0 H$.

- Dependence of f_r on the orientation of the external field η.

Figure 7.6: Simulated demagnetization field profile $H_D(y)$ for a $p = 800$ nm (black curve, left scale) and a $p = 300$ nm antidot lattice (gray curve, right scale). $\mu_0 H = 40$ mT. $\eta = 0°$. The demagnetization field is evaluated perpendicular to the external field for paths σ_1 centered in the middle between two holes (respectively for the $p = 800$ nm ADL) and σ_2 at the hole border (for the $p = 300$ nm ADL) of Fig. 7.3 (b). Simulation parameters are as in Fig. 7.3. Simulations according to set B (set C) for $p = 300$ nm ($p = 800$ nm), see A.3.

7.2.1 VNA-FMR study

It is instructive to begin the discussion with spectra obtained for a standard CPW with a wide inner conductor $w_{ic} = 20$ μm by VNA-FMR technique, see Sec. 3.2.1. The excited spin waves are close to $k = 0$. Data is obtained on $p = 800$ nm and $p = 400$ nm ADLs.

In Fig. 7.7, $|a_{12}|$ is depicted for $p = 800$ nm (a) and $p = 400$ nm (b) as a gray scale plot at $\mu_0 H = 40$ mT and varying η. Dark colors correspond to SW excitation. For $\eta < 25°$, two types of modes are resolved. Firstly, modes for which $df_r/d\eta > 0$, i.e. increasing resonance frequency f_r for increasing angle η. Second, modes for which the opposite behavior applies, i.e. $df_r/d\eta < 0$. While for $p = 800$ nm, only one mode (labeled ii in Fig 7.7 (a)) is observed with increasing f_r for increasing η, two such modes are observed for $p = 400$ nm (labeled i and ii in Fig 7.7 (b)). The amplitude of these two modes corresponding to the gray scale is very different with mode i showing much stronger signal than mode ii.
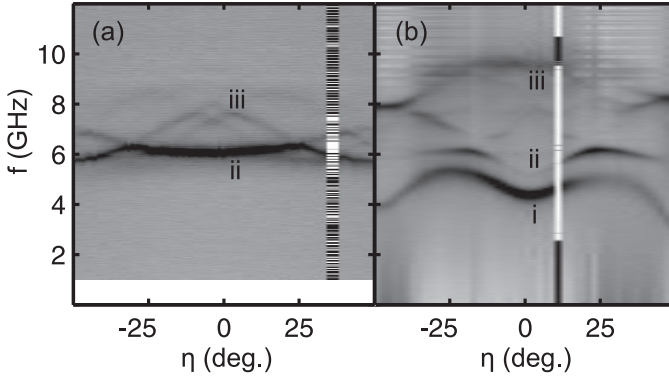
Figure 7.7: VNA-FMR data of $|a_{12}|$ obtained for a (a) $p = 800$ nm and (b) $p = 400$ nm sample for a $w_{ic} = 20$ μm standard CPW. $\mu_0 H = 40$ mT, $-50° \leq \eta \leq 50°$. Samples are SN80-7-A and SN80-7-C, respectively. Dark colors correspond to SW excitation.

To illustrate this further, in Fig. 7.8 (a), $|a_{12}|$ is depicted for the $p = 400$ nm sample for different values of the external field $\mu_0 H$ at $\eta = 0°$. The amplitude of mode i is found to decrease with increasing $\mu_0 H$, while the opposite dependence is observed for mode ii. For $\mu_0 H \approx 60$ mT, an avoided mode crossing is observed between those modes indicated by a vertical arrow in Fig. 7.8 (a).

Fig. 7.8 (b) depicts $|a_{12}|$ obtained for the $p = 400$ nm ADL at $\mu_0 H = 100$ mT for various η. The resonance frequencies f_r are shifted towards higher values as expected from Eq. 2.52. The low frequency mode i is only very weakly resolved. Besides this mode, one mode with $\mathrm{d}f_r/\mathrm{d}\eta > 0$ (labeled mode ii) and one mode with $\mathrm{d}f_r/\mathrm{d}\eta < 0$ at largest f_r (labeled mode iii) are resolved. In Fig. 7.9, $|a_{12}|$ data obtained for $\mu_0 H = 100$ mT on the $p = 800$ nm ADL sample SN80-7-A ($w_{ic} = 20$ μm) is depicted for completeness. Again, two modes are resolved: one mode with $\mathrm{d}f_r/\mathrm{d}\eta > 0$ (labeled mode ii) and one mode with $\mathrm{d}f_r/\mathrm{d}\eta < 0$ at largest f_r (labeled mode iii). However, discrepancies between the two spectra remain in that for the $p = 800$ nm ADL only a single mode with $\mathrm{d}f_r/\mathrm{d}\eta > 0$ is observed (labeled mode ii), whereas for $p = 400$ nm two such modes are observed (labeled mode i and ii).

To understand these differences between $p = 800$ nm and $p = 400$ nm SW spectra in greater detail, in the following it is instructive to first study SW spectra by AESWS for large lattice constants $p \geq 400$ nm in Sec. 7.2.2, followed by Sec. 7.2.3 where small lattice constants $p < 400$ nm are discussed.

7.2.2 AESWS for large periodicities ($p \geq 400$ nm)

In Fig. 7.10, AESWS data is depicted. Two different SW-transmission CPWs were used: in (a) and (b), the inner conductor width is $w_{\text{ic}} = 2$ μm and the propagation path is $s = 12$ μm. This corresponds to $k_{\text{CPW}} = 0.6 \times 10^4$ rad/cm. Differently, in (c) and (d), $w_{\text{ic}} = 340$ nm and $s = 6.5$ μm. This corresponds to $k_{\text{CPW}} = 2 \times 10^4$ rad/cm. The left column, i.e. (a) and (c), depicts reflection data $\Im a_{22}$, while the right column, i.e. (b) and (d) depicts transmission data $\Im a_{12}$. It is instructive to start the discussion with data obtained from a $w_{\text{ic}} = 2$ μm CPW, i.e. (a) and (b). This CPW exhibits an excitation spectrum $\rho(k)$ as depicted in Fig. 5.4 (b) with a maximum excitation strength at $k_{\text{CPW}} = 0.6 \times 10^4$ rad/cm. While a_{22} data contains signals from both propagating and standing SWs, see Sec. 2.3.1, the signal a_{12} only contains signal from propagating SWs (and parasitic signal due to magnetic crosstalk, see Sec. 5).

Agreement between data obtained from VNA-FMR and AESWS exists: compare Figs. 7.7 and 7.10. In particular, two modes are resolved which show the same dependence of f_{r} on η for AESWS and VNA-FMR measurements. While $\mathrm{d}f_{\text{r}}/\mathrm{d}\eta < 0$ for the high frequency mode mode iii ($\mathrm{d}\eta > 0$), the low frequency mode ii only shows a weak change in resonance frequency of opposite sign, i.e. $\mathrm{d}f_{\text{r}}/\mathrm{d}\eta \gtrsim 0$. The low frequency excitation labeled ii is resolved for a_{12} and a_{22} and is therefore a propagating mode. Differently, mode iii is clearly resolved only for a_{22} and not resolved for a_{12} and is therefore identified with a standing SW, see Sec. 2.3.1. Furthermore, mode ii shows a black-white-black contrast oscillation in Fig. 7.10 (b) corresponding to phase accumulation of the SW due to propagation.

Data obtained for the second CPW with $w_{\text{ic}} = 340$ nm and $s = 6.5$ μm in Figs. 7.10 (c) and (d) show characteristic changes if compared to $w_{\text{ic}} = 2$ μm data. In order to facilitate data analysis later on, three regimes for η are discussed. These regimes are $\eta = 0° \pm 5°$ (regime A), $\eta = 25° \pm 5°$ (regime B), and $\eta = 40° \pm 5°$ (regime C). They are highlighted by circles
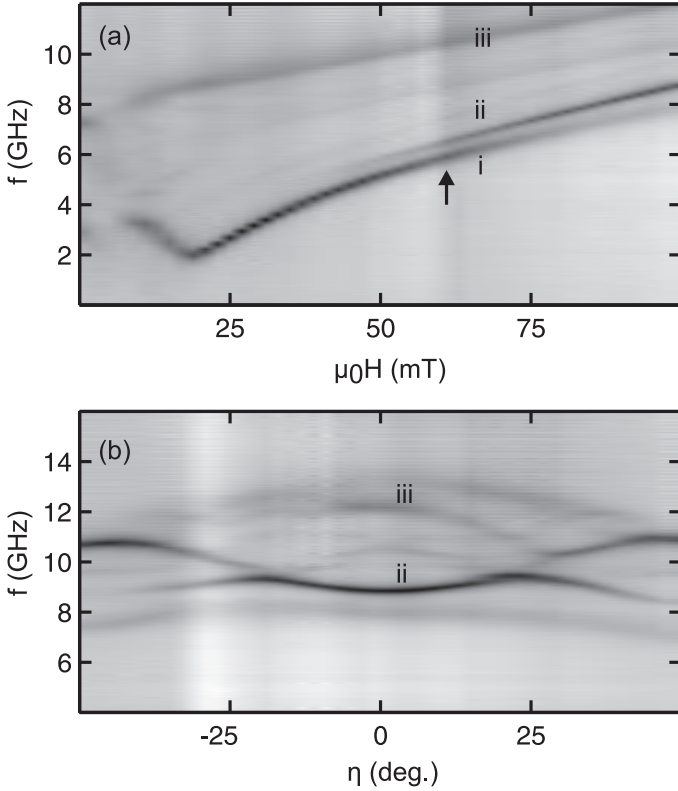
Figure 7.8: VNA-FMR data of $|a_{12}|$ obtained for a $p = 400$ nm ADL (SN80-7-C) for (a) various field strengths $0 \leq \mu_0 H \leq 100$ mT ($\eta = 0°$) and (b) for various orientations of the external field $-50° \leq \eta \leq 50°$ ($\mu_0 H = 100$ mT). Dark colors correspond to SW excitation.
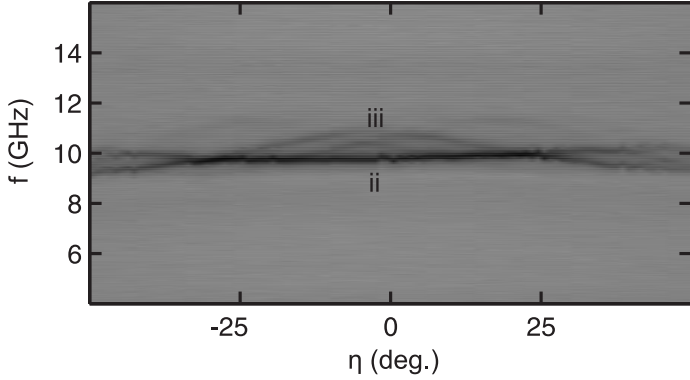
Figure 7.9: VNA-FMR data of $|a_{12}|$ obtained for a $p = 800$ nm ADL (SN80-7-A) for various orientations of the external field $-50° \leq \eta \leq 50°$ ($\mu_0 H = 100$ mT). Dark colors correspond to SW excitation.

in Fig. 7.10 (d). For $\eta = 25°$ (regime B), two modes are resolved, where the higher frequency mode shows black-white-black contrast oscillations. This is different to (b) ($w_{ic} = 2$ μm) where the low frequency mode shows the contrast oscillations. Differently, for regimes A and C, there are no significant differences resolved in the mode behaviors for the two CPW types. For both, $w_{ic} = 2$ μm and $w_{ic} = 0.34$ μm, the low frequency mode is found to propagate.

It is interesting to extract the maximum amplitude, i.e. the amplitude at f_r, for the propagating mode labeled ii from, both, $|a_{12}|$ and $|a_{22}|$ data. This is depicted in Fig. 7.11. The data is normalized to the maximum value. Both $|a_{22}|(f_r)$ and $|a_{12}|(f_r)$ are largest for $\eta = 0°$ and, overall, decrease for increasing η. $|a_{12}|(f_r)$ shows a comparably stronger dependence on η. In Sec. 8.2 it is shown that this originates from the decreasing group velocity v_g for increasing η. Furthermore, from such data the relaxation time τ is extracted in Sec. 7.3.

The dependence of $\Im a_{22}$ and $\Im a_{12}$ on $\mu_0 H$ is depicted in Fig. 7.12 (a) and (b), respectively. Data is obtained with the $w_{ic} = 340$ nm, $s = 6.5$ μm CPW of Fig. 7.10 (c) and (d) (sample SN88-1-A-M). No significant dependence of the number of modes on the field value $\mu_0 H$ is observed for $\mu_0 H > 5$ mT. In particular, no avoided crossing of SWs is observed,
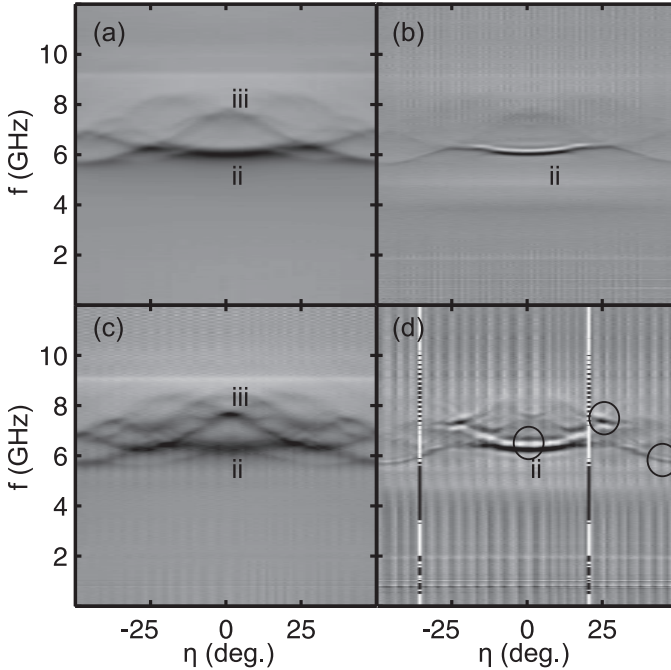
Figure 7.10: AESWS data obtained for two $p = 800$ nm samples (SN83-1-LO and SN88-1-A-M) with $w_{ic} = 2\,\mu$m and $w_{ic} = 340$ nm SW-transmission CPWs. $\mu_0 H = 40$ mT. $-50° \leq \eta \leq 50°$. (a) $\Im a_{22}$. $w_{ic} = 2\,\mu$m. (b) $\Im a_{12}$. $w_{ic} = 2\,\mu$m. $s = 12\,\mu$m. (c) $\Im a_{22}$. $w_{ic} = 340$ nm. (d) $\Im a_{12}$. $w_{ic} = 340$ nm. $s = 6.5\,\mu$m. For the reflection data in (a) and (c), dark contrast corresponds to large SW amplitude. For the transmission data in (b) and (d), the black white black contrast originates from the accumulated phase shift of propagating SWs according to Eq. 3.1. Circles in (d) indicate regimes, for which the propagation parameters are evaluated (see text).
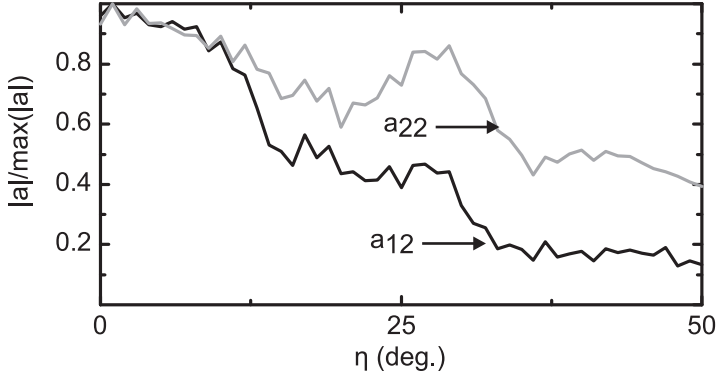
Figure 7.11: Maximum normalized amplitudes $|a_{12}|(f_r)$ (dark line) and $|a_{22}|(f_r)$ (light line) for $\mu_0 H = 20$ mT and $0° \leq \eta \leq 50°$ [Neu10]. These are AESWS data of the $p = 800$ nm ADL (SN88-1-A-M). Data is evaluated for f_r of mode ii (extended mode) from Fig. 7.10.

which is different to the $p = 400$ nm case as discussed in Sec. 7.2.1. The resolved modes are labeled according to Fig. 7.10 for $\mu_0 H = 40$ mT. The low frequency mode is mode ii, while the higher frequency mode is mode iii.

In Fig. 7.13, $|a_{22}|$ and $\Im a_{12}$ are depicted for a $p = 400$ nm ADL with a $w_{ic} = 2$ μm, $s = 12$ μm SW-transmission CPW, respectively. Data is shown for, both, $\mu_0 H = 20$ mT (a) and (b), as well as for $\mu_0 H = 40$ mT (c) and (d). Three modes are resolved for the a_{22} data, analogous to Fig. 7.7. For mode i and ii, $\mathrm{d}f_r/\mathrm{d}\eta > 0$ for $\mathrm{d}\eta > 0$. Differently, for mode iii, $\mathrm{d}f_r/\mathrm{d}\eta < 0$. The resonance frequencies f_r of mode i and ii are almost degenerate, i.e. for mode i $f_r = 3.7$ GHz and for mode ii $f_r = 4.3$ GHz at $\mu_0 H = 20$ mT. Mode i and mode ii are not clearly separated in frequency anymore. This is due to the different SW excitation spectra $\rho(k)$, see Fig. 5.4, if compared to Fig. 7.7. In particular, the oscillation of the amplitude in $\Im a_{12}$ is not well resolved anymore. This makes the determination of v_g from the phase oscillations difficult and results in a large uncertainty of v_g. Beyond this, mode ii and iii behave similarly to the $p = 800$ nm case.
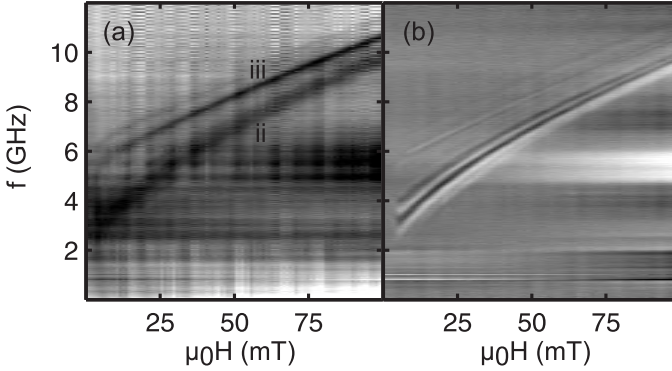
Figure 7.12: AESWS data obtained for the $p = 800$ nm sample (SN88-1-A-M) for a $w_{ic} = 340$ nm SW-transmission CPW for various values of $\mu_0 H$ ($\eta = 0°$, $k_{CPW} = 2 \times 10^4$ rad/cm). (a) $\Im a_{22}$. (b) $\Im a_{12}$.

7.2.3 AESWS for small periodicities ($p < 400$ nm)

AESWS data is depicted for $p = 300$ nm in Fig. 7.14. A $w_{ic} = 2$ μm, $s = 12$ μm SW-transmission CPW is used (SN89-4-4), i.e. $k_{CPW} = 0.6 \times 10^4$ rad/cm. As can be seen from the a_{22} data of Fig. 7.14 (a), three modes are resolved for $\eta = 0°$. The modes are labeled i-iii for increasing f. Only mode i is resolved in a_{12} data of Fig. 7.14 (b) and is therefore associated with a propagating mode. Mode i shows a strong dependence on $f_r(\eta)$ for small values of η, i.e. $\mathrm{d}f_r/\mathrm{d}\eta >> 0$ ($\mathrm{d}\eta > 0$). A weaker dependence, i.e. $\mathrm{d}f_r/\mathrm{d}\eta \gtrsim 0$ is found for mode ii, which is similar to the behavior of mode ii in the $p = 800$ nm ADL as depicted in Fig. 7.10. For mode iii, $\mathrm{d}f_r/\mathrm{d}\eta < 0$, which again is in agreement with the mode iii of $p = 800$ nm.

For even smaller lattice periods p, the Py filling fraction $\mathcal{F}$ is reduced. This reduces the magnetic signal. Furthermore, long exposure times limit the area which can be structured by focussed ion beam lithography. Because of this, transmission data a_{12} is not available for $p < 300$ nm. In Fig. 7.15 (a), $\Im a_{22}$ data of a $p = 200$ nm ADL is depicted. A $w_{ic} = 2$ μm, $s = 12$ μm SW-transmission CPW is used (SN89-4-2). In Fig. 7.15 (b), $\Im a_{22}$ data is depicted for a $p = 120$ nm ADL. The sample is SN61-
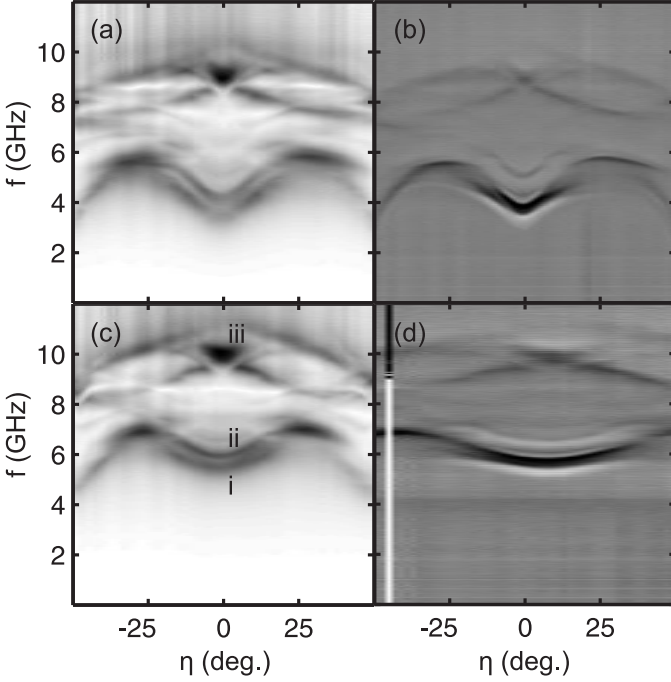
Figure 7.13: AESWS data obtained for a $p = 400$ nm sample (SN66-A-1-1) with $w_{ic} = 2$ μm SW-transmission CPW. (a) $\mu_0 H = 20$ mT. $|a_{22}|$. (b) $\mu_0 H = 20$ mT. $\Im a_{12}$. (c) $\mu_0 H = 40$ mT. $|a_{22}|$. (d) $\mu_0 H = 40$ mT. $\Im a_{12}$.

3-3 where a $w_{ic} = 2$ μm standard CPW is used. A SEM micrograph of the $p = 120$ nm ADL is depicted in Fig. 4.4. Data is evaluated for $\mu_0 H = 100$ mT to ensure excitation in the saturated regime and to maximize AESWS signal.

Only two modes are resolved. For the low frequency mode $df_r/d\eta > 0$ which motivates labeling this mode as i/ii in accordance with data obtained for $p = 800$ nm and $p = 300$ nm above. The high frequency mode shows decreasing eigenfrequencies f_r for increasing η, i.e. $df_r/d\eta < 0$, i.e. is labeled mode iii.
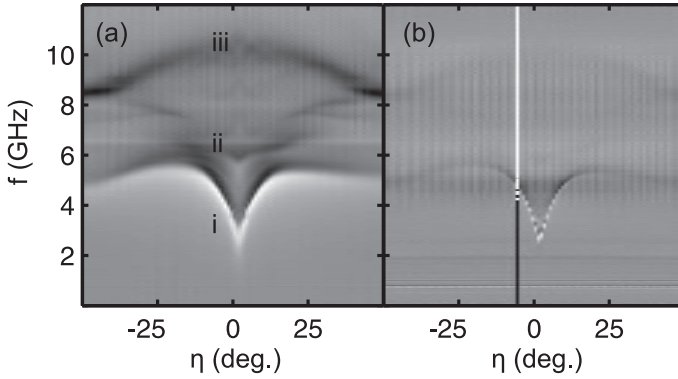
Figure 7.14: AESWS data obtained for a $p = 300$ nm sample (SN89-4-4) for a $w_{\mathrm{ic}} = 2$ μm ($s = 12$ μm) SW-transmission CPW. $\mu_0 H = 40$ mT. (a) $\Im a_{22}$. (b) $\Im a_{12}$.
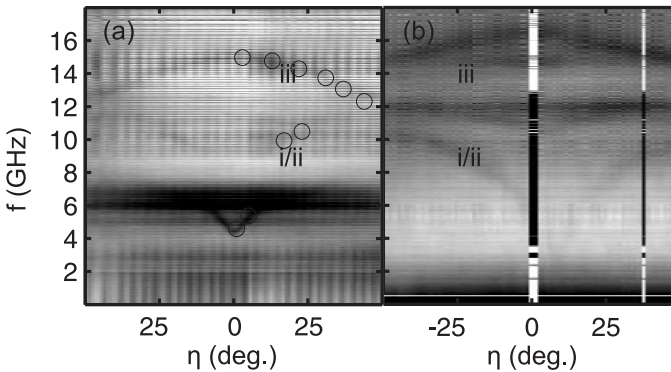
Figure 7.15: (a) AESWS data $\Im a_{22}$ obtained for a $p = 200$ nm ADL (SN89-4-2) at $\mu_0 H = 100$ mT. A $w_{\mathrm{ic}} = 2$ μm, $s = 12$ μm SW-transmission CPW is used. Circles highlight SW resonances for $\eta > 0°$. (b) AESWS data for a $p = 120$ nm ADL (SN61-3-3). A $w_{\mathrm{ic}} = 2$ μm standard CPW is used.

7.2.4 Comparison of AESWS data for different p

It is instructive to compare AESWS data for different periodicities p obtained in reflection measurements, i.e. $\Im a_{22}$, directly. This is done in Fig. 7.16 for $\mu_0 H = 100$ mT.

From this figure, the various findings of the preceeding sections are confirmed: First, only for $p = 300$ nm, i.e. Fig. 7.16 (e), three modes are resolved, i.e. modes i, ii, iii. For $p = 300$ nm and $p = 120$ nm, i.e. Fig. 7.16 (e) and (f), the low frequency mode shows a pronounced dependence of f_r on η, i.e. $\mathrm{d}f_r/\mathrm{d}\eta \gg 0$. This is different for the larger periodicities $p > 400$ nm in (b)-(d), where $\mathrm{d}f_r/\mathrm{d}\eta \gtrsim 0$. Third, the frequency difference between the largest and smallest observed f_r continuously decreases for increasing p. This frequency spread is indicated in Figs. 7.16 (b)-(f) by vertical bars. Intuitively, this is motivated by the increasing permalloy filling fraction $\mathcal{F}$ for increasing p, see Fig. 7.1: for $\mathcal{F} \to 1$, the observed spectra more and more resemble the plain film spectrum depicted in Fig. 7.16 (a) where the frequency spread is zero. For smaller values of the periodicity p, effects of mode quantization and demagnetization field, see Sec. 7.3, gain in significance and shift resonance frequencies f_r apart from each other.

For $p \geq 400$ nm, the number of resonances and the qualitative behavior is found to be constant, while for smaller periodicities p more resonances and different behavior of f_r on η is observed. At $p = 400$ nm, a transition occurs, which is consistent with VNA-FMR data as discussed in Sec. 7.2.1. To discuss the origin of this finding is subject of the following Sec. 7.3.

## 7.3 Quantization and Localization of Spin Waves

Three fundamentally different types of modes are found to exist in an antidot lattice: an edge mode close to the holes, a fundamental mode extending through the lattice perpendicular to the field, and a localized mode in between neighboring holes parallel to the field. For $p > 400$ nm, the edge mode is not resolved. For $p \leq 200$ nm, the fundamental mode and the edge mode hybridize.

To understand the qualitatively different behavior of $p > 400$ nm and $p < 400$ nm as discussed in the previous sections, it is instructive to per-
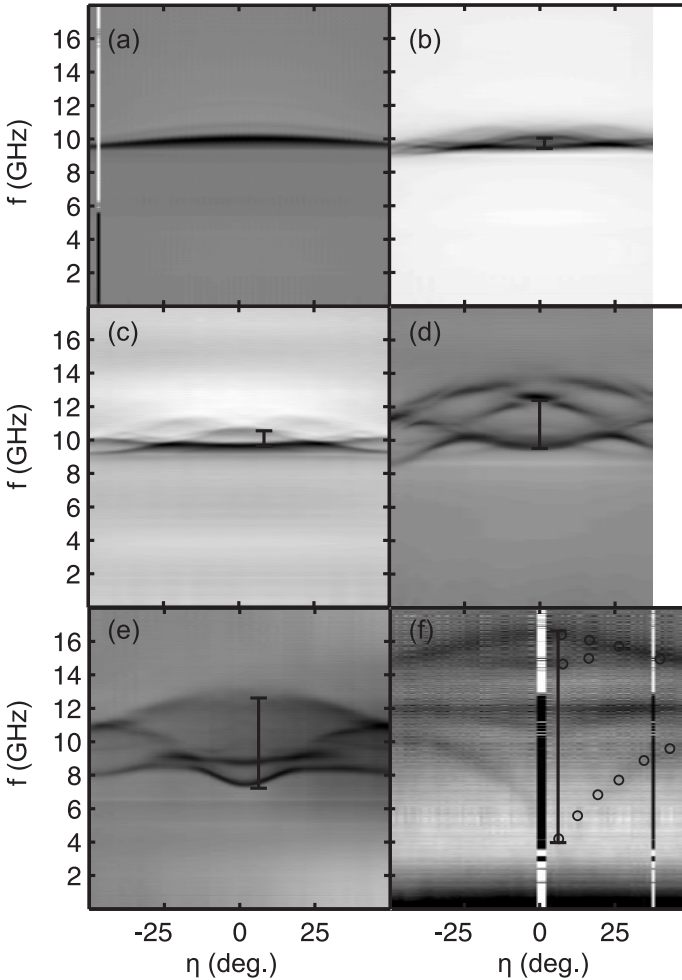
Figure 7.16: AESWS data $\Im a_{22}$ obtained for $\mu_0 H = 100$ mT and various period-icities p. (a) Plain film, i.e. $p \to \infty$. Sample is SN89-4-D. (b) $p = 1000$ nm. Sample is SN101-1-F-MR. (c) $p = 800$ nm. Sample is SN83-1-LO. (d) $p = 400$ nm. Sample is SN66-A-1-1. (e) $p = 300$ nm. Sample is SN89-4-4. (f) $p = 120$ nm. Sample is SN61-3-3. For all samples, $w_{\mathrm{ic}} = 2$ μm. Vertical bars indicate the frequency spread between lowest resolved f_{r} (mode i or mode ii) and largest resolved f_{r} (mode iii). Only the $p = 120$ nm sample has a hole diameter of $d = 87$ nm, all other samples are fabricated such that $d = 120$ nm.
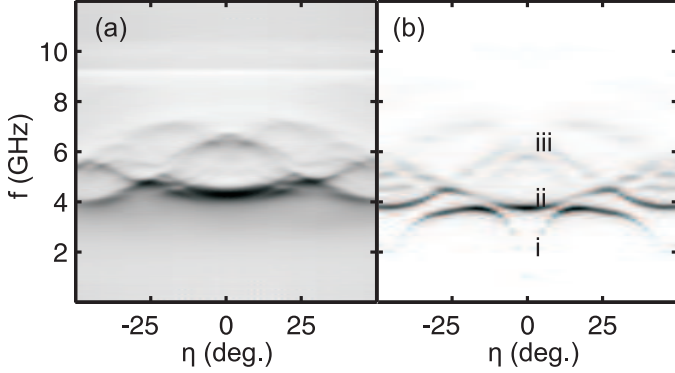
Figure 7.17: Comparison between AESWS measurements and micromagnetic simulations of a $p = 800$ nm antidot lattice for various η and $\mu_0 H = 20$ mT. Simulation parameters are according to set C. Dark (bright) contrast corresponds to large (small) SW signal. (a) AESWS data $\Im a_{22}$. (b) Micromagnetic simulations.

form micromagnetic simulations. By this it is possible to obtain spatial SW profiles allowing insights into the microscopic origins of a spin-wave resonance and based on this, further interpretation of the data.

7.3.1 $p = 800$ nm ADL: localized and extended modes

Micromagnetic simulations are performed for $k = 0$. A single unit cell of the antidot lattice with two-dimensional periodic boundary conditions is simulated, see Sec. 2.3.3. A spatially homogeneous field pulse of 8 mT is used to excite spin precession. Parameters are according to set C, see A.3. The angle of the external field with respect to the ADL unit cell axis is varied. This angle corresponds to η of the AESWS measurements.

From the temporal evolution of the averaged magnetization $\langle M_i(\tau) \rangle_i$, a Fourier transformation yields the integrated spectral response as introduced in Sec. 2.3.3. This data, corresponding to AESWS reflection measurements, is depicted in Fig. 7.17 (b). There is a one-to-one correspondence between simulated and measured data, except for the low frequency mode labeled i, which is not resolved in experiment.

Based on this good agreement, it is reasonable to obtain spatial spin-

precession maps of the resonances. This is along Ref. [Neu10] (copyright 2010, American Physical Society). In Fig. 7.18 local spin-precession amplitudes are displayed which are obtained from the micromagnetic simulations. Data is depicted for $\mu_0 H = 20$ mT, however mode profiles do not change significantly for increasing $\mu_0 H$. This is due to the constant magnetization profile for the saturated regime of Fig. 7.2.

- (Row 1) Mode i, edge mode (a), (b), (c). This mode is not resolved in the experiment. However, it is instructive to analyze the findings from simulation, nonetheless. This mode resides close to the edges of the holes constituting the antidot lattice. For $\eta = 0°$ and $\eta = 45°$, a symmetric behavior is found. The mode resides localized at each hole at the poles formed by the demagnetization field $\mathbf{H}_D$ [c.f. Fig. 7.5]. For $\eta = 22°$ coupling between nearest neighbors is observed.

- (Row 2) Mode ii, extended mode (d), (e), (f). For $\eta = 0°$ (d) and $\eta = 45°$ (f), stripe-like regions of large spin-precession amplitude are observed which extend through the lattice. Their effective width is determined to be about $w_{\text{eff}} = 600$ nm and $w_{\text{eff}} = 600$ nm$/\sqrt{2}$, respectively. The stripes are oriented perpendicular to the applied field $\mathbf{H}$. For $\eta = 22°$ (e), the profile of the propagating mode is found to be complex and significantly different from (d) and (f). The mode shows an extended character in y direction but localization between next-nearest neighboring holes.

- (Row 3) Mode iii, localized mode (g), (h), (i). This mode is localized in spin-wave channels formed parallel to the external field in between two nearest $\eta = 0°$ (g) second-next nearest $\eta = 22°$ (h) and next nearest $\eta = 45°$ (i) neighbors.

To further substantiate the excellent agreement between measured data and simulation data found in Fig. 7.17, spatio-temporal resolved MOKE technique, see Sec. 3.2.3, is employed. For this a sample is fabricated with a $p = 800$ nm antidot lattice on top of the CPW, see Sec. 3.1.2. Sample SN67-1-3. Only the extended mode (mode ii) is considered for this study. MOKE data is obtained for $\mu_0 H > 20$ mT in order to increase the signal-to-noise ratio. Despite this, a good one-to-one correspondence between the tr-MOKE data and simulated profiles is found in Fig. 7.19 for mode ii. It

is found that for $\mu_0 H > 15$ mT these profiles do not change significantly with increasing H.

7.3.2 $p = 300$ nm ADL: edge mode

As in the previous section for a $p = 800$ nm ADL, it is instructive to first compare the simulated integrated spectral response, see Sec.2.3.3 with measurement data. Exemplarily AESWS measured $|a_{22}|(\mu_0 H, \eta = 0°)$ is shown and compared with micromagnetic simulation data assuming $k = 0$ in Fig. 7.20 (a) and (b), respectively. Simulation parameters are according parameter set B. A one-to-one correspondence is found. The resonance frequency f_r of the lowest frequency mode takes a minimum at $\mu_0 H \approx 30$ mT. This is the anisotropy field beyond which the magnetization of the ADL starts to align with the applied field $\mathbf{H}$, i.e. $\langle M_\parallel \rangle / M_{\mathrm{Sat}} \approx 1$, see Sec. 7.1.2. This is in agreement with measured hysteresis curves, see Fig. 7.2.

Based on this good agreement, it is reasonable to discuss spatial spin-precession maps of the resonances, see Fig. 7.21 ($\eta = 1°$). Data is depicted for $\mu_0 H = 40$ mT, however spatial mode profiles do not change significantly for increasing $\mu_0 H$. The three mode types found correspond to the modes discussed for the $p = 800$ nm ADL above, i.e. edge mode, extended mode, and localized mode. The main discrepancy is found for the edge mode, see mode i in Fig. 7.21. Firstly, the edge mode is resolved experimentally for $p = 300$ nm, while for $p = 800$ nm the mode is not resolved. Compare Figs. 7.20 and 7.17. Secondly, the spatial spin-wave profile of the edge mode (mode i) in the case of $p = 300$ nm indicates that interconnected regions of non-zero spin-precession amplitude extend through the lattice, see Fig. 7.21. This is different for $p = 800$ nm.

From e.g. Fig. 7.17 it is found that the edge mode (mode i) shows a much stronger dependence of f_r on η than the extended mode (mode ii). $p = 400$ nm is interpreted as a transition periodicity: for $p > 400$ nm, the edge mode is not resolved.

7.3.3 $p = 120$ ADL: mode hybridization

For even smaller lattice period, i.e. $p = 200$ nm and $p = 120$ nm [c.f. Fig. 7.15], two relevant modes are resolved ($\eta = 0°$). To classify these modes, micromagnetic simulations are performed for a $p = 120$ nm ADL.
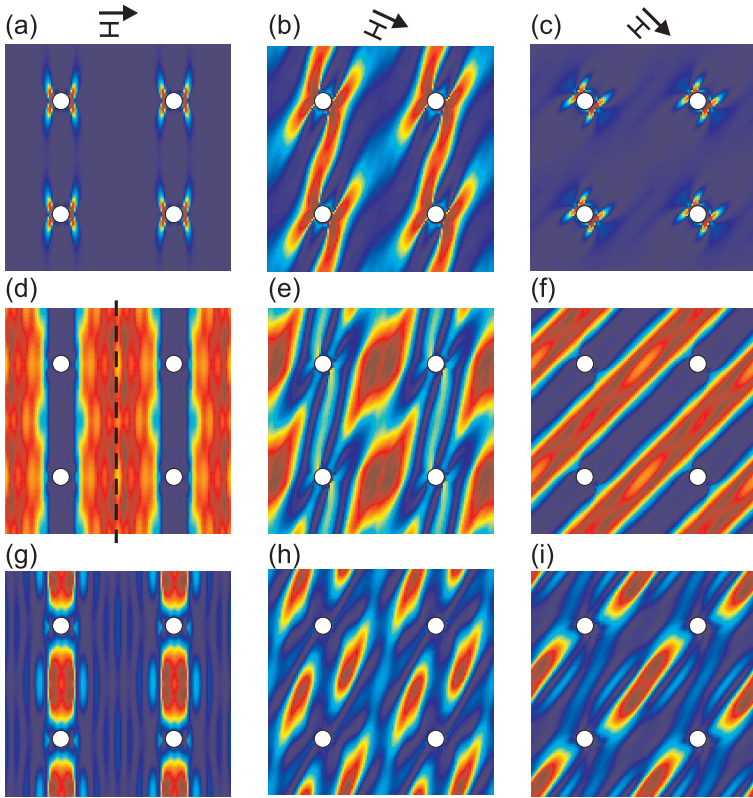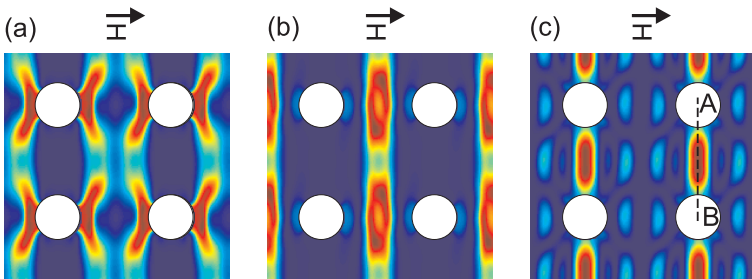
Figure 7.18: Micromagnetic simulation of spatial spin-wave profiles of a $p = 800$ nm antidot lattice for $\mu_0 H = 20$ mT. Simulation parameters are according set C. Red (blue) corresponds to large (small) spin-wave amplitudes. (a) $\eta = 0°$, $f = 1.5$ GHz. Edge mode. Individual resonances are localized at the holes' edges and are uncoupled. (b) $\eta = 22°$, $f = 3.5$ GHz. (c) $\eta = 45°$, $f = 2.2$ GHz. (d) $\eta = 0°$, $f = 3.7$ GHz. Extended or fundamental mode extending through the lattice in SW channels formed perpendicular to the extended field. Higher order fundamental modes, which are transversally quantized, are depicted in Fig. 8.8 (b) and (c). (e) $\eta = 22°$, $f = 4.0$ GHz. Fundamental mode showing quantization parallel *and* perpendicular to the external field. (f) $\eta = 45°$, $f = 3.6$ GHz. This mode is the counterpart of the $\eta = 0°$ fundamental mode and is also quantized perpendicular to the external field. (g) $\eta = 0°$, $f = 5.3$ GHz. Localized mode residing in SW channels formed parallel to the external field. (h) $\eta = 22°$, $f = 4.7$ GHz. (i) $\eta = 45°$, $f = 5.0$ GHz.
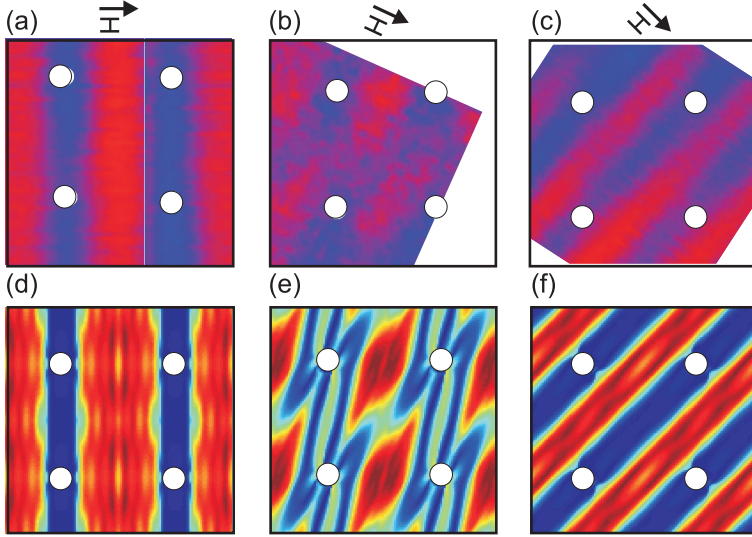
Figure 7.19: Comparison of spatial spin-wave profiles obtained from MOKE [Bau11] and micromagnetic simulations (simulation parameters are according set C) of the extended mode for a $p = 800$ nm ADL [Neu10]. Sample SN67-1-3. Red (blue) corresponds to large (small) spin-wave amplitudes. (a) $\eta = 0°$, $f = 8$ GHz, $\mu_0 H = 68$ mT. (b) $\eta = 25°$, $f = 5.2$ GHz, $\mu_0 H = 20$ mT. (c) $\eta = 30°$, $f = 8$ GHz, $\mu_0 H = 75$ mT. (d) $\eta = 0°$, $f = 3.8$ GHz, $\mu_0 H = 20$ mT. (e) $\eta = 22°$, $f = 4.3$ GHz, $\mu_0 H = 20$ mT. (f) $\eta = 45°$, $f = 3.9$ GHz, $\mu_0 H = 20$ mT. MOKE data is obtained for $\mu_0 H \geq 20$ mT to maximize the signal to noise ratio. Mode profiles are not found to change significantly for $\mu_0 H > 20$ mT. Good agreement between MOKE and micromagnetic simulations is obtained.
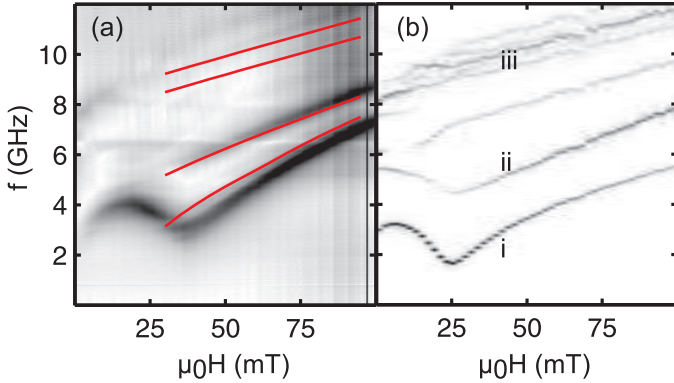
Figure 7.20: Comparison between AESWS measurements and micromagnetic simulations of a $p = 300$ nm antidot lattice for $\eta = 1°$ and various μH. Simulation parameters are according set B. (a) AESWS measurements, depicted is $|a_{22}|$. Red lines depict eigenfrequencies f_r obtained from the plane wave method, see Sec. 8.1.2. (b) Micromagnetic simulations. Labeling i-iii corresponds to Fig. 7.21 (a)-(c).

Figure 7.21: Micromagnetic simulation of spatial spin-wave profiles of a $p = 300$ nm ADL for $\mu_0 H = 40$ mT and $\eta = 1°$. Simulation parameters are according to set B, see A.3. (a) $f = 2.8$ GHz. Edge mode (mode i). b) $f = 5.0$ GHz. Extended mode (mode ii). (c) $f = 10.8$ GHz. Localized mode (mode iii). (a)-(c) correspond to modes i-iii of Fig. 7.20.
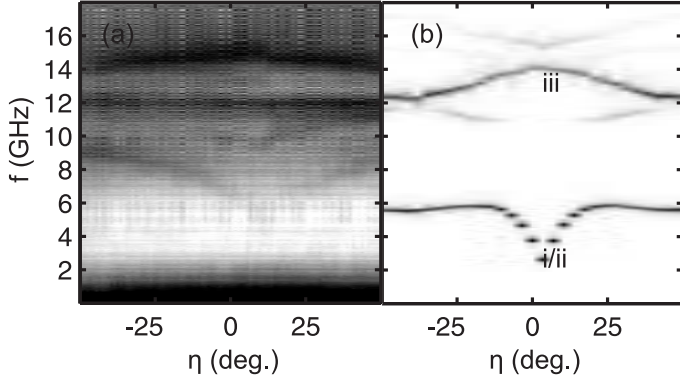
Figure 7.22: Comparison between (a) AESWS data $|a_{22}|$ and (b) micromagnetic simulations of a $p = 120$ nm antidot lattice (hole diameter $d = 86$ nm, see Fig. 4.4) for $\mu_0 H = 60$ mT and various η. Simulation parameters according to set E. Sample is SN61-3-3 ($w_{ic} = 2\ \mu$m standard CPW). (a) AESWS measurements, depicted is $|a_{22}|$. (b) Micromagnetic simulations.

Analyzing SEM images [c.f. Fig. 4.4], the hole diameter is evaluated as $d = 86$ nm. AESWS data is depicted in Fig. 7.22 (a) and the corresponding micromagnetic simulations are depicted in Fig. 7.22 (b). While some differences in the resolved frequencies remain, there is agreement in that only two major modes are observed in simulation. For $\eta = 0°$, the respective spatial mode profiles are depicted in Fig. 7.23. The lower frequency mode shows characteristics of, both, the extended and edge mode as observed for larger lattice periods, see Figs. 7.18 and 7.21. Mode hybridization is known in literature [Gri04] and recently has been observed between center and edge modes [Dem10a]. Mode hybridization can occur when modes overlap spatially and / or in frequency domain.

The higher frequency mode of the $p = 300$ nm ADL is identified as the localized mode, see Fig. 7.23 (b).

To conclude this section, over a wide regime of periodicities, for $300 \leq p \leq 800$ nm, the same modes are found to to be relevant in the ADL: Lowest in frequency is the edge mode (labeled i). The extended or fundamental mode (labeled ii) exhibits resonance frequencies close to the plain film resonance. Highest in frequency is the localized mode (labeled iii).
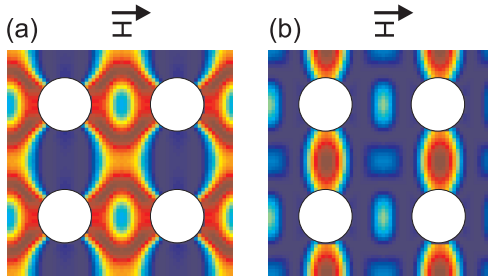
Figure 7.23: Spatial SW profiles of a $p = 120$ nm ADL obtained from micromagnetic simulations for $\eta = 0°$ at $\mu_0 H = 60$ mT. Simulation parameters according to set E. (a) $f = 2.7$ GHz. Hybridized edge / extended mode. (b) $f = 15.4$ GHz. Localized mode.

For $p = 120 - 200$ nm, edge and extended mode are found to hybridize.

7.4 Mode Behavior

The internal field evaluated for the spatial regions of the different mode types, i.e. edge, extended, and localized mode, is found to describe well the general tendencies of the mode eigenfrequencies. Quantization of the extended and localized mode due to the antidot lattice geometry is discussed by means of the BLS technique and a Wentzel-Kramer-Brillouin argument in experimental and theoretical terms, respectively.

7.4.1 Internal field analysis

The value of f_r and its dependence on η can be motivated by analyzing the demagnetization field H_D for the spatial regions where the respective modes exist in. It is found that the spatial mode profiles stay almost unchanged for $0° \leq \eta \leq 20°$ in the form as depicted in e.g. Fig. 7.18 (a), (d), (g) for $p = 800$ nm. Only for larger angles $\eta > 20°$, transitions occur. Therefore, to discuss the dependence of f_r for small angles $\eta \leq 20°$, in Fig. 7.5, the demagnetization field H_D is evaluated for $\eta = 0°$, and $\eta = 20°$ [McP05].

- Mode i, edge mode. The edge mode is localized close to the poles of the holes formed by the demagnetization field $\mathbf{H}_{\mathrm{D}}$, see Figs. 7.18 (a)-(c) and Fig. 8.11 (a). In these regions $\mu_0 H_{\mathrm{D}}$ is large and negative, see Fig. 7.5. From Eq. 2.73 it is known that smaller values of the effective field H_{eff}, i.e. of H_{D}, cause f_{r} to shift to lower values. This motivates the small value for f_{r}.

- Mode ii, extended mode. This modes extends through the lattice away from the holes in the channels formed perpendicular to the field. The mode is quantized in between holes neighboring in the direction parallel to the external field. From Fig. 7.5 (a) it is found that for these regions $\mu_0 H_{\mathrm{D}}$ has a small negative value $H_{\mathrm{D}} \lesssim 0$. This motivates that the resonance frequency f_{r} of the extended mode is close to the plain film value, e.g. $f_{\mathrm{r}}(\mu_0 H = 40 \text{ mT}) = 6 \text{ GHz}$, c.f. Fig. 7.7.

  In Sec. 7.2 it is found that for this mode the angular anisotropy for small $\eta < 20°$ is small and positive, i.e. $\mathrm{d}f_{\mathrm{r}}/\mathrm{d}\eta \gtrsim 0$ ($\mathrm{d}\eta > 0$). Again, this can be motivated by studying the dependence of H_{D} on η for the spatial region where the extended mode resides. From Fig. 7.5 one finds that the change in H_{D} is small and positive, i.e. for increasing η the value $\mu_0 H_{\mathrm{D}}$ increases. From Eq. 2.73 it is known that larger values of the effective field, i.e. of $\mu_0 H_{\mathrm{D}}$, cause f_{r} to shift to higher frequencies f. This is consistent with the observed angular behavior.

- Mode iii, localized mode. This mode resides between holes neighboring perpendicular to the field direction (for $\eta = 0°$), compare with Figs. 7.18 (g)-(i) and Fig. 8.11 (c) [Pec05, Neu08a]. From Fig. 7.5 (a) it is found that for these regions $\mu_0 H_{\mathrm{D}}$ has a large positive value $\mu_0 H_{\mathrm{D}} \approx 20 - 30$ mT. This motivates why the resonance frequency f_{r} of the extended mode is higher if compared to plain film value, e.g. $f_{\mathrm{r}}(\mu_0 H = 40 \text{ mT}) = 8 \text{ GHz}$, c.f. Fig. 7.7. Additionally, quantization of this mode, see below, contributes significantly to the exact value of f_{r}.

  In Sec. 7.2 it is found that for this mode the angular anisotropy for small $\eta < 20°$ is large and negative, i.e. $\mathrm{d}f_{\mathrm{r}}/\mathrm{d}\eta << 0$ ($\mathrm{d}\eta > 0$). Again, this can be motivated by studying the dependence of the demagnetization field on η for the spatial region where the localized

mode resides. From Fig. 7.5 one finds that the change in H_D is large and negative, e.g. for $\eta = 20°$, the value of H_D has decreased to $10 - 20$ mT. This is consistent with the observed angular behavior of reduced f_r for increased η.

7.4.2 Analysis of BLS data

The modes as described in the previous section are characterized by their quantization and extended character. Based on these findings, it is possible to analyze the mode quantization further using Brillouin light scattering [Tse09, Tac10b, Tac10a]. This is along Ref. [Neu10]. For this, BLS is employed in three different scattering configurations [c.f. insets in Fig. 7.24(a) to (c)]. In particular, **k** and **H** are always perpendicular to each another.

- In Fig. 7.24 (a) ($\eta = 0°$) one finds two nearly dispersionless modes (open circles) at high frequencies and one branch with positive dispersion (full circles) which starts at 4 GHz at $k = 0$ (low frequency mode). The blue squares mark f_r of AESWS a_{22} data obtained from Fig. 7.10 for the different CPWs with $k_{CPW} = 0.6 \times 10^4$ rad/cm and 2.0×10^4 rad/cm. The resolved low frequency mode with positive dispersion thus is identified with the extended mode, see Fig. 7.18 (d), and the higher frequency modes are localized modes, see Fig. 7.18 (g).

- The slope of the dispersion of the extended mode allows to extract a group velocity of $v_g = 4.0$ km/s in the direction extending perpendicular to the field **H**. According to the simulated and measured spatial mode profile, it is possible to assume a transversally quantized SW by considering the wave vector parallel to **H**, i.e. $k_\parallel$, to be quantized to a value of $k_\parallel = \pi/w_{eff} = \pi/600$ nm. The quantization reflects the effective stripe width as determined from Fig. 7.18 (d). The dispersion as a function of $k_\perp$ is calculated using Eq. 2.73 and found to be in good agreement with the measured data.

- In Fig. 7.18 (f) ($\eta = 45°$) again the low frequency mode exhibits $v_g > 0$. This mode is the extended mode as found from comparison with AESWS data. If compared to $\eta = 0°$, the stripes formed by the extended mode have a smaller width of $w_{eff} = 600$ nm$/\sqrt{2}$ [c.f.

Fig. 7.18 (f)]. A dispersion calculated with $k_\parallel = \pi/(600 \text{ nm}/\sqrt{2})$ (full line in Fig. 7.24 (c)) models BLS data well. One extracts $v_g = 2.7 \text{ km/s}$ from the BLS data.

- For $\eta = 25°$ the mode profile of the extended mode is more complex. In particular, different to $\eta = 0°$ and $\eta = 45°$, the low frequency mode does not show a dispersion, i.e. $v_g = 0$, and the higher frequency mode shows $v_g = 2.7 \text{ km/s}$. This is verified by AESWS measurements, see Fig. 7.10 (d).

- The high frequency mode, i.e. the localized mode, is present for $\eta = 0°, 25°,$ and $45°$ and in all cases shows no dispersive character. Therefore, BLS confirmed the standing SW behavior of this mode localized in between nearest ($\eta = 0°$) and next-nearest ($\eta = 45°$) neighboring holes, c.f. Fig. 7.18 (g) and (h) [Neu08a].

It is possible to conclude, that for $\eta = 0°$ and $\eta = 45°$ a high symmetry case is present where SWs travel in channels formed perpendicular to the field (extended mode). For $\eta = 25°$ a more complex situation is observed.

Next, it is instructive to compare BLS data to micromagnetic simulations. For this a simulation with local excitation is performed using simulation set A (with $M_{\text{Sat}} = 780 \text{ kA/m}$) for $\mu_0 H = 20 \text{ mT}$ and $\eta = 1°$. SWs up to ≈ 50 GHz are excited by a short field pulse for $12.0 \leq y \leq 12.8 \, \mu\text{m}$. The field pulse amplitude is 0.1 mT. Data is only analyzed in regions where the extended mode exists, i.e. $m_z(y_i, t)|_{\bar{x}_i}$ of Sec. 2.3.3 is evaluated only for x_i away from the holes' edges. The spatio temporal evolution of the dynamic out-of-plane magnetization component $m_z(y_i, t)|_{\bar{x}_i}$ is plotted in Fig. 7.25 (a). The SW propagating away from the excitation is visible and standing SWs for $y \approx 12 \, \mu\text{m}$. A 2d FFT of Fig. 7.25 (a) yields the SW dispersion depicted as a gray-scale plot in Fig. 7.25 (b). Depicted as open circles is further the respective BLS data [c.f. Fig. 7.24 (a)]. Simulation data and BLS data are in good agreement.

7.4.3 WKB method for the localized mode

To verify the standing SW character of the localized mode, it is possible to employ a semi-analytical Wentzel-Kramer-Brillouin (WKB) argument. For a standing SW, the resonance condition is that the accumulated phase
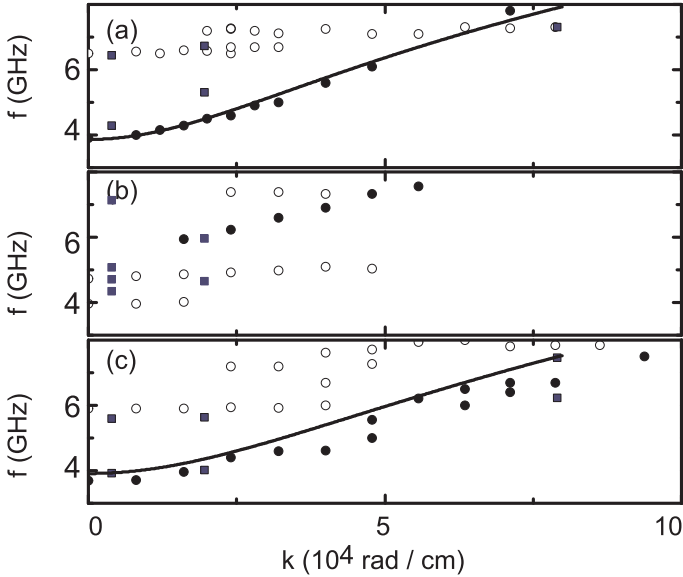
Figure 7.24: Spin-wave dispersion $f(k)$ for $\mu_0 H = 20$ mT of a $p = 800$ nm ADL (circles) [Neu10]. (a) $\eta = 0°$. (b) $\eta = 25°$. (c) $\eta = 45°$. Full circles indicate a mode with dispersive character, i.e. $\mathrm{d}f/\mathrm{d}k > 0$. Open circles indicate localized modes with $\mathrm{d}f/\mathrm{d}k = 0$. Full squares indicate AESWS data obtained for two different samples, i.e. SN83-1-LO with $w_{\mathrm{ic}} = 2\,\mu$m and $k_{\mathrm{CPW}} = 0.6 \times 10^4$ rad/cm, as well as SN88-1-A-M with $w_{\mathrm{ic}} = 2\,\mu$m and $k_{\mathrm{CPW}} = 2 \times 10^4$ rad/cm. Full lines in (a) and (c) are calculated dispersions obtained from a wire model with transversal quantization considering an effective width, see text. For BLS measurements, always $\mathbf{k} \perp \mathbf{H}$.
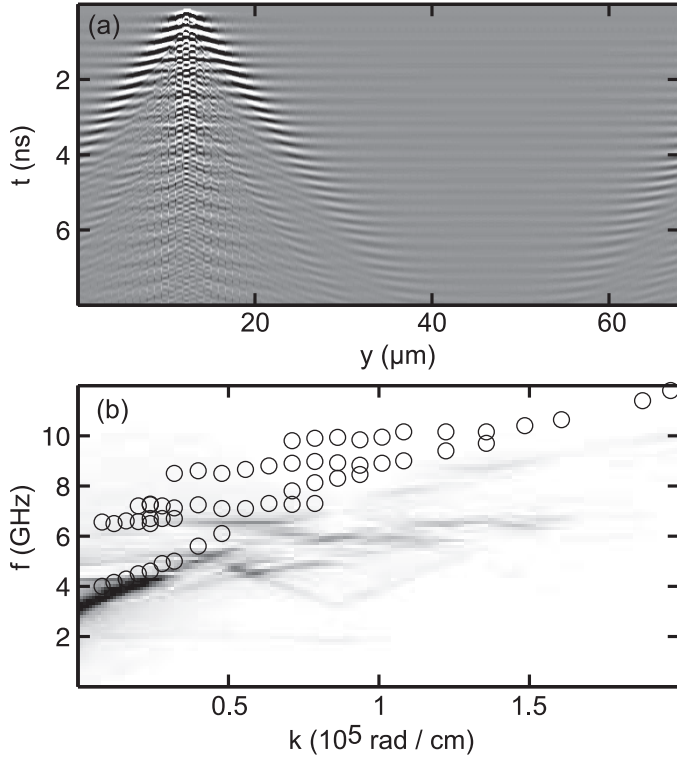
Figure 7.25: (a) Micromagnetic simulation of spatio-temporal SW propagation in y direction in a $p = 800$ nm ADL. Simulation parameters are according to set A. $\mu_0 H = 20$ mT, $\eta = 1°$. Field pulse amplitude is 0.1 mT. The field pulse has no x dependence and is localized at $12 \leq y \leq 12.8$ μm. (b) Spin-wave dispersion obtained from micromagnetic simulations (gray-scale plot) and BLS measurements (open circles). The simulated dispersion is obtained via a 2d Fourier transformation of (a).

is an integer multiple of π, i.e. [Gie07, Neu08b]

$$\phi_{\text{WKB}} = \int_A^B k_{\perp,\|}(f_{\text{r}}, H_{\text{eff}}(\kappa))\mathrm{d}\kappa = (p+1)\pi, \qquad (7.2)$$

where ϕ_{WKB} is the phase acquired by the standing spin wave between turning points A and B along a high symmetry axis κ. This high symmetry axis allows for decomposition of the wave vector in a component perpendicular (parallel) to the external field, i.e. $k_{\perp,\|}$. p is the order of the mode in the direction of the high symmetry axis with $p = 0, 1, 2, ...$ Eq. 7.2 must be fulfilled to form a standing spin wave. Turning points are defined by either an imaginary wave vector [Gus03], by a vanishing internal field [Jor02], or by geometrical edges of the holes [Yu04].

κ is chosen along the dashed line in Fig. 7.21 (c) for the localized mode with $f = 10.8$ GHz. The quantization transverse to κ must be anticipated from the spatial mode profile plot, as is done for the discussed case as $k_\| = 2\pi/150$ nm. This corresponds to a quantization slightly larger than half the hole diameter (which is $d = 120$ nm). From quasistatic simulations, one obtains $H_{\text{D}}(\kappa)$ (and via this $H_{\text{eff}}(\kappa)$), see Fig. 7.26. For each point along κ, the corresponding wave vector $k_\perp$, which fulfills the dispersion relation Eq. 2.73, is calculated; this is depicted in Fig. 7.26 (b). Analyzing Eq. 7.2 yields $\phi_{\text{WKB}} = 0.95\pi$. Therefore, it is motivated that the localized mode corresponds to a standing SW in the resonator formed in between to neighboring holes in y direction.
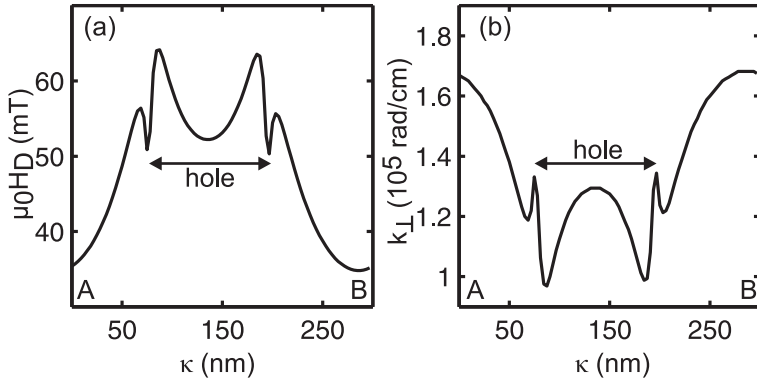
Figure 7.26: WKB analysis according to Eq. 7.2 for a $p = 300$ nm ADL at $\mu_0 H = 40$ mT, $\eta = 1°$ for the localized mode at $f = f_\text{r} = 10.8$ GHz. (a) Demagnetization field H_D along the high symmetry axis κ of the localized mode in y direction, see dashed line A-B in Fig. 7.21 (c). Data is obtained from micromagnetic simulations according to set B. The hole extends for 81 nm $\leq \kappa \leq 200$ nm as indicated. (b) Wavevector perpendicular to the external field (y direction) $k_\perp$ for the assumption of a longitudinal quantization of $k_\parallel = 2\pi/150$ nm as evaluated from Eq. 2.73 for values of H_D obtained from (a). Evaluation of the WKB equation Eq. 7.2 in the magnetic material yields an accumulated phase of $\phi_\text{WKB} = 0.96\pi$.

8 Antidot Lattices: Propagating Spin-Wave Properties

This chapter is organized as follows: First, in Sec. 8.1, the propagation properties for antidot lattices of various periodicities are investigated experimentally and by the plane wave method. In Secs. 8.2 and 8.3, the different propagation mechanisms of the edge and fundamental mode are discussed separately at small and large periodicities, respectively. Finally, in Sec. 8.4, transmission of SWs into a $p = 800$ nm ADL is studied.

Via AESWS it is possible to measure the group velocity v_g. For this the oscillations in $\Re a_{12}$ are analyzed. Exemplarily, $\Re a_{12}(\eta = 0°, \mu_0 H = 40\,\mathrm{mT})$ is depicted in Fig. 8.1 for $p = 300$ nm and 800 nm. Based on such data, the oscillation period of $\Re a_{12}$ and $\Im a_{12}$ labeled Δf is associated with a 2π phase shift. From this v_g is determined via Eq. 3.2.

8.1 Propagation Properties for various Periodicities

Propagation is analyzed for various periodicities p. For $p < 400$ nm only the edge mode is found to propagate, while for $p > 400$ nm only the extended mode is found to propagate. The mechanism of propagation of the edge mode is strong dipolar coupling of the SW excitations localized at the holes' edges.

The dependence of the group velocity v_g is studied for the propagating modes in antidot lattices of different periodicity p. In Fig. 8.2, v_g taken on the different ADLs for $\eta = 1$ to $2°$ are depicted as full circles. These angles η are chosen to compare with simulations later on and to avoid numerical artifacts originating from the high symmetry direction. They do not necessarily reflect the maximum achievable v_g, see below. The plain film value ($v_\mathrm{g} = 4.8$ km/s at 40 mT) is shown as a horizontal dashed line.
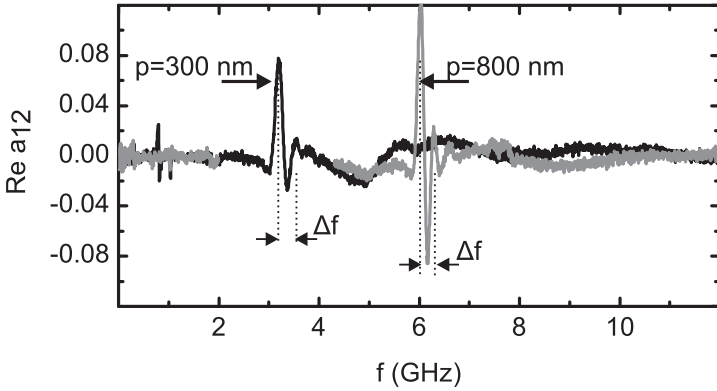
Figure 8.1: AESWS data obtained for a $p = 300$ nm sample (SN89-4-4) (black curve) and a $p = 800$ nm sample (SN83-1-LO) (gray curve), both with a $w_{ic} = 2$ μm SW-transmission CPW. $\mu_0 H = 40$ mT. $\eta = 1°$. The frequency difference Δf corresponds to a 2π phase shift of the propagating SW at the detector CPW and is used to evaluate v_g, see Sec. 3.2.2.

8.1.1 From localized to coupled dynamics

From Fig. 8.1 it is seen that for $p = 300$ nm a prominent propagation signal occurs for $f_r \approx 3.1$ GHz. This is a frequency much smaller if compared to $p = 800$ nm, where $f_r \approx 6.1$ GHz: from the difference in f_r it is found that for $p = 300$ nm the edge mode propagates, whereas for $p = 800$ nm the propagating mode is the extended mode. In Fig. 8.2 values v_g are summarized which are extracted from data such as those displayed in Fig. 8.1. They have been obtained on ADLs with different periodicity p.

From Fig. 8.2, the following statements can be made about the behavior of v_g on p. First, values of v_g in ADLs are close to the plain film values for small periodicities $p = 0.3$ μm and large periodicities $p \approx 4$ μm. A minimum v_g is observed for $p = 0.8$ μm. Second, to model BLS dispersion data in Fig. 7.24, a nanowire model has been introduced to calculate the corresponding SW dispersion, see Sec. 7.3. Convincingly the group velocities measured at $p = 0.8$ and 1.0 μm lie on the curve in Fig. 8.2 which reflects the nanowire model (full lines) for film thickness $t_s = 25...28$ nm. For small p this nanowire model is found not to be valid anymore. Third,

for small $p = 300 - 400$ nm, the SW group velocities recover to a value close to and even in excess of the plain film value. For $p = 0.4$ μm, a transition is observed: both extended as well as edge mode are found to propagate, see Fig. 7.13.

To understand why the edge mode is found to propagate only for $p \leq 400$ nm with a large group velocity v_{g} , it is instructive to recapitulate the demagnetization field profile obtained from micromagnetic simulations as depicted in Fig. 7.6. Analyzing the demagnetization field H_{D} along the axis of propagation of the edge mode at $\eta = 1°$, i.e. line σ_2 in Fig. 7.3, yields a strong peak-to-peak variation $\Delta H_{\mathrm{D}} \approx 100$ mT [light line in Fig. 7.6]. The amplitude of this variation is found to depend almost only on the hole shape and not on the ADL period p. Using the SW dispersion relation Eq. 2.73 for a quantization parallel to the field as present in a narrow wire [Kal86], one can identify regions in $H_{\mathrm{D}}(x, y)$ where spins can precess resonantly at $f_{\mathrm{r}} = 3.1$ GHz. This occurs for

$$4\pi\chi\left(H_{\mathrm{d}}, f_{\mathrm{r}}, M_{\mathrm{Sat}}\right) > -1, \tag{8.1}$$

where χ is the susceptibility [Gur96, Kos06]. Using the values $H_{\mathrm{D}}(x, y)$ obtained by micromagnetic simulations, one finds that *resonant* spin precession occurs only in the minima of H_{D} very close to the edges of the holes. In the intermediate regions, the non-zero amplitudes reflect *non-resonant* excitation. Considering this information one can attribute the experimental finding of large v_{g} of the edge mode for $p = 300$ nm to the fact that SWs tunnel between the neighboring resonant oscillators localized at the holes' edges [Dem04b, Kos06]. The strength of dipolar tunneling depends on the tunneling distance, the film thickness t_{s}, and the susceptibility of the material through which the SW tunnels [Dem04b, Kos10, Gub10]. A large susceptibility χ of the material amplifies the dipolar stray field and thus increases the dipolar coupling strength, i.e., tunneling probability [Gub10, Kos10]. In the ADL geometry, SWs in edge modes tunnel through ferromagnetic material of large χ. This feature is *unique* to the ADL geometry and different from magnetic elements separated by an air gap. It motivates the large v_{g} observed for $p = 300$ nm.

For $p = 0.8$ μm, the large distances between individual holes forbids SW tunneling and coherence between edge excitations is not induced. SW precession is only predicted close to the hole's edges and the local SW wells are not coupled, see Fig. 7.18 (a). In experiments on ADLs

with $p \geq 0.6$ μm, the edge mode is not resolved experimentally, see e.g. Fig. 7.17. This is attributed to edge roughness and variations in the hole diameters further decreasing the coherence [Neu08a]. Due to variations in the demagnetization field at different holes and the missing coherent coupling for large p, the individual resonances differ and the experimental linewidth broadens inhomogeneously.

Based on the observations, Tab. 8.1 provides an overview on the phenomenological findings corresponding to the three basic mode types, i.e. edge, extended, and localized mode. In particular the edge mode and the extended mode show a very different behavior depending on the lattice period p. Different physical phenomena dictate the propagation properties of the respective modes. It is therefore instructive to analyze the propagation characteristics of the extended mode for $p > 400$ nm and the edge mode for $p < 400$ nm separately in further detail in Secs. 8.2 and 8.3, respectively.

8.1.2 Plane wave method

The PWM has been adapted by Dr. Maciej Krawczyk and Dr. M.L. Sokolovskyy in Poznan, Poland[1] stimulated by the experimental data obtained in this thesis.

The PWM method, see Sec. 2.3.2, has been elaborated further by the Poznan group to calculate the eigenmodes of ADLs of different periodicity p. This is done to verify the findings obtained from experiments and micromagnetic simulations. First, it is instructive to consider the modes with zero precession amplitude within the holes, i.e. physical solutions, for $p = 300$ nm and various external field strengths in Fig. 7.20 (a) as solid red lines. Note that only symmetric modes are plotted in order to compare with AESWS [Gie05b]. The PWM results and the experimental data are in good agreement. For larger H, when the magnetic ground state in the ADL is more and more uniformly magnetized, the quantitative agreement is further improving. Spatial mode profiles calculated by PWM for modes i-ii [c.f. Fig. 8.3] agree well with micromagnetic simulations, see Figs. 7.21 (a) and (b), respectively.

Furthermore, the PWM is employed to elucidate the dependence of propagation characteristics on p. In Fig. 8.4, the frequency f_r of the rele-

---

[1]Surface Physics Division, Faculty of Physics, Adam Mickiewicz University, Umultowska 85, Poznań 61-614, Poland.
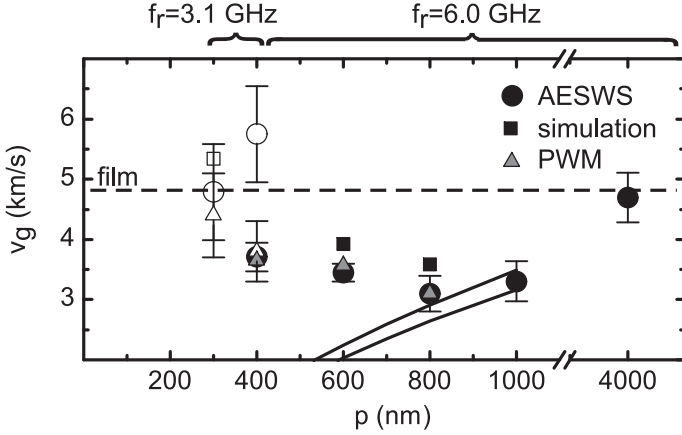
Figure 8.2: Group velocities v_g obtained for antidot lattices with various periodicity p and $d = 120$ nm. $\mu_0 H = 40$ mT. All ADLs are in a saturated state. η is chosen so that the field is aligned $1 - 2°$ off the high symmetry direction in order to avoid artifacts in the micromagnetic simulations. The plain film value is indicated as a horizontal dashed line. Full symbols mark data evaluated for the extended mode, see Fig. 7.18 (d) and open symbols mark data evaluated for the edge mode, see Fig. 7.21 (b). At $p = 400$ nm a transition occurs where both modes are found to propagate. Circles depict data obtained from AESWS. See Secs. 8.2 and 8.3. Samples with SW-transmission CPWs with $w_\mathrm{ic} = 2$ μm and $s = 12$ μm, i.e. $k_\mathrm{CPW} = 0.6 \times 10^4$ rad/cm are used. Triangles depict data obtained from the plane wave method for $k = 1.0 \times 10^4$ rad/cm, see Sec. 8.1.2. Squares mark data obtained from micromagnetic simulations for $k = 1.0 \times 10^4$ rad/cm. Local excitation of SWs is simulated and a subsequent 2d Fourier transformation yields the SW dispersion, see Fig. 8.12. From its slope v_g is evaluated. Full lines depict calculated v_g assuming quantization parallel to the field corresponding to an effective quantization width of $w_\mathrm{eff} = 600$ nm; $M_\mathrm{Sat} = 760$ kA/m, and $t_\mathrm{s} = 25$ nm (28 nm). This corresponds to the nanowire model depicted in Fig. 7.24 (a) and (c) as solid lines. Data for $p \geq 800$ nm is well described by this model. The transitions for $p = 400$ nm is due to onset dipolar coupling of the edge mode for smaller p. The large v_g for $p = 300$ nm are explained by the strong coupling through ferromagnetic material of large χ.

	$p = 120$ nm, $d = 87$ nm; $p = 200$ nm, $d = 120$ nm	300 nm $\leq p \leq 400$ nm, $d = 120$ nm	$p > 400$ nm, $d = 120$ nm
Edge mode	• Hybridized with extended mode. • No propagation experiment performed.	• Strong signal, coherent dipolar coupling (SW tunneling). • Large $v_\mathrm{g} \geq 5$ km/s resolved.	• Not resolved in experiment. Inhomogeneous line broadening assumed. $v_\mathrm{g} = 0$. • Present in simulation.
Extended mode	• Hybridized with edge mode. • No propagation experiment performed.	• Weak signal, $v_\mathrm{g} \approx 0$.	• Clearly resolved. • Propagating mode, $v_\mathrm{g} = 2 - 4$ km/s . • Described well by transversal quantized wire model.
Localized Mode	• Resolved, no propagation experiment performed.	• Resolved, not propagating. $v_\mathrm{g} = 0$.	• Resolved, not propagating. $v_\mathrm{g} = 0$.
Main investigated samples / techniques	SN61-3-3 (AESWS)	SN89-4-4 (AESWS, BLS)	SN88-1-A-M, SN83-1-LO (AESWS, BLS, MOKE)

Table 8.1: Overview over spin-wave mode behavior for antidot lattices of different periodicities p. Described is the behavior of the edge mode, the extended (fundamental) mode, and the localized mode.
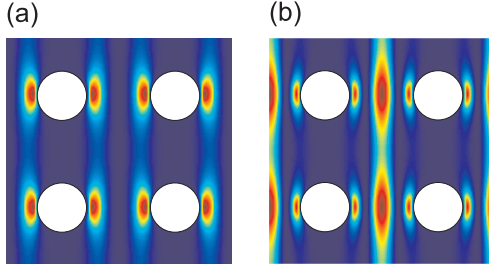
Figure 8.3: Spatial mode profiles for a $p = 300$ nm ADL obtained by plane wave method (PWM). Hole diameter 120 nm, $\mu_0 H = 40$ mT, $M_{\text{Sat}} = 860$ kA/m, exchange constant $A = 1.3 \times 10^{-11}$ J/m. (a) $f = 4.8$ GHz. Edge mode. (b) $f = 6.3$ GHz. Extended mode.
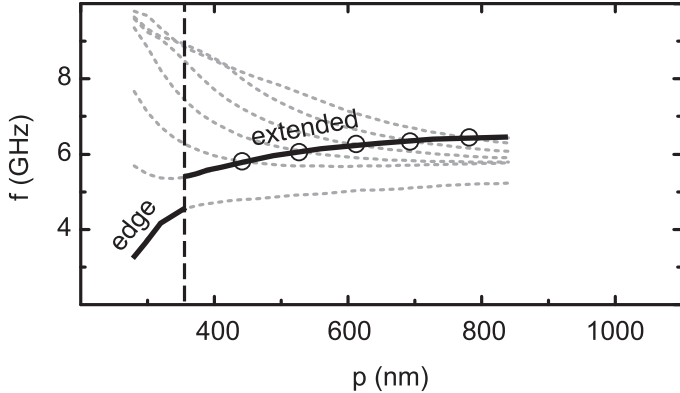
Figure 8.4: Resonance frequencies f_r for various p as obtained from the plane wave method (PWM) for $\eta = 0°$. $\mu_0 H = 40$ mT. The thick continuous lines mark the modes with largest v_g. At $p = 370$ nm a transition occurs. For $p < 370$ nm, the edge mode is found to propagate fastest, see Fig. 8.3 (a); for $p > 370$ nm, the extended mode is found to propagate fastest, see Fig. 8.3 (b). Circles indicate periodicities p for which mode hybridization with transversally quantized SWs is predicted. v_g obtained from this data is evaluated for $p = 300, 400, 600, 800$ nm and depicted as triangles in Fig. 8.2.

vant modes on the ADL periodicity p is plotted as obtained by the PWM. The thick solid lines marks the mode with highest v_g. For $p < 0.35$ μm, the edge mode (mode i) is found to propagate. At $p = 0.35$ μm, a transition occurs and for larger p, mode ii (extended mode) is found to propagate. This transition is in agreement with AESWS experiments, where the similar transition is observed for $p = 0.4$ μm, see Fig. 8.2. The extended mode hybridizes with transversally quantized modes for certain p highlighted by open circles in Fig. 8.4. This is not easily observed in experiment and out of the scope of this report. Therefore, v_g is extracted from PWM data only for certain values of p away from these points of hybridization. From the dispersion relation obtained from the PWM, v_g is calculated for $k = 1 \times 10^4$ rad/cm for $p = 0.3$, $p = 0.6$, and $p = 0.8$ μm. Results are depicted as triangles in Fig. 8.2 and are in good qualitative agreement with the simulation and the experimental data. However, calculated velocities have slightly larger values then experimental one. This discrepancy is mainly due to the angle η, assumed to be zero in the PWM calculations but ranging from $1°$ to $2°$ in the experiments depicted in Fig. 8.2. Note the good agreement between the $v_g = 5.8$ km/s obtained from PWM and maximum v_g obtained from AESWS as depicted in Fig. 8.10 (b) where $v_g \approx 6$ km/s.

8.2 Propagating Fundamental Mode

The extended mode shows propagation for $0° \leq \eta \leq 50°$. Both, v_g and τ exhibit an angular anisotropy which is stronger than in the plain film. Quantization of the extended mode parallel to the field is discussed.

For $p \geq 400$ nm the fundamental or extended mode is found to propagate through the antidot lattice. This mode originates from the plain film mode and is influenced by the antidot lattice via quantization parallel to the field (transverse to the propagation direction). This mode is found to propagate in a broad regime of parameters of the external field strength and alignment. The propagation characteristics are investigated.
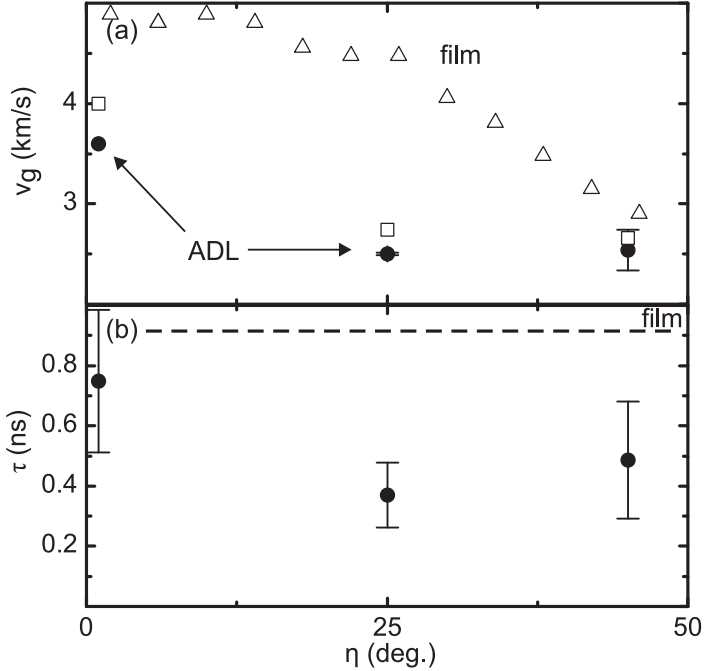
Figure 8.5: Propagation characteristics obtained for a $p = 800$ nm ADL at $\mu_0 H = 20$ mT using AESWS measurements [Neu10]. Sample is SN88-1-A-M with $w_{ic} = 2$ μm and $s = 6.5$ μm. Data is evaluated for $\eta = 0°, 25°$, and $45°$, according to regimes A-C (see text) and mode profiles depicted in Fig. 7.18 (d), (e), and (f), respectively. (a) Group velocity v_g. AESWS (BLS) data is depicted by full circles (open squares). Open triangles mark values obtained for a plain film sample (sample is KT003-5) obtained from AESWS measurements. (b) Relaxation time τ. For the $\eta = 45°$ AESWS data point, the propagation distance is assumed as $\sqrt{2}s$, see text. The horizontal dashed line is the plain film relaxation time τ, see Sec. 6.2.

8.2.1 Propagation anisotropy

The dependence of the SW group velocity v_g on η is discussed for the extended mode and $p = 800$ nm. This is along Ref. [Neu10] (copyright 2010, American Physical Society). It is instructive to analyze v_g only for three the angular regimes marked by circles in Fig. 7.10 (d), i.e. $\eta = 0° \pm 5°$ (regime A), $\eta = 25° \pm 5°$ (regime B), and $\eta = 40° \pm 5°$ (regime C). It is interesting that in angular regimes A and C SW propagation is observed between 4 and 5 GHz whereas in regime B this occurs at higher frequencies of about 6 to 7 GHz. One finds $v_g = 3.6$ km/s in regime A and $v_g = 2.5$ km/s in regimes B and C. When calculating v_g for $\eta = 45°$ via Eq. 3.2, it is considered that the SW propagation path between emitter and detector has increased by factor $\sqrt{2}$, because the propagating mode is found to extend diagonally through the lattice (perpendicular to the external field), see Fig. 7.18 (f). The values obtained for v_g from AESWS agree well with values obtained from BLS measurements [c.f. Fig. 7.24]. v_g data from AESWS (BLS) is plotted as full circles (open squares) in Fig. 8.5 (a). For small angles, the group velocities in the antidot lattice are considerably smaller than the values obtained on a plain film. For comparison in Fig. 8.5 values obtained on a plain film (KT-003-5) are depicted as open triangles. The angular dependent change of the propagation velocities v_g for the $p = 800$ nm ADL is more pronounced than in the plain film. It is, furthermore, larger than expected from the corresponding dispersion relations taking into account the frequency differences between modes A, B, and C via Eq. 2.77. Remarkably, near $\eta = 45°$, SWs experience the same velocity of about $v_g = 2.5$ km/s in, both, the antidot lattice and film.

Next, the relaxation τ of SWs in an ADL is determined according to Sec. 3.2.2. Figure 8.6 exemplarily shows fitted curves (solid lines) where τ of Eq. 3.3 is used as the free parameter to extract the relaxation characteristics of two different AESWS data sets at regimes A and B. It is instructive to recapitulate that for the unpatterned plain film one obtains a relaxation time of $\tau = 0.94 \pm 0.16$ ns which, in particular, does not depend on η [see Sec. 6.1 and Fig. 6.10]. For the antidot lattice one observes *angle-dependent* relaxation characteristics [full circles in Fig. 8.5(b)]. At $\eta = 0°$ (regime A) the effective relaxation time is 0.75 ± 0.2 ns, i.e., comparable with the plain film. A minimum relaxation time $\tau = 0.37 \pm 0.1$ ns is found at $\eta = 22°$ (regime B). If compared to regime A, the effective relaxation increases by a factor of almost two in regime B. A larger relaxation time
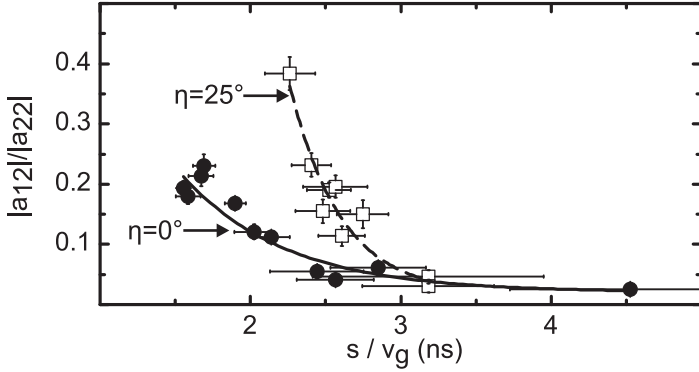
Figure 8.6: Transmission amplitude $|a_{12}|$ normalized on excitation amplitude $|a_{22}|$ obtained for $\eta = 0°$ (regime A, full circles, full line) and $\eta = 25°$ (regime B, open symbols, dashed line) on a $p = 800$ nm ADL [Neu10]. Sample SN88-1-A-M with $w_{ic} = 340$ nm and $s = 6.5$ μm. The lines are fits to the data using Eq. 3.3, i.e. exponential signal decay over time. Data points are obtained for various field $\mu_0 H > 15$ mT.

$\tau = 0.49 \pm 0.2$ ns is regained in regime C, but still the value is smaller than τ at $\eta = 0°$ and of the unpatterned film. The relaxation times vary with the characteristic mode profiles illustrated in Fig. 7.18 (d)-(f). In regime B the propagating mode has a higher oscillation amplitude near the edges of the holes if compared to regimes A and C. Near the hole edges, the internal field can vary due to edge roughness and reduced saturation magnetization through Gallium implantation by focussed ion beam etching. Via magnon-magnon scattering such irregularities can open further relaxation channels. This might explain the anisotropy of τ found in the angular dependent experiments. However a theory linking mode profiles and edge roughness with spin-wave relaxation is missing.

8.2.2 Effectively continuous dispersion and quantization

The transversal quantization in between neighboring holes parallel to the field is discussed for the extended mode. Content of this section has been

obtained in a collaboration between the Regensburg Group[1] (Prof. Christian Back, Hans Bauer, Dr. Georg Woltersdorf) and the author [Bau11]. In Fig. 8.7 the dispersion relation of a $p = 800$ nm ADL is depicted for $\mu_0 H = 20$ mT and $\eta = 1°$. The transferred wave vector k is orientated perpendicular to the field, i.e. $k \equiv k_\perp$. Data is obtained from MOKE measurements (full red squares), BLS measurements (full diamonds), and micromagnetic simulations (gray scale, where dark corresponds to large SW amplitude; simulation set A). The scale has been adapted to show features for small values of the wave vector, i.e. $0 \leq k \leq 2 \times 10^4$ rad/cm.

For $k \gtrsim 1 \times 10^4$ rad/cm it is found that the extended mode propagating through the $p = 800$ nm ADL is well described by a transversally quantized mode (extended mode ii), i.e. by

$$k_\parallel = n\pi/w_{\text{eff}}, \tag{8.2}$$

where the effective width of the wire $w_{\text{eff}} = 0.6$ μm. For $n = 1$, see full line in Fig. 7.24 ($f = 4$ GHz for $k = 0$). For $k \lesssim 1.5 \times 10^4$ rad/cm, however this wire mode does not agree well with the measured data (MOKE), depicted as full red squares in Fig. 8.7, and data obtained from micromagnetic simulations (grayscale). Instead, a *plain film* dispersion with reduced $M_{\text{Sat}}^\star = 600$ kA/m describes the data well (full red line).

Frequencies $f = 4.1, 4.4, 4.9$ GHz are the values of the intersection of the modes $k_\parallel = n\pi/w_{\text{eff}}$ with $n = 1...3$, depicted in Fig. 8.7 as black lines with the plain film dispersion of $M_{\text{Sat}}^\star = 600$ kA/m. Studying the spatial SW profiles obtained from micromagnetic simulations yields that for these frequencies the mode profiles change. The different mode profiles relate to higher transversal mode quantization, i.e. different values of n. See e.g. the transition for $n = 2$ ($f = 4.2$ GHz) to $n = 3$ ($f = 4.4$ GHz) as depicted in Fig. 8.8 (b) and (c).

It is interesting to test the influence of these mode transitions on the propagation properties. For this, $|a_{12}|$ spectra, obtained on $p = 800$ nm antidot lattices for $\mu_0 H = 20$ mT at $\eta = 0°$, are depicted in Fig. 8.9. Note the logarithmic scale. Samples are SN75-1-1 (thick dark line) , SN083-3 (thin light line), and SN88-1-A-M (thin dark line). Also depicted is data for sample SN75-4-4 (thick light line) where only a part $\xi = 12.5$ μm of the propagation distance s is structured to form a $p = 800$ nm ADL. The

---

[1]Institut für Experimentelle und Angewandte Physik, Universität Regensburg, D-93040 Regensburg, Germany
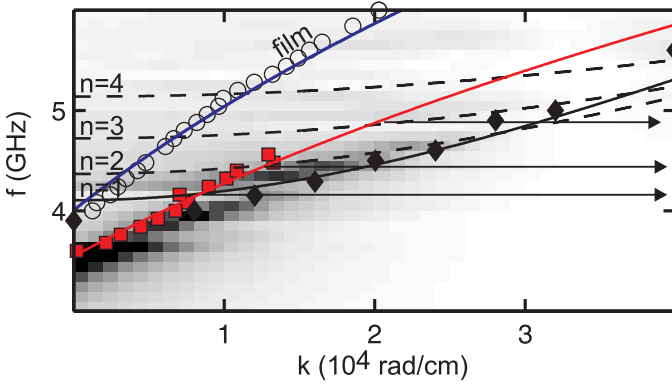
Figure 8.7: Spin-wave dispersion $f(k)$ obtained for $p = 800$ nm ADLs (full symbols, black and red lines, gray scale) and a reference plain film (open circles, full blue line) at $\mu_0 H = 20$ mT and $\eta = 1°$. Here the focus is on the regime of small k if compared to Fig. 7.24. Full red squares indicate data obtained by frequency and spatially resolved MOKE experiments [Bau11]. Full diamonds indicate data obtained from BLS measurements. The gray scale plot is obtained from micromagnetic simulation. Simulation parameters according to set A, where $M_{\mathrm{Sat}} = 760$ kA/m. Dark (light) colors correspond to large (small) SW amplitudes. The full red line corresponds to a plain film dispersion using an effective saturation magnetization of $M_{\mathrm{Sat}}^\star = 600$ kA/m. The full (dashed) black lines correspond to a calculated SW dispersion using a wire model, i.e. transverse quantization according to Eq. 8.2, with effective width of $w_{\mathrm{eff}} = 600$ nm and $n = 1$ $(2, 3, 4)$. Reference plain film: Open circles denote MOKE measurements obtained on a reference plain film [Bau11]. The full blue line corresponds to a plain film dispersion with $M_{\mathrm{Sat}} = 770$ kA/m, $t_{\mathrm{s}} = 25$ nm calculated according to Eq. 2.73.
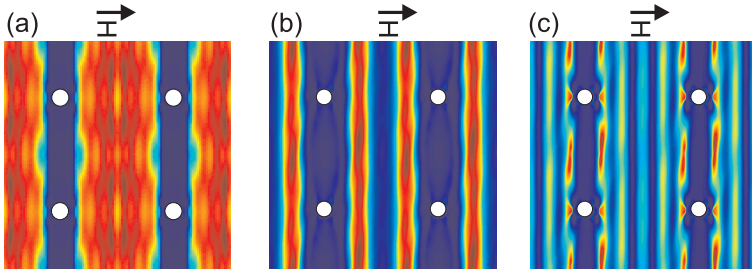
Figure 8.8: Simulation parameters according to parameter set C. Uniform pulsed excitation. $\mu_0 H = 20$ mT. $\eta = 1°$. Depicted is the extended mode which is quantized parallel to **H** by $n\pi/w_{\text{eff}}$. (a) $f = 3.7$ GHz. $n = 1$. (b) $f = 4.0$ GHz. $n = 2$. (c) $f = 4.5$ GHz. $n = 3$. The number of nodes is increasing in the direction transverse to the extended axis (parallel to the field). See also [Bau11].
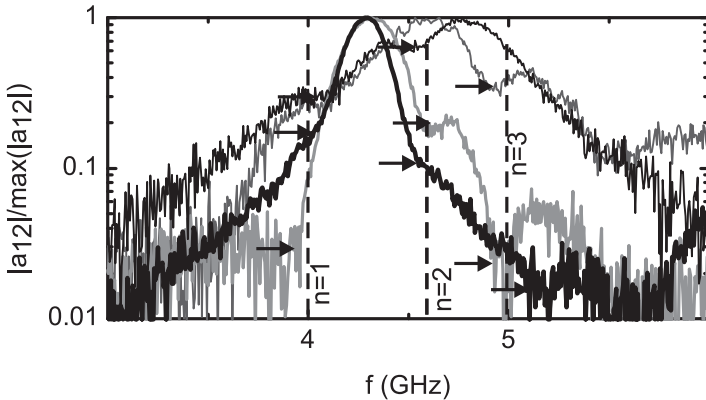
Figure 8.9: Normalized $|a_{12}|$ data obtained for $p = 800$ nm ADLs using different CPWs. $\mu_0 H = 20$ mT. $\eta = 0°$. Samples are SN75-1-1 with $w_{\text{ic}} = 4$ μm (thick dark line), SN75-4-4 with $w_{\text{ic}} = 4$ μm (thick light line), SN083-3-LO with $w_{\text{ic}} = 2$ μm (thin light line), and SN88-1-A-M $w_{\text{ic}} = 0.34$ μm (thin dark line). Vertical dashed lines indicate the transition of mode order. Horizontal arrows indicate the observed minima in the transmission for the various samples. Suppressed propagation is associated with a change in the transversal quantum number n, see Figs. 8.7 and 8.8.

integrated CPW is different from sample to sample, namely: $s = 19.5\ \mu$m, $w_{\text{ic}} = 4\ \mu$m (SN75-1-1,SN75-4-4), $s = 12\ \mu$m, $w_{\text{ic}} = 2\ \mu$m (SN083-3), and $s = 6.5\ \mu$m, $w_{\text{ic}} = 340$ nm (SN88-1-A-M). This results in a different excitation spectrum $\rho(k)$ and thus in a different measured signal, see Sec. 2.4.3. For decreasing w_{ic}, the frequency of maximum $|a_{12}|\ f_{\text{r}}$ shifts towards higher f. Nonetheless, for at least three of the four samples, a significant transmission suppression is resolved for $f = 4.0 \pm 0.1$ GHz, $f = 4.5 \pm 0.1$ GHz, and $f = 4.9 \pm 0.1$ GHz, as marked by the arrows and vertical dashed lines in Fig. 8.9.

These values of f coincide well with the values for which increasing transversal quantization is found from micromagnetic simulations and calculations as depicted in Fig. 8.7. For the transition points, increased SW decay is found. In a simple picture the different eigenmodes show avoided crossings for the discussed frequencies. Then the dispersion flattens and $v_{\text{g}} \approx 0$. This can explain the decreased signal measured in transmission for $|a_{12}|$.

8.3 Propagating Edge Mode

The edge mode is found to propagate only for precise alignment of the external field with the ADL primitive unit cell vectors, i.e. $-10° \leq \eta \leq 10°$. Dipolar coupling of the edge mode is interpreted as tight binding of the localized excitations. The strong angular anisotropy is explained by reduced dipolar coupling for misalignment of the field. Magnonic band formation is verified using Brillouin light scattering measurements and the plane wave method.

For $p \leq 400$ nm the edge mode is experimentally resolved and found to propagate with a large group velocity v_{g}. This behavior is unexpected from the dispersion Eq. 2.73 for a strongly confined mode. In Sec. 7.3 dipolar coupling was identified to dominate the propagation characteristics. Details are discussed in the following.

8.3.1 Propagation anisotropy

The dependence of the propagating edge mode on the angle η for $p = 0.3\ \mu$m is reported, see Fig. 8.10 (a). Symbols mark the resonance fre-

quency f_r for different η. A minimum of $f_r = 2.9$ GHz is found at $\eta = 1°$, i.e., $\eta \neq 0$. It marks the direction where H is collinear with the ADL unit cell edge. $\eta = 1°$ is thus attributed to the misalignment angle of the ADL with respect to the x axis, i.e. $\eta_{\text{lattice}} = 1°$, c.f. Fig. 3.3. Note that f_r varies significantly if η is changed by only $10°$. In particular $df_r/d\eta$ is much larger for the edge mode if compared to the extended mode at $p \geq 400$ nm, c.f. Figs. 7.10, 7.13.

The full circles in Fig. 8.10 (b) are for v_g of the edge mode for $p = 300$ nm. The largest v_g for $p = 0.3$ μm is observed at $\eta = 1°$ coincident with the minimum resonance frequency $f_r = 2.9$ GHz. It amounts to $v_g \approx 6.0$ km/s. The value strongly decreases when moving away from $\eta = 1°$, i.e., if H becomes misaligned with the ADL unit cell edge.

For $\mu_0 H = 40$ mT, the plain film propagation velocity is measured (calculated) to $v_g = 4.8$ km/s ($v_g = 4.4$ km/s) at a frequency of $f = 6.4$ GHz and $k = 1 \times 10^4$ rad/cm. Therefore, for precise alignment of external field, wave vector, and antidot lattice unit cell axis, the propagation velocity in the antidot lattice can be higher than in the plain film if compared for a given *field*. To compare at given *frequency*, one has to keep in mind that at $k = 1 \times 10^4$ rad/cm the minimum frequency for $\mu_0 H = 0$ mT amounts to $f = 2.87$ GHz. Here $v_g = 8.9$ km/ns. This is due to the inverse dependence of the plain film propagation velocity on the frequency, see Eq. 2.77.

The strong angular anisotropy of the group velocity v_g observed for $p = 0.3$ μm in Fig. 8.10 (b) is consistent with the dipolar coupling of edge modes as discussed above. Micromagnetic simulations are performed at a constant field $\mu_0 H = 40$ mT for various η. Results are depicted in Fig. 8.11. One finds that for $\eta \approx 10°$, the regions of large precession amplitude at neighboring holes do not overlap fully [Fig. 8.11 (a)] with decreasing overlap for increasing η [Fig. 8.11 (b) for $\eta = 15°$, and Fig. 8.11 (c) for $\eta = 20°$]. Dipolar coupling is significantly reduced and the edge modes do not support a propagating SW any longer, i.e., v_g is zero. This explains the strong anisotropy of v_g depicted in Fig. 8.10 (b). The angular anisotropy of v_g is much less pronounced in the plain film or for the ADL with $p = 0.8$ μm, see Fig. 8.5. The tunability from very large v_g to zero v_g is thus a unique feature of nanostructured ADLs originating from the coherent magnonic coupling of edge modes.
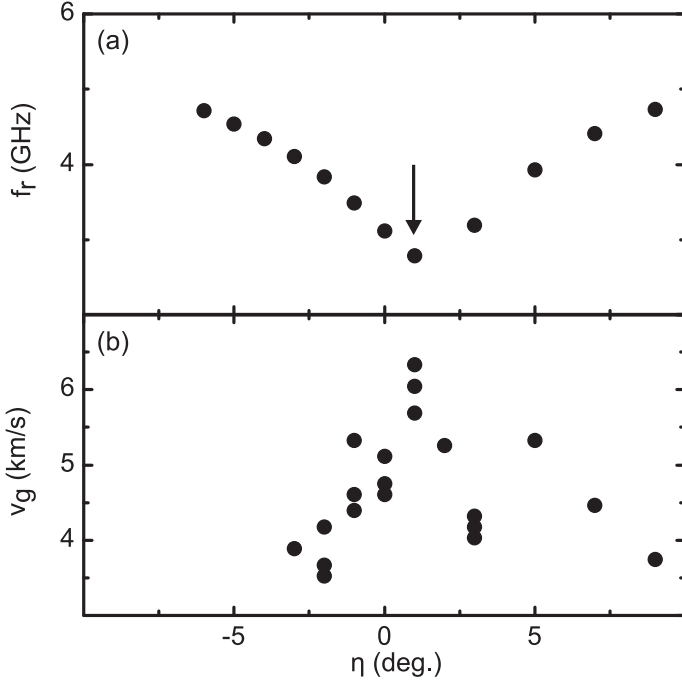
Figure 8.10: Properties of the edge mode in a $p = 300$ nm ADL for $-10° \leq \eta \leq 10°$ obtained from AESWS measurements at $\mu_0 H = 40$ mT. Sample is SN89-1-LO, $w_{ic} = 2$ μm and $s = 12$ μm. (a) Resonance frequency f_r. A pronounced minimum of f_r is observed for $\eta \approx 1°$ as marked by the vertical arrow. This angle is associated with the misalignment between CPW and ADL primitive lattice vectors, i.e. $\eta_{lattice} = 1°$, see Fig. 3.3. (b) Group velocities v_g. A maximum v_g is obtained for $\eta = 1°$, i.e. when **H** and ADL primitive lattice vectors enclose a $90°$ angle. $df_r/d\eta$ and $dv_g/d\eta$ are much larger than for the extended mode at a $p = 800$ nm ADL, c.f. Fig. 8.5.
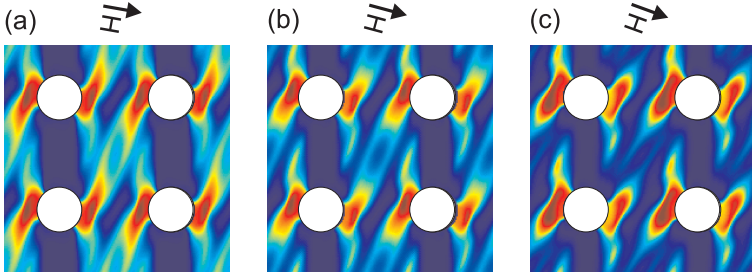
Figure 8.11: Micromagnetic simulation of spatial spin-wave profiles of a $p = 300$ nm antidot lattice for $\mu_0 H = 40$ mT and various η. Simulation parameters: set B. (a) $\eta = 10°$, $f = 4.0$ GHz. (b) $\eta = 15°$, $f = 4.4$ GHz. (c) $\eta = 20°$, $f = 4.6$ GHz. For increasing η from (a) to (c), the coupling between the edge modes is reduced. This motivates the strong dependence of v_g on η as observed in Fig. 8.10 (b).

8.3.2 Magnonic band formation

The coupling of the edge mode for $p < 0.4\ \mu$m, as described in Sec. 8.1 in detail, is consistent with a tight binding model [Sla54]: for large periodicities (large hole-to-hole separations) the edge modes are initially uncoupled and localized in the potential wells formed at the edges of the holes. For $p \leq 400$ nm, the edge modes are found to couple dynamically through the ferromagnetic material. However, resonant SW precession is only found close to the holes' edges.

For such an approach, periodicity of the SW dispersion $f(k)$ with respect to the Brillouin zone boundaries is expected. To test this, in Fig. 8.12 (a), both, wave vector resolved SW detection via BLS (open symbols) and micromagnetic simulations (gray scale plot) are used to explore the dispersion $f(k)$ for $p = 0.3\ \mu$m by experimental and theoretical means, respectively. Data is taken at $\mu_0 H = 60$ mT, where the wave vector resolved spectra exhibit a good signal-to-noise (SNR) ratio. Three different SW modes are resolved. They correspond to modes i-iii observed in Fig. 7.20 in ascending order for increasing f. Minimum frequency has mode i, the edge mode [c.f. Fig. 7.21 (a)], mode ii is the extended mode [c.f. Fig. 7.21 (b)], and mode iii corresponds to the mode localized in between neighboring holes [c.f. Fig. 7.21 (c)]. The resonance frequency f_r
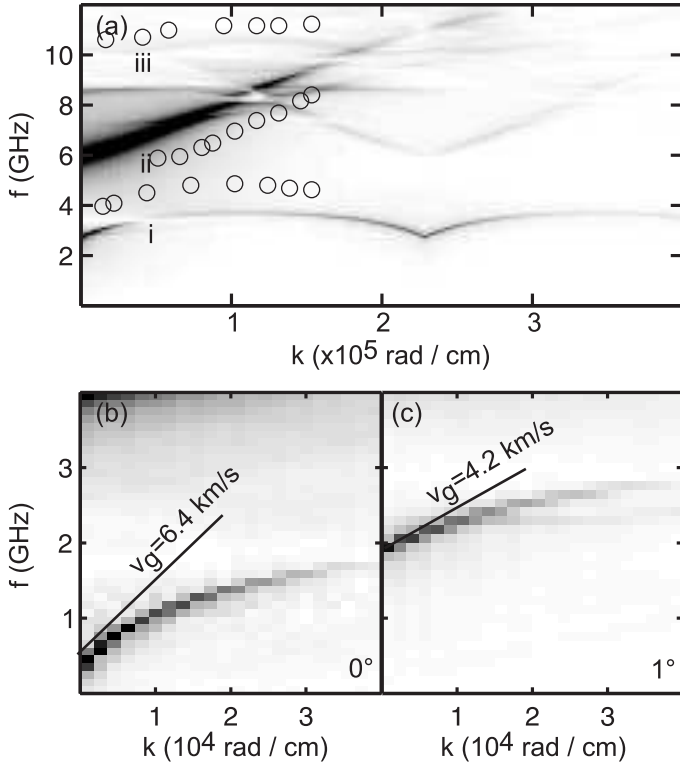
Figure 8.12: Spin-wave dispersion $f(k)$ for a $p = 300$ nm ADL. In (a) circles correspond to data obtained from BLS measurements and in (a)-(c), the gray scale plot corresponds to micromagnetic simulation (dark color correspond to large SW amplitudes). (a) Data obtained for $\mu_0 H = 60$ mT. Simulation is performed for $\eta = 1°$, BLS nominally aligned with the ADL high symmetry axis. Simulation parameters are according simulation parameter set A. SWs up to 50 GHz are excited by a short field pulse. (b) and (c) are micromagnetic simulation results for $\mu_0 H = 40$ mT and $\eta = 0°$ (b), $\eta = 1°$ (c). The dashed lines indicate group velocities extracted for small k from the simulation data, i.e. $v_g = 6.2$ km/s ($\eta = 0°$) and $v_g = 4.2$ km/s ($\eta = 1°$).

of the lowest-frequency branch (mode i, edge mode) varies characteristically as a function of k with a frequency maximum at $k \approx 1 \times 10^5$ rad/cm. Interestingly the Brillouin zone boundary of the ADL as defined by $k_{\mathrm{BZ}} = \pi/p = 1.05 \times 10^5$ rad/cm amounts to almost the same value. Beyond the Brillouin zone boundary, the frequency decreases again. This is consistent with a miniband. The slight difference of the simulated Brillouin zone (BZ) boundary of $\approx 5\,\%$ is not understood and most likely has its origin in the simulation unit cell discretization of 9.75 nm. The miniband bandwith is 0.6 GHz. Strikingly, in the BLS data, the higher-frequency branches do not exhibit such a behavior. In their case the measured frequency either grows continuously across k_{BZ} (extended mode ii) or remains constant beyond k_{BZ} (localized mode iii). The simulations displayed as a grayscale plot in Fig. 8.12 (a) remodel the observed miniband. A discrepancy remains in the absolute values of the resonance frequencies. This might be caused by two effects: firstly, η-dependent BLS data taken at $k = 0$ showed that it is not possible to exactly find $\eta = 1°$ due to the small SNR ratio. Secondly, mode i resides close to the hole edges and is influenced by their roughness which is not modeled [Neu08a].

It is possible to extract v_{g} from the data obtained from micromagnetic simulations. To compare with the other ADLs, see Fig. 8.2, this is done for $\mu_0 H = 40$ mT. For small k, $\mathrm{d}f/\mathrm{d}k$ becomes very large. Therefore, to obtain v_{g} from the simulations at $k = k_{\mathrm{CPW}}$ ($\mu_0 H = 40$ mT), it is necessary to plot the data at a different scale. This is done for $\eta = 0°$ and $\eta = 1°$ ($\mu_0 H = 40$ mT) in Fig. 8.12 (b) and (c), respectively. This particular sharp increase of v_{g} close to $k = 0$ is known to be a result of miniband formation in magnonic systems, see Fig. 2 in Ref. [Kos10]; it can thus be taken by itself as an indication for the observation of magnonic effects when relying on AESWS measurements with small k only. One finds $v_{\mathrm{g}} = 4.4$ km/s ($v_{\mathrm{g}} = 6.4$ km/s) for $\eta = 1°$ ($\eta = 0°$). The experimental values of $v_{\mathrm{g}} = 4.8$ km/s ($v_{\mathrm{g}} = 6.1$ km/s) measured at $\eta = 2°$ ($1°$) is in good agreement [c.f. Fig. 8.10].

Group velocities obtained in such a manner from micromagnetic simulations are summarized in Fig. 8.2 as squares which are taken at $\eta = 1°$ for p ranging between 0.3 and 0.8 μm. The experimentally observed values follow the simulated trend.

In Fig. 8.12 (a), experiments do show a MC band formation for the edge mode (mode i of Fig. 7.20 (b)), and only show a weak MC band formation for the extended mode (mode ii of Fig. 7.20 (b)). This is consistent with

the BLS measurements performed on a $p = 0.8$ μm lattice, see Fig. 7.24, where no band formation is observed for the extended mode. Interestingly, one can identify the coupling of edge modes with a tight binding approach [Sla54], while the extended mode originates from the undisturbed plain film mode and experiences some periodic modulation of the internal field [Blo29]. The weak periodicity of the dispersion of the extended mode compared to the edge mode is treated as an artefact due to the infinitely high signal to noise level in the simulations. Furthermore, BLS data and AESWS data (data not shown) show some interaction between the edge mode and the extended mode. Such interaction is a principally known effect [Dem10a] and is out of the scope of this thesis to be discussed in detail.

In experiments the extended mode shows no periodic modulation at the BZ boundary and only weak modulation in micromagnetic simulations. Differently, the edge mode shows periodic modulation. To understand the different behavior is the goal of the following Sec. 8.3.3.

8.3.3 Magnonic crystal classification

Figures of merit are introduced describing the prerequisites of magnonic band formation, i.e., sufficiently strong periodic modulation of the internal field, as well as sufficiently long coherence length of the propagating SW. It is found that fundamental mode (edge mode) shows weak (strong) modulation and short (long) relative coherence length, motivating the observed magnonic behavior.

The prerequisite for miniband formation is periodic patterning, i.e., periodic modulation of the magnetic properties. For the two modes propagating through the periodically patterned antidot lattice, i.e. edge mode and extended mode, the patterning is found to have a different influence on the dispersion: magnonic band formation is observed for the edge mode at $p = 300$ nm, c.f. Fig. 8.12. For the fundamental mode at $p = 800$ nm, no magnonic band formation is observed, c.f. Fig. 7.24.

To understand this finding, to classify the studied ADLs, and to compare them with previous work on MCs, the magnetic contrast ϱ and the relative coherence length l_c are used as figures of merit.
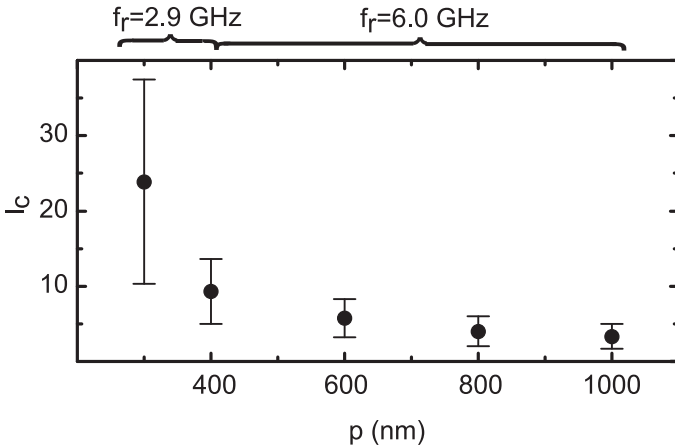
Figure 8.13: Relative coherence length $l_c = v_g \tau / p$ as obtained from AESWS measurements for $\eta = 1°$ for various ADL periodicities p at $\mu_0 H = 40$ mT. For $p = 300$ nm the edge mode is evaluated, for $p \geq 400$ nm the extended mode.

Coherence length

First, it has been argued that a miniband of large bandwidth is established only if the spin precession in a large number of neighboring unit cells couples coherently. This number is quantified by the relative coherence length [Kos10]

$$l_c = v_g \tau / p. \tag{8.3}$$

The relaxation time τ is measured by AESWS as described in Sec. 3.2.2. Using Eq. 8.3, the parameter l_c is calculated for the different ADLs. The results are shown in Fig. 8.13 as a function of p. For $p = 0.3$ μm and $v_g(k_{CPW})$, one finds $l_c = 24 \pm 13$ ($f = 3.1$ GHz, edge mode). For $p > 0.3$ μm, the extended mode ($f = 6$ GHz) propagates and l_c significantly reduces for increasing p. At $p = 0.8$ μm it amounts to $l_c = 4 \pm 2$. See Tab. 8.2.

Next, these results are compared to former work on 1D MCs. Considering arrays of stray-field coupled nanowires from Ref. [Kos10], a coherence length $l_c \approx 10$ is needed to form minibands (see Fig. 3 of Ref. [Kos10]). In Ref. [Kos08b] $l_c = 2$ and in Ref. [Top10] $l_c = 6$. From this it appears rea-

sonable that the edge mode is found to show magnonic band formation. To understand why this is not the case for the extended mode at $p = 800$ nm, one has to consider the magnetic contrast ϱ.

Magnetic contrast

Second, it has been argued that a large bandwidth (and thus a large $v_g = 2\pi\partial f/\partial k$) is obtained if the peak-to-peak amplitude of the periodic modulation is large. The magnetic contrast ϱ shall be defined by the amplitude of magnetic parameter variation normalized on the reference value.

In literature, different cases are present. For isolated magnetic elements [Kos04, Gub07], the magnetic parameters saturation magnetization M_{Sat} and exchange stiffness A vary between extreme values, i.e. for permalloy elements $M_{\mathrm{Sat},1} = 0$ in air and $M_{\mathrm{Sat},1} \approx 800$ kA/m in the magnetic material. Therefore

$$\varrho = \frac{M_{\mathrm{Sat},1} - M_{\mathrm{Sat},2}}{M_{\mathrm{Sat},1}} = 1.$$

Differently, in Refs. [Kru06, Kra08, Wan09] an alternating sequence of two different magnetic materials has been considered in close vicinity. Here

$$\varrho = \frac{M_{\mathrm{Sat},1} - M_{\mathrm{Sat},2}}{M_{\mathrm{Sat},1}} < 1.$$

In Ref. [Kra08], a strong band formation is observed for $M_{\mathrm{Sat},1}/M_{\mathrm{Sat},2} = 8$, i.e. $\varrho = 0.9$. In Ref. [Wan09], an alternating array of stripes made from Py and Co is used. The values of saturation magnetization are $M_{\mathrm{Sat},1} = 1.15 \times 10^3$ kA/m and $M_{\mathrm{Sat},2} = 0.658 \times 10^3$ kA/m, i.e. $\varrho = 0.43$.

In the present case, the magnetic contrast ϱ is quantified via the amplitude of the demagnetization field ΔH_{D} normalized to the effective field, i.e. by

$$\varrho = \frac{\Delta H_{\mathrm{D}}}{\mu_0 H + H_{\mathrm{D}}}. \tag{8.4}$$

The magnitude of modulation is found to be $\Delta H_{\mathrm{D}} = 0.1$ mT for $p = 0.8\,\mu\mathrm{m}$ (extended mode ii) [c.f. Fig. 7.6 (d), dark line] and three orders of magnitude stronger for $p = 0.3\,\mu\mathrm{m}$ (edge mode i), i.e. $\Delta H_{\mathrm{D}} = 80$ mT [c.f. Fig. 7.6 (d), light line]. This originates from a much weaker modulation of the internal field in regions away from the holes' edges, where the

period p	0.3 μm	0.6 μm	0.8 μm
	Edge mode	Extended mode	Extended mode
$f_{\rm r}$ (GHz)	3.1	6.0	6.0
τ (ns)	1.5 ± 0.6	1.0 ± 0.4	1.0 ± 0.4
$v_{\rm g}$ (km/s)	4.8	3.5	3.2
l_c	24 ± 13	6 ± 3	4 ± 2
ϱl_c	6.6	1×10^{-2}	$< 1 \times 10^{-2}$

Table 8.2: Parameters of different ADLs. $f_{\rm r}$ denotes the resonance frequency ($\mu_0 H = 40$ mT) of the propagating mode for which the relaxation time τ, magnetic contrast ϱ and coherence length l_c are evaluated.

extended mode [c.f. Fig. 7.18 (d)] resides. At $\mu_0 H = 40$ mT, one obtains for the extended mode ($p = 0.8$ μm) $\varrho = 0.1$ mT$/40$ mT $= 2.5 \times 10^{-3}$. For the edge mode at $p = 0.3$ μm, one obtains a value for the magnetic contrast amounting to $\varrho = 40$ mT$/ (80$ mT $+ 40$ mT$) = 0.3$.

The product ϱl_c, which measures the combined effect of the two parameters, varies by two orders of magnitude, see Tab. 8.2. The smaller this value, the less likely is the formation of a coherent magnonic effect such as a miniband. This weak modulation of the internal field in regions away from the edges explains why the magnonic band formation is not observed at $p = 0.3$ μm using BLS for the extended mode ii, see Fig. 8.12 (a).

Chumak *et al.* have used a periodic modulation of the internal field along a longitudinally magnetized magnetic wire with magnetic contrast $\varrho = 1$ mT$/160$ mT $\approx 6 \times 10^{-3}$ [Chu09a]. They observe the formation of a forbidden frequency gap. In the yttrium-iron-garnet $v_{\rm g}$ equals 26 km/s. Using $\tau \approx 500$ ns, one calculates $l_c = 43$ and $\varrho l_c = 0.26$.

For arrays of stripes with alternating material [Wan09, Wan10], one finds that group velocities were up to 4 km/s at $\mu_0 H = 0$ mT (extracted from Fig. 2 (a) of Ref. [Wan10] at $k \approx 1.2 \times 10^5$ rad/cm). With $\varrho = 0.4$ (see above), $p = 500$ nm, and $\tau \approx 1.0$ ns, one obtains $\varrho l_c = 3.2$.

For the $p = 0.3$ μm ADL studied here, the parameters $l_c = 24 \pm 14$ and $\varrho l_c = 6.6$ are even larger. The observation of a miniband thus seems to be consistent with these earlier works on 1D MCs. The parameter ϱl_c might prove to be helpful for MC classification as a figure of merit.

8.4 SW Injection into an Antidot Lattice: Metamaterial Limit

Spin-wave injection into an antidot lattice from a plain film is studied. It is found that for large periods and small wave vectors, transmission across the boundary is well described by the wave vector mismatch calculated for two continuous materials. The ADL acts as a metamaterial for SWs. Content of this section has been obtained in a collaboration between the Regensburg Group[1] (Prof. Christian Back, Hans Bauer, Dr. Georg Woltersdorf) and the author [Bau11].

For electromagnetic waves it is known that a structure much smaller than the incident wave length changes the propagation properties; effective and continuous properties can describe the effect of this so-called metamaterial (MM) [She01]. In particular, it is interesting to study the transmission of electromagnetic waves across the boundary from a conventional into a MM [Pen00]. In the following sections, it is shown that effectively continuous properties describe well the transmission into an ADL.

8.4.1 Calculation for effectively continuous films

The dispersion relation for SWs with wave vector $k \leq 1.5 \times 10^4 \,\mathrm{rad/cm}$ propagating through a $p = 800$ nm ADL is well described by a dispersion assuming a reduced, effective saturation magnetization $M_{\mathrm{Sat}}^{\star} = 600 \,\mathrm{kA/m}$, see Sec. 8.2 and Fig. 8.7 red line. As the wave length λ_{SW} is much larger than the ADL period p, this regime is labeled long wavelength limit (LWL). Stimulated by this phenomenological finding, it is instructive to make a gedankenexperiment. Imagine one calculates the transmission ψ of SWs of frequency f from one continuous media (M_{Sat1}, $k_1(f)$) into another continuous media (M_{Sat2}, $k_2(f)$) via the well known formula [Nol05]

$$\psi = \frac{2k_2}{k_1 + k_2}, \tag{8.5}$$

For the $p = 800$ nm ADL, the coefficient ψ is predicted to depend on f as shown in in Fig. 8.14 by the solid line. Here it is assumed that

---

[1]Institut für Experimentelle und Angewandte Physik, Universität Regensburg, D-93040 Regensburg, Germany
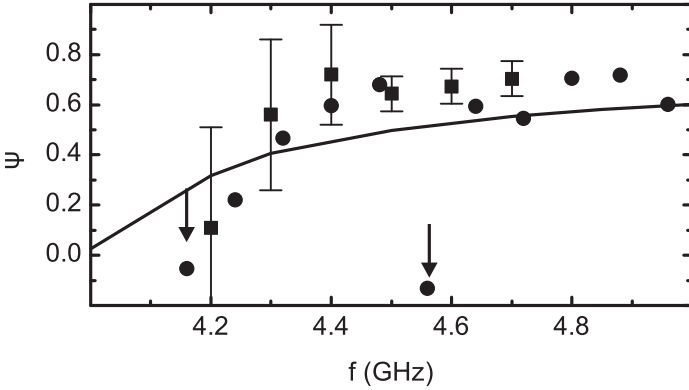
Figure 8.14: Transmission ψ obtained at $\mu_0 H = 20$ mT, $\eta = 0°$ for $4 \leq f \leq 5$ GHz from MOKE experiments (full circles) [Bau11] and micromagnetic simulations (full squares) for SW propagation from a plain film into a $p = 800$ nm ADL. Data is obtained by analyzing the SW interference between initial and back reflected SW, see text. Vertical arrows mark data points where $\psi < 0$, which is a result of the data evaluation. The full line marks the calculated ψ based on two plain film dispersions ($M_{\mathrm{Sat1}} = 770$ kA/m, $M_{\mathrm{Sat2}} = 600$ kA/m) and Eq. 8.5.

$M_{\mathrm{Sat1}} = 770$ kA/m and $M_{\mathrm{Sat2}} = M_{\mathrm{Sat}}^{\star} = 600$ kA/m for the film and ADL, respectively. This corresponds to the full blue and red lines in Fig. 8.7.

Next, transmission ψ is studied experimentally. As propagation parameters, i.e. group velocities v_{g} and relaxation times τ, are considerably different in the plain film and the ADL, see Sec. 8.2, transmission cannot be obtained from experiments by previously published methods [Sch10]. Based on all-electrical spin-wave spectroscopy (AESWS), see Sec. 3.2.2, and time and spatially resolved magneto-optical Kerr effect (MOKE) techniques, see Sec. 3.2.3, two new methods are presented to quantify transmission and reflection in this thesis.

8.4.2 MOKE transmission experiments

It is possible to measure the transmission ψ via MOKE. For this a sample is prepared, where only part of the plain film away from underneath the

standard CPW, see Sec. 3.1.2, is structured into an ADL. The inner conductor width is $w_{ic} = 4$ μm. This value ensures excitation of SWs in the LWL. Sample is SN87-4. SWs, which are transmitted from the emitter, need to enter the ADL from the plain film. A fraction r of the SW amplitude is back reflected at the boundary into the plain film. In a continuously driven (cw) experiment of fixed f, this reflected SW interferes with the incident SW. Maxima and minima are formed in between the CPW and the ADL boundary. Using MOKE, such amplitude oscillations are resolved. A spatio-frequency plot of the MOKE experiments is depicted in Fig. 8.15 (a). Black and white corresponds to a large value of $|\Re m_z|$. From two measurements with $90°$ phase shift between the driving microwave and the measured signal, the amplitude $|m_z|$ is derived. $|m_z|$ is depicted for $f = 4.48$ GHz in Fig. 8.15 (b) (dark full line).

The incident and reflected spin waves interfere. This is visible as an interference pattern in $|m_z|$. In the following, an expression for $|m_z|$ is derived which will allow to determine the reflection r from the experimental data. The out-of-plane precession of the initial wave is described by

$$m_z^i = a_{in} \exp(-iky) \exp(i\omega t). \tag{8.6}$$

The out-of-plane precession of the reflected wave is described by

$$m_z^{ii} = a_{out} \exp(ik(y - y_0)) \exp(i(\omega t + T')), \tag{8.7}$$

where T' is a phase shift and y_0 is the position of the boundary. a_{in} and a_{out} mark the incident and reflected SW amplitudes at the emitter site and at the boundary site, respectively. The reflection r is given by the relative strengths of amplitudes at the interface y_0, i.e.

$$r = \frac{a_{out}}{a_{in} \exp(-\zeta y_0)}, \tag{8.8}$$

where $\zeta = \Im k$, i.e. $\zeta \equiv \zeta_{film}$ is the spatial decay constant of the plain film. The transmission ψ

$$\psi = 1 - r. \tag{8.9}$$

The total amplitude $|m_z|$ is given by a superposition of the incident and reflected wave, i.e. by

$$|m_z| = |m_z^i + m_z^{ii}|. \tag{8.10}$$

One can calculate $|m_z|$ via substitution of a_{out} by r and a_{in}. It is then possible to neglect a term $\propto r^2$ and to use the Taylor approximation $\sqrt{1+x} \approx 1 + x/2$. Then $|m_z|$ is given by

$$\begin{aligned} |m_z| &= a_{in} \exp\left(-\zeta_{film}y\right) + a_{out} \exp\left(\zeta_{film}(y - y_0)\right) \times \quad (8.11) \\ &\times \cos\left(k(2y - y_0) + T'\right). \end{aligned}$$

The cosine term describes the interference of both SWs. Eq. 8.11 is fitted to the MOKE data, as exemplarily shown in Fig. 8.15 (b) as the light full line. One obtains $\zeta_{film} = 0.1 \ \mu m^{-1}$ in good agreement with Sec. 6.2. Values obtained for ψ at different f by this method are plotted in Fig. 8.14 as full circles. With the exception of the $f = 4.15$ and 4.55 GHz data points (marked by vertical arrows), they compare very well with the solid curve obtained for the transmission of SWs between two *continuous* films with $M_{Sat}^\star = 600$ kA/m and $M_{Sat} = 770$ kA/m obtained via Eq. 8.5. The exceptionally low values of ψ for $f = 4.15$ and 4.55 GHz can be associated with the frequencies where the transversal quantization of the SW modes in the ADL changes, see Sec. 8.2. Here, both, propagation as well as transmission characteristics are altered.

8.4.3 AESWS transmission experiments

AESWS measurements are performed on a sample partially structured into a $p = 800$ nm ADL. A $w_{ic} = 4 \ \mu m$ SW-transmission CPW, see Sec. 3.1.2, is used. This is done to ensure excitation of SWs in the LWL. Due to the large extents of the CPW, the propagation distance s between SW emitter and detector is $s = 19.5 \ \mu m$. This design offers a optimum performance considering two opposing trends: larger CPWs decrease the excited wave vector range (and address the LWL), however the propagation path s is increased until ultimately no signal can be detected. Only a part ξ of the propagation distances s is structured into an ADL, namely $\xi = 10.7 \ \mu m$, see Fig. 3.3. The sample is SN75-4-4, see Fig. 8.16.

The AESWS signal is depicted in Fig. 8.17. Here a_{11} resembles the signal obtained on a $p = 800$ nm ADL, while a_{22} is a plain film signal. For comparison see Figs. 7.10 (a) and Fig. 6.3 (b). As expected from the calculated sensitivity, see Eq. 2.105 and Fig. 5.5, the reflection signals practically only contain signal contributions obtained from the regions under-
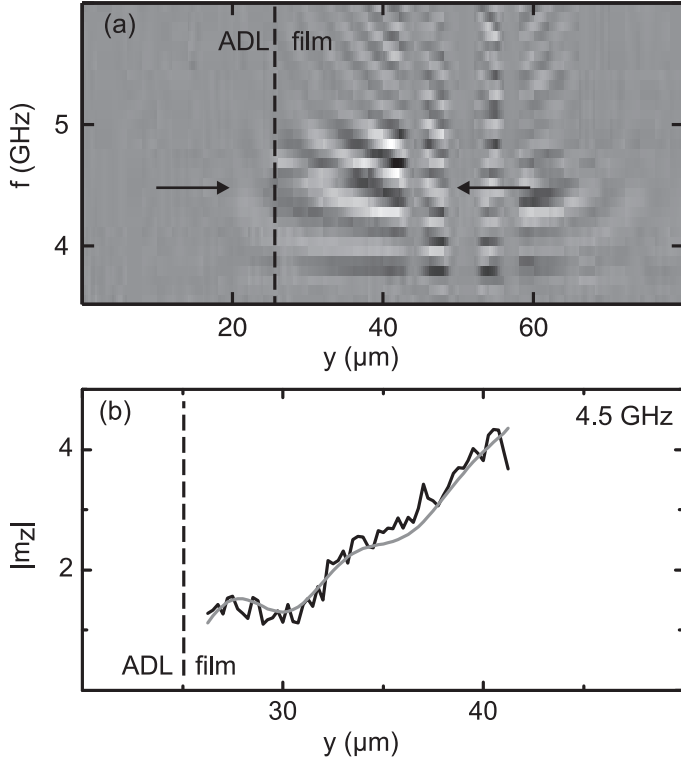
Figure 8.15: Spatio-frequency map of SW transmission from a plain film into an ADL obtained from MOKE experiments at $\mu_0 H = 20$ mT and $\eta = 0°$ [Bau11]. Sample is SN087-4. Depicted is $\Re m_z$, where dark (bright) colors correspond to large (small) values. The ADL - film boundary is located at $y = 25$ μm as marked by the vertical dashed line and the standard CPW is at $42 \leq y \leq 58$ μm. For $25 \leq y \leq 42$ μm, interference between incident and backreflected SWs is observed. Horizontal arrows mark the regime for which in (b) the signal amplitude $|m_z|$ (MOKE data depicted as dark curve) is analyzed further ($f = 4.5$ GHz). The light gray line is a fit to the data using Eq. 8.11. From this a transmission of $\psi = 0.68$ is evaluated as plotted in Fig. 8.14.
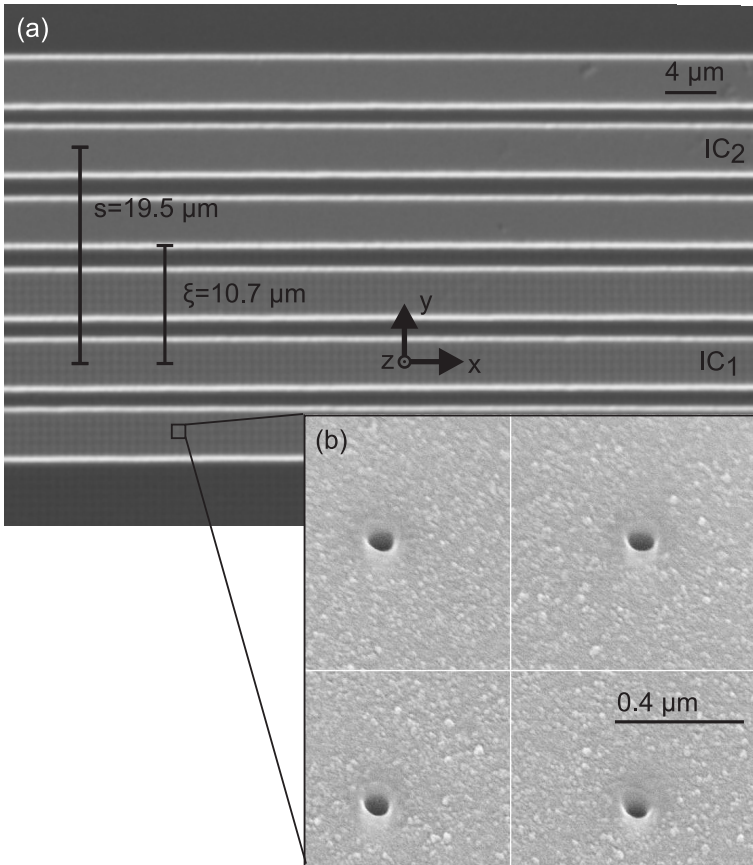
Figure 8.16: (a) Optical micrograph of a sample (SN75-4-4) for transmission measurements from a plain film into a $p = 800$ nm ADL. The Py mesa underneath the CPW is partly structured by focussed ion beam lithography to form an ADL. The structured distance is $\xi = 10.7$ μm, measured from the center of IC_1, see Fig. 3.3. The ADL is slightly visible as a checkerboard pattern. (b) SEM image of the antidot lattice. Hole diameter is 120 nm. Visible are the grains of the Py.
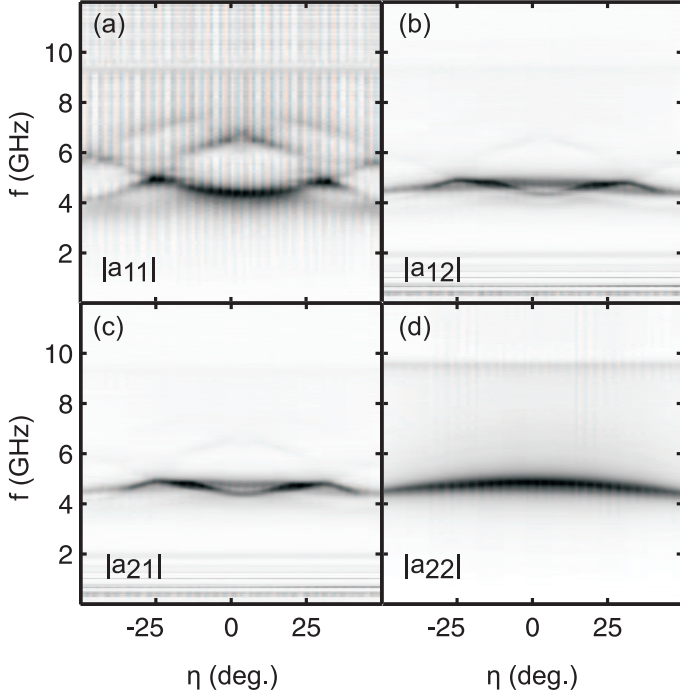
Figure 8.17: AESWS data obtained for a sample partially structured into a $p = 800$ nm antidot lattice for various angles η at $\mu_0 H = 20$ mT. Sample SN75-4-4. Dark colors correspond to large SW amplitude. The CPW is a SW-transmission CPW with $w_{ic} = 4$ μm and $s = 19.5$ μm. The transmission path $s = 19.5$ μm is structured only for a distance $\xi = 10.7$ μm to form an ADL, extending from CPW 1 [c.f. Fig. 8.16]. Signal amplitudes (a) $|a_{11}|$. (b) $|a_{12}|$. (c) $|a_{21}|$. (d) $|a_{22}|$. The spectra a_{11} and a_{22} correspond to reflection data obtained in the ADL and plain film, respectively. a_{12} (a_{21}) corresponds to transmission from the film into the ADL (vice versa).
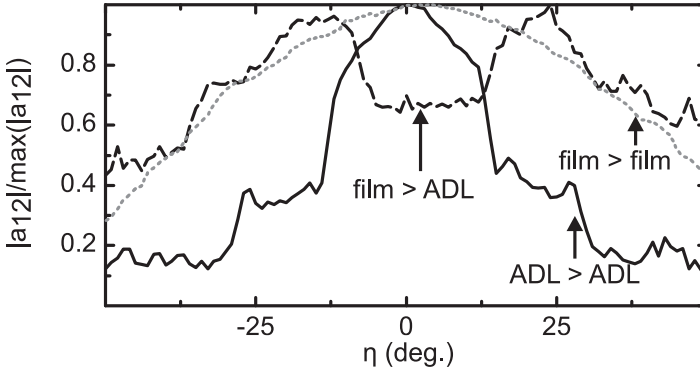
Figure 8.18: Normalized transmission amplitudes $|a_{12}|/\max(a_{12})$ obtained from AESWS measurements on various samples for $\mu_0 H = 20$ mT. Full line: signal obtained for a_{12} on sample SN75-4-4 only partially structured to form a $p = 800$ nm ADL ($\xi = 10.7$ μm). Signal corresponds to SW injection from the film into the ADL. Dashed line: Signal obtained on a $p = 800$ nm ADL a_{12}. Sample SN83-1-LO. Light dotted line: Signal obtained on a plain film a_{12}. Sample SN89-4-D. The ADL sample and the plain film sample both show maximum amplitude $|a_{12}|$ for $\eta = 0°$. Differently, the partially structured sample shows maximum amplitude $|a_{12}|$ for $10° \leq \eta \leq 20°$.

neath the respective inner conductors which only comprise ADL or plain film.

In Fig. 8.18, the normalized $|a_{12}|$ evaluated at f_r is depicted as a function of η for SWs propagating from the film into the ADL (solid line). From this data one finds that $|a_{12}|(f_r)$ exhibits a maximum value for $10° \leq \eta \leq 20°$. This is an intriguing finding, because the two constituents of this hybrid sample, namely a plain film and a sample fully structured into a $p = 800$ nm ADL, both show maximum $|a_{12}|(f_r)$ for $\eta = 0°$. This is depicted as the light dotted and full line, respectively. Therefore, the transmission SW signal shows properties which cannot simply be explained by a superposition of the two constituent materials. In order to understand this finding, AESWS experiments are performed that allow to determine the transmission ψ as a function of the angle η.

First, to obtain reference values for SWs propagating only through a

$p = 800$ nm antidot lattice (plain film), a sample which only comprise an ADL (plain film) is investigated. In particular, samples with identical CPW layout are chosen, i.e. $w_{\mathrm{ic}} = 4$ μm and $s = 19$ μm to leave the excitation spectrum $\rho(k)$ unaltered. The spin-wave excitation (detection) strength is given by a_{22}, the signal amplitude measured in reflection. a_{12} denotes the signal amplitude in transmission. Using Eq. 3.3 and Eq. 2.69, they relate by

$$a_{12}^{\mathrm{film}}/a_{22}^{\mathrm{film}} = \exp\left(-s \times \zeta_{\mathrm{film}}\right), \tag{8.12}$$

and accordingly for the ADL sample (with ζ_{lattice} instead). Eq. 8.12 is used to determine ζ_{film} and ζ_{lattice}, respectively. $\mu_0 H = 20$ mT and $\eta = 0°$. Samples are GD106-1-1 for the plain film and SN75-1-1 for the ADL (both: $w_{\mathrm{ic}} = 4$ μm, $s = 19.5$ μm). Data is not shown. For $\eta = 0°$, one finds $\zeta_{\mathrm{film}} = 0.12 \pm 0.02$ μm^{-1} in good agreement with MOKE data, and $\zeta_{\mathrm{lattice}} = 0.15 \pm 0.02$ μm^{-1}. This compares well with AESWS data of $\tau \approx 0.9$ ns [c.f.Fig. 6.9] and $v_{\mathrm{g}} \approx 7$ km/s for $\mu_0 H = 20$ mT [c.f. Fig. 6.7], and via Eq. 2.69, $\zeta_{\mathrm{film}} = 0.16$ μm^{-1}.

The amplitude a_{12} in the hybrid sample is

$$a_{12}/a_{22} = \psi \exp\left(-(s - \xi)\zeta_{\mathrm{film}}\right) \exp\left(-\xi\zeta_{\mathrm{lattice}}\right) \tag{8.13}$$

By evaluating Eqs. 8.12 and 8.13 to obtain the transmission ψ, one attributes for different spatial SW decay lengths ζ in the antidot lattice and the plain film; this goes beyond, e.g., Ref. [Sch10]. However, in this method, measurements on three different samples enter. The accuracy is limited and applicability is found to be restricted to the case of large amplitude throughout the samples; this is only the case for the frequency of maximum amplitude in the ADL measurements, i.e. f_{r} corresponding to maximum a_{11}, i.e. maximum amplitude in the ADL marked by full squares in Fig. 8.19 (a). For $\eta = 0°$ and $f = 4.4$ GHz, one obtains a value of $\psi = 0.5 \pm 0.1$ in good agreement with MOKE results.

AESWS data obtained for ψ for various η is depicted in Fig. 8.19 (b) as full circles. This dependence of the transmission ψ on the angle η is discussed. This is in particular interesting in the light of the unexpected behavior of the maximum amplitude $a_{12}(f_{\mathrm{r}})$ found from AESWS measurements in Fig. 8.18 showing a maximum value at $\eta = 25°$. Due to lower group velocities v_{g} for $\eta > 0°$, f resolved determination of ψ is not possible using MOKE. The study is restricted to AESWS data.

While for $\eta < 10°$ ψ remains constant at $\psi \approx 0.6$, there is a sudden increase to $\psi \approx 0.9$ around $\eta = 10°$. A motivation can be found from studying the dependence of f_r for the ADL and the plain film on η. For $10° \lesssim \eta \lesssim 30°$, frequencies f_r in the antidot lattice and in the plain film are almost degenerate [c.f. Fig. 8.19 (a), full circles and full squares]; even without exact knowledge of SW dispersion in this regime, it is possible conclude that $k_1 \approx k_2$ in Eq. 8.5 and the expected $\psi \approx 1$. The increase in ψ measured for $\eta > 10°$ is accompanied by a strong increase of the transmission signal amplitude $|a_{21}|$, see full line in Fig. 8.19 (b).

The unexpected dependence of $|a_{21}|$ on η therefore is found to have its origin in the angular dependence of the transmission ψ. Because for $\eta \approx 25°$, the eigenfrequencies of the SW modes in the ADL and in the plain film are degenerate, the wave vector mismatch determining ψ is minimized. A large value of ψ is accompanied by a large value of $|a_{12}|$.

8.4.4 Micromagnetic simulations of transmission

To further validate data obtained from MOKE and AESWS for the transmission ψ and to provide a microscopic insight, it is instructive to perform spatially resolved micromagnetic simulations. Simulations are performed, both, temporally resolved or frequency resolved, see Sec. 2.3.3.

For micromagnetic simulations, simulation set A is used. This corresponds to 1×85 ADL unit cells. Field pulse amplitude is $0.2\ \mathrm{mT}$ and the pulse extends $2\ \mu\mathrm{m}$ in y direction. In temporally resolved simulations, a short field pulse excites SWs up to $50\ \mathrm{GHz}$. In frequency resolved simulations, cw excitation of a single frequency is employed. The robustness of results obtained from micromagnetic simulations is tested by varying $760 \leq M_{\mathrm{Sat}} \leq 860\ \mathrm{kA/m}$, the film thickness between $t_s = 22\ \mathrm{nm}$ and $t_s = 28\ \mathrm{nm}$, and the hole diameter $d = 120 - 220\ \mathrm{nm}$. No significant changes in the transmission and / or mode profiles is observed and respective sensitivity is included the $\approx 5\%$ variation in the error bars of Fig. 8.14.

Time resolved micromagnetic simulations

It is instructive to begin analysis with micromagnetic simulations employing a short field pulse. The spatio-temporal plot corresponding to this simulation is plotted in Fig. 8.20 (a). Plotted is the dynamic out-of-plane precession amplitude m_z, where dark (bright) corresponds to large positive
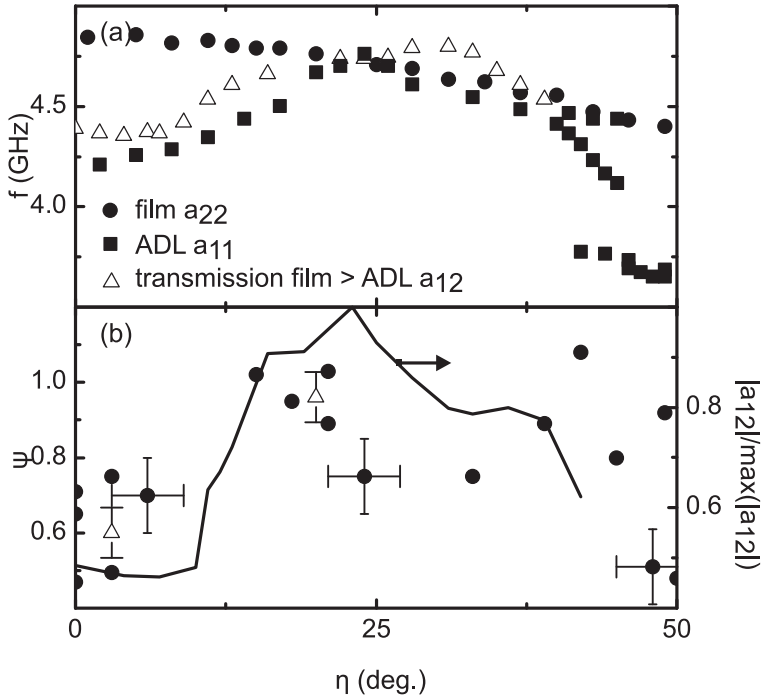
Figure 8.19: (a) Frequencies f_r of maximum signal amplitude as obtained from AESWS measurements. Sample is SN75-4-4. Full circles correspond to a_{22} reflection measurements on the CPW positioned above the plain film. Full squares correspond to a_{11} reflection measurements on the CPW positioned above the ADL. a_{12} corresponds to transmission measurements for spin waves emitted in the plain film and traveling into the ADL. For $\eta = 25°$ the frequencies of maximum amplitude are degenerated for all signals. (b) Data points (left axis) correspond to transmission ψ obtained from AESWS measurements (full circles) and micromagnetic simulation (open triangles). The full line (right axis) corresponds the maximum amplitude a_{12} of transmitted SWs.
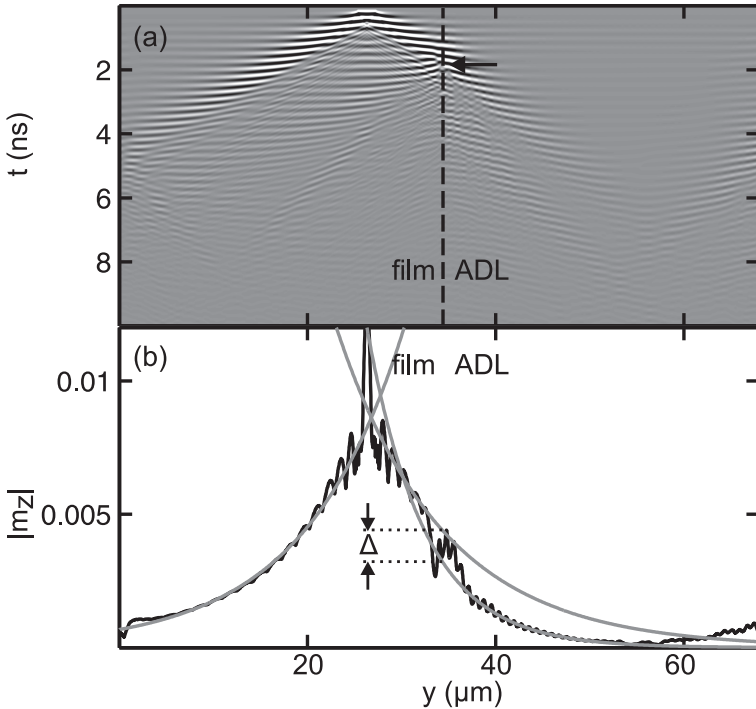
Figure 8.20: Micromagnetic simulation of spin-wave transmission from a plain film into an antidot lattice for $\mu_0 H = 20$ mT and $\eta = 1°$. Simulation parameters are set A. SWs up to 50 GHz are excited by a short field pulse at $26.0 \leq y \leq 28$ μm at $t = 0.1$ ns. (a) Spatio-temporal evolution of the dynamic out-of-plane precession amplitude m_z, where dark (bright) corresponds to large positive (negative) values. The film - ADL boundary is located at $y = 33$ μm as indicated by the dashed vertical line. Propagation of SWs towards this boundary and partial reflection is visible (horizontal arrow). (b) Maximum values of m_z taken over all times t (thick black line). This corresponds to the primary wave packets with highest amplitude. The light gray lines are exponential fits to the data. The offset marked Δ at the film - ADL boundary corresponds to backreflection.

(negative) values. The field pulse is centered around $y = 27\ \mu$m, the plain film is located at $y \leq y_b = 33\ \mu$m, and the the ADL lattice at $y > 33\ \mu$m. Propagation of SWs towards the film - ADL and partial reflection is visible (marked by the horizontal arrow). This data is further analyzed by plotting the amplitude $|m_z|$ (taken over all simulation times t) as plotted in Fig. 8.20 (b) as dark line. One finds that for $y < 27\ \mu$m the maximum signal amplitude decreases exponentially away from the excitation source. This is due to SW damping with increasing time and propagation distance.

The same decay is found for $27\ \mu$m $\leq y \lesssim 32\ \mu$m. The continuous light lines in Fig. 8.20 (b) mark exponential fits to the decay, according to $a_{\mathrm{film}}(y) = a_0 + A_0 \exp(-(y - y_0)/\zeta_{\mathrm{film}})$. One obtains $\zeta_{\mathrm{film}} = 0.10\ \mu$m^{-1}. The value of ζ_{film} depends on the values of α chosen for simulation. For $y \gtrsim 34\ \mu$m, the respective fit, see Fig. 8.20 (b), yields $\xi_{\mathrm{lattice}} = 0.17\ \mu$m^{-1}. At the boundary $y = y_b = 33\ \mu$m, locally the simulated maximum SW amplitudes deviate from the exponential decay. This is due to interface effects. Here the signal amplitudes of the fitted decay curves are evaluated to obtain the transmission

$$\psi = 1 - r = 1 - \frac{a_{\mathrm{lattice}}(y = y_b)}{a_{\mathrm{film}}(y = y_b)}. \tag{8.14}$$

Using Eq. 8.14, one finds for $\eta = 1°$ $\psi = 0.7 \pm 0.1$, in very good agreement with the data obtained by MOKE for $f > 4.5$ GHz.

Frequency resolved micromagnetic simulations

It is also possible to obtain data for ψ from simulations where only a single frequency is excited, i.e. using cw excitation. The simulation resembles the MOKE experiments explained in this section above. The respective spatio-temporal plot, corresponding to Fig. 8.20 for time resolved experiments, is plotted in Fig. 8.21 (a). SWs are excited by a sinusoidal driving field, e.g. as depicted for $f = 4.7$ GHz, which is spatially localized at $18.0 \leq y \leq 18.8\ \mu$m. For $t > 4$ ns a steady state is reached. Minima and maxima of $|m_z|$ are observed between the excitation source and the film-ADL boundary resulting from interference of the incident and reflected SWs. Extracting the maximum value $|m_z|$ from the steady state oscillations ($t > 4$ ns) yields the dark full line of Fig. 8.21 (b). This data is fitted with Eq. 8.11 (only adapted for the position of excitation signal and

film - ADL boundary being different in micromagnetic simulation than in the MOKE experiments) for $20 \ \mu\mathrm{m} \leq y \leq 30 \ \mu\mathrm{m}$, i.e. in the plain film between SW emitter and reflection boundary. The fitted curve is depicted as the light gray curve. From this, a transmission $\psi = 0.7$ is obtained. This value is depicted along with results for different f in Fig. 8.14 as full squares. The simulated data resembles the data obtained from MOKE well.

From the comparison of measured data of ψ (MOKE, full circles) and data for ψ obtained from micromagnetic simulation (full squares) on the one hand, with calculated data assuming an effective $M_{\mathrm{Sat}}^{\star} = 600 \ \mathrm{kA/m}$, one finds that the transmission ψ is well described by the assumption of an effectively continuous material for the ADL, i.e. reduced saturation magnetization. This is consistent with the finding that the dispersion $f(k)$ of SW propagating only through the $p = 800 \ \mathrm{nm}$ ADL is well described by the effectively continuous $M_{\mathrm{Sat}}^{\star} = 600 \ \mathrm{kA/m}$ as well.

Microscopically this finding is interpreted via strong dipolar coupling between SWs residing in neighboring stripes formed by the ADL. SWs separated by a row of holes oscillate in a coherent manner. However, SW profiles are affected by the periodic internal field modulation introduced by the holes. Considering, e.g., the limit of very large holes with very small hole to hole distances (small $\mathrm{Ni_{80}Fe_{20}}$ filling fraction $\mathcal{F}$, see Eq. 7.1), it is expected that a large fraction of the incident SWs is backreflected at the holes edges. Different to the case of small holes and SWs in the LWL regime as discussed here: while microscopically a rearrangement of the spin precession amplitude occurs when entering the antidot lattice, astonishingly good agreement is found for transmission macroscopically deduced from the assumption of a continuous material. It is therefore possible to consider this ADL as a MM for spin waves described by a reduced $M_{\mathrm{Sat}}^{\star}$.
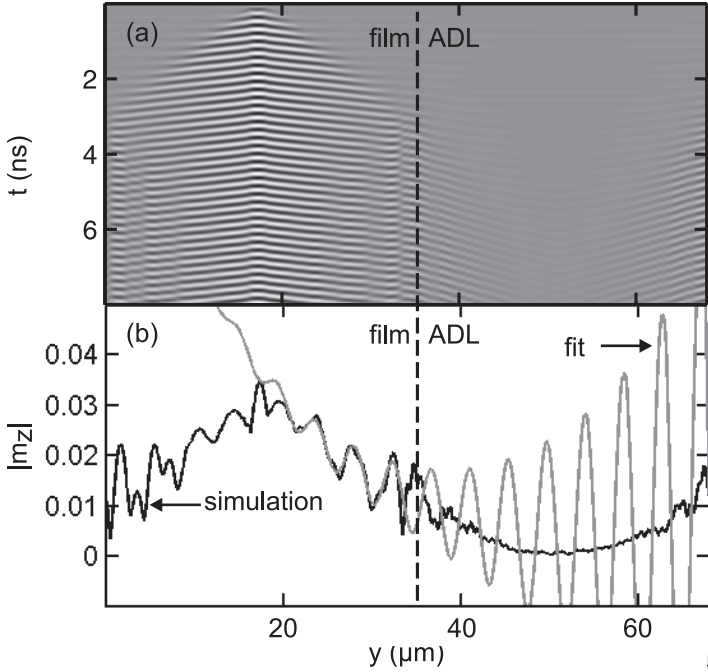
Figure 8.21: Micromagnetic simulation of spin-wave transmission from a plain film into an antidot lattice for $\mu_0 H = 20$ mT and $\eta = 1°$ for $f = 4.7$ GHz. Simulation parameters are set A. SWs are excited by a sinusoidal driving field of $f = 4.7$ GHz spatially localized at $18.0 \leq y \leq 18.8$ μm. (a) Spatio-temporal evolution of the dynamic out-of-plane precession amplitude m_z, where dark (bright) corresponds to large positive (negative) values. The film - ADL boundary is located at $y = 34.5$ μm as indicated by the dashed vertical line. For $t > 4$ ns a steady state is reached with an interference pattern of the primary and reflected wave visible for 20 μm $\leq y \leq 30$ μm. (b) Maximum values of m_z taken for 6 ns $\leq t \leq 8$ ns (thick black line). The light gray line is a fit to the data using Eq. 8.11 adapted to the simulated geometry for 20 μm $\leq y \leq 30$ μm. From this a transmission $\psi = 0.7$ is evaluated.

9 Summary and Outlook

In this thesis dynamic phenomena of spin waves (SWs) in antidot lattices (ADL) fabricated into $22-30$ nm thin films of $Ni_{80}Fe_{20}$ (permalloy) were investigated (saturation magnetization was experimentally determined as $M_{Sat} = 760 - 830$ kA/m). Samples were fabricated using focussed ion beam etching. The hole diameter was $d = 120$ nm. Primary focus was put on properties of propagating spin waves. Several measurement techniques were used to observe propagation characteristics, in particular the all-electrical spin-wave spectroscopy (AESWS) technique was developed further. Further measurement techniques employed as part of scientific collaboration were spatially resolved and time resolved magneto optical Kerr effect (MOKE) and Brillouin light scattering (BLS) technique for wave vector k resolution.

From the measurements a strong influence of, both, the ADL periodicity p and the SW wave vector k on the SW propagation properties was observed. Three different regimes, characterized by the relative magnitudes of p and k, were addressed.

- **Large p, large k: Anisotropic propagation**. A sample with $k \approx 2$ rad/μm and $p = 0.8$ μm was experimentally studied by AESWS and MOKE. The nanoscale SW emitter and detector allowed to confirm SW propagation for a broad regime of field magnitudes and alignments of the field $\mathbf{H}$ with the wave vector $\mathbf{k}$. Group velocity v_g and relaxation time τ were found to be strongly dependent on the orientation of the field with the wave vector. For the ADL one finds, e.g., $v_g = 3.5$ μm/ns ($\tau = 0.75$ ns) for $\sphericalangle(\mathbf{k}, \mathbf{H}) = 90°$ and $v_g = 2.5$ μm/ns ($\tau = 0.4$ ns) for $45° \leq \sphericalangle(\mathbf{k}, \mathbf{H}) \leq 65°$. The anisotropy is more pronounced if compared to an unpatterned film. Anisotropic propagation characteristics are attributed to the strong dependence of the spin wave's spatial profile on the external field orientation.

- **Large p, small k: Metamaterial limit.** An ADL sample with $k \approx 0.3$ rad/μm and $p = 0.8$ μm was experimentally studied by

AESWS and MOKE. SWs propagating through this sample behave as if the material is effectively continuous even though 1.7% of the material was removed and spin waves are quantized by the holes. In particular, a reduced saturation magnetization $M_{\mathrm{Sat}}^{\star} = 600 \ \mathrm{kA/m}$ was found to describe the propagation characteristics well. This value amounts to 79% of the plain film value. Moreover, this effectively continuous behavior also described well SW injection from a plain film into the ADL. The known wave vector mismatch between the two (effectively) continuous materials determines the transmission. Depending on the orientation of the external field $\mathbf{H}$ with the wave vector $\mathbf{k}$, the transmission was found to vary between 50% ($\triangleleft \left(\mathbf{k}, \mathbf{H} \right) = 90°$) and 100% ($\triangleleft \left(\mathbf{k}, \mathbf{H} \right) = 65°$). The microscopic rearrangement of the spatial SW amplitude due to the holes present in the ADL was, in particular, found not to inhibit the transmission.

- **Small p, small k: Magnonic limit.** A sample with $k \approx 0.6 - 1.0 \ \mathrm{rad}/\mu\mathrm{m}$ and $p = 0.3 \ \mu\mathrm{m}$ was studied by the AESWS and BLS techniques. SW modes, which are strongly localized at the holes' edges, were found to dynamically couple for a narrow regime of very defined alignment between wave vector and field, i.e. $\triangleleft \left(\mathbf{k}, \mathbf{H} \right) = 90° \pm 5°$. It is a specific advantage of the ADL geometry that this dipolar coupling occurs through ferromagnetic material and thus is comparably strong. The measured large SW velocities $v_{\mathrm{g}} = 5 - 6 \ \mu\mathrm{m/ns}$ close to the center of the Brillouin zone are a fingerprint of the strong dipolar magnonic coupling. The plane wave method allowed modeling of the devices, analysis of the miniband formation, and reproduced the experimental findings.

- **Small p, large k: Outlook.** Technological application of SWs becomes attractive for nanoscale devices. They will allow for large integration densities as well as for compensation of low SW group velocities. In order to harvest the rich functionality of nanostructured materials, this requires, both, nanoscale SW emitters (large k), as well as small nanostructures (small p).

Inductive excitation and detection of SWs becomes challenging for smaller and smaller antenna dimensions. This is because parasitic ohmic losses, as well as electromagnetic coupling for highly integrated electromagnetic circuitry begin to gain significance. A poten-

tial release to the excitation / detection problem might be to employ spin-transfer torque nano-oscillators as the source of the SWs.

To base future devices on the antidot lattice geometry was found to be promising: the large spin-wave velocities create novel perspectives in the field of nanoscale magnonic devices. Strong anisotropies allow to tune propagation parameters over a wide range by a small field change. Furthermore, it is generically easier to periodically remove material from a plain film, as done by focussed ion beam preparation in the course of this thesis, than to arrange individual magnetic elements in close vicinity. A promising next step is to tune the excitation spectrum of the SW antenna / receiver system to match directly the band gap of a nanoscale magnonic material.

A Appendix

A.1 List of Samples

Sample tag	Nanostructure	Details and CPW
SN89-4-D	Plain film	$w_{ic} = 2\ \mu\text{m}$, $s = 12\ \mu\text{m}$
SN75-4-4	Partially structured, $p = 0.8\ \mu\text{m}$ ADL	$w_{ic} = 4\ \mu\text{m}$, $s = 19.5\ \mu\text{m}$
SN88-1-A-M	$p = 0.8\ \mu\text{m}$ ADL	$w_{ic} = 340$ nm, $s = 6.5\ \mu\text{m}$
SN80-7-A	$p = 0.8\ \mu\text{m}$ ADL	$w_{ic} = 20\ \mu\text{m}$ standard CPW
SN80-7-C	$p = 0.4\ \mu\text{m}$ ADL	$w_{ic} = 20\ \mu\text{m}$ standard CPW
SN89-4-4	$p = 0.3\ \mu\text{m}$ ADL	$w_{ic} = 2\ \mu\text{m}$, $s = 12\ \mu\text{m}$
SN83-1-LO	$p = 0.8\ \mu\text{m}$ ADL	$w_{ic} = 2\ \mu\text{m}$, $s = 12\ \mu\text{m}$
SN87-5	$p = 0.8\ \mu\text{m}$ ADL	$w_{ic} = 2\ \mu\text{m}$, $s = 12\ \mu\text{m}$
SN87-4	Partially structured, $p = 0.8\ \mu\text{m}$ ADL	$w_{ic} = 4\ \mu\text{m}$
SN89-1-LO	$p = 0.3\ \mu\text{m}$ ADL	no CPW, optical only
SN89-1-RO	$p = 0.4\ \mu\text{m}$ ADL	no CPW, optical only
SN89-1-LU	$p = 0.16\ \mu\text{m}$ ADL	no CPW, optical only
SN89-1-RU	$p = 0.2\ \mu\text{m}$ ADL	no CPW, optical only
SN66-A-1-1	$p = 0.4\ \mu\text{m}$ ADL	$w_{ic} = 2\ \mu\text{m}$, $s = 12\ \mu\text{m}$
SN89-4-2	$p = 0.2\ \mu\text{m}$ ADL	$w_{ic} = 2\ \mu\text{m}$, $s = 12\ \mu\text{m}$
SN61-3-3	$p = 0.12\ \mu\text{m}$ ADL, $d = 86$ nm.	$w_{ic} = 2\ \mu\text{m}$ standard CPW
KT003-5	Plain film	$w_{ic} = 2\ \mu\text{m}$, $s = 12\ \mu\text{m}$
GD106-1-1	Plain film	$w_{ic} = 24\ \mu\text{m}$, $s = 19.5\ \mu\text{m}$
SN75-1-1	$p = 0.8\ \mu\text{m}$ ADL	$w_{ic} = 24\ \mu\text{m}$, $s = 19.5\ \mu\text{m}$
SN67-1-3	$p = 0.8\ \mu\text{m}$ ADL	$w_{ic} = 2\ \mu\text{m}$, $s = 12\ \mu\text{m}$ underneath Py
SN67-2-3	Plain film	$w_{ic} = 2\ \mu\text{m}$, $s = 12\ \mu\text{m}$ underneath Py
SN101-1-F-MR	$p = 1.0\ \mu\text{m}$ ADL	$w_{ic} = 2\ \mu\text{m}$, $s = 12\ \mu\text{m}$

A.2 List of Abbreviation

Abbreviation	Explicit	Details
DUT	Device under test	[Hie07]
VNA	Vector Network Analyzer	[Hie07]
AESWS	All electrical spin-wave spectroscopy	[Neu10]
PSWS	Propagating spin-wave spectroscopy	[Bai01]
SW	Spin wave	[Kal86]
FIB	Focussed ion beam	
ADL	Antidot lattice	[Neu08b]
MSSW	Magnetostatic surface spin wave	[Kal86]
MSBVW	Magneto static backward volume wave	[Kal86]
DE	Damon-Eshbach	[Kal86]
MOKE	Magneto optical Kerr effect	[Per08]
BLS	Brillouin light scattering	[Gub10]
Py	Permalloy	
PWM	Plane wave method	[Kra08]
1d	one dimensional	
2d	two dimensional	
3d	three dimensional	
AFM	Atomic force microscopy	[Bin86]
FMR	Ferromagnetic resonance	[Kit48]
em	Electromagnetic	
rf	Radio frequency	[Hie07]
S-Parameter	Scattering Parameter	[Hie07]
LWL	Long wavelength limit	
SEM	Scanning electron micrograph	
cw	continuous wave	
GaAs	Gallium Arsenide	
CMOS	complementary metal-oxide-semiconductor	[Raz01]
STNO	Spin-transfer torque nanoscale oscillator	[Kak05]
BZ	Brillouin zone	
MM	Metamaterial	
VNA-FMR	Vector network analyzer FMR	[Gie05b]
WKB	Wentzel-Kramer-Brillouin	[Neu08b]

A.3 Micromagnetic Simulation Parameter

Throughout this thesis, results of micromagnetic simulation are presented. The detailed simulation parameters are listed hereafter. When not stated explicitly below, the excitation of SWs is stated in the text.

Parameters which do not change are:

- Damping $\alpha = 0.005$.
- Exchange constant: $A = 1.6 \times 10^9$ J/m.
- Saved simulation timestep $\Delta\tau = 6$ ps.
- No crystal anisotropies.

Simulation parameter set A

Spatio-temporal resolved simulation for a $p = 800$ nm ADL.

- Saturation magnetization $M_{\mathrm{Sat}} = 760$ kA/m.
- Film thickness $t_{\mathrm{s}} = 25$ nm.
- Simulation cells $N = 48 \times 4096 \times 2$.
- Simulation cell size $\Omega = 16.7 \times 16.7 \times 12.5$ nm^3.
- Simulation duration: $T = 10$ ns.
- No out-of-plane anisotropy.

Spin waves are excited either by a short and spatially localized field pulse or by a spatially localized sinusoidal driving field of given frequency.

Simulation parameter set B

Temporal resolved simulation. This set of simulation parameters is used to simulate $p = 300$ nm ADL with uniform excitation.

- Saturation magnetization $M_{\mathrm{Sat}} = 760$ kA/m.
- Film thickness $t_{\mathrm{s}} = 22 - 25$ nm.
- Simulation cells $N = 96 \times 96 \times 2$.
- Simulation cell size $\Omega = 3.125 \times 3.125 \times 11$ nm^3.
- Simulation duration: $T = 8$ ns.
- No out-of-plane anisotropy.

Spin waves are excited by a spatially uniform, short field pulse.

Simulation parameter set C

Temporal resolved simulation. This set of simulation parameters is used to simulate $p = 800$ nm ADL with uniform excitation.

- Saturation magnetization $M_{\mathrm{Sat}} = 780$ kA/m.
- Film thickness $t_{\mathrm{s}} = 20.8$ nm.
- Simulation cells $N = 64 \times 64 \times 4$.
- Simulation cell size $\Omega = 12.5 \times 12.5 \times 5.2$ nm^3.
- Simulation duration: $T = 8$ ns.
- Out-of-plane anisotropy: 0.57 erg/cm.

Spin waves are excited by a spatially uniform, short field pulse.

Simulation parameter set D

Spatio-temporal resolved simulation for a $p = 300$ nm ADL.

- Saturation magnetization $M_{\mathrm{Sat}} = 760$ kA/m.
- Film thickness $t_{\mathrm{s}} = 22$ nm.
- Simulation cells $N = 32 \times 4096 \times 4$.
- Simulation cell size $\Omega = 9.375 \times 9.375 \times 5.5$ nm^3.
- Simulation duration: $T = 10$ ns.
- No out-of-plane anisotropy.

Spin waves are excited either by a short and spatially localized field pulse or by a spatially localized sinusoidal driving field of given frequency.

Simulation parameter set E

Spatio-temporal resolved simulation for a $p = 120$ nm ADL.

- Saturation magnetization $M_{\mathrm{Sat}} = 800$ kA/m.
- Film thickness $t_{\mathrm{s}} = 22$ nm.
- Simulation cells $N = 32 \times 32 \times 4$.
- Simulation cell size $\Omega = 3.75 \times 3.75 \times 5.5$ nm^3.
- Simulation duration: $T = 10$ ns.
- No out-of-plane anisotropy.

Spin waves are excited by a spatially uniform, short field pulse.
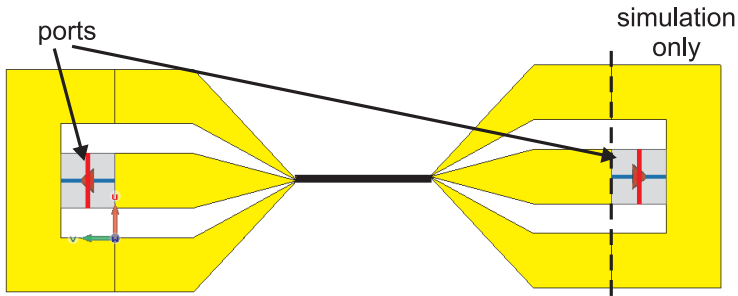
Figure A.1: Model of the CPW used for electromagnetic field simulations. Visible are the ports and the geometry used for mimicking the excitation through rf tips from above the CPW plane.

A.4 Electromagnetic Simulation Parameter

A great number of parameters enters the electromagnetic field parameter simulation. Not all of these parameters are known. Parameters are defined with respect to the software *Microwave Studio*[1].

Material and geometry parameters:

- Isolator thickness $t_{iso} = 15 - 35$ nm.
- Isolator permittivity is varied between $\epsilon_{iso} = 5 - 12$. Best agreement is obtained for $\epsilon_{iso} = 8$.
- The Py permeability is modeled according to a rf susceptibility with parameters $M_{Sat} = 800$ kA/m, $f_r = 6$ GHz, saturated along x axis.
- Py thickness $t_s = 30$ nm and CPW thickness 200 nm.
- Boundary conditions: beneath substrate: no transversal electric field. Otherwise: no transversal magnetic field.

Simulation parameters:

- Frequency domain solver, -40 dB accuracy.
- Hexahedral mesh, with 28-33 meshcells.
- Ports are modeled as 50 Ω discrete ports. A particular geometry is used to model the rf tip excitation in the experiment, see Fig. A.1.

---

[1]CST Corp., Darmstadt, Germany

List of Figures

Bibliography

[Ari99]   R. Arias and D. L. Mills: *Extrinsic contributions to the ferromagnetic resonance response of ultrathin films*, Phys. Rev. B **60**, 7395 (1999).

[AW99]   H. Al-Wahsh, A. Akjouj, B. Djafari-Rouhani, J. O. Vasseur, L. Dobrzynski and P. A. Deymier: *Large magnonic band gaps and defect modes in one-dimensional comblike structures*, Phys. Rev. B **59**, 8709 (1999).

[Bai88]   M. N. Baibich, J. M. Broto, A. Fert, F. N. Van Dau, F. Petroff, P. Etienne, G. Creuzet, A. Friederich and J. Chazelas: *Giant Magnetoresistance of (001)Fe/(001)Cr Magnetic Superlattices*, Phys. Rev. Lett. **61**, 2472 (1988).

[Bai01]   M. Bailleul, D. Olligs, C. Fermon and S. O. Demokritov: *Spin waves propagation and confinement in conducting films at the micrometer scale*, Europhys. Lett. **56**, 741 (2001).

[Bai03]   M. Bailleul, D. Olligs and C. Fermon: *Propagating spin wave spectroscopy in a permalloy film: A quantitative analysis*, Appl. Phys. Lett. **83**, 972 (2003).

[Bao08]   M. Bao, K. Wong, A. Khitun, J. Lee, Z. Hao, K. L. Wang, D. W. Lee and S. X. Wang: *Determining wave vector and material property from the phase-shift of spin-wave propagation*, Europhys. Lett. **84**, 27009 (2008).

[Bau11]   H. Bauer: *To be published.*, Ph.D. thesis (2011).

[Bay05]   C. Bayer, J. Jorzick, B. Hillebrands, S. O. Demokritov, R. Kouba, R. Bozinoski, A. N. Slavin, K. Y. Guslienko, D. V. Berkov, N. L. Gorn and M. P. Kostylev: *Spin-wave excitations in finite rectangular elements of $Ni_{80}Fe_{20}$*, Phys. Rev. B **72**, 064427 (2005).

[Ber91]   D. V. Berkov: *Micromagnetics of the single cylindrical particle*, J. Mag. Mag. Mat. **99**, L7 (1991).

[Ber93]   D. V. Berkov, K. Ramstcck and A. Hubert: *Solving Micromagnetic Problems. Towards an Optimal Numerical Method*, Phys. Stat. Sol. (a) **137**, 207 (1993).

[Ber96]   L. Berger: *Emission of spin waves by a magnetic multilayer traversed by a current*, Phys. Rev. B **54**, 9353 (1996).

[Ber98]   D. V. Berkov and N. L. Gorn: *Quasistatic remagnetization processes in two-dimensional systems with random on-site anisotropy and dipolar interaction: Numerical simulations*, Phys. Rev. B **57**, 14332 (1998).

[Ber08]   D. V. Berkov and N. L. Gorn: *Micromagus - software for micromagnetic simulations*, http://www.micromagus.de (2008).

[Bil07a]   C. Bilzer: *Microwave susceptibility of thin ferromagnetic films: metrology and insight into magnetization dynamics*, Ph.D. thesis, Faculte des sciences d'Orsay (2007).

[Bil07b]   C. Bilzer, T. Devolder, P. Crozat, C. Chappert, S. Cardoso and P. P. Freitas: *Vector network analyzer ferromagnetic resonance of thin films on coplanar waveguides: Comparison of different evaluation methods*, J. Appl. Phys. **101**, 074505 (2007).

[Bin86]   G. Binnig, C. F. Quate and C. Gerber: *Atomic Force Microscope*, Phys. Rev. Lett. **56**, 930 (1986).

[Blo29]   F. Bloch: *Über die Quantenmechanik der Elektronen in Kristallgittern*, Zeitschrift für Physik A Hadrons and Nuclei **52**, 555 (1929).

[Blu01]   S. Blundell: *Magnetism in Condensed Matter*, Oxford University Press, Oxford, 2001.

[Bue04]   M. Buess, R. Höllinger, T. Haug, K. Perzlmaier, U. Krey, D. Pescia, M. R. Scheinfein, D. Weiss and C. H. Back: *Fourier Transform Imaging of Spin Vortex Eigenmodes*, Phys. Rev. Lett. **93**, 077207 (2004).

[Cho06]   S. Choi, K.-S. Lee and S.-K. Kim: *Spin-wave interference*, Appl. Phys. Lett. **89**, 062501 (2006).

[Chu08]   A. V. Chumak, A. A. Serga, B. Hillebrands and M. P. Kostylev: *Scattering of backward spin waves in a one-dimensional magnonic crystal*, Appl. Phys. Lett. **93**, 022508 (2008).

[Chu09a]   A. V. Chumak, T. Neumann, A. A. Serga, B. Hillebrands and M. P. Kostylev: *A current-controlled, dynamic magnonic crystal*, J. Phys. D **42**, 205005 (2009).

[Chu09b]   A. V. Chumak, P. Pirro, A. A. Serga, M. P. Kostylev, R. L. Stamps, H. Schultheiss, K. Vogt, S. J. Hermsdoerfer, B. Laegel, P. A. Beck and B. Hillebrands: *Spin-wave propagation in a microstructured magnonic crystal*, Appl. Phys. Lett. **95**, 262508 (2009).

[Cou04]   G. Counil, J.-V. Kim, T. Devolder, C. Chappert, K. Shigeto and Y. Otani: *Spin wave contributions to the high-frequency magnetic response of thin films obtained with inductive methods*, J. Appl. Phys. **95**, 5646 (2004).

[Cov02]   M. Covington, T. M. Crawford and G. J. Parker: *Time-Resolved Measurement of Propagating Spin Waves in Ferromagnetic Thin Films*, Phys. Rev. Lett. **89**, 237202 (2002).

[Dem01]   S. O. Demokritov, B. Hillebrands and A. N. Slavin: *Brillouin light scattering studies of confined spin waves: linear and nonlinear confinement*, Physics Reports **348**, 441 (2001).

[Dem04a]   V. E. Demidov, S. O. Demokritov, B. Hillebrands, M. Laufenberg and P. P. Freitas: *Radiation of spin waves by a single micrometer-sized magnetic element*, Appl. Phys. Lett. **85**, 2866 (2004).

[Dem04b]   S. O. Demokritov, A. A. Serga, A. Andr, V. E. Demidov, M. P. Kostylev, B. Hillebrands and A. N. Slavin: *Tunneling of Dipolar Spin Waves through a Region of Inhomogeneous Magnetic Field*, Phys. Rev. Lett. **93**, 047201 (2004).

[Dem08]   V. E. Demidov, S. O. Demokritov, K. Rott, P. Krzysteczko and G. Reiss: *Nano-optics with spin waves at microwave frequencies*, Appl. Phys. Lett. **92**, 232503 (2008).

[Dem09] V. E. Demidov, M. P. Kostylev, K. Rott, P. Krzysteczko, G. Reiss and S. O. Demokritov: *Excitation of microwaveguide modes by a stripe antenna*, Appl. Phys. Lett. **95**, 112509 (2009).

[Dem10a] V. E. Demidov, M. Buchmeier, K. Rott, P. Krzysteczko, J. Münchenberger, G. Reiss and S. O. Demokritov: *Nonlinear Hybridization of the Fundamental Eigenmodes of Microscopic Ferromagnetic Ellipses*, Phys. Rev. Lett. **104**, 217203 (2010).

[Dem10b] V. E. Demidov, S. Urazhdin and S. O. Demokritov: *Direct observation and mapping of spin waves emitted by spin-torque nano-oscillators*, Nat. Mater. **9**, 984 (2010).

[Erc97] A. Ercole, A. O. Adeyeye, C. Daboo, J. A. C. Bland and D. G. Hasko: *Finite size effects in the static and dynamic magnetic properties of FeNi wire array structures*, J. Appl. Phys. **81**, 5452 (1997).

[Fli00] T. Fliessbach: *Quantenmechanik*, Spektrum Heidelberg Berlin, 2000.

[Gao10] H. Gao, W. Zhou and T. W. Odom: *Plasmonic crystals: a platform to catalog resonances from ultraviolet to near-infrared wavelengths in a plasmonic library*, Adv. Funct. Mater. **20**, 529 (2010).

[Ghi87] G. Ghione and C. Naldi: *Coplanar Waveguides for MMIC Applications: Effect of Upper Shielding, Conductor Backing, Finite-Extent Ground Planes, and Line-to-Line Coupling*, IEEE Trans. Micro. Theo. Tech. **35**, 260 (1987).

[Gie05a] F. Giesen: *Magnetization dynamics of nanostructured ferromagnetic rings and rectangular elements*, Ph.D. thesis, Universität Hamburg, Fachbereich Physik (2005).

[Gie05b] F. Giesen, J. Podbielski, T. Korn and D. Grundler: *Multiple ferromagnetic resonance in mesoscopic permalloy rings*, J. Appl. Phys. **97**, 10A712 (2005).

[Gie07] F. Giesen, J. Podbielski and D. Grundler: *Mode localization transition in ferromagnetic microscopic rings*, Phys. Rev. B **76**, 014431 (2007).

[Gil55] T. Gilbert: *A Lagrangian Formulation of the Gyromagnetic Equation of the Magnetization Field*, Phys. Rev. **100**, 1243 (1955).

[Gio07] L. Giovannini, F. Montoncello and F. Nizzoli: *Effect of interdot coupling on spin-wave modes in nanoparticle arrays*, Phys. Rev. B **75**, 024416 (2007).

[Gof01] C. Goffaux and J. P. Vigneron: *Theoretical study of a tunable phononic band gap system*, Phys. Rev. B **64**, 075118 (2001).

[Gri04] M. Grimsditch, L. Giovannini, F. Montoncello, F. Nizzoli, G. K. Leaf and H. G. Kaper: *Magnetic normal modes in ferromagnetic nanoparticles: A dynamical matrix approach*, Phys. Rev. B **70**, 054409 (2004).

[Gub02] G. Gubbiotti, G. Carlotti, F. Nizzoli, R. Zivieri, T. Okuno and T. Shinjo: *Magnetic properties of submicron circular permalloy dots*, IEEE Trans. Mag. **38**, 2532 (2002).

[Gub06] G. Gubbiotti, M. Madami, S. Tacchi, G. Carlotti and T. Okuno: *Normal mode splitting in interacting arrays of cylindrical permalloy dots*, J. Appl. Phys. **99**, 08C701 (2006).

[Gub07]   G. Gubbiotti, S. Tacchi, G. Carlotti, N. Singh, S. Goolaup, A. O. Adeyeye and M. Kostylev: *Collective spin modes in monodimensional magnonic crystals consisting of dipolarly coupled nanowires*, Appl. Phys. Lett. **90**, 092503 (2007).

[Gub10]   G. Gubbiotti, S. Tacchi, M. Madami, G. Carlotti, A. O. Adeyeye and M. Kostylev: *Brillouin light scattering studies of planar metallic magnonic crystals*, J. Phys. D **43**, 264003 (2010).

[Gue00]   I. Guedes, N. J. Zaluzec, M. Grimsditch, V. Metlushko, P. Vavassori, B. Ilic, P. Neuzil and R. Kumar: *Magnetization of negative magnetic arrays: Elliptical holes on a square lattice*, Phys. Rev. B **62**, 11719 (2000).

[Gul03]   Y. Gulyaev, S. Nikitov, L. Zhivotovskii, A. Klimov, P. Tailhades, L. Presmanes, C. Bonningue, C. Tsai, S. Vysotskii and Y. Filimonov: *Ferromagnetic films with magnon bandgap periodic structures: Magnon crystals*, JETP Lett. **77**, 567 (2003).

[Gur96]   A. Gurevich and G. Melkov: *Magnetization oscillations and waves*, CRC Press, Boca Raton, 1996.

[Gus02]   K. Y. Guslienko, S. O. Demokritov, B. Hillebrands and A. N. Slavin: *Effective dipolar boundary conditions for dynamic magnetization in thin magnetic stripes*, Phys. Rev. B **66**, 132402 (2002).

[Gus03]   K. Y. Guslienko, R. W. Chantrell and A. N. Slavin: *Dipolar localization of quantized spin-wave modes in thin rectangular magnetic elements*, Phys. Rev. B **68**, 024422 (2003).

[Har68]   K. J. Harte: *Theory of Magnetization Ripple in Ferromagnetic Films*, J. Appl. Phys. **39**, 1503 (1968).

[Hei85]   B. Heinrich, J. F. Cochran and R. Hasegawa: *FMR linebroadening in metals due to two-magnon scattering*, J. Appl. Phys. **57**, 3690 (1985).

[Her01]   R. Hertel: *Micromagnetic simulations of magnetostatically coupled Nickel nanowires*, J. Appl. Phys. **90**, 5752 (2001).

[Hey06]   L. J. Heyderman, F. Nolting, D. Backes, S. Czekaj, L. Lopez-Diaz, M. Kläui, U. Rüdiger, C. A. F. Vaz, J. A. C. Bland, R. J. Matelon, U. G. Volkmann and P. Fischer: *Magnetization reversal in cobalt antidot arrays*, Phys. Rev. B **73**, 214429 (2006).

[Hie07]   M. Hiebl: *Grundlagen der vektoriellen Netzwerkanalyse*, Rohde & Schwarz, 2007.

[Hub00]   A. Hubert and R. Schäfer: *Magnetic Domains - The Analysis of Magnetic Microstructures*, Springer, Berlin, 2000.

[Jac62]   J. D. Jackson: *Classical Electrodynamics*, John Wiley & Sons, New York, 1962.

[Jer10]   J. Jersch, V. E. Demidov, H. Fuchs, K. Rott, P. Krzysteczko, J. Münchenberger, G. Reiss and S. O. Demokritov: *Mapping of localized spin-wave excitations by near-field Brillouin light scattering*, Appl. Phys. Lett. **97**, 152502 (2010).

[Joa08]   J. D. Joannopoulos *et al.*: *Photonic Crystals: Molding the Flow of Light*, Princeton Univ. Press., Princeton, 2008, Second edn..

[Jor99]   J. Jorzick, S. O. Demokritov, C. Mathieu, B. Hillebrands, B. Bartenlian, C. Chappert, F. Rousseaux and A. N. Slavin: *Brillouin light scattering from quantized spin waves in micron-size magnetic wires*, Phys. Rev. B **60**, 15194 (1999).

[Jor02]   J. Jorzick, S. O. Demokritov, B. Hillebrands, M. Bailleul, C. Fermon, K. Y. Guslienko, A. N. Slavin, D. V. Berkov and N. L. Gorn: *Spin Wave Wells in Nonellipsoidal Micrometer Size Magnetic Elements*, Phys. Rev. Lett. **88**, 047204 (2002).

[Kak05]   S. Kaka, M. R. Pufall, W. H. Rippard, T. J. Silva, S. E. Russek and J. A. Katine: *Mutual phase-locking of microwave spin torque nano-oscillators*, Nature **437**, 389 (2005).

[Kal86]   B. Kalinikos and A. Slavin: *Theory of dipole-exchange spin wave spectrum for ferromagnetic films with mixed exchange boundary conditions*, J. Phys. C **19**, 7013 (1986).

[Kal06]   S. S. Kalarickal, P. Krivosik, M. Wu, C. E. Patton, M. L. Schneider, P. Kabos, T. J. Silva and J. P. Nibarger: *Ferromagnetic resonance linewidth in metallic thin films: Comparison of measurement methods*, J. Appl. Phys. **99**, 093909 (2006).

[Kam75]   V. Kambersky and C. E. Patton: *Spin-wave relaxation and phenomenological damping in ferromagnetic resonance*, Phys. Rev. B **11**, 2668 (1975).

[Ken07]   K. J. Kennewell, M. Kostylev and R. L. Stamps: *Calculation of spin wave mode response induced by a coplanar microwave line*, J. Appl. Phys. **101**, 09D107 (2007).

[Khi08a] A. Khitun, M. Bao, J. Lee, K. Wang, D. Lee, S. Wang and I. Roshchin: *Inductively Coupled Circuits with Spin Wave Bus for Information Processing*, J. Nanoelectr. Optoelctr. **3**, 24 (2008).

[Khi08b] A. Khitun, M. Bao, Y. Wu, J.-Y. Kim, A. Hong, A. Jacob, K. Galatsis and K. L. Wang: *Spin Wave Logic Circuit on Silicon Platform*, IEEE Comp. Soc. , 1107 (2008).

[Kis03]   S. I. Kiselev, J. C. Sankey, I. N. Krivorotov, N. C. Emley, R. J. Schoelkopf, R. A. Buhrman and D. C. Ralph: *Microwave oscillations of a nanomagnet driven by a spin-polarized current*, Nature **425**, 380 (2003).

[Kit48]   C. Kittel: *On the Theory of Ferromagnetic Resonance Absorption*, Phys. Rev. **73**, 155 (1948).

[Kos04]   M. P. Kostylev, A. A. Stashkevich and N. A. Sergeeva: *Collective magnetostatic modes on a one-dimensional array of ferromagnetic stripes*, Phys. Rev. B **69**, 064408 (2004).

[Kos05]   M. P. Kostylev, A. A. Serga, T. Schneider, B. Leven and B. Hillebrands: *Spin-wave logical gates*, Appl. Phys. Lett. **87**, 153501 (2005).

[Kos06]   M. P. Kostylev and N. A. Sergeeva: *Collective and individual modes on one dimensional bi-layered magnetic structures*, Transworld Research Network, Kerala, 2006.

[Kos08a]   M. Kostylev, G. Gubbiotti, G. Carlotti, G. Socino, S. Tacchi, C. Wang, N. Singh, A. O. Adeyeye and R. L. Stamps: *Propagating volume and localized spin wave modes on a lattice of circular magnetic antidots*, J. Appl. Phys. **103**, 07C507 (2008).

[Kos08b]   M. Kostylev, P. Schrader, R. L. Stamps, G. Gubbiotti, G. Carlotti, A. O. Adeyeye, S. Goolaup and N. Singh: *Partial frequency band gap in one-dimensional magnonic crystals*, Appl. Phys. Lett. **92**, 132504 (2008).

[Kos10]   M. P. Kostylev and A. A. Stashkevich: *Stochastic properties and Brillouin light scattering response of thermally driven collective magnonic modes on the arrays of dipole coupled nanostripes*, Phys. Rev. B **81**, 054418 (2010).

[Kra08]   M. Krawczyk and H. Puszkarski: *Plane-wave theory of three-dimensional magnonic crystals*, Phys. Rev. B **77**, 054437 (2008).

[Kru06]   V. Kruglyak and R. Hicken: *Magnonics: Experiment to prove the concept*, J. Mag. Mag. Mat. **306**, 191 (2006).

[Kru10]   V. V. Kruglyak, S. O. Demokritov and D. Grundler: *Magnonics*, J. Phys. D **43**, 264001 (2010).

[Kua05]   B. Kuanr, R. E. Camley and Z. Celinski: *Narrowing of the frequency-linewidth in structured magnetic strips: Experiment and theory*, Appl. Phys. Lett. **87**, 012502 (2005).

[Lee08]   K.-S. Lee and S.-K. Kim: *Conceptual design of spin wave logic gates based on a Mach–Zehnder-type spin wave interferometer for universal logic functions*, J. Appl. Phys. **104**, 053909 (2008).

[Lee09]   K.-S. Lee, D.-S. Han and S.-K. Kim: *Physical Origin and Generic Control of Magnonic Band Gaps of Dipole-Exchange Spin Waves in Width-Modulated Nanostrip Waveguides*, Phys. Rev. Lett. **102**, 127202 (2009).

[Leu93]   K. M. Leung: *Photonic Band Gaps and Localization*, Plenum Press, New York, 1993.

[Liu07]   Z. Liu, F. Giesen, X. Zhu, R. D. Sydora and M. R. Freeman: *Spin Wave Dynamics and the Determination of Intrinsic Damping in Locally Excited Permalloy Thin Films*, Phys. Rev. Lett. **98**, 087201 (2007).

[Mad10]   M. Madami, S. Tacchi, G. Gubbiotti, G. Carlotti, F. Montoncello, G. Capuzzo and F. Nizzoli: *Magnetic normal modes of elliptical NiFe nanoring studied by micro-focused Brillouin light scattering*, J. Phys. **200**, 042008 (2010).

[McP05]   S. McPhail, C. M. Gürtler, J. M. Shilton, N. J. Curson and J. A. C. Bland: *Coupling of spin-wave modes in extended ferromagnetic thin film antidot arrays*, Phys. Rev. B **72**, 094414 (2005).

[Mel01]   G. A. Melkov, Y. V. Kobljanskyj, A. A. Serga, V. S. Tiberkevich and A. N. Slavin: *Reversal of Momentum Relaxation*, Phys. Rev. Lett. **86**, 4918 (2001).

[Neu06a] I. Neudecker: *Magnetization Dynamics of Confined Ferromagnetic Systems*, Ph.D. thesis, Fakultät für Physik, Universität Regensburg (2006).

[Neu06b] I. Neudecker, M. Kläui, K. Perzlmaier, D. Backes, L. J. Heyderman, C. A. F. Vaz, J. A. C. Bland, U. Rüdiger and C. H. Back: *Spatially Resolved Dynamic Eigenmode Spectrum of Co Rings*, Phys. Rev. Lett. **96**, 057207 (2006).

[Neu08a] S. Neusser, B. Botters, M. Becherer, D. Schmitt-Landsiedel and D. Grundler: *Spin-wave localization between nearest and next-nearest neighboring holes in an antidot lattice*, Appl. Phys. Lett. **93**, 122501 (2008).

[Neu08b] S. Neusser, B. Botters and D. Grundler: *Spin wave modes in antidot lattices: Localization, confinement, and field-controlled propagation*, Phys. Rev. B **78**, 087825 (2008).

[Neu09] S. Neusser and D. Grundler: *Magnonics: Spin Waves on the Nanoscale*, Advanced Materials **21**, 2927 (2009).

[Neu10] S. Neusser, G. Duerr, H. G. Bauer, S. Tacchi, M. Madami, G. Woltersdorf, G. Gubbiotti, C. H. Back and D. Grundler: *Anisotropic Propagation and Damping of Spin Waves in a Nanopatterned Antidot Lattice*, Phys. Rev. Lett. **105**, 067208 (2010).

[Nib03] J. P. Nibarger, R. Lopusnik and T. J. Silva: *Damping as a function of pulsed field amplitude and bias field in thin film Permalloy*, Appl. Phys. Lett. **82**, 2112 (2003).

[Nol05] W. Nolting: *Grundkurs Theoretische Physik 4*, Springer, Berlin, 2005.

[Pat75] C. E. Patton, Z. Frait and C. H. Wilts: *Frequency dependence of the parallel and perpendicular ferromagnetic resonance linewidth in Permalloy films, 2-36 GHz*, J. Appl. Phys. **46**, 5002 (1975).

[Pec05] M. J. Pechan, C. Yu, R. L. Compton, J. P. Park and P. A. Crowell: *Direct measurement of spatially localized ferromagnetic-resonance modes in an antidot lattice (invited)*, J. Appl. Phys. **97**, 10J903 (2005).

[Pen00] J. B. Pendry: *Negative Refraction Makes a Perfect Lens*, Phys. Rev. Lett. **85**, 3966 (2000).

[Pen10] Y. Pennec, J. O. Vasseur, B. Djafari-Rouhani, L. Dobrzynski and P. A. Deymier: *Two-dimensional phononic crystals: Examples and applications*, Surf. Sci. Rep. **65**, 229 (2010).

[Per05] K. Perzlmaier, M. Buess, C. H. Back, V. E. Demidov, B. Hillebrands and S. O. Demokritov: *Spin-Wave Eigenmodes of Permalloy Squares with a Closure Domain Structure*, Phys. Rev. Lett. **94**, 057202 (2005).

[Per08] K. Perzlmaier, G. Woltersdorf and C. H. Back: *Observation of the propagation and interference of spin waves in ferromagnetic thin films*, Phys. Rev. B **77**, 054425 (2008).

[Pod06] J. Podbielski, F. Giesen and D. Grundler: *Spin-Wave Interference in Microscopic Rings*, Phys. Rev. Lett. **96**, 167207 (2006).

[Pon97]   G. E. Ponchak, E. M. Tentzeris and L. P. B. Katehi: *Characterization of finite ground coplanar waveguide with narrow ground planes*, International Journal of Microcircuits and Electronic Packaging **20**, 167 (1997).

[Pon98]   G. E. Ponchak, E. M. Tentzeris and L. P. B. Katehi: *Finite ground coplanar (FGC) waveguide: It's characteristics and advantages for use in RF and wireless communication circuits*, 3rd International Wireless Communications Conference (WCC 98) , 75 (1998).

[Pus03]   H. Puszkarski and M. Krawczyk: *Magnonic Crystals the Magnetic Counterpart of Photonic Crystals*, Sol. Stat. Phen. **94**, 125 (2003).

[Raz01]   B. Razavi: *Design of Analog CMOS Integrated Circuits*, McGraw-Hill, Boston, 2001.

[San99]   G. M. Sandler, H. N. Bertram, T. J. Silva and T. M. Crawford: *Determination of the magnetic damping constant in NiFe films*, J. Appl. Phys. **85**, 5080 (1999).

[Sch88]   M. E. Schabes and H. N. Bertram: *Magnetization processes in ferromagnetic cubes*, J. Appl. Phys. **64**, 1347 (1988).

[Sch04]   M. L. Schneider, A. B. Kos and T. J. Silva: *Finite coplanar waveguide width effects in pulsed inductive microwave magnetometry*, Appl. Phys. Lett. **85**, 254 (2004).

[Sch08a] T. Schneider, A. A. Serga, B. Leven, B. Hillebrands, R. L. Stamps and M. P. Kostylev: *Realization of spin-wave logic gates*, Appl. Phys. Lett. **92**, 022505 (2008).

[Sch08b] T. Schneider, A. A. Serga, T. Neumann, B. Hillebrands and M. P. Kostylev: *Phase reciprocity of spin-wave excitation by a microstrip antenna*, Phys. Rev. B **77**, 214411 (2008).

[Sch08c] H. Schultheiss, S. Schäfer, P. Candeloro, B. Leven, B. Hillebrands and A. N. Slavin: *Observation of Coherence and Partial Decoherence of Quantized Spin Waves in Nanoscaled Magnetic Ring Structures*, Phys. Rev. Lett. **100**, 047204 (2008).

[Sch10]   T. Schneider, A. A. Serga, A. V. Chumak, B. Hillebrands, R. L. Stamps and M. P. Kostylev: *Spin-wave tunnelling through a mechanical gap*, Europhys. Lett. **90**, 27003 (2010).

[Sek10]   K. Sekiguchi, K. Yamada, S. M. Seo, K. J. Lee, D. Chiba, K. Kobayashi and T. Ono: *Nonreciprocal emission of spin-wave packet in FeNi film*, Appl. Phys. Lett. **97**, 022508 (2010).

[Ser10]   A. A. Serga, A. V. Chumak and B. Hillebrands: *YIG magnonics*, J. Phys. D **43**, 264002 (2010).

[She01]   R. A. Shelby, D. R. Smith and S. Schultz: *Experimental Verification of a Negative Index of Refraction*, Science **292**, 77 (2001).

[Sil99]   T. J. Silva, C. S. Lee, T. M. Crawford and C. T. Rogers: *Inductive measurement of ultrafast magnetization dynamics in thin-film Permalloy*, J. Appl. Phys. **85**, 7849 (1999).

[Sim01]   R. N. Simons: *Coplanar Waveguide, Circuits, Components, And Systems*, John Wiley & Sons, New York, 2001.

[Sko08]   R. Skomski: *Simple Models of Magnetism*, Oxford University Press, Oxford, 2008.

[Sla54]   J. C. Slater and G. F. Koster: *Simplified LCAO Method for the Periodic Potential Problem*, Phys. Rev. **94**, 1498 (1954).

[Sta10]   R. L. Stamps: *Dynamic Magnetic Properties of Ferroic Films, Multilayers, and Patterned Elements*, Adv. Funct. Mater. **20**, 2380 (2010).

[Tac10a]   S. Tacchi, M. Madami, G. Gubbiotti, G. Carlotti, A. Adeyeye, S. Neusser, B. Botters and D. Grundler: *Magnetic Normal Modes in Squared Antidot Array With Circular Holes: A Combined Brillouin Light Scattering and Broadband Ferromagnetic Resonance Study*, IEEE Trans. Mag. **46**, 172 (2010).

[Tac10b]   S. Tacchi, M. Madami, G. Gubbiotti, G. Carlotti, A. O. Adeyeye, S. Neusser, B. Botters and D. Grundler: *Angular Dependence of Magnetic Normal Modes in NiFe Antidot Lattices With Different Lattice Symmetry*, IEEE Trans. Mag. **46**, 1440 (2010).

[Tac10c]   S. Tacchi, M. Madami, G. Gubbiotti, G. Carlotti, H. Tanigawa, T. Ono and M. P. Kostylev: *Anisotropic dynamical coupling for propagating collective modes in a two-dimensional magnonic crystal consisting of interacting squared nanodots*, Phys. Rev. B **82**, 024401 (2010).

[Top09]   J. Topp: *Magnetization Dynamics in Ferromagnetic Nanowires: From Single Structures to Magnonic Crystals*, Ph.D. thesis, Department Physik, Universität Hamburg (2009).

[Top10]   J. Topp, D. Heitmann, M. P. Kostylev and D. Grundler: *Making a Reconfigurable Artificial Crystal by Ordering Bistable Magnetic Nanowires*, Phys. Rev. Lett. **104**, 207205 (2010).

[Tri10]   D. Tripathy, P. Vavassori, J. M. Porro, A. O. Adeyeye and N. Singh: *Magnetization reversal and anisotropic magnetoresistance behavior in bicomponent antidot nanostructures*, Appl. Phys. Lett. **97**, 042512 (2010).

[Tse09]   D. H. Y. Tse, S. J. Steinmuller, T. Trypiniotis, D. Anderson, G. A. C. Jones, J. A. C. Bland and C. H. W. Barnes: *Static and dynamic magnetic properties of $Ni_{80}Fe_{20}$ square antidot arrays*, Phys. Rev. B **79**, 054426 (2009).

[Tso00]   M. Tsoi, A. G. M. Jansen, J. Bass, W.-C. Chiang, V. Tsoi and P. Wyder: *Generation and detection of phase-coherent current-driven magnons in magnetic multilayers*, Nature **406**, 46 (2000).

[Vas96]   J. O. Vasseur, L. Dobrzynski, B. Djafari-Rouhani and H. Puszkarski: *Magnon band structure of periodic composites*, Phys. Rev. B **54**, 1043 (1996).

[Vla10]   V. Vlaminck and M. Bailleul: *Spin-wave transduction at the submicrometer scale: Experiment and modeling*, Phys. Rev. B **81**, 014425 (2010).

[Vog09]   K. Vogt, H. Schultheiss, S. J. Hermsdoerfer, P. Pirro, A. A. Serga and B. Hillebrands: *All-optical detection of phase fronts of propagating spin waves in a $Ni_{81}Fe_{19}$ microstripe*, Appl. Phys. Lett. **95**, 182508 (2009).

[VV50]   J. H. Van Vleck: *Concerning the Theory of Ferromagnetic Resonance Absorption*, Phys. Rev. **78**, 266 (1950).

[Wan02]   Z. K. Wang, M. H. Kuok, S. C. Ng, D. J. Lockwood, M. G. Cottam, K. Nielsch, R. B. Wehrspohn and U. Gsele: *Spin-Wave Quantization in Ferromagnetic Nickel Nanowires*, Phys. Rev. Lett. **89**, 027201 (2002).

[Wan06]   C. C. Wang, A. O. Adeyeye and N. Singh: *Magnetic antidot nanostructures: effect of lattice geometry*, Nanotech. **17**, 1629 (2006).

[Wan09]   Z. K. Wang, V. L. Zhang, H. S. Lim, S. C. Ng, M. H. Kuok, S. Jain and A. O. Adeyeye: *Observation of frequency band gaps in a one-dimensional nanostructured magnonic crystal*, Appl. Phys. Lett. **94**, 083112 (2009).

[Wan10]   Z. K. Wang, V. L. Zhang, H. S. Lim, S. C. Ng, M. H. Kuok, S. Jain and A. O. Adeyeye: *Nanostructured Magnonic Crystals with Size-Tunable Bandgaps*, ACS Nano **4**, 643 (2010).

[Wei08]   T. Weiland, M. Timm and I. Munteanu: *A practical guide to 3-D simulation*, IEEE Microwave Mag. **9**, 62 (2008).

[Wol09]   G. Woltersdorf, M. Kiessling, G. Meyer, J.-U. Thiele and C. H. Back: *Damping by Slow Relaxing Rare Earth Impurities in $Ni_{80}Fe_{20}$*, Phys. Rev. Lett. **102**, 257602 (2009).

[Yu00]   C. T. Yu, H. Jiang, L. Shen, P. J. Flanders and G. J. Mankey: *The magnetic anisotropy and domain structure of permalloy antidot arrays* **87**, 6322 (2000).

[Yu04]   C. Yu, M. J. Pechan, W. A. Burgei and G. J. Mankey: *Lateral standing spin waves in permalloy antidot arrays*, J. Appl. Phys. **95**, 6648 (2004).

[Yu10]   J.-K. Yu, S. Mitrovic, D. Tham, J. Varghese and J. R. Heath: *Reduction of thermal conductivity in phononic nanomesh structures*, Nat. Nano **5**, 718 (2010).

[Yua92]   S. Yuan and H. Bertram: *Fast adaptive algorithms for micromagnetics*, IEEE. Trans. Mag. **28**, 2031 (1992).

Publications

- <u>S. Neusser</u>, B. Botter, D. Grundler: *Localization, confinement, and field-controlled propagation*, Phys. Rev. B **78**, 087825 (2008)

- <u>S. Neusser</u>, B. Botter, M. Becherer, D. Schmitt-Landsiedel, D. Grundler: *Spin-wave localization between nearest and next-nearest neighboring holes in an antidot lattice*, Appl. Phys. Lett. **93**, 122501 (2008)

- <u>S. Neusser</u>, D. Grundler: *Magnonics: Spin Waves on the Nanoscale*, Adv. Mat. **21**, 2927 (2009)

- R. Huber, P. Klemm, <u>S. Neusser</u>, B. Botters, A. Wittmann, M. Weiler, S.T.B. Goennenwein, C. Heyn, M. Schneider, P. Böni, D. Grundler: *Advanced techniques for all-electrical spectroscopy on spin caloric phenomena*, Sol. Stat. Comm. **150**, 492 (2009)

- S. Tacchi, M. Madami, G. Gubbiotti, G. Carlotti, A.O.A. Adeyeye, <u>S. Neusser</u>, B. Botters, D. Grundler: *Magnetic Normal Modes in Squared Antidot Array With Circular Holes: A Combined Brillouin Light Scattering and Broadband Ferromagnetic Resonance Study*, IEEE Trans. Mag., **46**, 172 (2010)

- S. Tacchi, M. Madami, G. Gubbiotti, G. Carlotti, A.O.A. Adeyeye, <u>S. Neusser</u>, B. Botters, D. Grundler: *Angular Dependence of Magnetic Normal Modes in NiFe Antidot Lattices With Different Lattice Symmetry*, IEEE Trans. Mag., **46**, 1440 (2010)

- <u>S. Neusser</u>, G. Dürr, H. G. Bauer, S. Tacchi, M. Madami, G. Woltersdorf, G. Gubbiotti, C.H. Back, D. Grundler: *Anisotropic Propagation and Damping of Spin Waves in a Nanopatterned Antidot Lattice*, Phys. Rev. Lett. **105**, 067208 (2010)

Acknowledgements

I would like to express gratitude to all people who contributed to this work. In particular:

- Prof. Dr. Harald Friedrich for supervision of the PhD examination, Prof. Dr. Dirk Grundler for being the first examiner, Prof. Dr. Rudolf Gross for being the second examiner.
- Prof. Dr. Dirk Grundler for giving me the possibility to work at E10, fruitful supervision, and insights into the methods of science far in excess than could be expected.
- Munich coworkers Markus Becherer, Bernhard Botters, Florian Brandl, Georg Dürr, Rupert Huber, Philippe Klemm, Thomas Schwarze, Klaus Thurner for collaborative efforts.
- FP7 collaborators, in particular Dr. Dimitri Berkov, Dr. Gianluca Gubbiotti, Dr. Maciej Krawczyk, Dr. Volodymyr Kruglyak, Dr. Marco Madami, Dr. M.L. Sokolovskyy, and Dr. Silvia Tacchi for scientific exchange and discussions. I want to thank the Perugia group (Dr. Gianluca Gubbiotti, Dr. Marco Madami, Dr. Silvia Tacchi) for performing the BLS measurements and the Poznan group (Dr. Maciej Krawczyk and Dr. M.L. Sokolovskyy) for performing the PWM calculations.
- Collaborators at Universität Regensburg: Prof. Dr. Christian Back, Dr. Georg Woltersdorf and specially Hans Bauer for scientific exchange and discussions and performing the MOKE measurements.
- E10 technical staff, in particular Thomas Rapp, for the very valuable help on short notice.
- Prof. Alexander Holleitner and Peter Weiser for providing access to and continuous maintenance of the nanolithography facilities. Claudia Paulus for operating the laser writer.
- Dr. Paul Berberich for help and advice in all situations encountered.
- Roswitha Hoppen and Claudine Völcker for organizational support.
- Everybody at E10 for the good work atmosphere.
- My wife, my parents, and my brother for the mental support and good times.